

**An Extensive
Case Study on the
Dispersibility
Parameters of HI-
Assisted Reduced
Graphene Oxide
and its Graphene
Oxide Precursor**

MSc Thesis

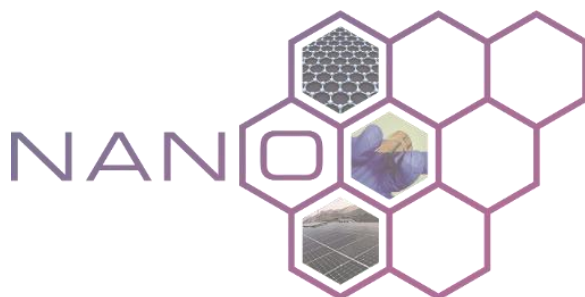
Katerina
Anagnostou

Preface:

The presented MSc thesis was realised in the laboratory of the Nanomaterials for Printed Electronics and Energy Devices Group (NANO-Group) at the Hellenic Mediterranean University (HMU) in Heraklion under the supervision and guidance of Dr. Minas Stylianakis and Prof. Emmanuel Kymakis. All experiments and material preparations were carried out on location at the laboratories of NANO Group with the exception of some measurements which were performed at the Institute of Electronic Structure and laser (IESL) housed in the Foundation for Research & Technology-Hellas (FORTH) and the University of Cyprus.

Acknowledgements:

I would like to dedicate this thesis to my parents and my grandparents, who have supported and encouraged me in every way possible throughout my academic journey. I would like to thank Prof. Emmanuel Kymakis and NANO Group for providing the environment and tools to accomplish the work presented here. A special thank you to Dr. Minas Stylianakis who provided guidance and insight throughout the course of this project. I would like to thank Grigoris Atsalakis who proved to be a capable and reliable laboratory partner and offered his assistance freely during the entirety of this work. Finally, I would like to thank Dr. George Kenanakis from the Institute of Electronic Structure and laser (IESL) housed in the Foundation for Research & Technology-Hellas (FORTH) and Dr. Athanasios Skouras of the European University of Cyprus, whose assistance was employed for measurements not possible at NANO laboratories.



Abstract

In this work, the optimal dispersibility conditions of chemically prepared graphene oxide (GO) and reduced graphene oxide (RGO) has been extensively investigated in 25 different organic and inorganic solvents. Graphite oxide was prepared chemically from graphite powder via modified Hummers' method. It was then dispersed with an initial concentration of 0.5 mg/ml in 25 different solvents using ultrasonic probe to create GO suspensions. Likewise, reduced graphite oxide, which was chemically prepared from graphite oxide using hydroiodic acid and acetic acid and dispersed in the same 25 solvents. All dispersions were centrifugated and left for 2 weeks before measurements and characterisation in order to insure stability of the suspended materials. The difference in the dispersion behaviour of these two materials was investigated by determining the final concentration of GO and RGO in each solvent through Beer-Lamberts law after determining the maximum absorbance via UV-Vis spectroscopy. The use of an ultrasonic probe is an improvement on previous investigations of the dispersion behaviour of GO and RGO, which achieved liquid exfoliation using an ultrasonic bath. Concentrations of up to 189 µg/ml for GO and 87 µg/ml for RGO were achieved in de-ionised water and o-dichlorobenzene respectively. The Hansen Solubility Parameters (HSP) of GO and RGO were calculated in hopes of providing insight into their affinity for these solvents for future work. An attempt to measure the zeta-potential of each dispersion in order to evaluate their stability was made. These characterisations, however, were not feasible due to intense agglomeration of GO and/or RGO occurring in some dispersions during the measurement of both GO and RGO. Finally, the average flake size distribution and polydispersity indices of GO and RGO in all solvents were estimated using dynamic light scattering (DLS), as a quality control of the effect of a solvent's nature on the dispersion behavior of the materials.

Περίληψη:

Στην παρούσα εργασία πραγματοποιήθηκε εκτεταμένη μελέτη των ιδανικών συνθηκών διασποράς του οξειδίου του γραφενίου και του ανηγμένου οξειδίου του γραφενίου σε 25 διαφορετικούς διαλύτες. Αρχικά, οξείδιο του γραφίτη παρασκευάστηκε χημικά μέσω τροποποιημένης μεθόδου Hummers και διασπάρθηκε με χρήση ακίδας υπερήχησης σε 25 διαφορετικούς διαλύτες με αποτέλεσμα την δημιουργία 25 εναιωρημάτων οξειδίου του γραφενίου (GO). Η ίδια διαδικασία επαναλήφθηκε με ανηγμένο οξείδιο του γραφίτη το οποίο παρασκευάστηκε ανάγοντας οξείδιο του γραφίτη με υδροϊώδιο και οξικό οξύ και έπειτα διασπάρθηκε στους ίδιους 25 διαλύτες με αποτέλεσμα τη δημιουργία 25 εναιωρημάτων ανηγμένου οξειδίου του γραφενίου (RGO). Όλα τα εναιωρήματα υπόκειντο σε φυγοκέντρηση και αφέθηκαν για 2 βδομάδες ώστε να εξασφαλιστεί η σταθερότητα των διεσπαρμένων σωματιδίων. Στη συνέχεια διερευνήθηκε η διαφορά της συμπεριφοράς διασποράς των δύο αυτών γραφενικών δομών με υπολογισμό της συγκέντρωσης του κάθε εναιωρήματος μέσω του νόμου Beer-Lambert μετά από τον προσδιορισμό της μέγιστης απορρόφησης με φασματοφωτομετρία υπεριώδους-ορατού (UV-Vis). Η χρήση ακίδας υπερήχησης αποτελεί βελτίωση προηγούμενης παρεμφερούς εργασίας στην οποία η διασπορά πραγματοποιήθηκε με χρήση λουτρού υπερήχων. Η μέγιστη συγκέντρωση για εναιώρημα GO ήταν 189 μg/ml σε απιονισμένο νερό, ενώ για RGO ήταν 87 μg/ml σε ο-διχλωροβενζόλιο. Έπειτα, υπολογίστηκαν οι παράμετροι διαλυτότητας Hansen με σκοπό την ερμηνεία της συγγένειας των GO και RGO προς τους επιλεγμένους διαλύτες. Πραγματοποιήθηκε προσπάθεια μέτρησης του ζ-δυναμικού κάθε εναιωρήματος χωρίς αποτελέσματα λόγω ισχυρών φαινομένων συσσωμάτωσης των στερεών. Τέλος, μετρήθηκε η μέση τιμή μεγέθους και ο δείκτης πολυδιασποράς του κάθε εναιωρήματος μέσω της μεθόδου δυναμικής σκέδασης φωτός (Dynamic Light Scattering, DLS) με σκοπό την αξιολόγηση της επιρροής που έχει ο διαλύτης στην ποιότητα και σταθερότητα του εναιωρήματος.

Contents

Abbreviations list: -----	3
Chapter 1: Carbon and Carbon Allotropes-----	4
1.1. Carbon: -----	4
1.1. Hybridisation of carbon: -----	5
1.2. Carbon Allotropes -----	7
1.2.1. Diamonds: -----	8
1.2.2. Fullerenes: -----	9
1.2.3. Nanotubes: -----	10
1.2.4. Graphite: -----	11
1.2.5. Graphene:-----	13
Chapter 2: Graphene -----	15
2.1. Structure of graphene -----	15
2.2. Preparation of graphene-----	17
2.2.1. Top-down methods:-----	17
2.2.2. Bottom-up methods:-----	21
2.3. Properties of Graphene: -----	22
2.3.1. Thickness-Flexibility -----	23
2.3.2. Conductivity/Electron mobility -----	23
2.3.3. Thermal conductivity-----	26
2.3.4. Hardness/strength-----	26
2.3.5. Transparency-----	26
2.3.6. Absorption-----	27
2.4. Absorption Coefficient of Graphene, GO and RGO: -----	28
Chapter 3: Graphene Oxide -----	31
3.1. Structure of Graphene Oxide: -----	31
3.2. Preparation of graphite oxide and graphene oxide -----	35
3.2.1. Top-down methods:-----	35
3.2.2 Bottom-up methods -----	39
Chapter 4: Reduced Graphene Oxide -----	41
4.1. Preparation of reduced graphene oxide: -----	41
4.1.1. Thermal reduction: -----	41
4.1.2. Chemical reduction: -----	43

Chapter 5: Applications of graphene and graphene derivatives	49
5.1. Electronics	49
5.1.1. Photovoltaic cells:	49
5.1.2. Gas sensing:	50
5.1.3. Light Emitting Diodes (LEDs):	51
5.2. Energy storage	53
5.2.1. Batteries:	53
5.2.2. Supercapacitors:	53
5.3. Biomedical applications	54
5.3.1. Biosensing:	54
5.3.2. Drug delivery systems:	56
5.3.3. Tissue engineering:	58
5.4. Environmental:	60
5.4.1. Water treatment and filtration:	60
5.4.2. Decontamination:	62
Chapter 6: Investigating the liquid processability of GO and RGO	65
6.1. Importance of liquid processable graphene-based materials-Past work	65
6.2. Investigating the dispersibility of GO and RGO with the Hansen Solubility Parameters:	67
6.2.1. The past: Hildebrand Solubility Parameter	68
6.2.2. The present: The Hansen Solubility Parameters:	75
6.2.3. Hansen Solubility Parameters-The Basics:	76
6.2.4. Three-dimensional Hansen’s Space-The HSP Sphere:	79
6.2.5. Hansen’s Solubility Parameters and Graphene Derivatives:	81
Chapter 7: Experimental Section	84
7.1. Preparation of Graphite Oxide:	90
7.2. Preparation of Reduced Graphite Oxide:	99
7.3. Characterisation of prepared materials:	101
7.3.1. FT-IR Spectroscopy:	101
7.3.2. Raman Spectroscopy:	103
7.4. Preparation of GO and RGO dispersions with liquid phase ultrasonic exfoliation:	108
Chapter 8: Characterisation-Results-Discussion	115
8.1. Optical observation:	115

8.2.	Absorption measurement via UV-Vis Spectroscopy:-----	116
8.3.	Calculation of Hansen solubility Parameters of GO and RGO:-----	134
8.3.1.	Investigating the final concentrations of GO and RGO dispersions:-----	138
8.3.2.	Investigating the calculated HSP for GO and RGO:-----	140
8.3.3.	Investigating the calculated Ra values:-----	146
8.4.	Zeta potential measurements-----	150
8.5.	Dynamic Light Scattering measurements-----	152
8.5.1.	Particle Size Distribution-----	152
8.5.2.	Polydispersity Index-----	165
8.6.	Scanning electron microscopy (SEM):-----	168
8.6.1.	Sample Preparation:-----	169
8.6.2.	SEM Images:-----	170
Chapter 9:	Conclusions-----	173
Chapter 10:	Future work-----	176
References:	-----	178

Abbreviations list:

All abbreviations featured in this thesis are presented below with their full meaning in alphabetical order. Not included are the abbreviations for the solvents and the reagents used, as they are listed separately in Table 4 and in Table 4 respectively in Chapter 7.

AC-TEM	Aberration corrected Transmission Electron Microscopy
AFM	Atomic Force Microscopy
CNTs	Carbon Nano Tubes
CVD	Chemical Vapour Deposition
DDS	Drug Delivery System
DLS	Dynamic Light Scattering
E_F	Fermi level
FET	Field-Effect transistor
FRET	Fluorescence-Resonance-Energy Transfer
FT-IR	Fourier-Transform Infrared Spectroscopy
GO	Graphene Oxide
HP	Hildebrand Parameter
HSP	Hansen Solubility Parameters
ITO	Indium Tin Oxide
LED	Light Emitting Diode
PEG	Polyethylene Glycol
RGO	Reduced Graphene Oxide
SEM	Scanning Electron Microscopy
TEM	Transmission Electron Microscopy
XPS	X-ray Photoelectron Microscopy
ΔE_F	Fermi level shift

Chapter 1: Carbon and Carbon Allotropes

1.1. Carbon:

Carbon is a non-metal and the lightest element of the 4th periodic table group with an atomic number of 6 and an atomic weight of 12.011 amu. Carbon occurs naturally as carbon-12 (^{12}C) which makes up almost 99 percent of the carbon in the universe; carbon-13 (^{13}C) which makes up about 1 percent; and carbon-14 (^{14}C), which makes up a minuscule amount of overall carbon but is very important in dating organic objects and is a radioactive isotope with a half-life time of about 5730 years [1]. Carbon is the fourth most abundant element of our solar system and comprises a large percentage of all living organisms. The number of carbon-based compounds, otherwise known as organic compounds, is so vast, that there is a whole branch of chemistry dedicated to their study i.e. organic chemistry. The reason that all life on Earth is carbon based is due to carbon's ability to form four covalent chemical bonds via four valence electrons. It can form single, double or triple bonds with other atoms which are very stable due to carbon's small atomic radius [2].

Carbon does not stabilise in its atomic form as this form is very short-lived. Therefore, carbon stabilises in various multi-atomic structures known as carbon allotropes. Carbon allotropes that occur naturally are amorphous carbon, graphite and diamonds [3]. These two materials, although are both composed of pure carbon, have extremely different both in appearance and physiochemical properties. Graphite has an opaque, metallic, dark grey color whereas diamonds are remarkably transparent and reflect light making them shine brilliantly. Graphite has a rating of 1-2 on the Mohs hardness scale, is rather inexpensive at about \$0.50 per gram and is mainly used as pencil charcoal or as a lubricant. Diamonds on the other hand has a 10 rating on the Mohs hardness scale making them the hardest known natural substance on Earth. They are also the fourth most expensive material with a cost of \$55,000 to \$108,000 per gram depending on the carat value. Graphite shows high electrical conductivity owing to the free movement of electrons [4]. In diamonds on the other hand, the electrons are

spatially confined making them excellent electrical insulators [5]. The reason graphite and diamonds are so fundamentally different despite them both being comprised of only carbon atoms, is the structure of the carbon atoms themselves. Graphite has a layered, planar structure in which the carbon atoms are linked covalently, and the layers are held together via weak Van der Waals interactions. In the case of diamonds, the carbon atoms form a diamond cubic crystal structure (Figure 1). There are more carbon allotropes both natural and synthetic such as fullerenes and nanotubes. All these forms of carbon will be further analysed in the chapter “carbon allotropes”.

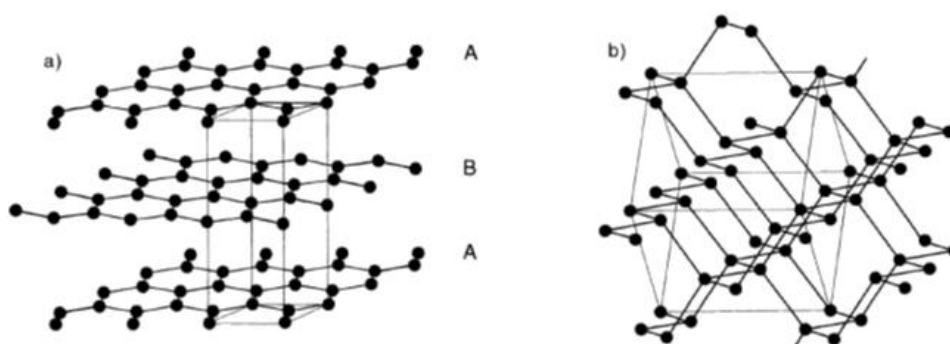


Figure 1 Crystallographic structures of the two most representative natural carbon allotropes: (a)hexagonal graphite (b) cubic face centered diamond. Image taken from reference 16.

1.1. Hybridisation of carbon:

The extraordinary properties of carbon nanomaterials can be traced from the hybridization of carbon; electrons in the innermost shell of carbon atoms make up an electron ‘core’ adequately enclosed to allow the outer electrons to mix with other atoms to form linear or one-dimensional (1D), plane or two-dimensional (2D) and tetrahedral or three dimensional (3D) materials.

The electronic structure of the carbon atom in the ground state is: $1s^2, 2s^2, 2p_x^1, sp_y^1$ (Figure 2). In the ground state the carbon atom only has two valance electrons available, yet it is able to form four covalent bonds. This is possible due to hybridisation of the carbon atom.

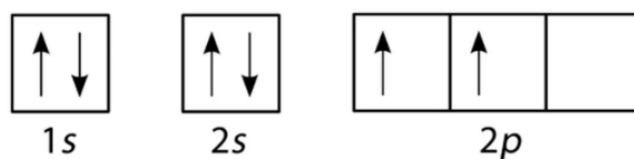


Figure 2 Orbital diagram of carbon atom. Image source: chem.libretexts.org

For the carbon atom to form four covalent bonds, four unpaired electrons are needed. These unpaired electrons are made available when one electron is transferred from the 2s to the $2p_z$ orbital creating the electronic structure: $1s^2, 2s^1, 2p_x^1, 2p_y^1, 2p_z^1$. This is the excited state of the carbon atom (Figure 4). The 2s and 2p orbitals of the carbon atom can hybridise forming sp^x hybridised orbitals. When the 2s orbital hybridises with one of the three 2p orbitals, two sp hybridised orbitals are created. When the 2s orbital hybridises with two of the three 2p orbitals, then three sp^2 hybridised orbitals are formed. Lastly, when the 2s orbital hybridises with three 2p orbitals, it leads to the formation of four sp^3 hybridised orbitals. Hybridisation is the reason that carbon can form four covalent bonds, even though in the ground state it only has two available valence electrons.

Depending on the type of hybridisation, the carbon atoms are linked together forming different structures with covalent bonds of various lengths and angles. This is why the carbon atoms in methane create a tetrahedral structure forming H-C-H bonds with a 109.5° angle, whereas in ethylene they create a planar structure with C-C-H or H-C-H bonds with an average angle of about 120° and, finally, in acetylene the C atoms form a linear molecule with a C-C-H angle of 180° (Figure 3).

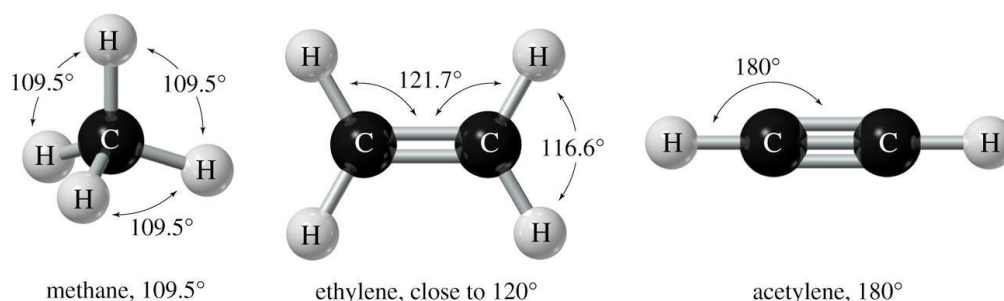


Figure 3 Molecular structure of methane, ethylene and acetylene. Image source: Organic Chemistry, 9th Edition, Leroy G. Wade, Jan W. Simek.

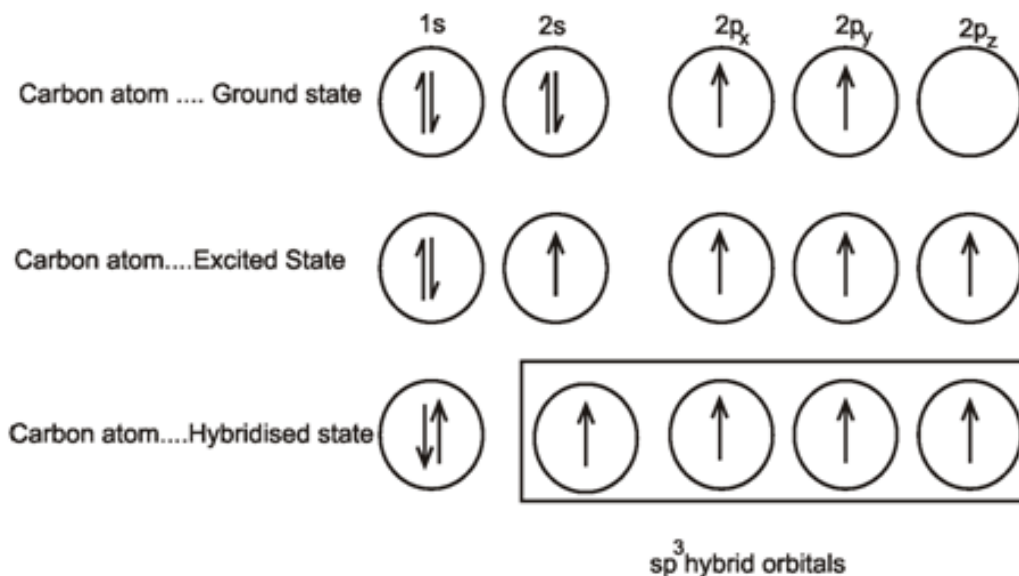


Figure 4 Carbon atom orbitals in the a) Ground state b) excited state and c) hybridised state.

1.2. Carbon Allotropes

Carbon allotropes can appear naturally or be created through synthetic procedures. It should be mentioned that there exist several virtual allotropes of carbon such as L-carbon [6], Novamene [7] and the K_4 crystal [8]. These are purely theoretical predictions and have not been proven experimentally. The carbon allotropes that this thesis will mention are graphite and, consequently graphene, diamonds, fullerenes and carbon nanotubes with the main focus lying in graphene (Figure 5).

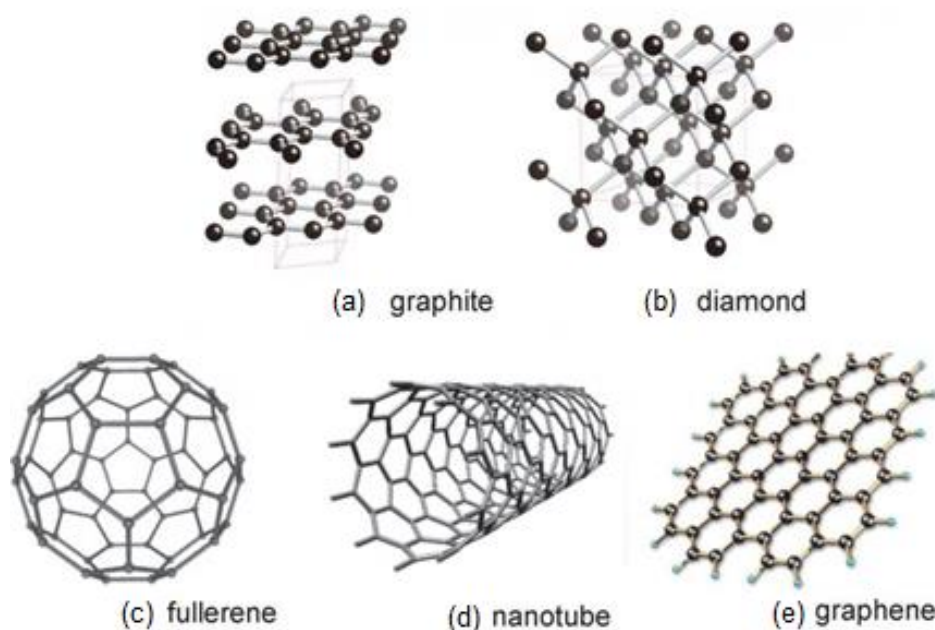


Figure 5: Carbon allotropes (a) graphite and (b) diamond, the two 3D allotropes. (c) fullerene (0D), (d) carbon nanotube (1D) and (e) graphene (2D). Image taken from reference 9.

1.2.1. Diamonds:

Most of the group four elements in the periodic table exist in tetrahedral bonding, that is, each atom in a crystal has four neighbouring atoms surrounding it in a pyramid arrangement. In the case of carbon, this material is a diamond. In the diamond structure every carbon atom is linked via strong covalent sp^3 bonds with four other carbon atoms forming a regular tetrahedron as shown in **Error! Reference source not found. b)**. The crystal structure is cubic face centred. The cubic diamond phase is known not only for its aesthetically pleasing appearance and high value, but also for its unique hardness and stability under high pressure. A hexagonal form of diamond known as a Lonsdaleite diamond exists with the same crystal symmetry as hexagonal graphite but with different site locations and a smaller interplanar separation [10]. In the Lonsdaleite structure the bonds between the carbon atoms are tetrahedrally linked but in eclipsed conformation which defines the axis of hexagonal symmetry. The building blocks that form a cubic and Lonsdaleite diamond respectively as well as the resulting lattices are shown in Figure 6.

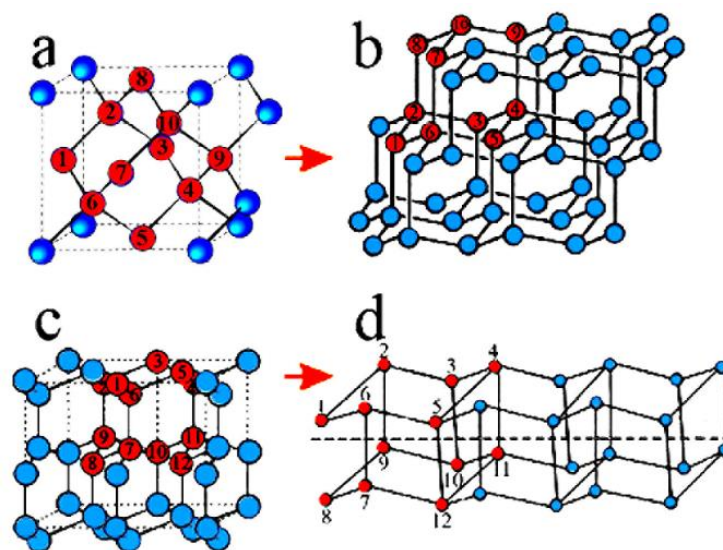
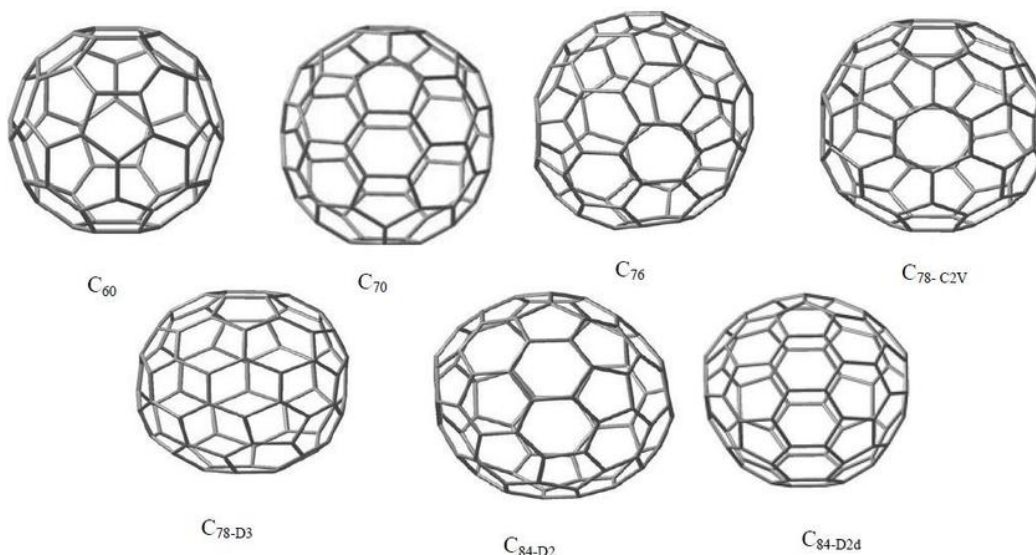


Figure 6 Multiplication of building blocks of diamond. a) Unit cell of cubic diamond with two interpenetrating face-centered cubic lattices b) Multiplication of C10 (adamantane) units forming cubic diamond c) Unit cell structure of hexagonal lattice d) C12 build

1.2.2. Fullerenes:

Fullerenes consist of 20 hexagonal and 12 pentagonal carbon rings forming a closed cage structure with icosahedral symmetry. Each carbon atom is sp^2 hybridised and is linked to three neighbouring carbon atoms via sp^2 - sp^2 covalent bonds. It crystallises at room temperature in a cubic face centred system. The C_{60} fullerene molecule has two bond lengths - the 6:6 ring bonds can be considered "double bonds" and are shorter than the 6:5 bonds. C_{60} is not "super-aromatic" as it tends to avoid double bonds in the pentagonal rings, resulting in poor electron delocalisation. As a result, C_{60} behaves like an electron deficient alkene, and reacts readily with electron rich species. The electronic bonding factors in the structure account for the stability of the molecule. In theory, an infinite number of fullerenes can exist, their structure based on pentagonal and hexagonal rings, constructed according to rules for making icosahedra. Because of this high molecular symmetry C_{60} has attracted a lot of interest in physics and chemistry. Because of this high molecular symmetry C_{60} has attracted a lot of interest in physics and chemistry. The next fullerenes beyond C_{60} that satisfy the isolated pentagon rule are C_{70} and C_{76} . Currently significant or small quantities of C_{70} , C_{76} ,

C_{78} and C_{84} have been isolated (Figure 7). The structure and properties of these higher mass fullerenes are now under study. Finally, a C_{36} molecule has also been detected experimentally which shows that new molecular forms of carbon have yet to be discovered [11].



*Figure 7 Structure of C_{60} , C_{70} , C_{76} , C_{78} , C_{84} fullerenes including two isomers for C_{78} and C_{84} .
Image taken from reference 12.*

1.2.3. Nanotubes:

Carbon nanotubes (CNTs) are long, needle-like cylinders of carbon resulting from graphene sheets being rolled up (Figure 8). They were discovered in 1991 by Sumio Iijima [13]. Typical carbon nanotubes are 1-25 nm across with a length up to 1 μm . They consist of 1-50 graphene cylinders wrapped around each other along a common long axis. Those consisting of one graphene sheet are single layer CNTs and those comprised of two or more sheets are multiple wall CNTs in which there are carbon cylinders wrapped inside other carbon cylinders. As shown by transmission electron microscopy (TEM) these nanotubes with different diameters can be either capped or open [16]. CNTs are large macromolecules that are unique for their size, shape, and remarkable physical properties. These molecules have a very broad range of electronic, thermal, and structural properties that change depending on the different diameter, length, and chirality. There has been significant practical interest in the conductivity of CNTs. Their conductivity has

been proved to be a function of their diameter as well as their chirality (degree of twist). CNTs can be either semi-conducting or metallic in their electrical behavior.

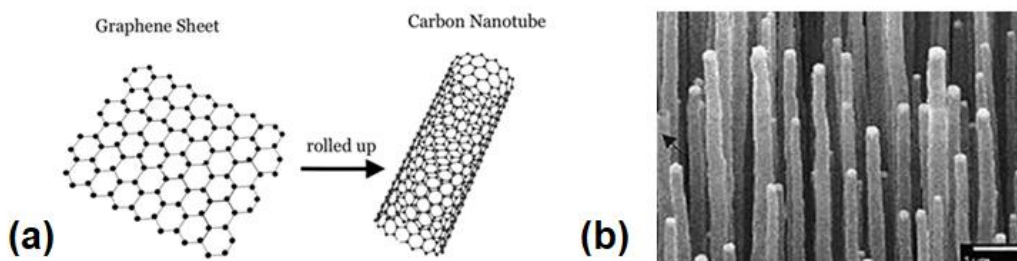


Figure 8 (a) Carbon nanotube as a result of rolled graphene. (b) SEM image of aligned carbon nanotubes. Image taken from reference 14.

1.2.4. Graphite:

Graphite was discovered and named around 1789 by Abraham Gottlob Werner. He named it from the Greek word “graphein”, meaning to ‘write’ or to ‘draw’. Graphite can be classified into both natural and synthetic categories. It occurs naturally i.e. in metamorphic and igneous rocks or can be synthesised in the lab from petroleum coke and coal tar pitch. Various graphite forms within the same classification vary considerably in crystallinity; hence, natural graphite is further sub-divided into flake (crystalline), vein (lump) and microcrystalline (amorphous) graphite, with flake graphite being the form most commonly found in nature [18]. SEM images of these three natural graphite forms are shown in Figure 9 [15].

Flake graphite occurs as individual, flat plate-like particles (flakes) with hexagonal edges when unbroken or irregular edges when broken. They are generally classified according to flake size with diameters ranging from 50 to 800 μm and thicknesses from 1 to 150 μm . Lump graphite, occurs in filling fissures, the cracks in rocks, and in veins in metamorphic or igneous rocks. This type of natural graphite has forms that range in size, from fine powder to lumps of 10. Amorphous graphite or microcrystalline graphite is a coal or soot with no defined crystal structure. It occurs in metamorphic anthracite coal beds or in carbonaceous sedimentary rocks in the form of extremely fine crystalline grains. Its graphite content ranges from 25 to 85%, depending on geological conditions of the source.

It is a form of natural graphite with a high degree of graphitisation and microcrystals oriented in different directions.

The high degree of graphitisation of amorphous graphite led to the accidental discovery of synthetic graphite by Edward Goodrich Acheson Tamashausky, (2006). He discovered synthetic graphite while manufacturing silicon carbide. Essentially, there are two forms of synthetic graphite, which are produced differently. The first form is electro-graphite, which has high carbon content and is produced from petroleum coke calcined at 1300°C. It is then crushed, and the blended particles are mixed with binder pitch and extruded to get a green artefact, which is then graphitised at 2800°C, in an electric furnace. The other form is produced from heating petroleum pitch calcined at 2800°C; the resulting synthetic graphite has low density, high porosity and high resistance. However, thermal heating under pressure of materials produced through chemical vapour deposition (CVD) yields synthetic graphite known as highly oriented pyrolytic graphite. Synthetic graphites are polycrystalline materials with variable degrees of crystallite perfection, crystallite dimensions and preferred orientation. They also vary with regard to properties such as electrical resistivity, porosity and optical texture (Ragan & Marsh, (1983). Graphite products can be moulded into diverse shapes and sizes based on their application. Synthetic graphite tends to be of higher purity, lower density, higher porosity and higher electrical resistance than naturally occurring graphite. Synthetic Graphite consists mainly of graphitic carbon that has been obtained by graphitization.

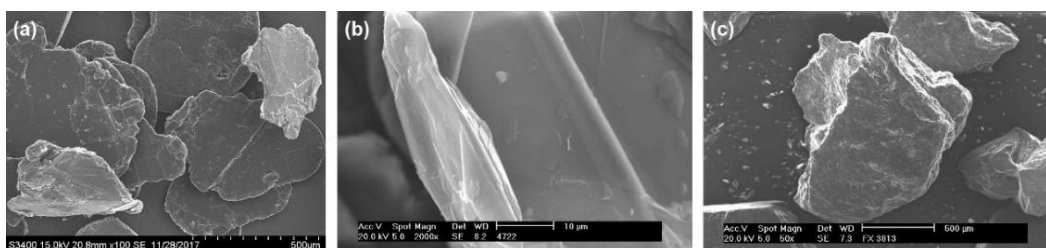


Figure 9 SEM images of (a) flake graphite, (b) vein graphite and (c) amorphous graphite. Image taken from reference 15.

Graphite has a layered, planar structure. The individual two-dimensional layers are called graphene. In each layer, the carbon atoms are arranged in a

“honeycomb” lattice in which six carbon atoms are linked to form hexagons. The carbon atoms are bonded covalently with a bond length of 0.142 nm. The 2D planes are held together via Van der Waals interactions with a distance of 0.335 nm [16]. The weak Van der Waals forces allow layers of graphite to be easily separated, or to slide past each other [17]. The atoms in graphite bond in such a way that only three of the four potential bonding sites satisfied. The fourth electron is free to migrate in the plane, making graphite electrically conductive. However, it does not conduct in a direction at right angles to the plane.

There are two known forms of graphite, α -graphite which has a hexagonal structure and β -graphite with a rhombohedral structure. Both α and β -graphite have very similar physical properties, the only difference being that the graphene layers stack slightly differently, as seen in Figure 10 [18,19]. The alpha graphite may be either flat or buckled [20]. The two forms of graphite are interchangeable with suitable processing [21].

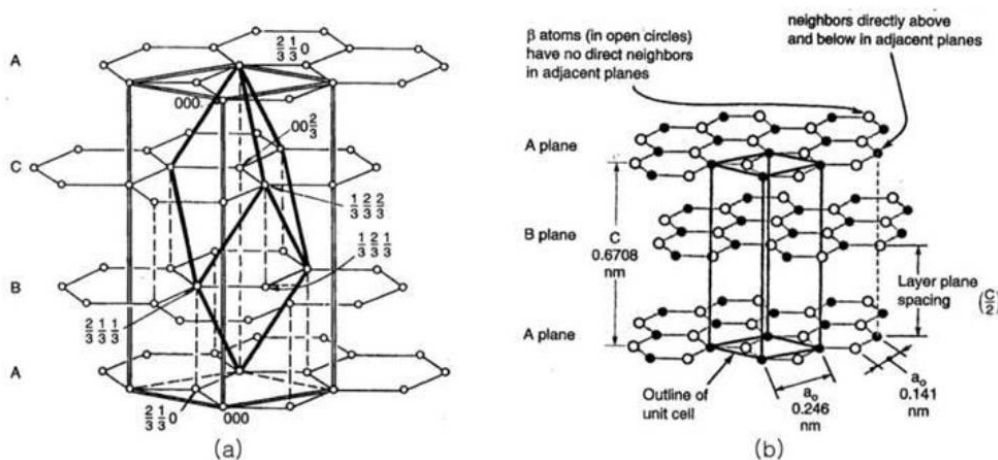


Figure 10 Stacking arrangement of the layers in (a) α -graphite (hexagonal) and (b) β -graphite (rhombohedral). Image taken from reference 18.

1.2.5. Graphene:

Graphene is the two-dimensional form of graphite. When the Van der Waals forces that develop between the individual graphite sheets are overcome, the result is a single sheet of graphene with a thickness of one carbon atom. This

carbon allotrope will be discussed in detail, including structure, properties and preparation methods in Chapter 2. Graphene can be functionalised with heteroatoms to produce new materials with new and tunable properties. For example, these heteroatoms can be oxygen. When graphene is oxidised, the result is graphene oxide, a material with a different structure and properties to its precursor. Graphene oxide can be reduced either mechanically or chemically to remove some of the oxygen atoms, resulting in reduced graphene oxide, a material that has intermediate structural characteristics and properties. Both graphene oxide (GO) and reduced graphene oxide (RGO) will be discussed in chapters 3 and 4 respectively.

Chapter 2: Graphene

2.1. Structure of graphene

The carbon atoms in graphene are arranged in a hexagonal lattice forming a planar monolayer in which the atoms create a two-dimensional (2D) honeycomb structure. The length of the carbon-carbon (C-C) bond is about 0.142 nm and each hexagonal carbon ring has an area of 0.052 nm² [22]. The C-C linking is the result of the overlap of two sp² orbitals (one from each C atom) forming a σ bond and two p orbitals perpendicular to the lattice plane forming a π bond. More specifically, there are three σ bonds in each lattice with strong connections forming a stable hexagonal structure. The electrical conductivity of graphene is mostly attributed from the π bond located vertically to the lattice plane. Graphene's stability is due to its tightly packed carbon atoms and a sp² orbital hybridization—a combination of orbitals s, p_x, and p_y that constitute the σ -bond. The final p_z electron makes up the π -bond. The π -bonds hybridise together to form the π -band and π^* -bands. These bands are responsible for most of graphene's notable electronic properties, via the half-filled band that permits free-moving electrons. The structure of graphene is extremely stable even though the thickness of a single layer is only 0.35 nm. The bonding between the carbon atoms is strong enough to endure external force by a twisting lattice plane while avoiding the reconfiguration of atoms. The edge of graphene can be classified into zigzag and armchair structures according to different carbon chains as shown in Figure 11 (b) [22]. The variety in edges leads to various conducting behaviours. A graphene nanoribbon with a zigzag edge usually behaves like a metal while a nanoribbon with an armchair edge could conduct electricity like either metal or a semiconductor. Graphene imaging can be achieved by Scanning Electron Microscopy (SEM), as demonstrated by Figure 12.

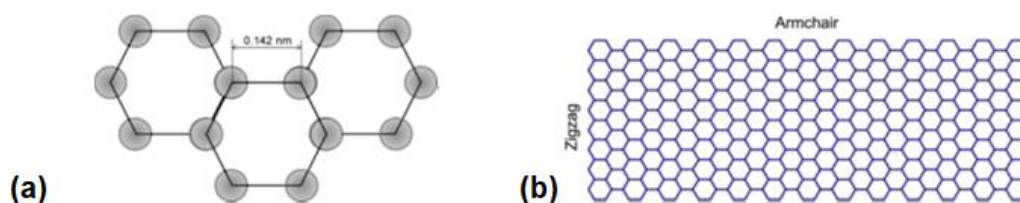


Figure 11 (a) Covalent C-C bond length in graphene (b) Zigzag and armchair edges of a graphene layer. Image taken from reference 22.

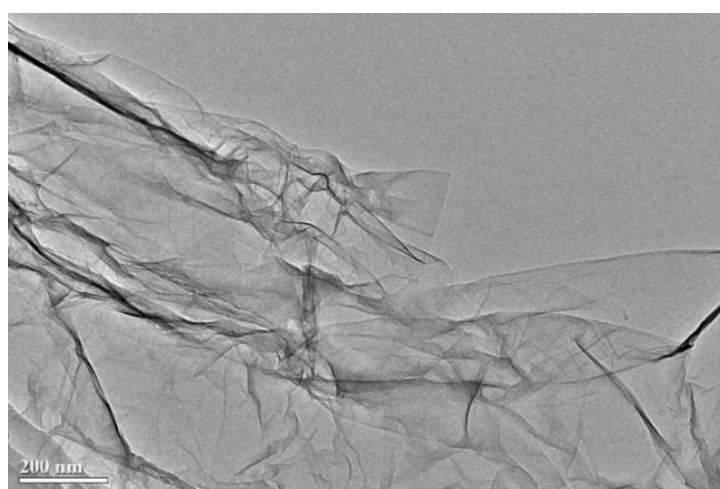


Figure 12 SEM image of single layer graphene. Scalebar: 200nm. Image source: ACS Material Advanced Chemical Supplier (www.acsmaterial.com).

The morphology of a graphene layer can be revealed by Atomic Force Microscopy (AFM). Figure 13 shows an AFM image of single layer CVD-grown graphene taken by Zhao et al. on a silicon wafer substrate [23]. The graphene surface is dominated by micron-sized wrinkles that are 2–6 nm in height. In addition to the wrinkles, there are also many particles, several nanometres in height, which are residues of the poly (methyl methacrylate) polymer that was used to transfer the graphene onto the silicon wafer and should be ignored. The thickness of the graphene layer was measured and found to be about 0.9 nm.

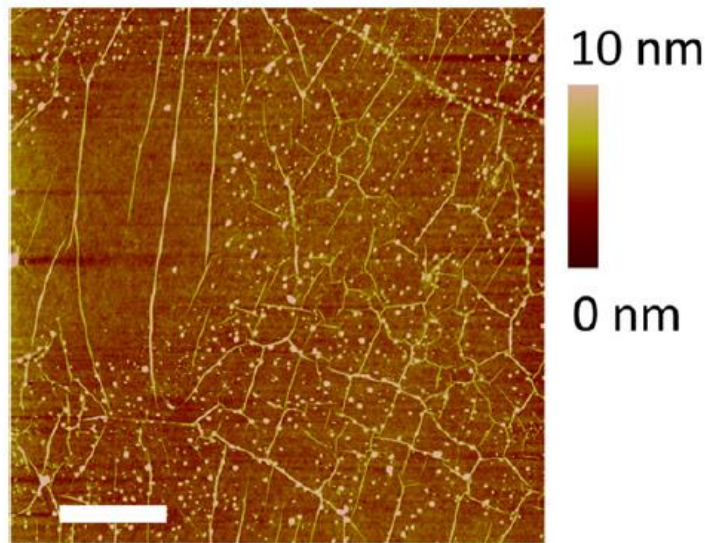


Figure 13 AFM image of single layer graphene prepared by CVD on a silicon wafer. Scalebar: 1 μm . Image taken from reference [23].

2.2. Preparation of graphene

2.1.1. Top-down methods:

- **Mechanical Exfoliation:** Graphene was first prepared in 2004 by Kostya Novoselov and Andre Geim and their co-workers by detaching it directly from a graphite crystal. This is a micromechanical exfoliation method which is widely known as the Scotch™ tape method. This low-cost isolation method is the what initiated the rapid growth of interest for graphene [42]. In this exfoliation method, adhesive tape is used to peel the graphite crystal resulting in multiple layer graphene remaining on the adhesive tape. By repeating it the peeling process the multi-layer graphene is cleaved into flakes of varying size. The tape is then attached to the desired substrate and the glue is dissolved, e.g. by acetone, to detach and remove the tape. Finally, one last peeling with a new piece of adhesive tape is performed to result in single layer graphene on the substrate. In this method, the size of the graphene flakes cannot be controlled.

- Liquid phase exfoliation-Dispersion: Graphite can be dispersed in a suitable organic solvent e.g. dimethyl formamide (DMF) or N-Methyl-2-pyrrolidone (NMP) to produce large amounts of graphene in liquid phase [24], a method which allows for upscaling in graphene production. The organic solvent must have similar surface energy to that of graphite in order to achieve sufficient dispersibility. Similar surface energy reduces the energy barrier which must be overcome in order to detach a graphene layer from the graphite crystal [25]. The exfoliation of graphite in the organic solvent is induced by an external source such as ultrasonic frequencies (Figure 14a).

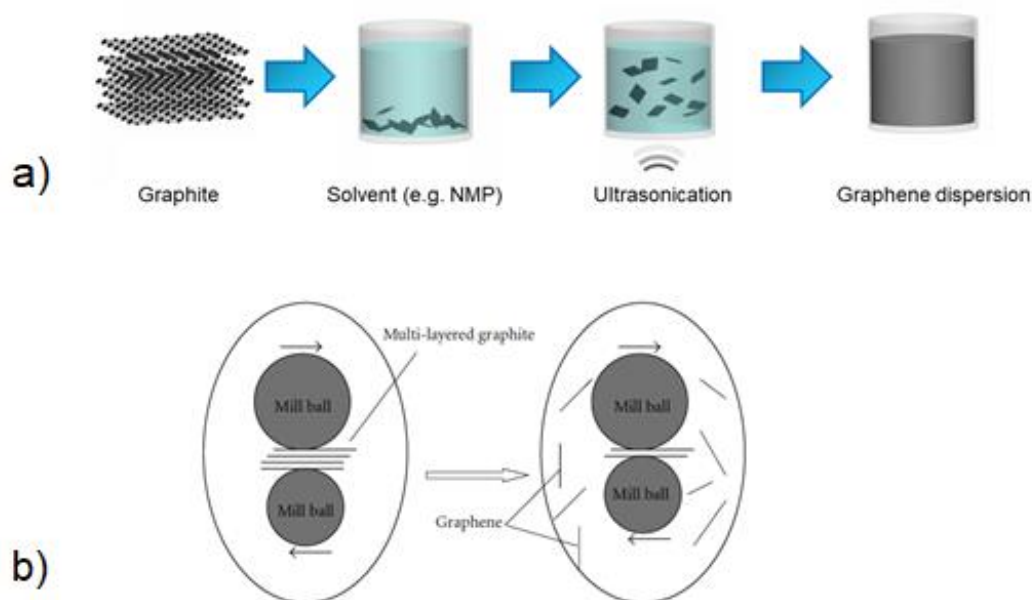


Figure 14 Schematic representation of: a) Preparation of liquid phase graphene assisted by ultrasonication of graphite in an organic solvent and b) Graphite exfoliation with wet ball-milling method.

An alternative method for separating the graphene layers is wet ball-milling, as (Figure 14b) [26]. Graphene can also be dispersed in water with the use of suitable surfactants, such as sodium cholate, which make the graphene suspensions more stable (Figure 15) [27]. Alternatively, external voltage can be applied to an ionic solution containing graphite, thus achieving electrochemical exfoliation in the liquid phase [Error! Bookmark not defined.]. In either case, the

resulting dispersion must be centrifuged to dispose of the larger, heavier flakes in the form of a sediment. As with mechanical exfoliation, the size of the resulting graphene flakes cannot be controlled with this method. However, it does allow for the preparation of large amounts of graphene.

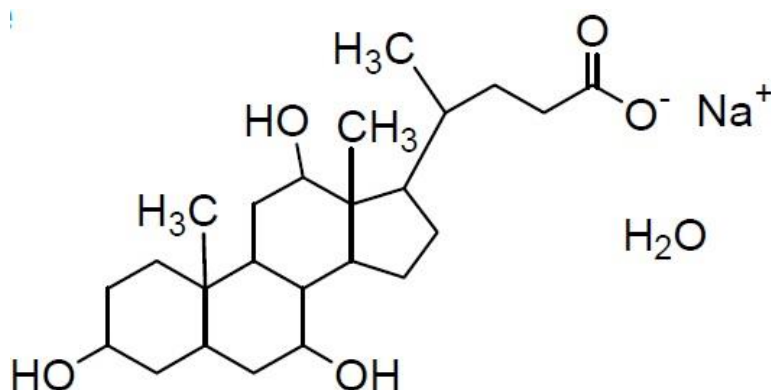


Figure 15 Chemical structure of sodium cholate; a surfactant used to maintain graphene suspended in water. Image taken from: www.dojindo.eu.com

- Graphite Oxide Exfoliation and Reduction: Graphene can also be synthesised through reduction of graphene oxide. Graphite oxide is exfoliated via sonication in liquid phase to produce graphene oxide (GO), usually in water since graphene oxide is highly hydrophilic owing to the oxygen functional groups. The GO sheets become negatively charged and electrical repulsion inhibits the recombination of the layers. Once the GO dispersion is centrifuged, it is reduced either thermally or chemically [28] to produce liquid phase graphene. However, it is not possible to remove all oxygen groups from GO with a reported C/O ratio of ~10 reported by S. Stankovich et al. for hydrazine reduced GO [29]. Therefore, the product of this chemical reduction differs from pristine graphene. The liquid phase exfoliation of GO is mostly preferred when GO itself is the desired product. When graphene is the desired end product, this particular method is considered to be more complex since the additional reduction step is required. However, graphite oxide GO are dispersible in a wider variety

of solvents making them more processable compared to graphite and graphene.

- *Solid State Graphene Preparation:* Graphene which has been dispersed as previously mentioned can be used in a non-liquid phase through vacuum filtration. In this process the graphene dispersion is drawn through a membrane using a vacuum pump. The result is graphene paper which forms as the graphene flakes dry on the membrane surface (Figure 16) [30, 31]. Alternatively, deposition of graphene onto a substrate can be achieved via drop casting. In this method, a drop of graphene dispersion is placed onto the desired substrate, which can be heated, depending on the substrate material. Once the solvent has evaporated, a graphene flakes are formed on the surface [32]. Spin coating can be used for a more homogenous graphene coating. In this method, the deposited dispersion is spread across the substrate surface due to centrifugal force [33]. Spray-coating is also a method that results in highly uniform graphene films and in addition offers the option for large area deposition [34].

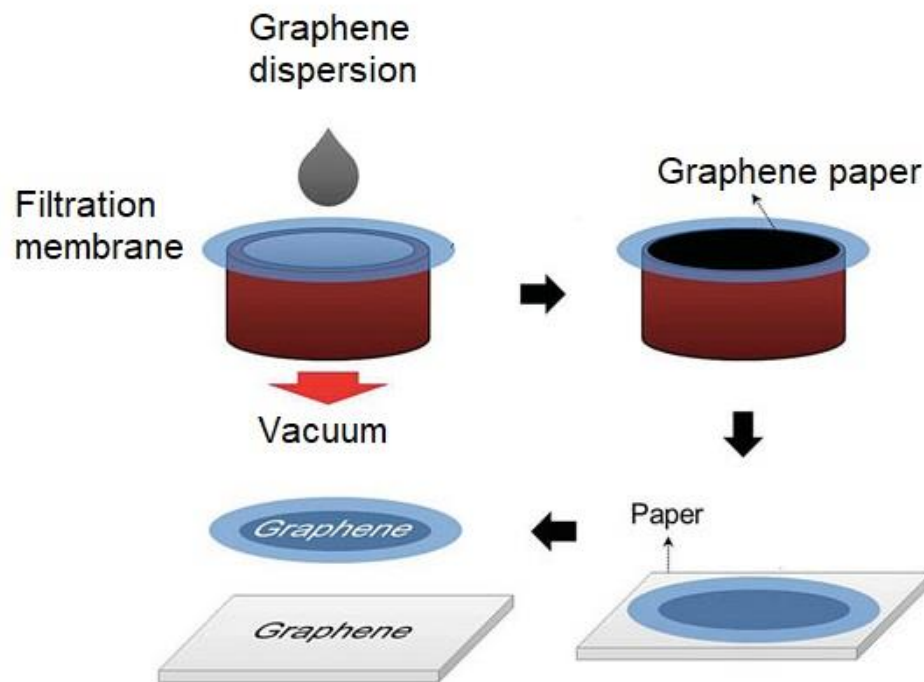


Figure 16 Graphene paper preparation via vacuum filtration. Image taken from reference [35].

2.2.2. Bottom-up methods:

- Growth on surfaces: Graphene can also be obtained by growing the material directly onto a surface. This method makes the size of the created graphene layers independent from the initial graphite crystal. Graphene growth can be succeeded either with chemical vapour deposition (CVD) of carbon containing gases onto a catalytic metal surface or through growth of already existing carbon on a substrate, also known as epitaxial growth.
 - Epitaxial growth: The first report of epitaxial growth of graphene was in 1979 by M. Eizenberg and J.M. Blakely when they condensed a monolayer of carbon on a surface of C-doped nickel single crystals [36]. Since then, single or few-layer graphene has been grown on C-doped metals such as Fe, Pt, Pd, and Co [37,38].

- Chemical Vapour Deposition (CVD): In brief, CVD is a method of deposition in which a substrate is exposed to desired gaseous compounds which decompose on the substrate surface resulting in a thin film while the by-products evaporate. To achieve this, the carbon containing sample must be heated e.g. with a filament or plasma. Single and few-layer graphene can be synthesised on Ni foil via CVD by exposing the Ni substrate to a gas mixture of H_2 , CH_4 and Ar at $900^\circ C$ in a quartz tubular furnace under a pressure of 750 Torr [39]. Growth of graphene can also be achieved by atmospheric pressure CVD, in which a low-carbon solubility such as Cu is required. Studies so far have shown that the graphene growth rate is usually low, and the size of the graphene domains are small, resulting in a defective graphene layer [40]. A brief schematic summary of this method is featured in Figure 17.

Synthesis of Graphene via Chemical Vapour Deposition (CVD)

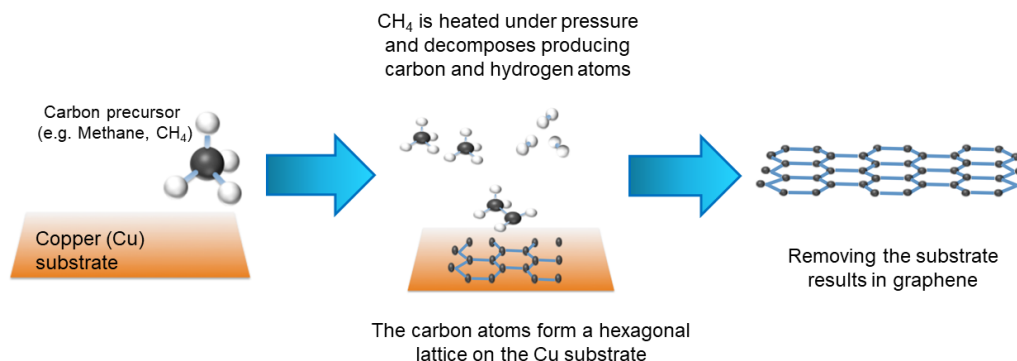


Figure 17 Graphene synthesis through Chemical Vapour Deposition (CVD). Generally, a carbon precursor is heated under pressure in the presence of a metallic substrate. The carbon atoms that are generated self-assemble onto the substrate forming a hexagonal lattice. (Images taken from: nixor.co.uk)

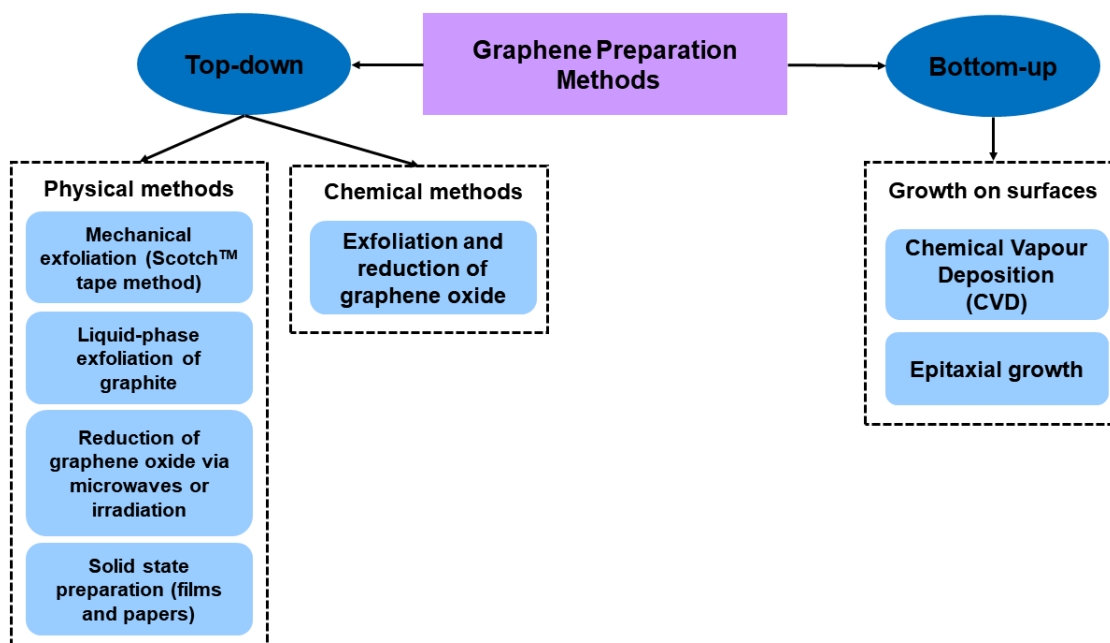


Figure 18 Schematic summary of the most common graphene preparation methods.

2.3. Properties of Graphene:

Graphene possesses many outstanding properties in terms of optical transparency, electric conductivity, mechanical strength, and thermal conductivity. Unlike other 2D structures, it remains stable in atmosphere. It has a high electrical mobility and conductivity, high thermal conductivity and is a zero-bandgap semiconductor (semi-metal). Many of these interesting properties stem from the behaviour of its low-energy electronic excitations: rather than obeying classical equations of motion like ordinary metals or semiconductors, the quasiparticles in graphene obey the massless Dirac equation, establishing it as a fundamental member of a distinct class of Dirac materials. The nature of the low-energy excitations in graphene and the many-body interactions that modify them form the basis of our knowledge of the electronic properties of graphene. The electronic structure of graphene has been shown to evolve with the number of layers with the 3D limit for graphene is at 10 layers [41]. Single layer or bilayer graphene are zero-bandgap materials with one type of electron and one type of hole. For graphene of three or more layers, several charge carriers are observed, and the conduction and valence bands start notably overlapping [42]. There for single, double and few-

layer graphene are separated into three categories of 2D crystals. Thicker structures (multi-layer graphene) are considered as thin films of graphite (3D).

2.3.1. Thickness-Flexibility

Graphene is a super light material with a planar density of 0.77 mg/m^2 and each hexagonal carbon ring with an area of 0.052 nm^2 [22]. Each one of these unit-rings only consists of two carbon atoms since each atom at vertex is shared by three-unit rings. Since graphene has a thickness of only one carbon atom it has the advantage of being super thin and ultralight.

Graphene is also a very flexible material which, rather like a sheet of paper, can be curved and bended.

2.3.2. Conductivity/Electron mobility

Thus far, graphene is the most conductive material at room temperature, with a conductivity of 10^6 S/m and a sheet resistance of $31 \text{ } \Omega/\text{sq}$ as measured by Kim et al. using high crystallinity CVD grown graphene [43]. The high conductivity value is attributed to ultrahigh electron mobility with a value of $2 \times 10^5 \text{ cm}^2/\text{V}\cdot\text{s}$ which is almost 140 times the mobility in silicon [44]. The high electron mobility is attributed to the π electrons. Carbon atoms in graphene are sp^2 hybridised, donating one extra electron to the π bond. The π electrons are free to move with ease at room temperature resulting in high conductivity. Additionally, graphene is a semi-metal. There is virtually no overlap between the valence band and the conduction band, meaning that the energy bandgap is practically zero. As a result, electrons can flow easily from the top of the valence band to the bottom of the conduction band without heat stimulation. The valence and conduction bands of graphene exhibit cone-like structures located at two inequivalent Brillouin zone corners that meet at the Dirac point (charge neutrality point) (Figure 19). In these cones, the two-dimensional (2D) energy dispersion relation is linear, and the electron dynamics can be treated as ‘relativistic’, in which the Fermi velocity of the graphene substitutes for the speed of light [45].

At the Dirac point the conduction and valence bands are symmetrical. The superior electrical and optical characteristics in graphene are because of linear

dispersion of Dirac massless electrons moving with a fraction of the speed of light. In pure graphene, neutral graphene where the valence band (π bonding states) is filled with electrons and the conduction band (π^* anti-bonding states) is completely empty. The conduction band and the valence band energies only co-inside at discrete K points within the Brillouin zone. The fermi energy lies at charge neutrality point, so its electronic properties near K-point (Dirac point), the conductance is expected to be a minimum.

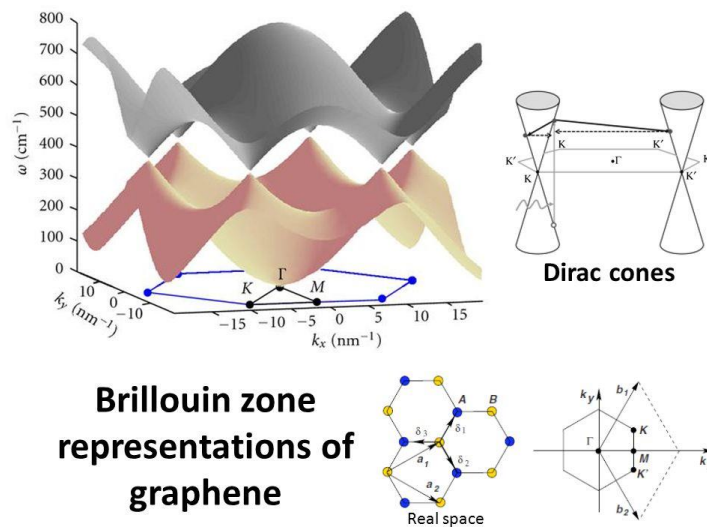


Figure 19 Valence and conduction bands of graphene which intercept at the Dirac point. Image taken from reference 46.

The linear dispersion of Dirac massless electrons moving with a fraction of the speed of light is the source of graphene’s superior electrical properties. In pure graphene, the fermi energy lies at the Dirac point, so the conductance is at a minimum. The fermi level can be shifted through external stimuli so that the conductivity of graphene can be tuned [46]. In the case of doped graphene, either positively doped (p-doped) or negatively doped (n-doped), the Fermi level shifts away from the Dirac point. In the case of p-doped graphene, which is a result of graphene being in contact with an electron withdrawing species, electrons are partially drained from the valence band and the Fermi level is displaced to a position below the Dirac point. Conversely, n-doped graphene is the result of graphene being in contacts with an electron donating species. In this case, extra electrons are forced into the conduction band and the Fermi level is shifted above the Dirac point. The Fermi level shift (ΔE_F) of the doped graphene is defined as the energy difference between the Fermi level (E_F) and the Dirac point [47]. In Figure

20, the red areas indicate the levels filled with electrons and the blue areas indicate the levels void of electrons (holes). The electron transport in graphene is described by the quantum Hall effect and characteristics of relativistic particles [48].

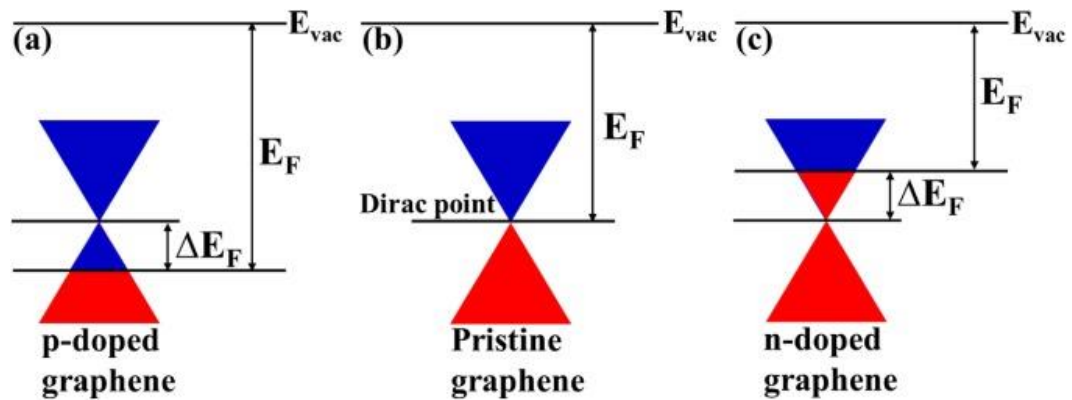


Figure 20 Energy band diagrams of pristine graphene, p-doped graphene and n-doped graphene. Image taken from reference 47.

2.3.3. Thermal conductivity

Graphene also exhibits impressive thermal conductivity and mechanical strength. The thermal conductivity of graphene at room temperature is about 53×10^3 W/mK, which is 10 times higher than the thermal conductivity of copper (401 W/mK) [49].

2.3.4. Hardness/strength

Graphene has the hardest crystal structure among all known materials with a tensile strength of 125 GPa and elastic modulus of 1.1 TPa while its strength limit reaches 42 N/m [22]. This means that between graphene and steel of the same thickness, graphene is about 100 times stronger than steel. More specifically, a 1 m² layer of graphene could withstand 4 kg of weight [22]. Finally, the surface area of graphene reaches 2630 m²/g [50]. Additionally, AFM-based nanoindentation technique offers the ability to measure the elasticity of graphene. Recently, H. Li

and K. Leifer reported stiffness of 1 TPa for free-standing graphene and 100 GPa for graphene deposited on a substrate, which constitutes graphene as a reinforced ultrathin layered material [51].

2.3.5. Transparency

Benefiting from this one atomic thickness, graphene has a very high transparency of $T=97.7\%$ [52]. According to Nair et al., graphene yields an opacity of 2.3 % and negligible reflectance ($<0.1\%$) as shown in Figure 21 (a). Optical spectroscopy also showed that the opacity is essentially independent of wavelength (λ) and increases with membranes' thickness so that each graphene layer adds another 2.3% to the total opacity. Due to this direct correlation, the transparency of graphene becomes an effective indication of the numbers of graphene layer. This theory is confirmed by simulations using non-interacting Dirac fermion theory as shown in Figure 21 (b).

2.3.6. Absorption

Even though the optical absorption of monolayer or few-layer graphene on a solid substrate (e.g. SiO_2) has been well confirmed, the optical absorption in liquid phase is much more intriguing and is being investigated to determine the factors that effect it. Graphene only reflects $<0.1\%$ of the incident light in the visible region, a number that rises to about 2% for ten layers [53]. Due to this fact we can consider the optical absorption of graphene to be proportional to the number of layers with each layer absorbing $A \approx 1 - T \approx \pi\alpha \approx 2.3\%$ over the visible spectrum. The absorption spectrum of single layer graphene is rather flat from 300 to 2,500 nm with a peak in the ultraviolet region (~ 270 nm), due to the exciton-shifted van Hove singularity in the graphene density of states [54]. In few-layer graphene on the other hand, more absorption features can be seen at lower energies, that derive from interband transitions [55,56].

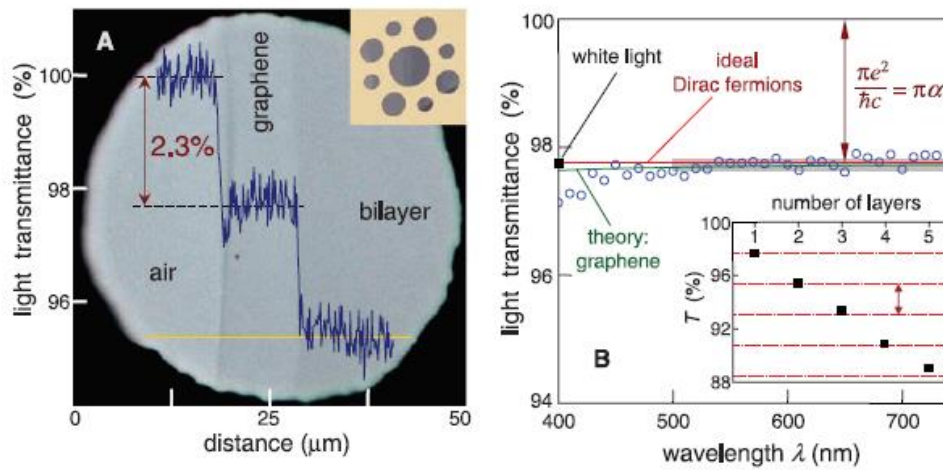


Figure 21 (a) Transparency of single layer graphene (b) Theoretical transparency of graphene: the transparency decreases as the number of graphene layers increases. Image taken from reference 23.

2.4. Absorption Coefficient of Graphene, GO and RGO:

Compared with the studies devoted to understanding the electronic structure and properties of graphene, the equivalent information on GO and RGO remains largely unexplored due to the structural disorder.

The optical absorbance and the optical bandgap of GO and RGO can be tuned by varying factors such as the extent of reduction, the film thickness and the concentration of solution. The typical optical absorption of GO shows a peak in the UV region at around 230 nm, which is attributed to the $\pi \rightarrow \pi^*$ transitions of the aromatic C-C bonds and a broad shoulder near 300 nm attributed to the $n \rightarrow \pi^*$ transitions of the ketonic functional groups (C=O) [57]. When GO is reduced, the maximum absorption peak redshifts to 270 nm and the overall absorption increases for wavelengths larger than 230 nm, as seen in Figure 22. This shift corresponds to the increased π -electron density and the restoration of the sp^2 carbon arrangement upon reduction [58]. This change in absorption is dependent on the reduction time as shown in **Error! Reference source not found.**

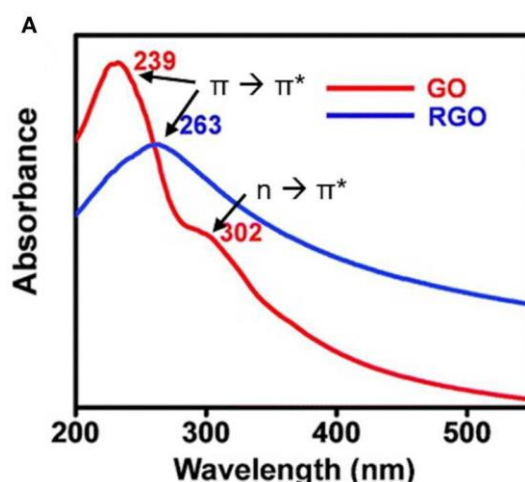


Figure 22 Absorption spectra of GO and RGO. The redshift of λ_{max} is attributed to more $\pi \rightarrow \pi^*$ transitions which are equivalent to a more ordered structure and larger sp^2 domains. A shoulder appearing at a wavelength of ~ 300 nm indicates the $n \rightarrow \pi^*$ transition of carbonyl groups. Image lifted from reference [83]

The absorption coefficient value for GO and RGO differs depending on the number of layers per flake, the lateral size of each flake and the functional groups present on the lattice [59]. In 2008, Coleman et al. initially reported a constant value of $a=2460 \text{ ml}\cdot\text{mg}^{-1}\cdot\text{m}^{-1}$ for RGO in different solvents [60]. They later expanded their work by preparing different exfoliated GO dispersions in N-methyl-

pyrrolidone (NMP) with varying low power sonication times. Their results yielded a mean a value of $a=3620 \text{ mL mg}^{-1} \text{ m}^{-1}$ [61]. Through further research, Coleman et al. presented a range of values from $a=1390$ to $a=6600 \text{ ml}\cdot\text{mg}^{-1}\cdot\text{m}^{-1}$ [62,63,64]. R. Su et al. noticed that the absorption coefficient of RGO in NMP increases from 2.67×10^6 to 6.72×10^6 as the number of small size flakes ($\leq 500 \text{ nm}$) decreases and as the number of layers per flake increases [Error! Bookmark not defined.]. Their interpretation of these findings is that an extended π -conjugated system enhances light absorption intensity. RGO dispersions with smaller flakes and more layers yield smaller absorption coefficients whereas those with larger flake sizes and fewer layers have higher values. It is worth noting that Su et al. found that the absorption coefficient increases as the C/O and C/N ratios increase. They argue that they found such high absorption coefficient values (3 orders of magnitude higher than Coleman's team) due to the presence of nitrogen atoms on the RGO lattice originating from the NMP solute as well as hydroxyl and carboxyl functional groups. Defects are also correlated to the change in absorption coefficient values.

Defects of the RGO lattice are related to the presence of oxygen and vacancies, or more simply, holes in the lattice created during the reduction process. Large holes in the RGO lattice damage the π -conjugated system leading to a smaller absorption coefficient. Conversely, X-ray Photoelectron Microscopy (XPS) data has shown that the absorption coefficient increases with higher oxygen content [Error! Bookmark not defined.].

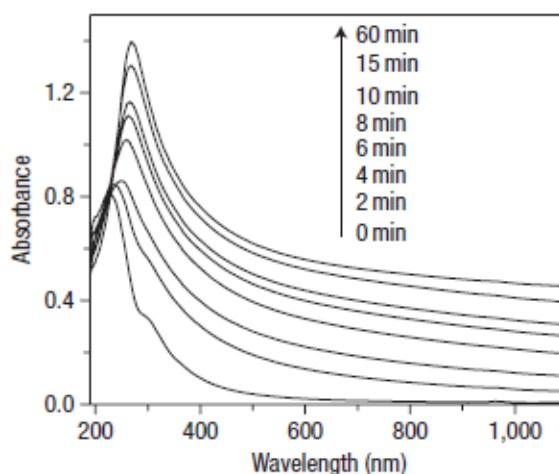


Figure 23 Change in absorption spectrum of GO with reduction time using hydrazine as the reducing agent. Image taken from reference Error! Bookmark not defined..

Another important factor which effects the absorbance behaviour of graphene derivatives is the flake size. According to Hashemi et al. ultra-small GO flakes with an average size of about 12 nm show higher optical absorbance than small GO flakes with an average flake size of about 166 nm (**Error! Reference source not found.**) [65]. This observation was more prominent at a wavelength around 800 nm. Hashemi and his team theorise that the increased dispersibility of the ultra-small GO flakes leads to the increase in light absorption.

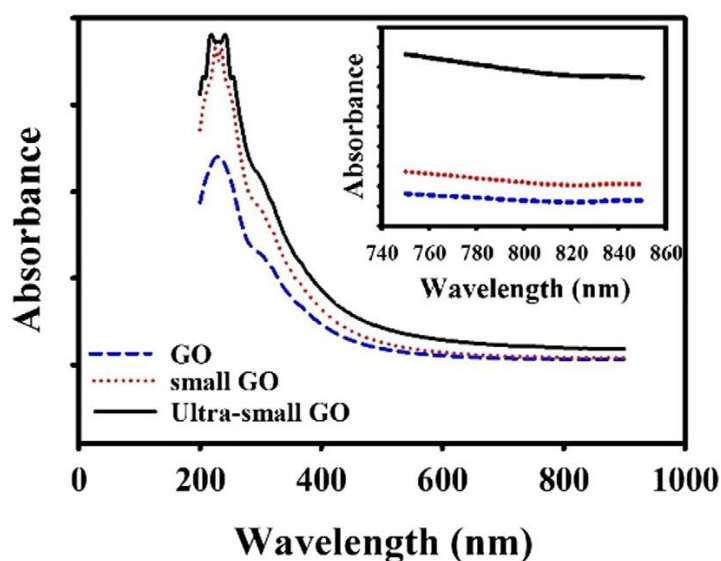


Figure 24 UV-Vis absorption spectra of GO samples varying in flake size. The reference GO flakes (blue line) has an average size of $\geq 3\mu\text{m}$, the small GO flakes (red line) had an average size of 166 nm and the ultra-small GO lakes (black line) had an average size of 12 nm. As the flake size decreases, the light absorption of the GO sample increases., especially at 800 nm. (Image taken from reference **Error! Bookmark not defined.**)

Chapter 3: Graphene Oxide

As mentioned in the previous chapter, graphene can be functionalised with oxygen functional groups to produce graphene oxide (GO). This is a derivative of graphene with new and improved properties that can be tuned by controlling the level of oxidation. Depending on the application, GO can be the desired end product due to its unique properties or it may be an intermediate for the preparation of graphene. Because high quality sheets of graphene prepared by CVD require expensive equipment, using solution processable GO for the preparation of graphene is an appealing alternative.

3.1. Structure of Graphene Oxide:

GO is a complex material and its precise chemical structure has been the subject of much research and debate for years, as no specific model has been produced thus far. Many GO structure models have been proposed over the years (Figure 25) [66]. Generally, a single sheet of GO can be described as graphene decorated with oxygen functional groups on both sides of the basal plane and around the edges of the lattice [67, **Error! Bookmark not defined.**]. The functional groups lie above and below the carbon lattice forming a layer of oxygen atoms on each side. The oxygen groups present in GO are hydroxyl (C-OH), epoxy (C-O-C) and carboxyl (-COOH) groups. According to He et al. (1998), during deoxygenation of GO phenol groups are formed. This indicated that the C-OH and C-O-C groups of GO are close to each other [67]. They also note that the oxygen functional groups are randomly distributed and that the oxygen containing benzene rings are not necessarily identical. The hydroxyl and epoxy groups are perpendicular to the GO plane. Hydroxyl groups are found both on the basal plane and around the lattice edges, whereas carboxyl groups are present only around the edges of the graphitic lattice.

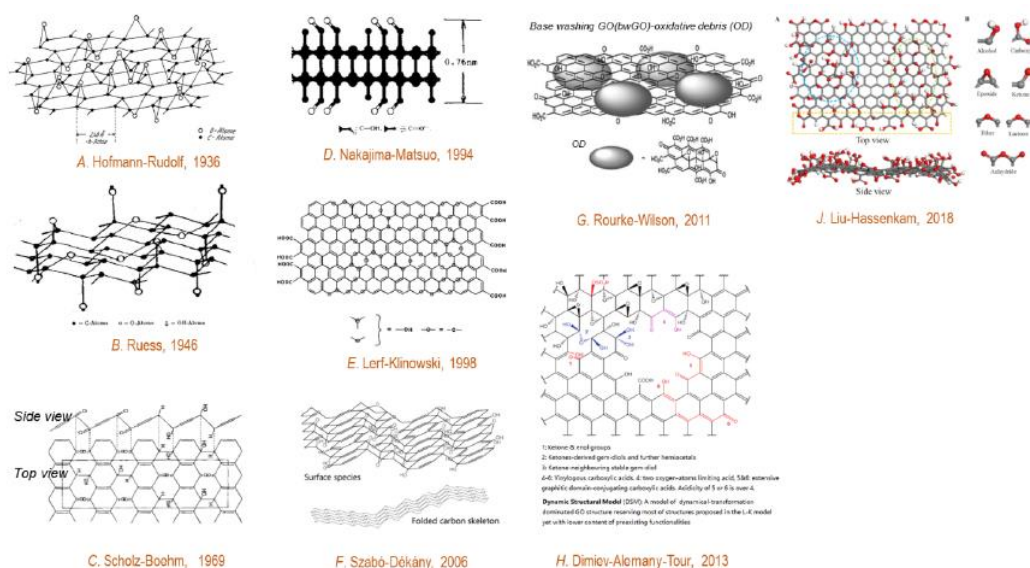


Figure 25 Theoretical structure models for graphene oxide (Image taken from reference 66).

GO sheets contain two types of regions: aromatic regions (unoxidised benzene rings) and oxygenated regions containing aliphatic six-membered rings, as shown in (Figure 26) [67]. The relative size of each type of region depends on the degree of oxidation. The presence of aromatic rings, double bonds and epoxide groups in a region of the GO sheets results in a flat structure. However, the oxygen containing regions do not obey a planar structure due to the disruption of aromaticity. The carbon atoms which are attached to hydroxyl groups have a slightly distorted tetrahedral configuration, therefore distorting the planarity of the lattice and creating “wrinkled” regions. Essentially, the oxygen-containing functionalization disrupts the sp^2 order of the graphene backbone such that regions of sp^2 (ordered) are interrupted by the sp^3 (disordered) in the carbon basal plane [67].

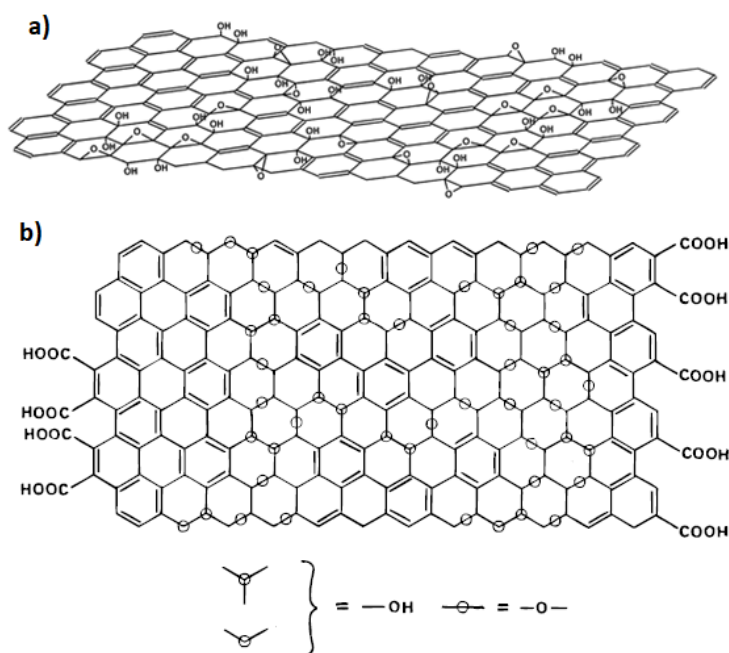


Figure 26 Model for the structure of a single sheet of graphene oxide suggested by He et al. in 1998. Hydroxyl and epoxy groups are perpendicular to the graphitic plane and the carboxyl groups decorate the edges of the lattice. The actual GO lattice is not planar as shown in this graphical representation. Image taken from reference 68.

Meanwhile, direct observation of GO sheets shows that the structure consists of long-range-ordered sp^2 regions along with much smaller patches of amorphous material and/or defects, which are not attributed to the presence of oxygen atoms. Erickson et al. found that, following oxidation of graphene, the produced GO, is highly inhomogeneous structure-wise [69]. Aberration corrected TEM (AC-TEM) images of GO, as seen in Figure 27, revealed three major features: holes in the lattice (blue), graphitic regions identical to those of graphene (yellow) and disordered regions (red), indicating areas of high oxidation. These three features had area percentages of approximately 2%, 16%, and 82%, respectively. Holes form in GO as CO and CO₂ are released during the aggressive oxidation and sheet exfoliation [70]. Erickson and his colleagues found these holes to have an area of $\leq 5 \text{ nm}^2$.

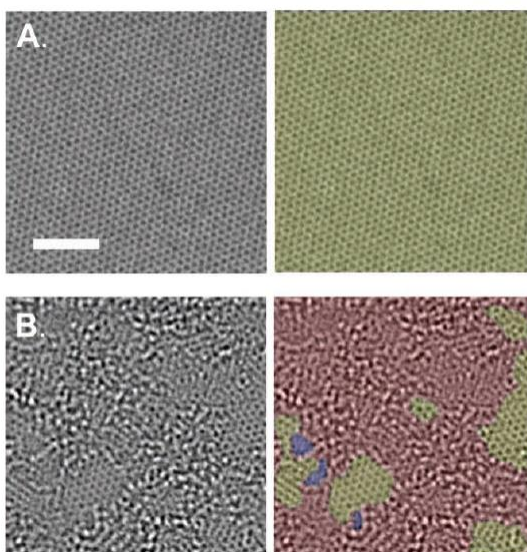


Figure 27 A) Single sheet of graphene with the graphitic area shown in yellow (right). B) Single sheet of GO. Holes are indicated in blue, graphitic areas in yellow, and disordered regions, indicating oxygen functionalities, in red (right). The scale bar is 2 nm. Image taken from reference 69.

The presence of oxygen groups on the GO lattice effects the properties of this material since the electronic structure is modified compared to that of pristine graphene. This effect can be controlled by chemically, thermally, or electrochemically engineering and manipulating the amount, the type and the distribution of oxygen functional groups on the graphene lattice.

High-resolution transmission electron microscopy has been used to determine the atomic structure of GO. These studies report long-range order of sp^2 lattice with isolated defect clusters. More specifically, there is evidence of nanocrystalline regions of sp^2 lattice which are surrounded by regions of disorder. However, the presence of contaminants that adsorb to the surface of the GO at room temperature prevents clear observation of the intrinsic atomic structure material [71]. To combat this issue, Dave et al. used an in-situ heating holder with AC-TEM to study the atomic structure of nanocrystalline GO from room temperature to 700 °C. They reported that as the temperature increases to above 500 °C, the adsorbed impurities detach from the GO and allowing its atomic structure to be imaged more clearly. This structure appears to be to be small crystalline domains with a size of 2-4 nm within a polycrystalline GO film as seen in Figure 28.

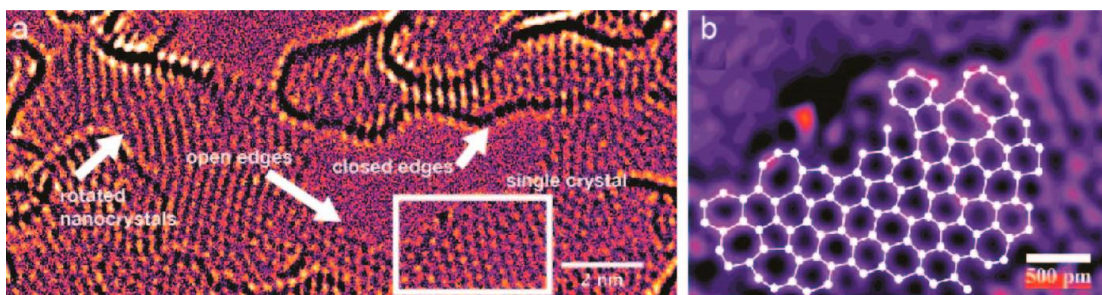


Figure 28 a) Atomic structure can be resolved using in situ heating with AC-TEM at 700 °C. b) Sufficient resolution is achieved to identify defects in the bond structure. The directly resolved atomic structure is indicated by white dots and lines. Image taken from reference 71.

3.2. Preparation of graphite oxide and graphene oxide

3.2.1. Top-down methods:

➤ **Chemical synthesis:** Chemical oxidation is the earliest top-down method with which aqueous graphene was prepared. Various chemical oxidation methods have been developed since the 19th century and have been modified and improved upon since then, giving us the most efficient methods, which are used even to this day. The most common large-scale preparation method is the oxidation of graphite to graphite oxide using concentrated acids in the presence of strong oxidants with the best-known being Brodie's method, Staudenmeier's method, Hoffman's method and Hummer's method. Chemical synthesis is a highly facile, low-cost and large-scale method for graphene oxide preparation.

1. **Brodie's method:** In 1859 B.C. Brodie developed an oxidation method of graphite using potassium chlorate (KClO_3) and fuming nitric acid (HNO_3) [72]. The KClO_3 is a highly strong oxidizing agent and it oxidises the graphite powder in acids solution and typically also is an in-situ source of dioxygen, which acts as the reactive species. Through this process, a new compound was developed with an increased mass compared to graphite that was later determined to contain carbon, hydrogen and oxygen atoms. Brodie found that this new compound, which he determined had a C:H:O percentage composition of 61.04:1.85:37.11, was dispersible in water or basic solutions but not in acidic solutions. For this reason, he called the new material graphitic

acid. The disadvantages of this oxidising method are mainly the long reaction time required and the release of toxic gases [73]. The Brodie method may yield high quality graphite oxide; however, the pH of the final solution must be raised with the addition of NaOH or KOH [74].

2. *Staudenmeier method*: In 1898, L. Staudenmeier expanded on Brodie's work by introducing concentrated sulfuric acid (H_2SO_4) to the oxidation process to increase the acidity of the mixture and by adding $KClO_3$ in multiple doses over time [75]. This modification was an improvement on Brodie's method resulting in extended oxidation. However, the process lasted over a week making this method very time consuming. Furthermore, the addition of $KClO_3$ for that amount of time produced chlorine dioxide gases (ClO_2) which needed to be removed by an inert gas. This made the process an explosion hazard. Since then, modified version of the Staudenmeier method have been tested through the years [76, 77].
3. *Hofmann method*: This method differs from the previous oxidation methods mentioned in that the HNO_3 is added not as fumes but rather as a concentrated solution. This process was first performed by U. Hoffmann et al. in 1937 [78]. Since then, the Hofmann method has been used for the synthesis of graphite oxide and has been investigated to determine the effects on graphite oxide properties and structure [79,80].
4. *Hummers method*: In 1958 Hummers and Offeman performed an oxidation method in which the main reducing agent was no longer potassium chlorate, but rather potassium permanganate ($KMnO_4$) and nitric acid was replaced by sodium nitrate ($NaNO_3$) [81]. According to Hummers and Offeman themselves, this method yields graphite oxide with a C/O ratio varying from 2.1 to 2.9. Since 1958 there have been many reported modifications on the Hummers method, with interest peaking after the discovery of graphene in 2004 [42]. The Hummers method and variations of it are currently used for large scale chemical synthesis of graphene oxide. Each modified Hummers method yields different results, such as varying oxygen content, types of oxygen functional groups, structure, electrical properties, optical properties

etc. [82]. Muzyka et al. prepared graphite oxide samples using sodium dichromate ($\text{Na}_2\text{Cr}_2\text{O}_7$) as the main oxidising agent instead of KMnO_4 [82]. Sodium dichromate is a mild oxidising agent therefore a longer oxidation time was required compared to that needed with potassium permanganate (72 h with $\text{Na}_2\text{Cr}_2\text{O}_7$ versus 0.5 to 24 h with KMnO_4). Furthermore, the group reported a lower oxygen content and increased graphitic domains and lattice distortion due to mild oxidation.

In 2010, J.M. Tour's group altered the Hummers oxidation method by eliminating the addition of NaNO_3 , increasing the amount of added KMnO_4 and adding phosphoric acid (H_3PO_4) [83]. With the exclusion of NaNO_3 , in situ formation of nitric acid through reaction with KMnO_4 is avoided, providing a safer alternative route. Although this process yields highly oxidised and therefore hydrophilic graphite oxide, the graphene oxide sheets prepared by the Tour's method have a high content of carboxyl groups leading to a very low integrity in the GO sheets. In 2017 Zaaba et al. investigated the omission of NaNO_3 and found that it does not affect the oxidation of graphite and indeed reduces the emission of toxic gases such as NO_2 and N_2O_4 [84, 73]. Currently, the most widely used modified Hummers methods include the addition of hydrogen peroxide solution to stop the oxidation reaction and also remove any traces of excess KMnO_4 [85, 86].

The conventional Hummers oxidation may often include a second step in which water is added before the addition of H_2O_2 . J. H. Kang and his colleagues reported that this additional step results in diminishes sp^2 conjugated domains within the GO lattice and an increased number of carboxyl and hydroxyl groups compared to that of epoxy groups [87]. They interpreted these findings as a result of the oxidative cleavage of $\text{C}=\text{C}$ double bonds by permanganate in acidic aqueous conditions and/or the acid-catalysed hydrolysis of epoxies. Chen et al. have added an additional purification step using a dialysis membrane for one week [88]. The result of this purification process was graphene oxide flakes of similar size regardless of the initial graphite flakes.

In 2018, Ibarra-Hernández and her colleagues utilised microwaves to assist the chemical oxidation via Hummers method [89]. The use of microwaves increases the reaction rate by orders of magnitude. The water

molecules are susceptible to microwave irradiation. The irradiated water dissociates and decomposes into radicals, namely $\cdot\text{OH}$, OH^- , H^+ , and $\text{H}\cdot$. The oxidation reaction has a synergistic effect between the dissociated water and the delocalised π -electrons promoted by microwave radiation. The results that Hernandez's team obtained suggest that the permanganate ion produces reducing species during the oxidation process through a reversible reaction between the permanganate ion with π electrons, ions, and radicals produced after treatment with microwave radiation.

The graphite oxide samples that are prepared from the oxidation methods mentioned above have been compared in terms of structure and properties in manuscripts such as that published by Poh et al [90] and Chua et al [91]. The various oxidation methods influence the structure, oxygen content and optoelectrical properties of the resulting graphite oxide and graphene oxide. The oxidation routes that utilise KClO_3 yield GO with a lower amount of carbonyl and carboxyl groups when compared to those that use KMnO_4 . The methods which utilise NaNO_3 and KMnO_4 produce GO with enhanced electrochemical properties, namely a high electron transfer rate. After comparing the Brodie, Staudemeier and Hummers methods, Ciszewski et al. report that Brodie synthesised GO showed a lack of sulphur contaminants, the Staudermeier GO has a high oxidation level but takes 100 to 300 h and, finally, Hummers GO possesses a large amount of sp^2 regions, however this was the least time-consuming oxidation process [92].

- **Liquid phase exfoliation of graphite oxide:** Mechanical exfoliation of graphite oxide may be performed in the liquid phase, resulting in a dispersion of graphene oxide in suitable solvents. Graphite oxide is highly hydrophilic due to the presence of multiple oxygen groups, making it dispersible in water and other polar solvents. An ultrasonication bath or an ultrasonic probe can provide adequate energy to overcome the Van der Waals interaction between the graphene oxide flakes resulting in dispersion of single layer graphene oxide.

3.2.2 Bottom-up methods

An alternative approach for GO preparation are bottom-up methods that avoid using the strong oxidising agents that chemical GO synthesis utilises. The following methods also have the addition advantage of controllable GO flake size and tuneable thickness.

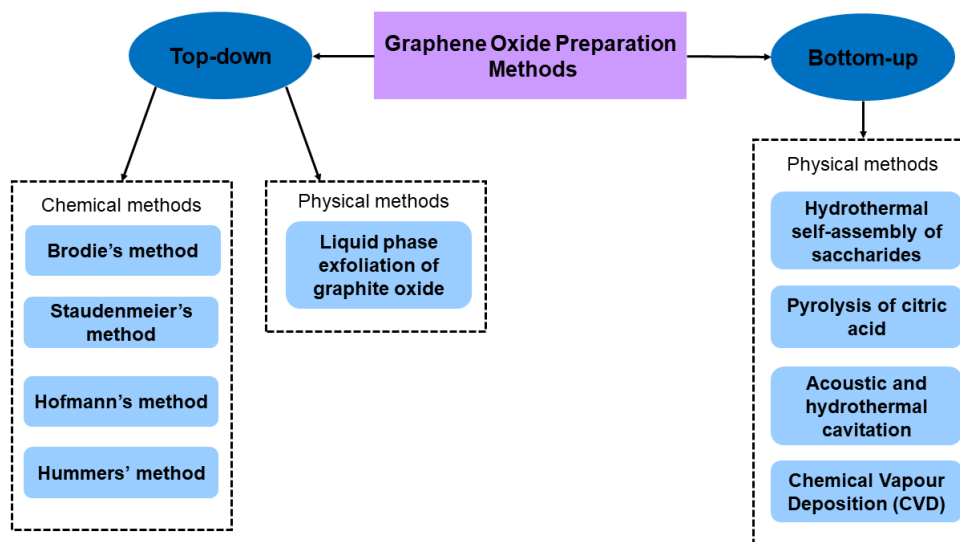


Figure 29 Schematic summary of GO preparation methods.

- Hydrothermal self-assembly: GO nanosheets can be grown from glucose and other saccharides (e.g. sucrose and fructose) through a route known as the Tang-Lau method, a low-cost and environmentally friendly process [93]. Tang et al. developed this method by heating an aqueous glucose solution in an autoclave to prepare monolayer and few-layer GO through polymerisation.
- Pyrolysis of citric acid: Dong and his colleagues developed another preparation method by tuning the carbonization degree of citric acid through pyrolysis and dispersing the carbonized products into alkaline solutions [94].
- Acoustic and hydrothermal cavitation: The most recent bottom-up GO synthesis method was developed in 2019 by R. J. Price et al. through acoustic cavitation and hydrodynamic cavitation, generated by ultrasound

and in fast flowing liquids respectively [95]. In this method, GO platelets are synthesised from diaromatic species such as 1-methylnaphthalene at very high temperatures (>5000K) and pressures (>1000 atm).

- *Chemical Vapour Deposition*: As with graphene, GO can be prepared through CVD methods. However, CVD is a complex method that requires precise control of parameters, namely temperature, pressure, choice of precursors, and deposition time [96].

Chapter 4: Reduced Graphene Oxide

4.1. Preparation of reduced graphene oxide:

The most efficient and therefore common methods for the preparation of RGO are top to bottom methods. It is more time-efficient and cost-effective to reduce GO rather than grow RGO. Furthermore, the level of reduction of GO can be regulated in order to consequently control properties such as flake size and conductivity of the outcoming product [101]. Lastly, these methods offer the option of RGO functionalisation for further tuning.

4.1.1. Thermal reduction:

- Thermal annealing: The mechanism of thermal exfoliation of GO is mainly attributed to the removal of oxygen functional groups in the form of CO and CO₂ gases during rapid heating [97]. The level of reduction is dictated by the heating temperature and reduction time. However, this procedure is found to produce small size flakes and wrinkled sheets [98]. This is mainly because the decomposition of oxygen-containing groups also removes carbon atoms from the graphitic plane. This cracks the graphene sheets into smaller pieces, distorts the carbon plane and creates holes in the lattice due to the release of CO₂. S. N. Alam et al. demonstrate an extremely simple method of GO reduction in which GO powder is placed in an empty beaker which is then placed on a hotplate at 350°C for 10 mins [99]. However, thermal treatment of GO is usually carried out in a vacuum or inert atmosphere [100,101]. Wang et al. thermally reduced GO films on preheated quartz substrates under inert conditions (Ar) [101]. The reduction is indicated by the change of film colour from light brown to grey. The conductivity of the RGO films increased with the increase in annealing temperature (from 550 to 110°C).

In thermal reduction, temperature place a key role in deoxygenation degree of GO [102]. Yang et al. reported that thermal annealing of GO at 500, 700 and 900°C yielded RGO sample with C/O ratios of 8.9, 13.2,

and 14.1 respectively. Thermal reduction also has an effect in the species of oxygen groups that are removed. After thermal annealing at about 1000 °C, the GO's carboxyl groups will be removed, but GO's carbonyl groups will remain [102].

- **Microwave reduction:** Microwaves have been used as an alternative heat source for GO reduction [103, 104]. Hassan et al. performed microwave irradiation on GO sheets in an aqueous or organic phase in the presence of metal nanoparticles to create nano-catalysts on the graphene surface [103]. Zhu and his colleagues followed a different approach by irradiating GO powder in a microwave oven in ambient condition for 1 minute [104]. This resulted in the reduction of the GO powder accompanied by an increase in volume (Figure 30).

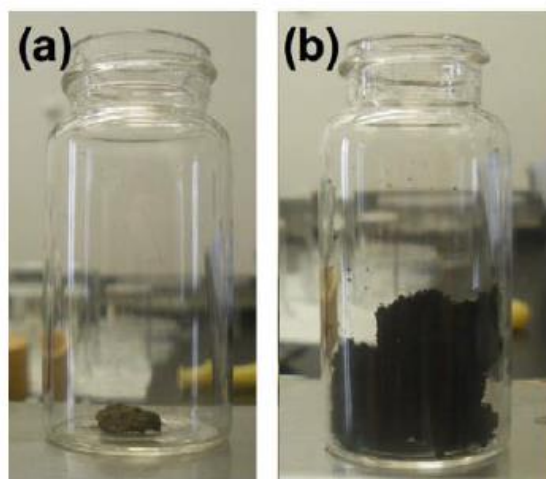


Figure 30 a) GO powder b) RGO powder produced with microwave irradiation [104].

- **Photoirradiation:** An alternative route is reduction via photo-irradiation. This may be reduction using a femtosecond laser [105] or flash reduction with a xenon lamp [106, 107]. Zhang et al. used a femtosecond laser to create graphene microcircuits on graphene oxide films according to pre-programmed patterns (Figure 31). By altering the output power of the laser, the conductivity of the resulting RGO films can be adjusted.

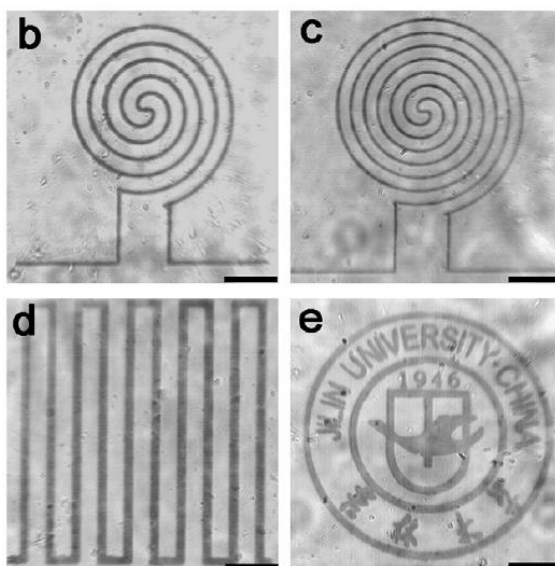


Figure 31 RGO patterns created by laser reduction on GO films which have been spin coated onto a substrate [105].

Flash reduction of free-standing GO films can be achieved with a single, close-up flash of a xenon lamp found on a camera [106]. The xenon lamp emits a broad emission spectrum ranging from 190 nm to 800 nm. This spectrum range matches well with that of the maximum resonance absorption peak of the GO sheets at 235 nm. This results in the bonds in GO generating resonance with light, which accelerates the removal of oxygen functional groups and restores of the original structure of graphene [107].

4.1.2. Chemical reduction:

Chemical reduction of GO can usually be realised at room temperature or with moderate heating. This means that it requires less equipment than thermal annealing or photoirradiation reduction and is also more cost-effective. Furthermore, there are a variety of reducing agents ranging from mild to powerful, including green, biocompatible reagents. Lastly, it has the capacity to yield large amounts of products. All the above constitute chemical reduction of GO as the most common route for the preparation of

RGO. The degree of reduction (C/O ratio), and by extension, the properties of the resulting RGO, is dependent on the reaction conditions (time and temperature) and the type of reductants used. There have been many reducing agents for chemical RGO synthesis, a few of which are listed below.

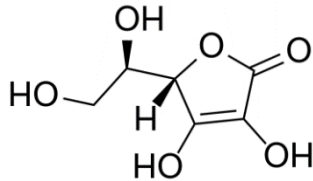
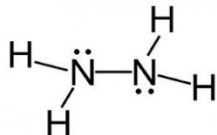
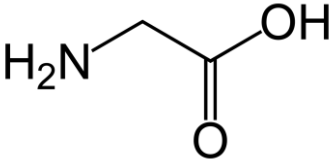
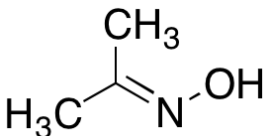
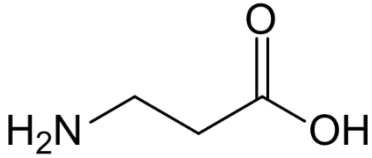
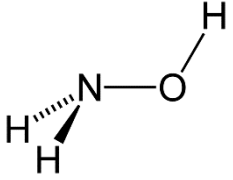
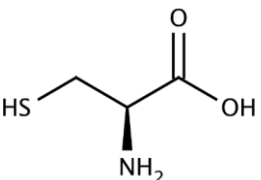
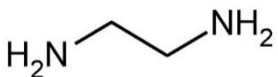
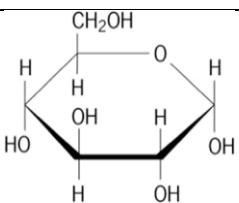
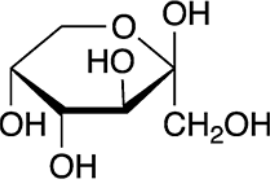
- *Hydroiodic acid*: Another strong reducing agent used for preparing RGO is hydroiodic acid (HI) [108, 109, 110]. Two separate studies of this reduction method reported resulting RGO films with conductivities of about 300 S/cm and a C/O ratio of around 15, which is an improvement of previously performed reductions with hydrazine [109,110]. As with hydrazine, reduction with HI can be carried out at room temperature or it can be heat-assisted. Furthermore, it may be performed by adding HI to a GO dispersion or on GO films deposited on a glass or polyethylenesubstrate using HI vapours. A variation of this method is the addition of acetic acid (CH₃COOH) which acts like a mild reducing agent.
- *Metal hydrides*: Metal hydrides, such as sodium hydride (NaH), sodium borohydride (NaBH₄) [111, 112] and lithium aluminium hydride (LiAlH₄) [113], are widely utilised in organic chemistry as strong reducing reagents. However, these reductants show a slight to very strong reactivity with water, which is the most common solvent for the dispersion of GO. Therefore, they are not suitable for liquid-phase reduction of aqueous GO solutions. NaBH₄ is an exception, however, since although it is hydrolysed by water, its use is kinetically slow enough that the formed solution functions effectively to reduce GO [114]. Furthermore, Shin et al. reported that NaBH₄ has a reducing effect comparable to that of hydrazine. Additionally, NaBH₄ is most effective at reducing C=O groups, has low efficiency at epoxy and -COOH group reduction and leaves the C-OH groups intact.
- *“Green” reducing agents*: The reductants mentioned above are strong chemicals, are highly toxic. This makes the reduction methods which

use them non-biocompatible and not eco-friendly, even though they yield impressive results and large amounts of RGO. When the RGO products are intended to be used in biomedical applications, it is crucial that both the final product and the chemical agents used throughout the synthesis process are safe, non-toxic, biocompatible or, in a word, “green”. There have been many reports of various green routes for GO reduction and it is a field that is continuously being expanded upon [115]. L-Ascorbic acid or Vitamin C has a mild reductive ability is widely used as a reductant for RGO synthesis [116, 117, 118]. Other bio-friendly reductive agents have also been investigated such as amino acids (e.g. glycine [119], alanine [120] and L-cysteine [121]) and sugars (e.g. glucose [122, 123, 124], fructose and sucrose [122]). Some intriguing reducing routes for RGO synthesis have been recently reported and they involve the use of green tea leaves [125, 126], dried figs [127] and spinach extract [128].

- *Nitrogen-containing reducing agents*: One of the most common and strongest reducing agents [129] applied for the reduction of graphene oxide is hydrazine, which was first used in 2007 by S. Stankovich et al. [130]. Hydrazine can be added to a GO suspension to perform heat-assisted reduction in the liquid phase. The result is RGO nanosheets that agglomerate due to increased hydrophobicity. When dried and washed, RGO powder with a C/O ratio of ~10 can be obtained [130]. Alternatively, GO powder can be reduced in the presence of hydrazine vapours [131, 132]. The highest reported conductivity of RGO films prepared via hydrazine reduction is 99.6 S/cm with a C/O ratio of ~12.5 [133]. P. Su et al. reduced GO using dimethyl ketoxime, resulting in reduced GO with higher conductivity in which nitrogen atoms were incorporated into the graphitic lattice [134]. Hydroxylamine [135] and ethylenediamine [136] have also yielded N-doped reduced graphene oxide.

- Hydrothermal treatment: Another reduction method that can be classified as “green”, is the hydrothermal treatment of GO, since it can be performed without any toxic or harsh chemical agents. In this reduction route, only deionised water and an external heat source, such as an autoclave, are necessary [137, 138]. For example, Zheng et al. synthesised RGO by transferring an aqueous solution of GO to a Teflon®-lined autoclave and heating at 180°C for 30 minutes in acidic and alkaline conditions [139]. They then proposed a mechanism for the hydrothermal reduction. They propose that the hydrothermal reduction of GO can be described as the combination of a ring-opening of epoxy groups to form hydroxyl groups which then undergo H⁺ catalysed dehydration through thermal treatment. The supercritical water in this system acts as a source of H⁺ for the protonation of C-OH groups. This can take place both in acidic and alkaline conditions, the difference being in whether the dehydration is intermolecular or intramolecular. In alkaline conditions, the GO sheets are dissolved and separated, and the reduction process follows intramolecular dehydration. Hydroxyl groups are eliminated with hydrogen atoms nearby, followed by the recovery of π -bonding, which increases the average size of sp² carbon domain. In acidic conditions on the other hand, the oxygen-containing groups are protonated, and the GO sheets are poorly dissolved forming aggregates. In this case, the reduction of GO follows intermolecular dehydration. Two C-OH groups on the edge of different GO sheets eliminate a water molecule and form an ether group without the recovery of π -bonding. Ideally, for efficient GO reduction both inter- and intramolecular reduction should take place.

Table 1 Chemical reducing agents used for GO reduction and their chemical structure.

Reducing Agents for Chemical Reduction of GO:			
"Green" Reducing Agents		Nitrogen-containing Reducing Agents	
L-ascorbic acid (Vitamin C)		Hydrazine	
Glycine		Dimethyl ketoxime	
β-Alanine		Hydroxylamine	
L-cysteine		Ethylenediamine	
Glucose			
Fructose			

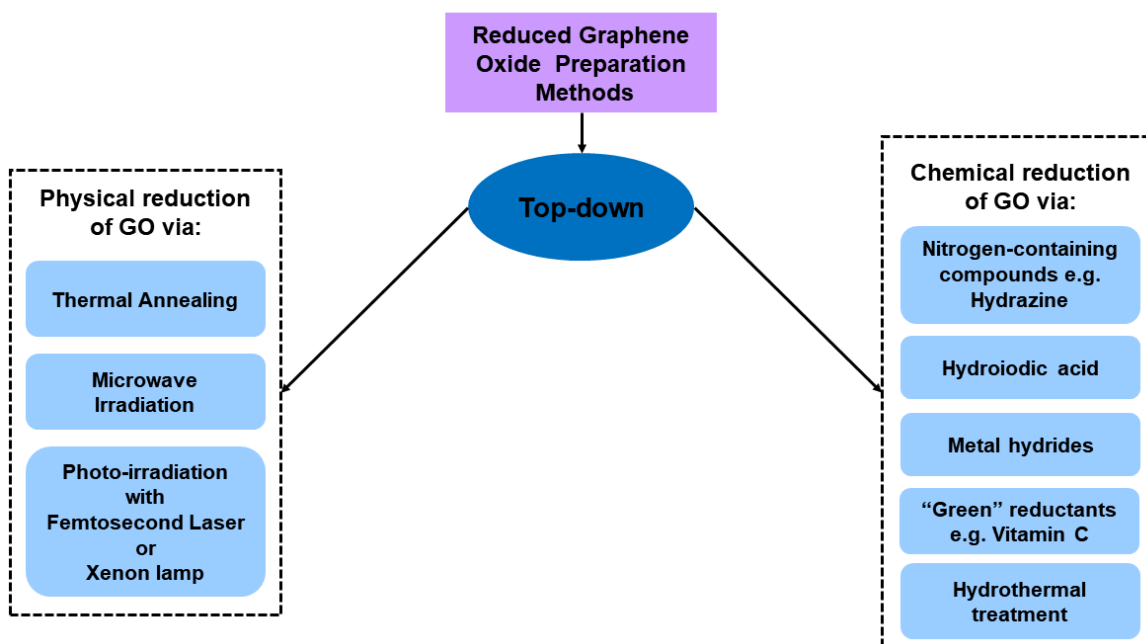
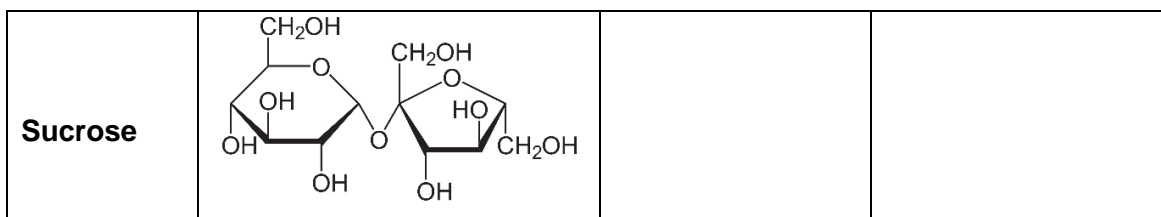


Figure 32 Preparation methods of reduced graphene oxide.

Chapter 5: Applications of graphene and graphene derivatives

Owing to all the impressive properties mentioned in the previous chapter, graphene has been utilised in various electronic and electrical devices, in clean energy applications and in the biomedical field. Following are a few key examples of graphene-based applications.

5.1. Electronics

5.1.1. Photovoltaic cells:

Due to its high conductivity and transparency graphene has been investigated for years as an alternative to metal-based electrodes such as Indium Tin Oxide (ITO) in organic and dye-sensitised solar cells. In 2008, Wang et al. obtained stable graphene films exhibiting a high conductivity of 550 S/cm and a transparency of more than 70% to be used as electrodes in solid state dye-sensitised solar cells [140]. Transparent conductive electrodes based on graphene are more cost effective, easily processable and more stable. Furthermore, they offer the possibility of a more lightweight product with the choice of flexibility. However, graphene's sheet resistance is higher than that of traditional metal based conductive electrodes. Therefore, efforts have been made to combine the positive characteristics of each group and create hybrid electrodes e.g. combining as ITO and poly(3,4-ethylenedioxythiophene) polystyrene sulfonate (PEDOT:PSS) with graphene [141].

Graphene has also been utilised in perovskite solar cells (PSCs) as a transparent electrode [142], an electron transport layer [143] and a hole transport layer [144]. Although PSCs exhibit higher power conversion efficiencies than other third generation photovoltaics e.g. organic solar cells, they show very poor tolerance against oxygen, moisture and high temperatures. There is great need to increase the stability of PSCs in order to exploit their efficiency. A crucial factor in this goal is the stability of the

hole transport layer (HTL), which acts as a protectant of the rest of the solar device and development of non-hydroscopic HTL materials is imperative for overall PSC stability. PMMA, an insulating hydrophobic polymer could serve as such a material if it weren't for its lack of p-conjugation. To combat this set back, a conductive material is applied resulting in an insulator/conductor composite [145]. Single-walled carbon nanotubes (SWCNTs) act as a charge transporter to serve as the conductive material that is paired with PMMA. In a different case, SWCNTs can act as a stabilizer for the conducting polymer P3HT and therefore serve as a protectant for the photoactive layer after the HTL of the PSC [146]. This photovoltaic device architecture is presented in (Figure 33).

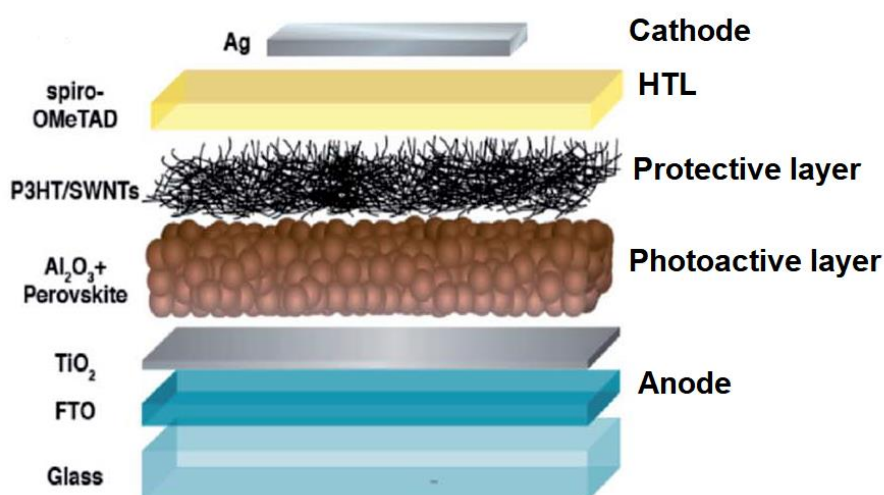


Figure 33 PSC structure which utilises single-layer carbon nanotubes paired with the conductive polymer P3HT to create an insulating hydrophobic layer as a protectant of the photoactive layer. Image taken from reference [146].

5.1.2. Gas sensing:

Graphene's large surface area of 2630 m²/g makes it a useful material to be used in gas sensing. In resistive graphene-based gas sensors, vapours are detected by monitoring the dramatic change in resistance induced by adsorption and desorption of gas molecules onto the surface of

graphene [147]. Additionally, graphene exhibits a strong field effect making graphene-based FET gas sensors very promising [148]. FET gas sensors detect gas using the dependency of the current on the field strength. When gas molecules are adsorbed onto the graphene's surface, the local concentration of charge carriers changes, resulting in a change in current. The adsorption energy of graphene is enhanced when it is oxidised to give graphene oxide [149]. According to Peng and Li, the presence of surface epoxy and hydroxyl groups promote the adsorption of ammonia molecules onto GO sheets. These oxygen functional groups also aid the binding of water molecules via hydrogen bonds onto GO making it an excellent humidity detector material [150]. Graphene-based vapour sensors have been developed for detection of gas molecules such as NH_3 [151], NO_2 [152], CO_2 [153], SO_2 [154], volatile organic compounds such as acetone [155], chemical warfare agents [156] and more. An example of graphene in gas sensing is presented in Figure 34, in which ammonia and nitrogen dioxide molecules are adsorbed onto a graphene substrate.

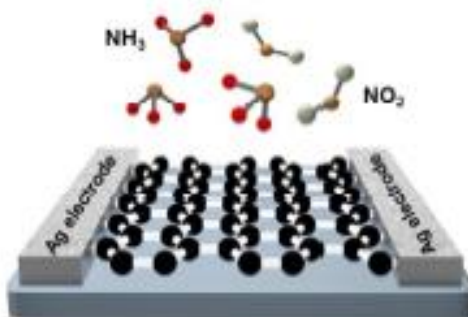


Figure 34 Adsorption of NH_3 and NO_2 gas molecules onto graphene substrate causes fluctuation in electrical current, indicating the concentration of the adsorbed gas. Image lifted from reference [151]

5.1.3. Light Emitting Diodes (LEDs):

In recent years LEDs have found application in optoelectronics, light communications and smart displays [157,158]. One of the determining factors when evaluating the performance of an LED is the external quantum

efficiency (EQE), which is the ratio of the number of photons emitted from the LED to the number of electrons passing through the device. It essentially describes how efficiently the LED converts electrons into photons and also how efficiently those photons are emitted from the device. The EQE is known to be dominated by the light extraction efficiency and internal quantum efficiency (IQE) [159]. Although the IQE has recently reached the theoretical limit of over 90%, the light extraction efficiency is yet to be improved [160].

High transparency, low sheet resistance electrodes are the key to increase light extraction in LEDs. ITO has been widely used for this purpose, as it has an optical transparency of >80% from 450 to 550 nm and a sheet resistance of 250 Ω/sq [161]. Despite these advantages, ITO shows drawbacks such as high cost, rigidity and brittleness, meaning it is not suitable for flexible or stretchable devices. Graphene and carbon nanotubes have been developed to replace ITO in LEDs to achieve higher performances [162, 163].

A recent example of graphene-based electrode in an LED device was introduced by Huang et al., who developed graphene-encapsulated Cu nanowires (NWs) (Figure 35). These low-cost Cu NWs proved more than adequate competition for ITO, as they showed transmittance of about 93% and a sheet resistance of 51 Ω/sq [164]. Graphene was used to encapsulate the Cu NWs to prevent oxidation and improve stability, while maintaining transparency and low sheet resistance.

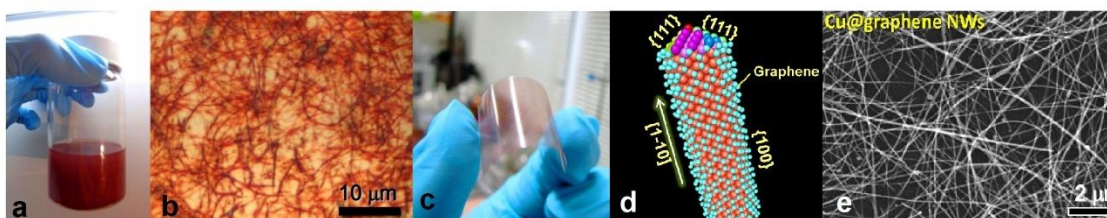


Figure 35 (a) Cu NWs ink (b) Microscope image of Cu NWs. (c) Cu NWs deposited on flexible PET substrate showing very high transparency, (d) Encapsulation of Cu NWs with graphene to increase stability. (e) SEM image of graphene encapsulated Cu NWs.

5.2. Energy storage

5.2.1. Batteries:

Due to their limited capabilities and mainly the finite supply of materials such as cobalt and nickel, the conventional lithium-ion batteries are not a long-term choice for portable energy storage. A more sustainable alternative is imperative in regard to the chemistry of the batteries we use, and graphene appears promising in providing a solution.

Graphene has commonly been utilised as the anode in graphene-based batteries. A strong example of this is the work of J. Hassoun et al., who used graphene ink as the anode and lithium iron phosphate as the cathode [165]. Kim et al. have proposed an all-graphene battery with characteristics resembling both those of a conventional lithium-ion battery and those of a supercapacitor [166]. The cathode and anode consisted of functionalised graphene and reduced graphene oxide respectively. This battery exhibited an energy density of about 225 W/kg which is similar to that of a lithium-ion battery. The energy density was retained even at second level charge-discharge rates exhibiting 6450 W/kg, making the all-graphene battery also comparable to a supercapacitor.

5.2.2. Supercapacitors:

Supercapacitors are energy storage units much like regular capacitors, but with a higher capacitance. They store energy by means of static charge rather than an electrochemical reaction as regular capacitors do. They have low energy density, but a large power density and an exceptional cycle life. Because supercapacitors can deliver power 1 to 100 times greater than that of a conventional lithium-ion battery, they are used in applications that require a large amount of power for a relatively short time, such as electric rail systems [167]. They are also utilised in applications in which a very high number of charge/discharge cycles or a longer lifetime is required, such as power tools.

As in batteries, graphene-based materials have been utilised in supercapacitors as electrodes. Ruoff et al. first utilised chemically reduced graphene oxide as

electrodes in electrochemical double layer supercapacitors [168]. Composites of graphene derivatives and conducting polymers have also been fabricated as electrode materials e.g. GO and polypyrrole composited to create layered GO structures intercalated with the conducting polymer [169]. More recently a 3D graphene-polypyrrole composite hydrogel was developed to be utilised as a flexible supercapacitor electrode (Figure 36) [170].

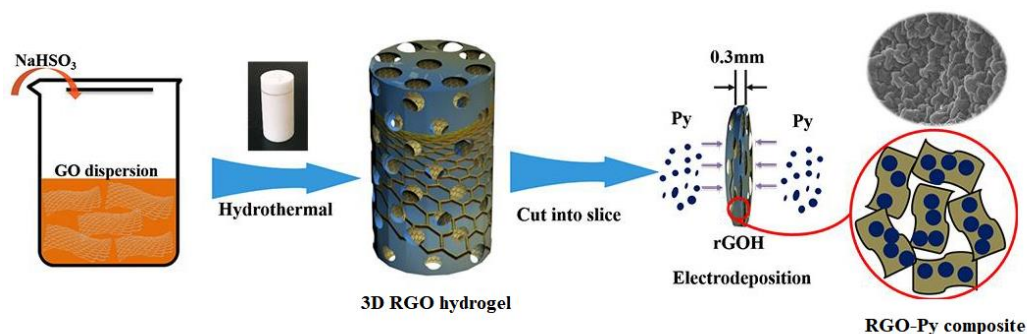


Figure 36 Preparation method of GO-polypyrrole composite hydrogel by X. Zhang et al. as flexible electrode material for supercapacitors. Image taken from reference [170].

5.3. Biomedical applications

5.3.1. Biosensing:

Graphene has been utilised in biosensors for the detection of nucleic acids, small molecules, ions, proteins and cells [171]. To gain insight into how biosensors operate, they generally consist of two elements: a receptor and a transducer (Figure 37). The receptor is an organic or inorganic material that interacts selectively with the target molecule (analyte), which can be an organic or inorganic molecule or even whole cells. The transducer is the component of the sensor, which, after interacting with the analyte, converts chemical information into detectable measurements. Graphene and graphene-based nanomaterials are used as transducers in biosensors due to their large surface area, electrical conductivity and their ability to attach various molecules via EDC/NHS chemistry or physisorption (Figure 37 b).

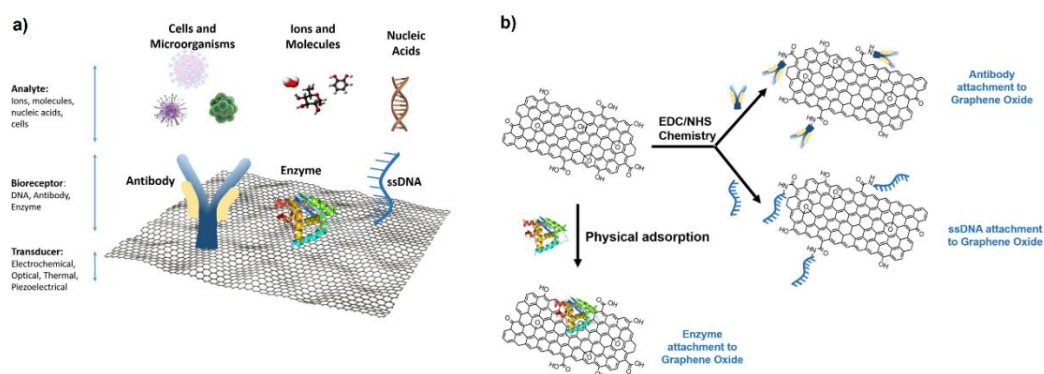


Figure 37 a) Examples of biosensors and components on a graphene platform. Shown: different analytes and the bioreceptor that they bind to. b) Processes in which different types of bioreceptors attach to the graphene platform. Image taken from reference [171]

Graphene and graphene-based nanomaterials have been used in fluorescence-resonance-energy transfer (FRET) biosensor development [172]. FRET function is based on the transfer of energy from a donor fluorophore to an acceptor fluorophore and is one of the advanced tools available for measuring nanometer-scale distance and changes, both in vivo and in vitro [173]. Briefly, the principles of operation of graphene-based FRETs, which is represented schematically in Figure 38, is as follows: ssDNA, aptamers or molecular beacons which act as probes are adsorbed onto the planar graphene surface. Fluorophore labels on the ends of these probes are quenched rapidly when adsorbed onto the graphene surface. When analytes (complementary DNA (cDNA), thrombin and a designed complementary ssDNA or functional nucleic acids like survivin mRNA) are introduced to the graphene-probe system and bind their probes (ssDNA, aptamer and molecular beacons, respectively), the probe fluorescence is recovered, allowing detection and measurement of the analyte [174].

Compared with organic quenchers, graphene has been shown to offer advantages in this role such as superior quenching efficiency various fluorophores, a low background and high signal-to-noise ratio as well as structural advantages such as resistance to enzymatic cleavage [172]. Furthermore, graphene and GO have been reported to interact strongly

with nucleic acids through π - π stacking between the ring structures in the nucleic acid bases and the hexagonal rings of graphene and GO.

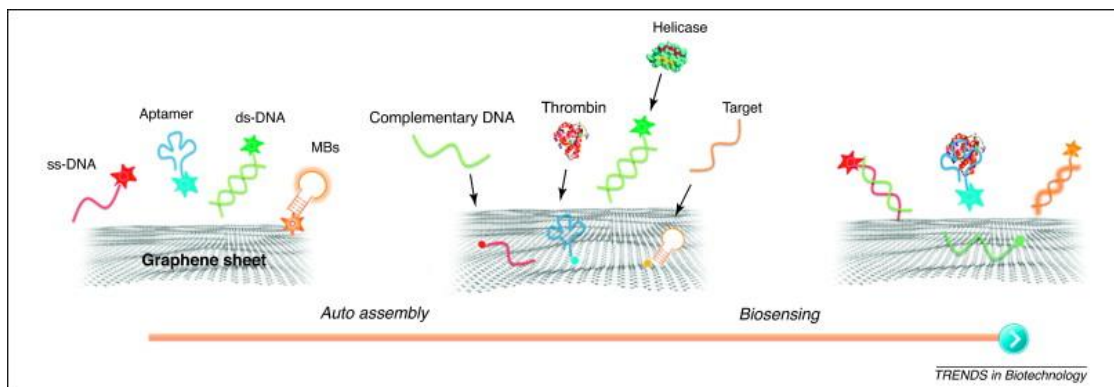


Figure 38 Schematic representation of graphene-based FRET. The fluorophore probe adsorbs to the graphene sheet which causes quenching. The respective analyte interacts with the probe which leads to recovery of fluorescence. Image taken from reference [Error! Bookmark not defined.]

5.3.2. Drug delivery systems:

One of the key factors in constructing drug delivery systems is the selection of an appropriate carrier. For years there has been advancements in the development of drug delivery systems (DDSs) with the aid of graphene-based nanomaterials and now they have been considered one of the optimal choices, which can be engineered to integrate multiple functions in a single system. The innovative efforts to incorporate graphene into DDSs began with Liu et al. at Stanford University when they functionalised nanoscale GO (NGO) with biocompatible branched polyethylene glycol (PEG) to design a water-soluble carrier for SN38, an insoluble camptothecin (CPT) analogue which acts as an anti-cancer drug [175]. The chemical structure of the NGO-PEG-SN38 complex can be seen in Figure 39. Since then, graphene-based DDSs are being intensively explored by many research groups. Many promising results have been produced and efforts have been made to overcome challenges such as the nonbiodegradable nature of graphene and its potential long-term toxicity [176].

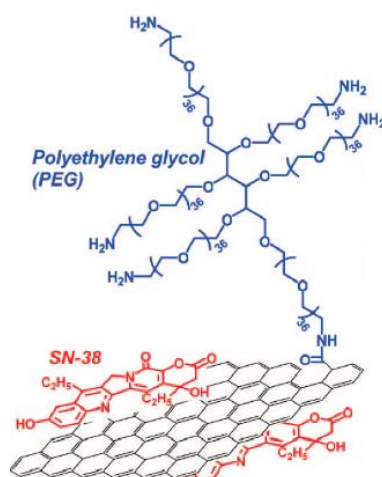


Figure 39 Chemical structure of PEGylated GO nanosheet; a water-soluble carrier for the anticancer drug SN38. Image taken from reference 175.

Many recent advances have been made in graphene-based drug carriers for anticancer drugs such as doxorubicin (DOX) [177]. When considering cancer therapy, it is extremely important to specifically target tumour cells while leaving healthy cells and tissues intact. This makes accurate targeting a crucial factor in anticancer drug development. There are two methods of tumour cell targeting design to achieve this goal: active targeting and passive targeting. In passive targeting, the carrier reaches the target administration site without the aid of conjugated target-specific ligands to serve as homing devices. A disadvantage of this targeting mechanism is that low drug concentrations ultimately reach the target cell due to leakage, inactivation of drug and encounter of obstacles during the prolonged circulation. Moreover, the ionic interaction of the electronegative cell membrane and the electropositive nanoparticles could cause toxicity and off-target side-effects [178]. In contrast, active targeting is a mechanism in which the surface of the carrier is functionalised with ligands designed to act as homing devices by recognising and binding to specific administration sites. This could achieve enhanced therapeutic effects and reduced side effects by the interactions between ligand and corresponding targeted cell.

5.3.3. Tissue engineering:

Tissue engineering is a branch of the medical field which embraces the potential of repairing and regenerating damaged tissues and replacing defective body parts or organs that have been affected by disease and trauma. Being potentially biocompatible with striking chemical, biological and optical properties, graphene-based materials have been employed to further the advancement of tissue engineering.

Functionalised graphene has been used to generate 2D and 3D scaffolds which are necessary for tissue regeneration in a cell culture (Figure 40) [179]. Biopolymers such as chitin and gelatine have been used to create scaffolds for human osteosarcoma cells and human embryonic stem cell growth, respectively [180, 181, 182]. Other polymers have similarly been utilised. Since then, graphene and graphene-based materials have been proven very promising in generating improved scaffolds for engineering various types of cells and tissues, such as bone tissue [183, 184], muscle tissue [185] and cardiac tissue [186]. A recent example is the work of B. Nyambat et al. who developed a sponge-scaffold for skin tissue engineering by generating a nanocomposite comprising of GO and genipin-crosslinked ECM (cell-derived extracellular matrix) taken from rabbit adipose derived stem cells (Figure 41) [187].

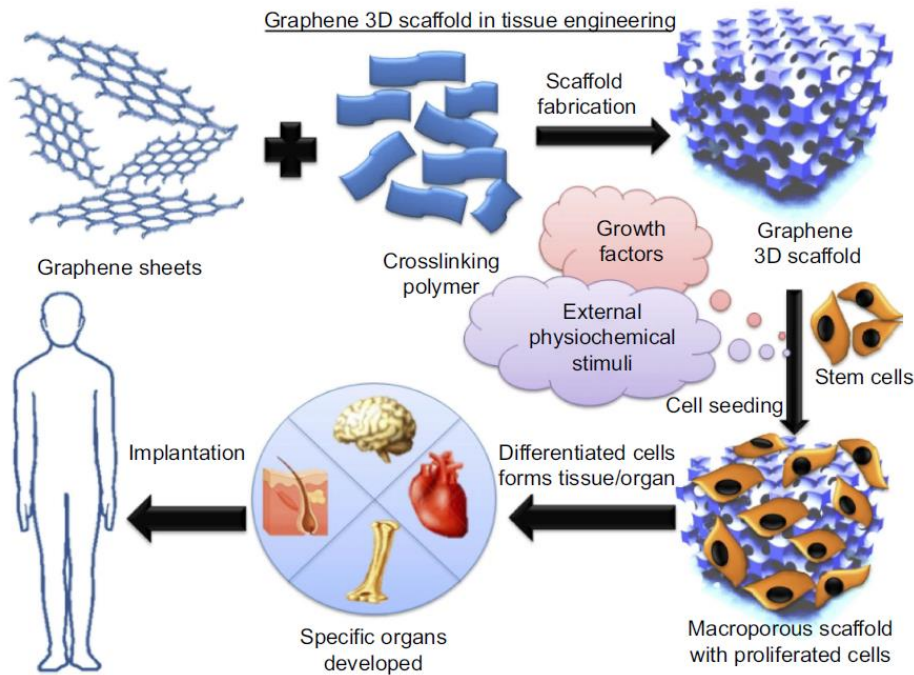


Figure 40 Schematic showing the utilisation of graphene in the engineering of 3D scaffolds for tissue regeneration. Image taken from reference [179].

Graphene-based materials have also been used or tissue engineering in the dental field [188]. A strong example of graphene in dental tissue engineering is the proliferation and differentiation of dental pulp stem cells. According to work carried out by Gronthos et al., these cells have the ability to differentiate into odontoblasts/osteoblasts, adipocytes and neural-like cells [189]. They also express genes that are linked to initiating mineralisation and bone homeostasis, which is essentially bone remodelling i.e. removing old bone tissue and replacing it with new bone tissue [190]. Graphene-based scaffolds have been made for the production of dental pulp stem cells. Although there was no difference in proliferation to be seen when compared to a reference glass substrate, the graphene-based scaffold proved to promote mRNA expression resulting in higher gene expression [191].

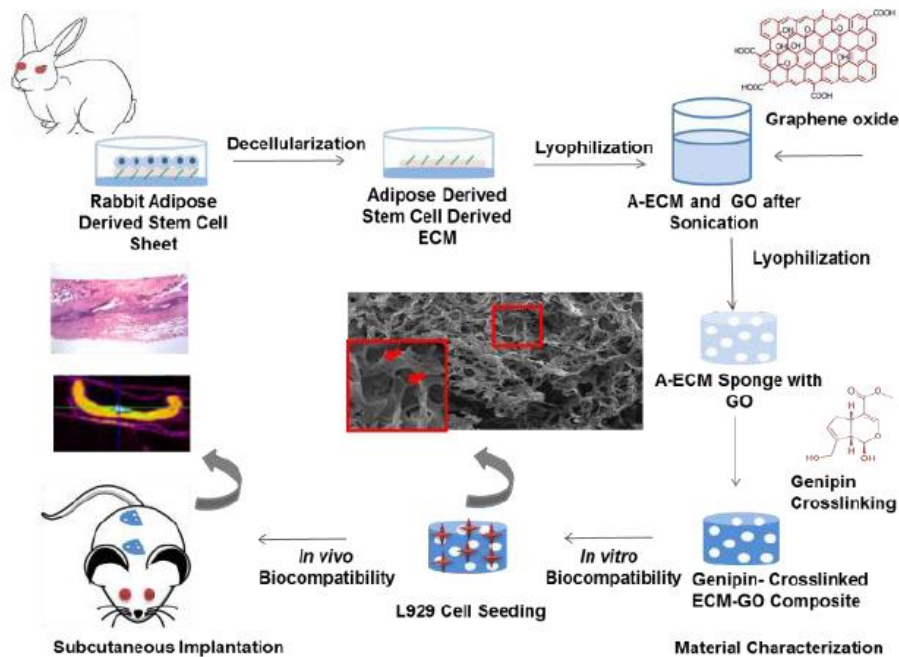


Figure 41 Step-by-step process for developing Genipin crosslinked ECM-GO sponges for skin tissue engineering. Image taken from reference [187].

5.4. Environmental:

5.4.1. Water treatment and filtration:

Graphene-based materials have found application in water treatment, desalination and anti-fouling [192, 193]. Membranes consisting of nano porous graphene, GO frameworks and CNTs have been developed to be utilised as membranes in water desalination [194, 195]. Desalination is the process of removing salts from seawater through filters that trap the salts while allowing the fresh water to pass through and is more energy efficient than the conventional desalination method which involves water evaporation.

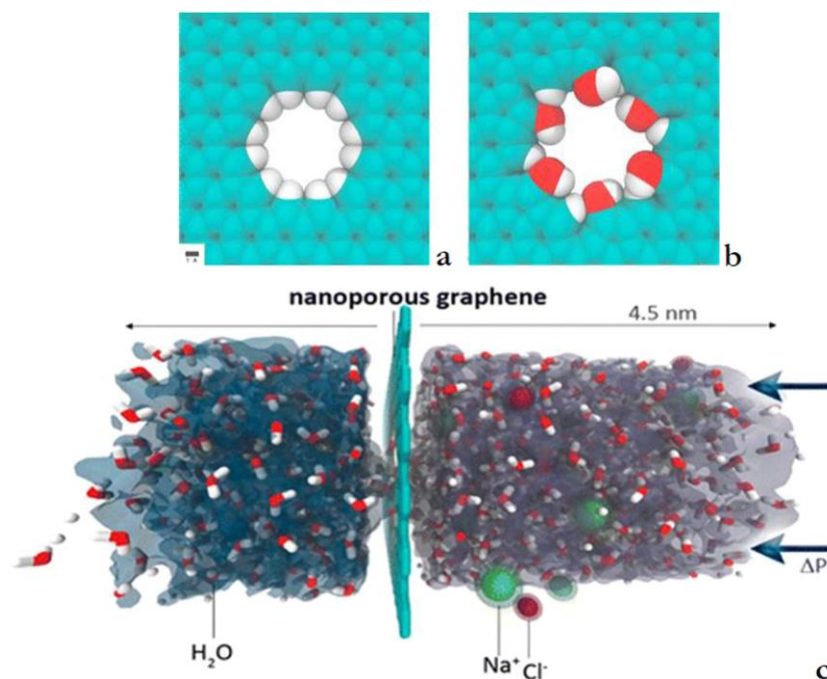


Figure 42 Desalination of seawater via nano-porous graphene membrane based on difference in pressure. The pores in the graphene membrane withhold NaCl molecules while allowing the water molecules to permeate. Image lifted from reference [194].

A novel example is the work of Yang et al. who have reported a graphene nano-mesh (GNM) and single-wall carbon nano-tubes (SWCNT) hybrid to serve as a porous membrane that features mechanical strength for removal of solute ions or molecules, enabling size-selective separation [195]. A layer of interconnecting SWCNT is transferred onto a CVD-grown layer of graphene. A layer of mesoporous SiO₂ is grown on the graphene-SWCNT membrane to act as a porous template and holes are then drilled into the graphene-SWCNT membrane using O₂ plasma treatment. When the SiO₂ template is removed the result is a free-standing GNM/SWCNT hybrid membrane, shown in Figure 43, which successfully withholds NaCl from seawater with a measured salt rejection of ~98.1% [195].

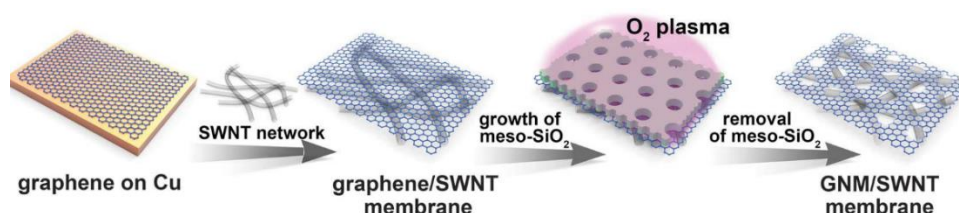


Figure 43 Fabrication process for graphene nano-mesh (GNM) and single-wall carbon nano-tubes (SWCNT) hybrid membrane for water desalination. Image lifted from reference [195]

Graphene oxide has also been utilised in water purification and treatment. M. Abolhassani and his colleagues fabricated and evaluated chitosan-GO composite films as pressure-driven water filtration membranes [196]. A chitosan suspension was functionalised with GO particles and deposited via evaporative phase inversion to create a hybrid membrane that exhibited a rejection of at least 95% for cationic methylene blue dye and 66-99% for methyl orange dye.

GO may also be used to improve existing water purification technologies by offering advanced new properties. For example, GO exhibits antibacterial effects that can prove beneficial in the enhancement of water filtration membranes. F. Perreault et al. functionalised polyamide membranes with biocidal GO nanosheets to develop improved membranes resistant to bacterial growth [197]. Perreault and his colleagues found that the GO-polyamide membranes exhibited E. Coli inactivation of up to 59%, showing very promising anti-fouling effects.

5.4.2. Decontamination:

Metal ions are toxic pollutants that enter aquatic environments and drinking water supplies through mining and industrial activities or corrosion of piping and other plumbing materials [198]. Metal ions cannot be degraded via chemical reactions and adsorption has been proven to be the most effective method for their removal [199]. Graphene-based materials can serve this purpose by acting as an adsorbent for metal ion contaminants. Pb (II) ions have been efficiently adsorbed from aqueous solutions onto graphene nanosheets [200]

GO is preferable to pristine graphene for metal ion adsorption due to its high content of oxygen functional groups available to interact with metal ions. Electrostatic interaction is considered the primary adsorption mechanism,

although Huang et al. suggested that the delocalized p-electrons in the sp^2 network of the graphene regions of GO may act as Lewis bases donating electrons to metal ions. Kinetic studies also suggest that the adsorption of metal ions onto GO is of a chemical nature, therefore it is characterised as chemisorption [201]. S.-T. Yang et al. demonstrated successful removal of Cu (II) cations using GO through interaction of the positive charge of the Cu (II) ions and the negatively charged GO oxygen groups [202]. GO and functionalised GO has also shown impressive adsorbance for other metal ions such as Zn^{2+} , Cd^{2+} , Pb^{2+} , Ni^{2+} and Co^{2+} [201, 203].

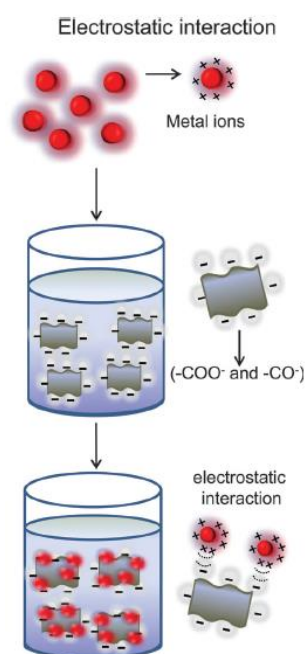


Figure 44 Adsorption of metal cations onto GO via electrostatic interaction with the negatively charged oxygen groups. Image lifted from reference [197]

Chapter 6: Investigating the liquid processability of GO and RGO

6.1. Importance of liquid processable graphene-based materials-Past work

Graphene and its derivatives are lightweight, cost-effective and offer the option of scalable production, making them a very attractive material. They have remarkable and tunable properties which are continuously being investigated and manipulated to yield new graphene-based materials and novel preparation methods. Nevertheless, there is one more crucial aspect that must be further investigated and improved upon: processability. Since graphene's discovery, it became important to find ways to handle it via methods beyond Novoselov's Scotch tape method [42]. In most cases, in order to deposit graphene-based materials on the desired device or set-up, it is necessary that they are first prepared in a liquid phase. Such deposition methods include drop-casting [204], spin coating [205], spray coating [206], vacuum filtration [207] and inkjet printing [208]. Therefore, the stability of graphene and functionalised graphene such as GO and RGO in various solvents is a critical point in developing graphene-based technologies.

For a long time, there has been reported work of successful GO processing in aqueous media [209, 210, 211]. The oxygen functional groups of GO offer this material hydrophilicity making it dispersible in water and other polar solvents. This constitutes GO highly 2D solution processable. It should be noted that although GO may be sufficiently dispersed in many solvents owing to the presence of oxygen groups, it is these very same oxygen groups that distort the sp^2 system on the graphitic lattice. This significantly decreases the conductivity which distinguishes graphene making GO an insulator. It is apparent that the dispersibility of this material is a trade-off with the preservation of its unique properties.

The fact that it is dispersible in water, the “universal solvent”, offers the option of creating non-toxic biocompatible dispersions to be utilised in bio-applications. However, the preparation of GO dispersions in other solvents, particularly organic solvents, is highly desirable because it may facilitate the practical use of this material and broaden the spectrum of applications. The dispersibility and stability of GO in various solvents has been investigated by several groups in the past [212, 213, 214, 215, 216]. J.I. Paredes et al. investigated the dispersibility of GO

in 13 organic solvents and successfully prepared stable, high concentration dispersions in ethylene glycol, DMF, NMP and THF (Figure 45) Solvent mixtures of varying ratios have also been investigated in hopes of enhancing the stability of GO by combining the physical properties of multiple solvents. For example, V. Neklyudov et al. prepared GO dispersions in water and ethylene glycol (EG) mixtures and concluded that the blend of 60% EG-40% H₂O yielded the most stable GO suspensions [217].

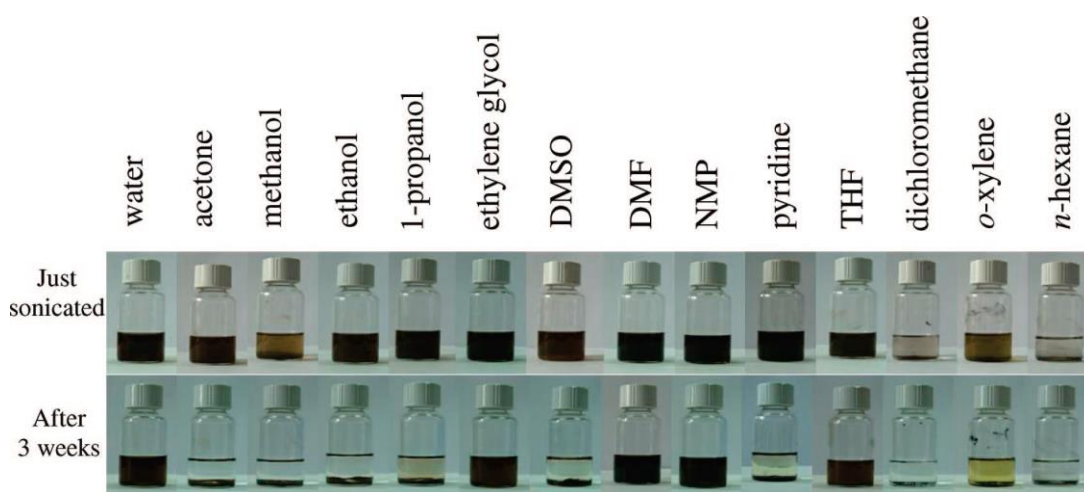


Figure 45 GO dispersions in various organic solvents prepared by J. I. Paredes et al. via ultrasonic bath (1h). The photograph features the dispersions right after ultrasonication and after being left for 3 weeks to test the stability.

RGO has a different structure and therefore dispersion behaviour compared to GO. On one hand, it has less oxygen functional groups, depending on the level of reduction, making it incompatible water and polar solvents. Furthermore, the van der Waals forces between the graphene layers lead to agglomeration of RGO. On the other hand, RGO contains more aromatic regions with conjugated double bonds, making it much more conductive than GO and an excellent candidate for electronic applications. It is apparent that RGO has very desirable electronic properties, but its chemical structure inhibits it from being compatible with most common solvents. Although there have been past publications that investigate the subject, the literature on its stability in various solvents in comparison to that of GO is lacking [218, 219, 238]. It is vital to gain insight into the stability of RGO dispersions in order to promote and improve technologies that rely on RGO's electrical and optical properties.

RGO remains suspended in organic solvents such as N-Methyl-2-pyrrolidone (NMP) and dimethylformamide (DMF) (Figure 45) [220]. Nevertheless, the study of RGO's dispersibility in other solvents will prove valuable in the future of graphene-based applications and technologies.

Knowing the most suitable solvents in which to successfully disperse GO and RGO is key to achieving exfoliation in the liquid phase and producing liquid processable graphene derivatives that are more readily and more efficiently utilised in applications. For this purpose, the HSP offer a unique way of predicting the dispersibility of GO and RGO in different solvents and solvent mixtures of varying ratios. Furthermore, they may open doors for the development of new, novel applications, since these materials will no longer be inhibited by their lack of processability in liquid phase.

6.2. Investigating the dispersibility of GO and RGO with the Hansen Solubility Parameters:

After discussing the wide variety of applications that graphene and graphene derivatives it is evident that processability is imperative if these benefits are to be exploited and liquid exfoliation has become a well sought-after method. Therefore, discovering the most appropriate solvents is the next substantial step in liquid processable graphene and HSP can significantly aid in this effort.

Solubility parameters were initially made for molecules and were mainly used in the coatings industry to aid in the selection of suitable solvents. Since then, they have been used to predict compatibility of polymers, chemical resistance, and permeation rates and even to characterise the surfaces of pigments, fibres, and fillers. Most solubility parameters are based on the indirect determination of solubility, but all concepts of solubility parameters are based on the old paradigm “like dissolve like” [230]. The closer the solubility parameter of the component (molecule or polymer) and the liquid it is to be dissolved in, the higher the solubility of this component and vice versa. This is also applicable between two or more liquids, i.e. liquids with similar solubility parameters will be miscible. Since then, the classic “like dissolves like” principal has been seen more as “like sees like”, as the materials do not necessarily dissolve, as is the case with nanoparticles (NPs) which are dispersed in suitable solvents.

6.2.1. The past: Hildebrand Solubility Parameter

In 1936, Joel H. Hildebrand proposed a simple “solubility parameter” that described the miscibility behaviour of solvents [221]. Simply put, it is a numerical value that indicates the relative solvency behaviour of a specific solvent and is a reflection of the total Van der Waals forces. It is derived from the cohesive energy density of the solvent, which in turn is derived from the heat of vapourisation. More specifically, this solubility parameter, δ , is defined as the square root of the cohesive energy density. The cohesive energy density is the amount of energy needed to completely remove unit volume of molecules from their neighbours to infinite separation and is equal to the heat of vapourisation of the compound divided by its molar volume in the condensed phase (Equation $\delta = \sqrt{\frac{\Delta H_v - RT}{V_m}}$).

The cohesive energy of a material essentially describes the binding energy between two molecules and can be considered a measure of mutual attraction between these molecules. For a material to dissolve in a solvent, the interactions between the neighbouring molecules (Van der Waals forces) must be overcome, so they can separate from each other and be surrounded by the solvent.

$$\delta = \sqrt{\frac{\Delta H_v - RT}{V_m}} \quad (1)$$

where ΔH_v is the heat of vaporisation, V_m is the molecular volume and RT is the ideal gas term for PV , which is subtracted from ΔH_v to obtain the energy of vaporisation. Typical units for the Hildebrand parameter (HP) are 1 Hildebrand = 1 $\text{cal}^{1/2} \text{cm}^{-3/2} = 2.045 \text{MPa}^{1/2}$ with $\text{MPa}^{1/2}$ being the SI unit [222]. The principal utility of the HP is that it provides predictions of phase equilibrium based on a parameter that is readily available for most materials.

To better understand the definition of the solubility parameter from a thermodynamic perspective, the following terms should be defined and explained.

➤ Heat of vaporisation (ΔH_v):

When a liquid is heated, energy in the form of heat is added to the liquid, resulting in an increase in its temperature. When the liquid reaches its boiling point, however, the further addition of heat does not cause a further increase in temperature. Instead, the added energy is used in its entirety to separate the molecules of the liquid and convert them into a gaseous phase. Only when the liquid has been completely vaporised will the temperature of the system again begin to rise. If we measure the *amount* of energy in calories that was added from the onset of boiling to the point when all the liquid has boiled away, we will have a direct indication of the amount of energy required to separate the liquid into a gas, and thus the amount of van der Waals forces that held the molecules of the liquid together.

When discussing the solubility parameter in thermodynamic terms, the boiling temperature is not important, but the amount of heat needed to separate the liquid molecules is. A liquid with a low boiling point may require a considerable amount of heat to vaporise, while a liquid with a higher boiling point may vaporise quite readily. The amount of heat required to completely vaporise a liquid is known as the heat of vaporisation (ΔH_v). The stronger the intermolecular forces holding the liquid molecules together, the higher the heat of vaporisation.

➤ Cohesive Energy Density (C):

The cohesive energy density (C) of a liquid is derived from the heat of vaporization, in calories per cubic centimetre (cm^3) of liquid, by the following expression

$$C = \frac{\Delta H_v - RT}{V_m} \quad (2)$$

where: C=cohesive energy density, ΔH_v =heat of vaporization, R=gas constant, T=temperature (K), V_m =molar volume. As mentioned previously, the heat of vaporisation is higher when strong intermolecular forces hold the liquid molecule together. This translates into the cohesive energy density, which is dependent on the heat of vaporisation (Equation $C = \frac{\Delta H_v - RT}{V_m}$

(2).

➤ Gibbs Free Energy (ΔG_M):

Thermodynamics state that the Gibbs free energy of mixing (ΔG_M) must be zero or negative for the solution to occur spontaneously. The free energy change for the solution process is given by Equation ($\Delta G_M = \Delta H_M - T \cdot \Delta S_M$

(3).

$$\Delta G_M = \Delta H_M - T \cdot \Delta S_M \quad (3)$$

Where ΔG_M is the free energy of mixing, ΔH_M is the heat of mixing, T is the absolute temperature and ΔS_M is the entropy change in the mixing process.

$$\Delta H_M = \varphi_1 \varphi_2 V_m (\delta_1 \delta_2)^{1/2} \quad (4)$$

Where φ_1 and φ_2 are volume fractions of solvent and polymer and V_m is the total volume of the mixture. Equation $\Delta H_M = \varphi_1 \varphi_2 V_m (\delta_1 \delta_2)^{1/2}$

(4), however, is not considered to be correct, as

it states that only positive heats of mixing are allowed. According to D.

Patterson and G. Delmas, equation $\Delta H_M = \varphi_1 \varphi_2 V_m (\delta_1 \delta_2)^{1/2}$

(4) gives the value of $\Delta G_{Mnoncomb}$ and not ΔH_M [223]. Therefore, the correct equation is:

$$\Delta G_{Mnoncomb} = \varphi_1 \varphi_2 V_m (\delta_1 - \delta_2)^{1/2} \quad (5)$$

where $\Delta G_{Mnoncomb}$ is the noncombinatorial free energy of the solution. This value includes all free energy effects other than the combinatorial entropy of solution which occurs simply by mixing the components. Equation $\Delta G_{Mnoncomb} = \varphi_1 \varphi_2 V_m (\delta_1 - \delta_2)^{1/2}$ (5) predicts both positive and negative heats of mixing.

The previous information demonstrates that the solubility parameter should be considered a free energy parameter. The combinatorial entropy enters as a constant factor in the plots of solubility in different solvents, for example, since the concentrations are usually constant for a given study. A match in solubility parameters leads to a zero change in noncombinatorial free energy and the combinatorial entropy change will ensure solution is possible from a thermodynamic point of view.

The ΔH_M value is small if the solubility parameter values are close, and ΔG tends to be zero or negative. The maximum difference in solubility parameters, with which solution still occurs, is found by setting the noncombinatorial free energy change equal to the combinatorial entropy change:

$$\Delta G_{Mnoncomb} = T \cdot \Delta S_{Mcomb} \quad (6)$$

Equation ($\Delta G_{Mnoncomb} = T \cdot \Delta S_{Mcomb}$)

(6) shows that there is an entropy change which constitutes the limit of solubility. This change in entropy dictates how close the solubility parameters must be for a mixture to occur spontaneously. Solvents with smaller molecular volumes will be thermodynamically better than larger ones having identical solubility parameters. A practical aspect of this effect is that solvents with relatively low molecular volumes, such as methanol and acetone, can dissolve a polymer at larger solubility parameter differences than expected from comparisons with other solvents with larger molecular volumes. The converse

is also true. Larger molecular species may not dissolve, even though solubility parameter considerations might predict this [224].

According to Equation ($\Delta G_M = \Delta H_M - T \cdot \Delta S_M$

(3), entropy change has a positive effect on mixing.

When multiplied by the temperature, the result is a more negative free energy of mixing. This is the usual case, although there are exceptions. Patterson and his colleagues showed that increasing the temperature does not always lead to improved solubility [223,225]. By working with non-polar systems, they found that an increase in temperature may lead to insolubility. Increasing temperature can also lead to a nonsolvent becoming a solvent and then a nonsolvent again with further increase in temperature. This phenomenon occurs with liquids more so than with polymers, as polymer solubility parameters are virtually temperature independent, whereas those of a liquid frequently decrease rapidly with temperature [225]. This situation allows a nonsolvent with a solubility parameter which is initially too high to transition into a soluble state to once more be converted into a nonsolvent as the temperature increases. These are usually “boundary” solvents on solubility parameter plots.

Some HP values were presented in the Journal of Paint Technology in 1967 (Table 2) [226].

Table 2 Hildebrand values for various solvents.

Solvent	MPa ^{1/2}
n-Pentane	14.4
n-Hexane	14.9
n-Heptane	15.3
Diethyl ether	15.4
n-Dodecane	16
Turpentine	16.6
Cyclohexane	16.8
Carbon tetrachloride	18
Xylene	18.2

Ethyl acetate	18.2
Toluene	18.3
Tetrahydrofuran	18.5
Benzene	18.7
Chloroform	18.7
Acetone	19.7
Pyridine	21.7
Dimethylformamide	24.7
n-Propyl alcohol	24.9
Ethyl alcohol	26.2
Dimethyl sulphoxide	26.4
n-Butyl alcohol	28.7
Methyl alcohol	29.7
Ethylene glycol	34.9
Glycerol	36.2
Water	48

By ranking the solvents in the table above according to solubility parameter, a spectrum can be obtained. In this spectrum, solvents that are close to each other are more likely to dissolve the same materials. For example, it is apparent that if a material is readily dissolved in acetone, then one might expect that the same material will also be soluble in ethyl methyl ketone, because these two solvents have similar internal energies. Conversely, the same material would not dissolve in solutes such as hexane, due to the large difference in internal energy values [227]. Theoretically, there will be a contiguous group of solvents that will dissolve a particular material, while the rest of the solvents in the spectrum will not. Some materials will dissolve in a large range of solvents, while other might be soluble in only a few. A material that cannot be dissolved at all, such as a crosslinked three-dimensional polymer, would exhibit swelling behaviour in precisely the same way (Figure 46) [227].

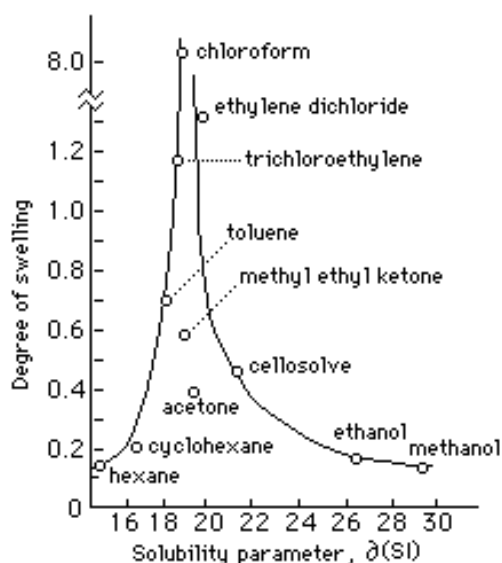


Figure 46 Swelling of Linseed Oil Film in Solvents Arranged According to Solubility Parameter (Image taken from reference [228])

Interestingly, a HP can be calculated for a solvent mixture by averaging the Hildebrand values of the individual solvents by volume. For example, a mixture of two parts toluene and one-part acetone will have a Hildebrand value of 18.7 as calculated by: $18.3 \times \frac{2}{3} + 19.7 \times \frac{1}{3}$. Chloroform also has a Hildebrand value of 18.7. Therefore, a 2:1 mixture of toluene and acetone should have the same solubility capacity as chloroform.

There is, however, a drawback to the HP, as no differentiation between the types of interactions, e.g. polar or non-polar, is established. This issue will be addressed in the future by Dr. Charles M. Hansen, who divided the HP into three parts which specifically represent each type of interaction: the dispersion parameter (δ_D) describing the contribution of non-polar London interactions, the polar parameter (δ_P) describing the forces of two permanent dipoles and the hydrogen parameter (δ_H) which accounts for hydrogen bonding and the ability of electron exchange based on the acid and base concept of Lewis [229].

6.2.2. The present: The Hansen Solubility Parameters

The Hildebrand solubility parameter was the only tool to determine the miscibility of solvents, until 1967, when Dr. Charles Hansen proposed his own alternative. In Hansen’s approach, the HP is split into three components. These three new parameters were: δ_D , δ_P and δ_H which represented the Dispersive (van der Waals), Polar and Hydrogen-bonding aspects of a solvent, a polymer, or a pigment. These were later named the Hansen Solubility Parameters (HSP) by A. Beerbower, Hansen’s colleague [230]. Hansen’s theory is based on the principle of “like dissolves like”. Solvents and solutes with similar HSP are more likely to form stable solutions than those with significantly different parameters.

The reason Hansen developed this new approach was because the HP was lacking in many situations. The predictions derived from the HP are useful for nonpolar and slightly polar (dipole moment < 2 debyes) systems, and does not include hydrogen bonding and polar solvents, since the theory was based on the behaviour of hydrocarbon solvents. Hansen himself realised that the original Hildebrand solubility parameter could only apply to relatively non-polar and non-hydrogen-bonding molecules. In other words, the main limitation of using one solubility parameter is that it applies only to positive deviations from Raoult's law ("like dissolves like") [231]. It cannot account for negative deviations from Raoult's law.

In one of his publications, Dr. Hansen presents a simple example in which the HP fails [232]. The HPs for n-Butanol and nitroethane are identical. Neither solvent dissolves a typical epoxy, but a 50:50 mixture of the two solvents does. Hildebrand does not offer a coherent theory with which to tackle solvent blends. The Hansen Solubility Parameters offers an interpretation of this phenomenon where the HP fails. A typical Epoxy has HSP of [17, 8, 8]. Butanol is [16, 5.7, 15.8] and an HSP distance (R_a) of 8.4. Nitroethane is [16.0, 15.5, 4.5] with an R_a of 8.5. The 50:50 mix is [16, 10.5, 10.3] with an R_a of 3.9. Although the dividing line between “solvent” and “non-solvent” for a polymer can vary, an R_a of 8 is typically a good estimate. Both nitroethane and n-Butanol individually are beyond that R_a but their mixture is well inside. These values were not simply a theoretical prediction, but rather lab-based experimental data collected by Hansen and his colleagues. In a similar

fashion, Hansen discovered more than 60 pairs of non-solvents which, when mixed with the correct ratio, were able to dissolve 22 different polymers.

It is evident that Hansen's work was simply an expansion on that of Hildebrand, allowing for the application in a wider variety of solvents. By following an engineering approach, Hansen developed a concrete, consistent and experimentally valid way to divide the HP into three components and to generate large tables of values for practical use. For more than 50 years HSP have proven to be a powerful, practical way to understand issues of solubility, dispersibility, swelling and other material interactions. They have extended their use from industrial application to research and academic laboratories where users have gained insight into solvent, polymer and nanoparticle behaviour.

6.2.3. Hansen Solubility Parameters-The Basics:

The golden rule when mixing is “like attracts like” therefore “like dissolves like”. There needs to be a less vague definition as to what “like” is. If a formula for “like” is established, the solubility of a compound or the dispersibility of a nanoparticle in a solvent can be determined by how compatible or “alike” they are.

The entire theory for the HSP is born similarly to that of the HP. It all begins, once again, with the heat of vapourisation (ΔH_v). Evaporation is an endothermic process which means that for a solvent to be evaporated, energy must be provided to the system. This energy is the ΔH_v of the solvent. When the solvent is condensed, the same amount of energy is released from the system. This is the heat of condensation (ΔH_{cond}) and the relation between the two is $\Delta H_v = -\Delta H_{\text{cond}}$.

If a portion of a solvent is evaporated and then condensed in an equal volume of a different solvent, the two solvents are considered miscible if the energy cost of doing this is minimal. If the two solvents are not “alike”, then energy provided during evaporation and the energy released during condensation are extremely unequal and miscibility is low.

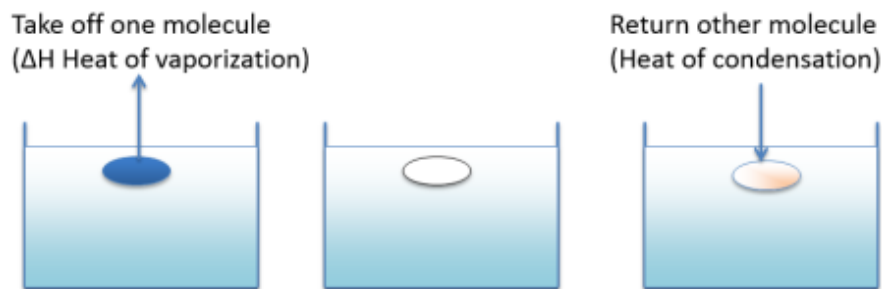


Figure 47 Heat of vaporisation and heat of condensation of a solvent. Image source: www.hansen-solubility.com

Perhaps it is more relevant to talk about the cohesive energy (E) of a solvent. As mentioned in paragraph 6.2.1., this is the amount of energy required to separate a solvent into gas molecules. It is, in other words, a measure of the inter-molecular energy of a substance. When discussing liquids, the cohesive energy represents almost entirely the inter-molecular binding energy of the liquid molecules, since this energy in gases is extremely small. When E is broken into three components (dispersion, polar and hydrogen-bonding), the result is the following relation:

$$E = E_D + E_P + E_H \quad (7)$$

The cohesive energy is linked to the heat of vapourisation and the universal gas constant (R) through the following equation:

$$E = H_v - RT \quad (8)$$

The cohesive energy is dependent on the nature of the liquid in question as it is related to the size and the polarity of the molecules. Molecules of bigger size have a larger cohesive energy. Therefore, to make the cohesive energies of each liquid comparable, the term cohesive energy density is more suitable. The cohesive energy density is calculated when C is divided by the molar volume (V), as seen in the following equation:

$$\frac{E}{V} = \frac{E_D}{V} + \frac{E_P}{V} + \frac{E_H}{V} \quad (9)$$

When $\frac{E}{V}$ is replaced with δ^2 the result is the Hansen solubility parameter which is divided into its three components: $\delta_D, \delta_P, \delta_H$ according to the following formula:

$$\delta_T^2 = \delta_D^2 + \delta_P^2 + \delta_H^2 \quad (10)$$

The typical units of the solubility parameters are $\text{MPa}^{1/2}$.

Returning to the discussion of “like”, there is measure of how “alike” two molecules are which is called HSP distance (R_a). This value is essentially the net difference between the HSP of two materials. The smaller the R_a between two molecules, the more “alike” they are. The formula for the calculation of the R_a value is the following:

$$R_a = \sqrt{4(\delta_{D1} - \delta_{D2})^2 + (\delta_{P1} - \delta_{P2})^2 + (\delta_{H1} - \delta_{H2})^2} \quad (11)$$

The factor of 4 is justified by Hansen and his colleagues through experimental evidence produced resulting in spherical HSP plots. As mentioned previously, the Hildebrand solubility parameter is inherently limited to molecules without functional groups i.e. hydrocarbons or similar molecules. Predictions for dipolar and hydrogen bonded molecules were not included in this theory. The HSP include the cohesive energy derived from dipolar and hydrogen bonds as well as the dispersive bonds. By extent, Hansen’s methodology divides the total cohesive energy into separate energies, one for each type of molecule interaction. These three ways in which molecules may interact differ in a very important manor which is the source of the introduction of the “factor of 4”.

Hydrogen bonds and dipoles have directionality and are responsible for fairly strong bonds between molecules. Dispersion interactions on the other hand are not directional and rapidly change position, but they also yield a net cohesive energy over time. Due to their directional nature dipole and hydrogen bonds may effectively prevent about half of their potential interactions with neighbouring molecules. The cohesive energy discussed previously is associated with the heat for evaporation of single molecules. But in this case, at least half of the single molecules are not available for because they have formed pairs. The result is that half of the functional groups are prevented from rapid motion and potential interaction with neighbouring molecules. Due to this fact, if we accept that the effective cohesive energy is reduced, then the dipolar and the hydrogen bonding parameters are each reduced by $\frac{1}{2}$. The total solubility parameter is the square root of the cohesive energy, according to Equation (10), therefore the factor of $\frac{1}{2}$ becomes $\frac{1}{4}$ for δ_D and δ_H .

Initially, Hansen and his colleagues inserted the “factor of 4” because it was convenient in a practical sense. It allowed the dipolar and hydrogen bonding parameters to be plotted with a coefficient “1”. When used for theoretical purposes the coefficients in the equation should be 1, $\frac{1}{4}$, $\frac{1}{4}$, respectively, and not 4, 1, 1 as is in practical use.

6.2.4. Three-dimensional Hansen’s Space-The HSP Sphere:

The three HSP provide coordinates for a three-dimensional interaction space for every solvent known as Hansen’s solubility sphere or Hansen’s space. In contrast to the case of the HP, solubility is not expressed by comparison of cohesion energy density, but rather by what is known as an HSP sphere. When searching for “good” solvents for a material, a sphere is constructed with all the “good” solvents inside it and all the “bad” ones outside. The centre of the sphere is the HSP of the material of interest and the radius (R_0) defines its limits in which a “good” solvent can exist [233]. Any solvent with HSP outside of the R_0 radius is considered “bad”.

It is possible to plot a sphere for a molecule with a radius of R_0 whose centre are the coordinates given by its HSP and contains all the “good” solvents. All the “bad”

solvents are excluded from this sphere. This way a Relative Energy Difference (RED) can be defined which allows the observer to ascertain whether a solute is in the solubility (or dispersibility) space of a molecule or not. Similarly, the RED value can demonstrate whether two liquids are miscible or not. The RED value is given by the following equation:

$$RED = \frac{R_a}{R_0} \quad (12)$$

If $RED > 1$, meaning that $R_a > R_0$, then the molecule is soluble in the solvent in question or the two solvents are miscible. In other words, they are “alike”. If, conversely, $RED < 1$, meaning that $R_a < R_0$, then the molecules being investigated are not “alike”.

A simple example of this provided by Hansen presents the HSP sphere of polylactic acid (PLA) with HSP (18.72, 7.00, 7.00) [233]. R_a is the distance of PLA’s HSP from the HSP of any solvent. The bold green dot represents the estimated HSP of this particular type of PLA used. The blue dots represent good solvents for this material and are located either inside the green sphere or at least on the boundaries ($R_a < R_0$). The red dots represent bad solvents for PLA and are located at a distance larger than PLA’s HSP sphere radius ($R_a > R_0$). For instance, according to the schematic in Figure 48, dimethyl sulfoxide (HSP: 18.4, 6.4, 10.2) is a good solvent for PLA whereas ethanol (HSP: 15.8, 8.8, 19.4) is a bad solvent. A score of “1” or “0” is used to evaluate the solubility. If PLA is soluble in a certain solvent, then the solvents gets a score of “1”. If conversely it is insoluble in a solvent, then the solvent earns a score of “0” [233].

This theory is also applied for materials that are to be dispersed in a certain solvent. Not only does the R_a value have to be smaller than the R_0 of the material for successful dispersion to be achieved, but, also, as a general rule, the lower the R_a value, the higher the concentration of the dispersion will. However, there are exceptions, such as in the case of graphene dispersed in acetone, where a higher R_a value yielded higher concentrations [234].

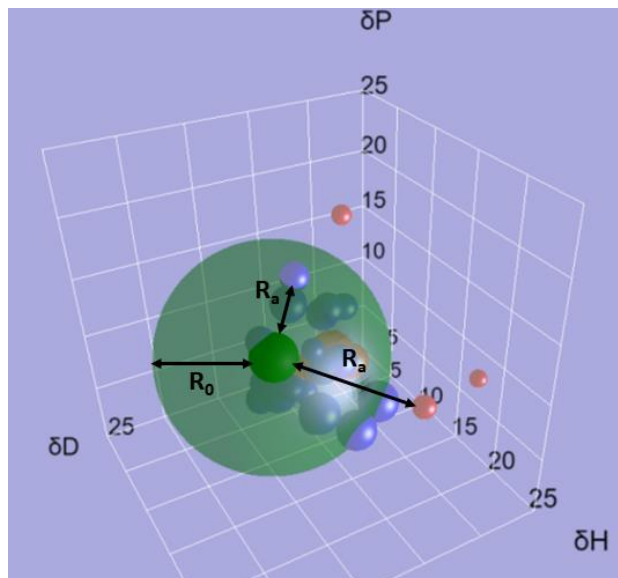


Figure 48 HSP sphere of polylactic acid (PLA), the estimated HSP of which are represented by the bold green dot at the centre of the green sphere. All good solvents are represented in blue and all bad solvents are represented in red.

6.2.5. Hansen's Solubility Parameters and Graphene Derivatives:

Before the HSP are discussed in terms of graphene and graphene related materials, it should be noted that the term “solubility” in this case may be misleading. When discussing molecules, their evaluation in terms of solubility is rather clear; either they dissolve sufficiently in a particular solvent or they do not. In the case of graphene and its derivatives, we are discussing nanoparticles and not molecules. Therefore, these materials must be evaluated based on whether they disperse in a particular solvent or not. S. Süß and his colleagues suggested the term “Hansen Dispersibility Parameters” or HDP when discussing nanoparticles [229]. “Dispersibility” clearly refers to the ability of a particle to agglomerate whereas “solubility” refers to the dissolution of a particle into its molecules, making dispersibility a much more suitable term when discussing graphene and its derivatives. For simplification reasons, throughout this thesis, the term “HSP” will be used and not the recently suggested “HDP”, however the terms

“soluble” and “solubility” will be replaced with the more suitable terms “dispersible” and “dispersibility” when discussing graphene, GO and RGO.

The Hansen solubility parameters have been utilised to identify the most suitable solvents for dispersing graphene and to understand what attributes constitute a high-performance solvent for the liquid exfoliation of graphite to graphene [235, 236]. Hernandez et al. showed that the most suitable solvents for graphene have Hansen parameters of $\delta_D \sim 18 \text{ MPa}^{1/2}$, $\delta_P \sim 9.3 \text{ MPa}^{1/2}$, and $\delta_H \sim 7.7 \text{ MPa}^{1/2}$, with NMP being the best out of 40 tried solvents. They also found that nonzero values of the δ_P and δ_H Hansen parameters are required for a solvent to efficiently disperse graphene, which was unexpected since graphene is highly non-polar. Additionally, graphene was found to be successfully exfoliated in solvents that do not have the needed Hansen parameters to achieve dispersions. It is worth mentioning that the HSP for C_{60} fullerene, which is considered a graphene based small molecule, have been calculated by C. M. Hansen and A. L. Smith [237].

However, there is a lack of similar investigation for GO and even more so for RGO. There have been publications exploring the dispersion behaviours of GO and RGO [238], although when considering the unique properties and the wide range of application that these materials have, it is clear that more extensive research is needed. As done with graphene in the past, determining the correct Hansen parameters that a solvent must have to successfully disperse GO and RGO is crucial. These efforts would aid in discovering new suitable solvents in which these materials can be dispersed, thus Improving their processability and extending their area of effect. In 2014, D. Konios and his colleagues investigated the dispersibility of GO and RGO samples in various solvents with the help of HSP [238].

By calculating the HSP for GO and RGO, predictions can be made for their dispersibility in a variety of solvents or even a solvent mixture of suitable ratios. There exists a database of HSP for solvents that have been theoretically calculated and experimentally determined. Hansen’s handbook features the HSP values for a variety of solvents. The HSP (at 25°C) for the solvents used in this thesis are presented in the table below [239].

Table 3 HSP values of all solvents used in this project to disperse GO and RGO including other useful information regarding the solvents, namely boiling point (BP), molar volume (V_m), surface tension (σ) and enthalpy of vapourisation (ΔH_v). All HSP

values featured were derived from references [226, 230, 254] and the δ_T was calculated using equation (10). The listed surface tension values are at 25°C.

	Solvent name	δ_D (MPa^{1/2})	δ_P (MPa^{1/2})	δ_H (MPa^{1/2})	δ_T (MPa^{1/2})	BP (°C)	V_m (cm³/mol)	σ (mN/m)	ΔH_v° (kJ/mol)
1	Deionised water	15.5	16.0	42.3	47.89	100	18.0	72.8	43.77
2	Methanol	15.1	12.3	22.3	29.61	56	40.7	22.7	37.96
3	Ethanol	15.8	8.8	19.4	26.52	78	58.6	22.1	42.32
4	Isopropyl alcohol	15.8	6.1	16.4	23.57	82	76.8	21.66	48.68
5	1-Butanol	16.0	5.7	15.8	23.18	118	91.5	24.20	49.58
6	Acetone	15.5	10.4	7.0	19.93	132	74.0	33.6	32.19
7	Chlorobenzene	19.0	4.3	2.0	19.58	144	102.1	33.60	41.00
8	o-Dichlorobenzene	19.2	6.3	3.3	20.47	189	112.8	36.61	49.07
9	Chloroform	17.8	3.1	5.7	18.95	68	80.7	18.43	31.68
10	1-Chloronaphthalene	19.9	4.9	2.5	20.65	110	135.5	28.4	62.30
11	Dichloromethane	18.2	6.3	6.1	20.20	209	63.9	26.50	29.23
12	Carbon tetrachloride	17.8	0.0	0.6	17.81	66	97.1	26.4	32.55
13	Acetylacetone	16.1	11.2	6.2	20.57	174	105.3	36.7	43.20
14	Ethylene glycol	17.0	11.0	26.0	32.95	56	55.9	25.2	68.95
15	Ethylacetate	15.8	5.3	7.2	18.15	202	98.5	40.1	35.0
16	Diethylether	14.5	2.9	5.1	15.64	39	104.8	26.5	27.73
17	Hexane	14.9	0	0	14.90	61	131.4	27.5	18.43
18	Toluene	18.0	1.4	2.0	18.16	263	106.8	41.8	38.34
19	o-Xylene	17.6	1.0	3.1	17.90	204	121.2	30.10	43.73
20	Dimethyl sulfoxide	18.4	16.4	10.2	26.67	76	71.3	43.54	51.96
21	Diethylsulfate	15.8	14.7	7.2	22.75	153	131.5	37.1	57.00
22	N,N-Dimethylformamide	17.4	13.7	11.3	24.86	197	24.9	47.7	46.91
23	Tetrahydrofuran	16.8	5.7	8.0	19.46	77	81.7	26.40	32.47
24	N-Methyl-2-pyrrolidone	18.0	12.3	7.2	22.96	34	96.5	17	53.45
25	γ -Butyrolactone	19	16.5	7.3	47.89	140	73.77	31.2	53.00

Chapter 7: Experimental Section

Materials:

For the purposes of the present thesis GO and RGO dispersions were prepared in various solvents and the dispersibility of each material in each solvent was investigated through the determination of the Hansen parameters. The solvents used are presented in Table 4 and their chemical structures are shown in Table 5. The reagents used for the preparation of GO and RGO are presented in

Table 6.

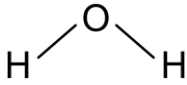
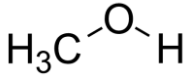
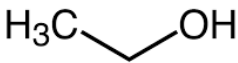
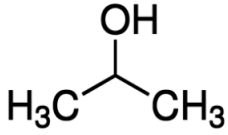
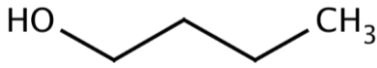
Reagent:	Purchased from:
Graphite powder (<20 µm)	SIGMA-ALDRICH
Sulfuric acid (H ₂ SO ₄ , 95-97%)	HONEYWELL
Sodium nitrate (NaNO ₃)	SIGMA-ALDRICH
Potassium permanganate (KMnO ₄)	SIGMA-ALDRICH
Hydrogen peroxide (H ₂ O ₂ , 30%)	SIGMA-ALDRICH
Hydroiodic acid (HI, 55%)	SIGMA-ALDRICH
Glacial Acetic acid (CH ₃ COOH or AcOH, 100%)	MERCK
Sodium bicarbonate (NaHCO ₃)	SIGMA-ALDRICH
Acetone (CH ₃ COCH ₃ , 99%)	SIGMA-ALDRICH

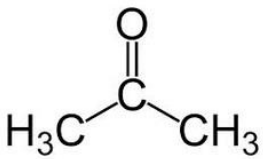
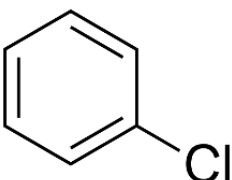
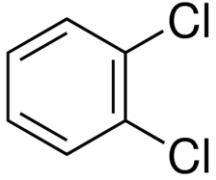
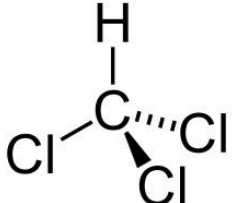
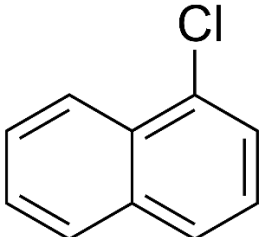
Table 4 Various solvents used for the investigation of GO and RGO dispersibility.

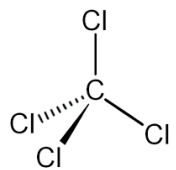
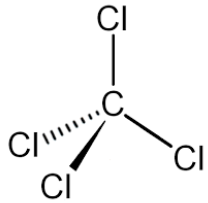
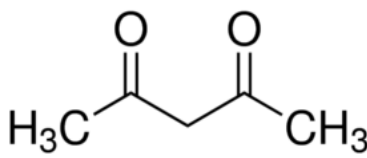
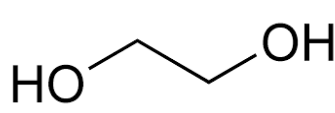
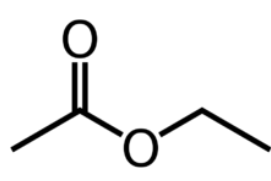
	Solvent Name	Abbreviation	Supplier
1	Deionised water	DH ₂ O	-
2	Methanol	MeOH	HONEYWELL
3	Ethanol	EtOH	FISCHER
4	Isopropyl alcohol	IPA	HONEYWELL
5	1-Butanol	BuOH	SIGMA-ALDRICH
6	Acetone	Act	SIGMA-ALDRICH
7	Chlorobenzene	CB	SIGMA-ALDRICH
8	o-Dichlorobenzene	DCB	SIGMA-ALDRICH
9	Chloroform	CF	SIGMA-ALDRICH
10	1-Chloronaphthalene	CN	MERCK
11	Dichloromethane	DCM	SIGMA-ALDRICH
12	Carbon tetrachloride	CCl ₄	VIORYL

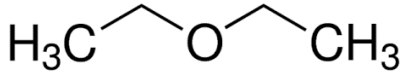
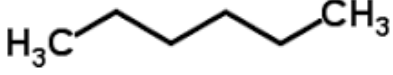
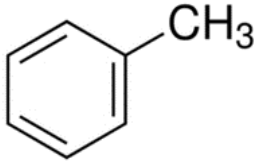
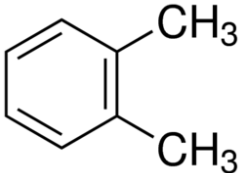
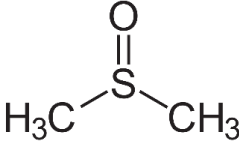
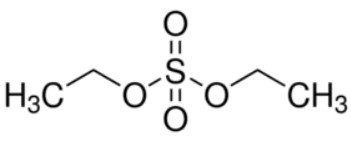
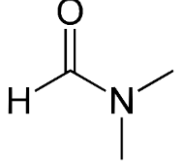
13	Acetylacetone	AcAc	FLUKA
14	Ethylene glycol	EG	MERCK
15	Ethylacetate	EA	SIGMA-ALDRICH
16	Diethylether	DET	FISCHER
17	Hexane	Hex	SIGMA-ALDRICH
18	Toluene	Tol	SIGMA-ALDRICH
19	o-Xylene	Xyl	ALFA-AESAR
20	Dimethyl sulfoxide	DMSO	FISCHER
21	Diethylsulfate	DES	SIGMA-ALDRICH
22	N,N-Dimethylformamide	DMF	SIGMA-ALDRICH
23	Tetrahydrofuran	THF	RIEDEL-DE-HAEN
24	N-Methyl-2-pyrrolidone	NMP	SIGMA-ALDRICH
25	γ-Butyrolactone (GBL)	GBL	SIGMA-ALDRICH

Table 5 Chemical structure of each solvent used.

	Solvent Name	Chemical structure
1	Deionised water	
2	Methanol	
3	Ethanol	
4	Isopropyl alcohol	
5	1-Butanol	

6	Acetone	
7	Chlorobenzene	
8	o-Dichlorobenzene	
9	Chloroform	
10	1-Chloronaphthalene	

11	Dichloromethane	
12	Carbon tetrachloride	
13	Acetylacetone	
14	Ethylene glycol	
15	Ethylacetate	

16	Diethylether	
17	Hexane	
18	Toluene	
19	o-Xylene	
20	Dimethyl sulfoxide	
21	Diethylsulfate	
22	N,N-Dimethylformamide	

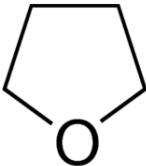
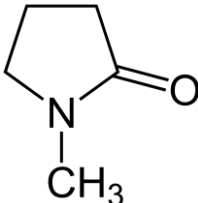
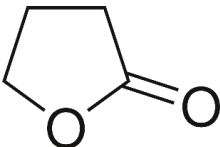
23	Tetrahydrofuran	
24	N-Methyl-2-pyrrolidone	
25	γ-Butyrolactone	

Table 6 Materials used for synthesis of graphene oxide and reduced graphene oxide

Reagent:	Purchased from:
Graphite powder (<20 μm)	SIGMA-ALDRICH
Sulfuric acid (H ₂ SO ₄ , 95-97%)	HONEYWELL
Sodium nitrate (NaNO ₃)	SIGMA-ALDRICH
Potassium permanganate (KMnO ₄)	SIGMA-ALDRICH
Hydrogen peroxide (H ₂ O ₂ , 30%)	SIGMA-ALDRICH
Hydroiodic acid (HI, 55%)	SIGMA-ALDRICH
Glacial Acetic acid (CH ₃ COOH or AcOH, 100%)	MERCK
Sodium bicarbonate (NaHCO ₃)	SIGMA-ALDRICH
Acetone (CH ₃ COCH ₃ , 99%)	SIGMA-ALDRICH

Equipment:

Centrifugations were carried out using a Beckman Coulter Allegra X-22 Centrifuge. Dispersions of GO and RGO were prepared using a Hielscher UP200Ht ultrasonic probe. All UV-Vis absorption measurements were performed with a Shimadzu UV-2401 PC Recording Spectrophotometer.

Note: The photographs featured in this chapter were taken on location at NanoGroup Laboratories.

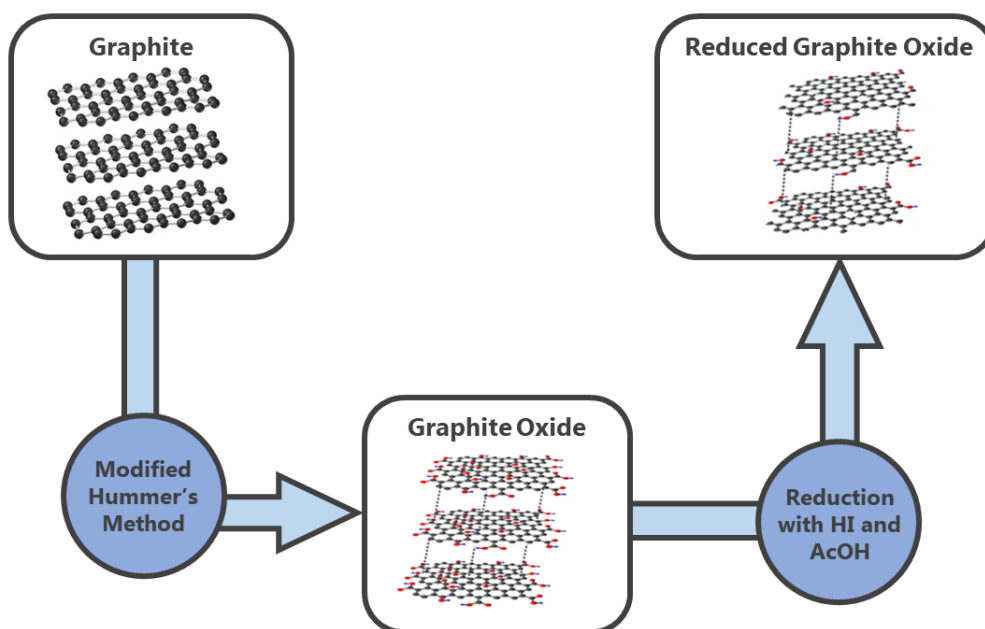


Figure 49 Schematic summary of processes for the synthesis of graphite oxide and reduced graphene oxide.

7.1. Preparation of Graphite Oxide:

The oxidation procedure of graphite, which is explained in detail in this chapter, can be briefly described by the following steps:

1. Addition of H_2SO_4 (46ml, 95-98%) to of graphite (1g). Stir for 20 min in ice bath.
2. Addition of NaNO_3 (1g). Stir for 1 h.
3. Addition of KMnO_4 (6g). Stir for 24 h.
4. Stir at 35°C for 1 h 40 min.
5. Turn heat up to 90°C . Addition of DI H_2O (80 ml). Stir for 40 min.
6. Addition of DI H_2O (200 ml) followed by the addition of H_2O_2 (20 ml, 30%).
7. Stir until solution reaches room temperature.
8. Centrifugation of entire solution volume at 4200 rpm for 20 min.

9. Washing of sediment with warm (65°C) DI H₂O (200 ml).
10. Washing of sediment with DI H₂O at room temperature until the supernatant reaches a pH of 7.
11. Drying of sediment.

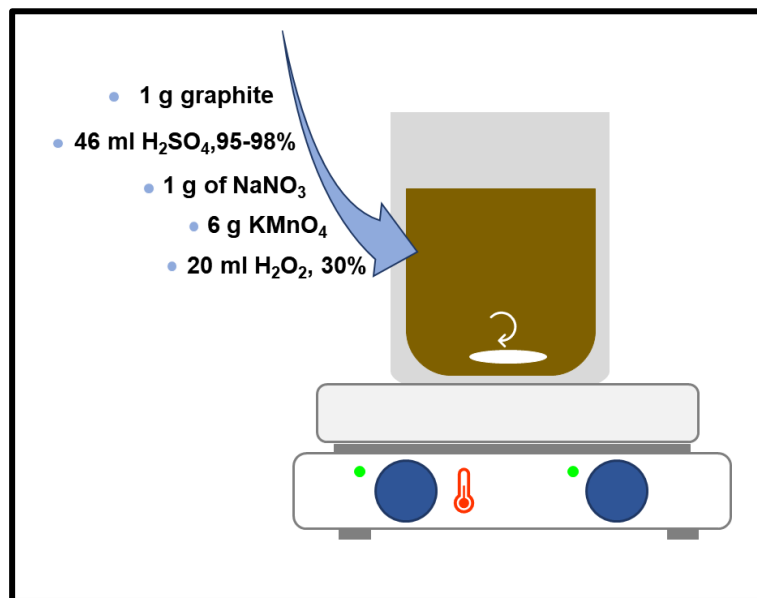


Figure 50 Reagents required for oxidation of graphite via modified Hummers' method.



Figure 51 Experimental set up for preparation of graphite oxide via modified Hummers method. An ice bath and magnetic stirrer are needed. Sodium nitrate and potassium permanganate are added as oxidising agents in a mixture of graphite in sulfuric acid.

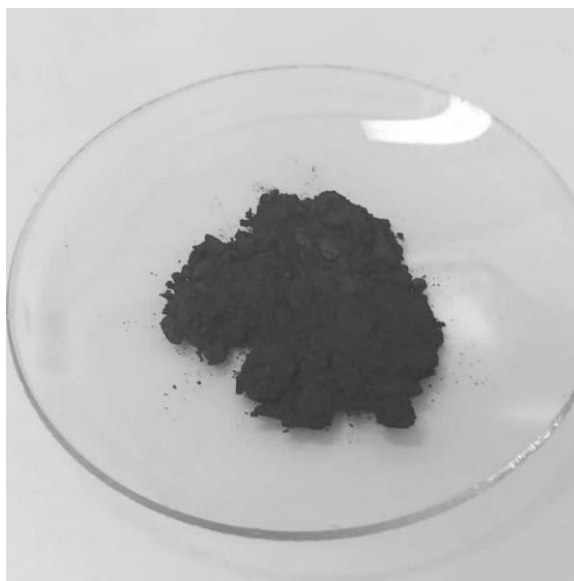
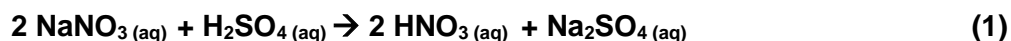


Figure 52 1g of graphite powder used to chemically synthesise graphite oxide via modified Hummer's method.

Graphite oxide was chemically synthesized from graphite using a modified Hummer's method. More specifically, 1 g of graphite powder (Figure 52) is added to a 600 ml beaker containing a large stirring magnet followed by 46 ml of sulfuric acid (H₂SO₄, 95-98%). The beaker is placed in an ice bath and the mixture is left stirring for 20 min (Figure 53). Then, 1 g of sodium nitrate (NaNO₃) is added slowly and small amounts at a time as the reaction is exothermic. The mixture is left stirring for 1 h. The reaction that takes place is:



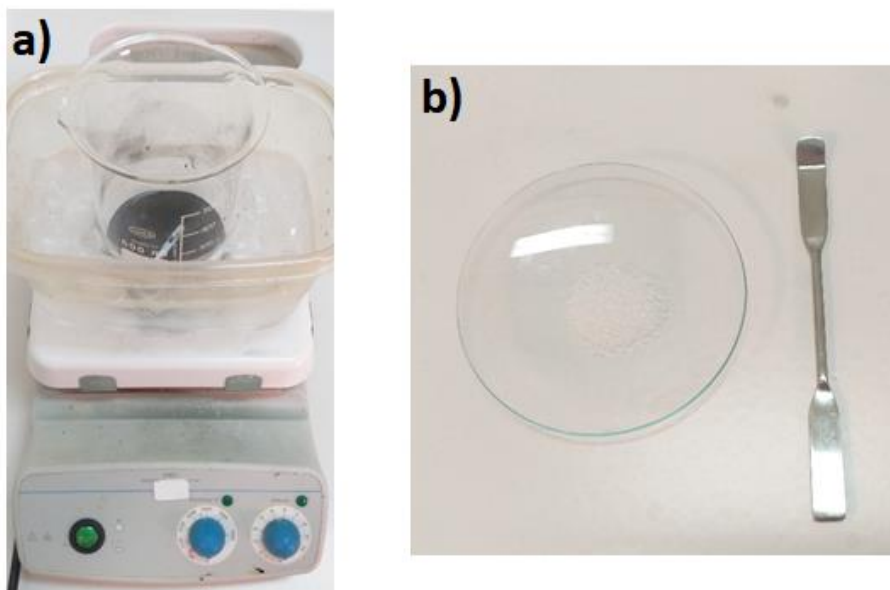


Figure 53 a) The graphite-H₂SO₄ mixture is placed in an ice bath as the reaction that are about to occur are highly exothermic. b) 1g of NaNO₃ is then added.

NaNO₃ acts as an oxidising agent. The intercalation of graphite by H₂SO₄ cannot take place without an oxidizing agent. This is HNO₃ which is produced from the reaction of NaNO₃ with H₂SO₄. That way NaNO₃ enhances oxidation on the basal planes of graphite. This was proven with UV-Vis absorption measurements, in which graphite oxide with the addition of NaNO₃ had a higher absorption peak than graphite oxide without the addition of NaNO₃. It has also been shown that NaNO₃ increases the distance between the graphene layers and results in GO with smaller crystallite size [240].

When the hour is up, 6 g of potassium permanganate (KMnO₄) is added very slowly and in small amounts as the reaction that takes place is violently exothermic. Although the Hummers method is generally not considered hazardous, the addition of KMnO₄ must be performed with care, as the reaction between H₂SO₄ and KMnO₄ forms dimanganese heptoxide (Mn₂O₇), a highly reactive species [241]. Mn₂O₇ is known to detonate at temperatures higher than 55°C.

With the addition of KMnO_4 a thick, green solution is observed (Figure 54). KMnO_4 is a strong oxidising agent. When it is added to the H_2SO_4 solution the following reactions occur:

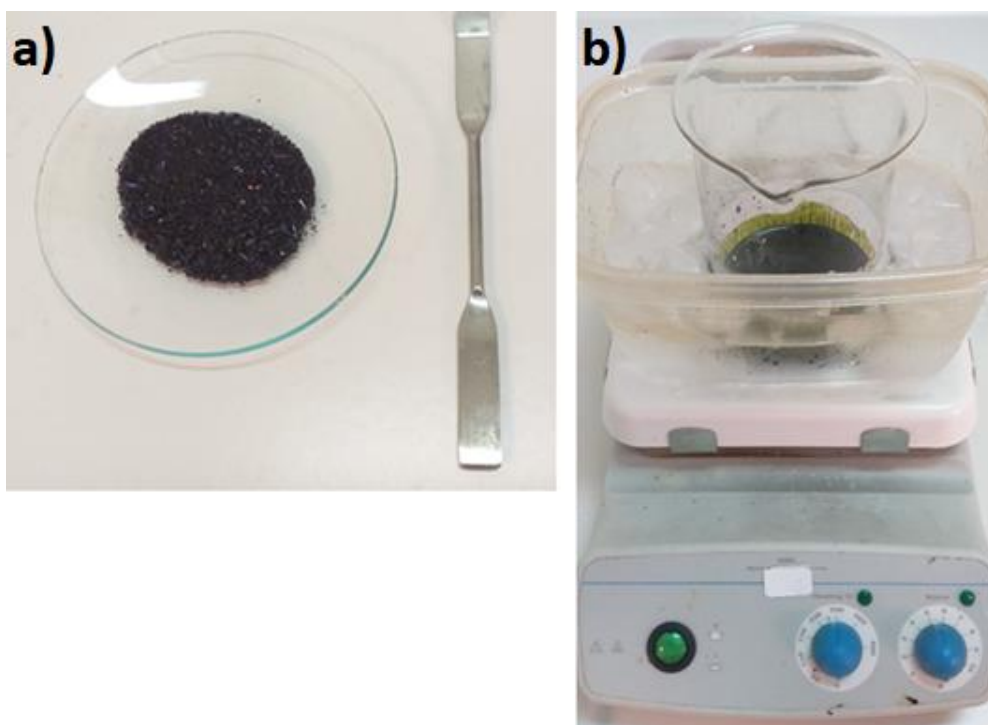
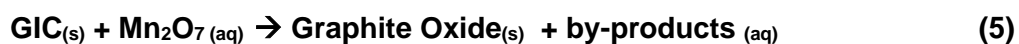


Figure 54 a) KMnO_4 crystals used as strong oxidising agent. b) With the addition of KMnO_4 , the solution turns green.

At this stage, the graphite is in the form of the graphite intercalation compound (GIC). This is essentially graphite with H_2SO_4 molecules occupying the space between the graphene sheets (Figure 55) [242]. When KMnO_4 is added, the oxidising agent manganese (III) oxide (MnO_3^+) is formed according to reaction equation (2). This is what gives the solution its green colour. The oxidising agent manganese (VII) oxide (Mn_2O_7) is also generated according to reaction equations (3) and (4).

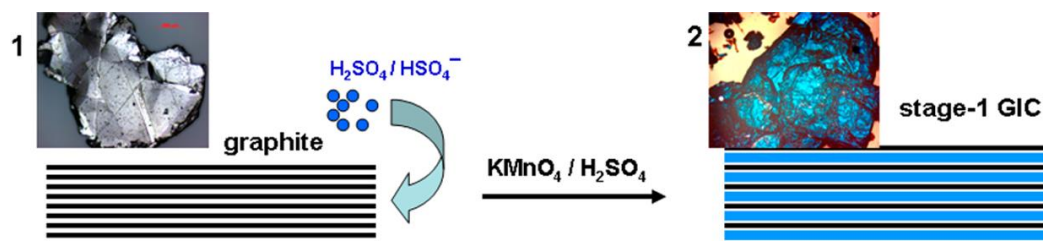


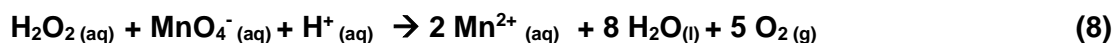
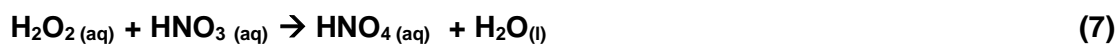
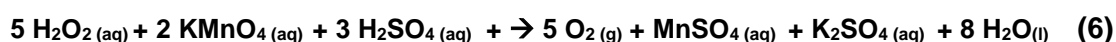
Figure 55 Schematic representation of H_2SO_4 intercalation between the graphene layers of graphite. The black lines represent the graphene layers and the blue lines represent the $\text{H}_2\text{SO}_4 / \text{HSO}_4^-$ intercalant [242].

After the addition of KMnO_4 the solution is left stirring for 24 h. The next day, the solution is then stirred at 35°C for 1h and 40 min. The colour of the mixture is now a dark brown (Figure 56). The heat is turned up to 90°C and 80 ml of deionised water (DI H_2O) are added very slowly. The reaction is left stirring at 90°C for 40 min. After 40 min the reaction is removed from the hotplate and 200 ml of DI water are added followed by 20 ml hydrogen peroxide solution (H_2O_2 , 30%) which is added slowly and carefully. The additional water further exfoliates the graphite planes while H_2O_2 is added to stop the oxidation reaction and additionally remove any traces of excess KMnO_4 [240].



Figure 56 After 24 hours, the mixture has turned a dark brown colour.

Although H_2O_2 itself is an oxidising agent, in this reaction it has reducing properties. In acidic condition, such as in the presence of H_2SO_4 solution, H_2O_2 reduces Mn^{7+} cations to colourless Mn^{2+} cations while H_2O_2 itself is oxidised releasing oxygen gas, as seen in reaction equation (8). This prevents further oxidation of the GOC by MnO_4^- ions. The reactions that take place with the addition of H_2O_2 are:



With the addition of H_2O_2 , bubbling is observed due to the generation of O_2 gas, and the solution turns a green-brown colour, as seen in (Figure 57). The reaction is then left stirring until it reaches room temperature. The final colour of the reaction should be green-brown, confirming successful oxidation of the graphite flakes.

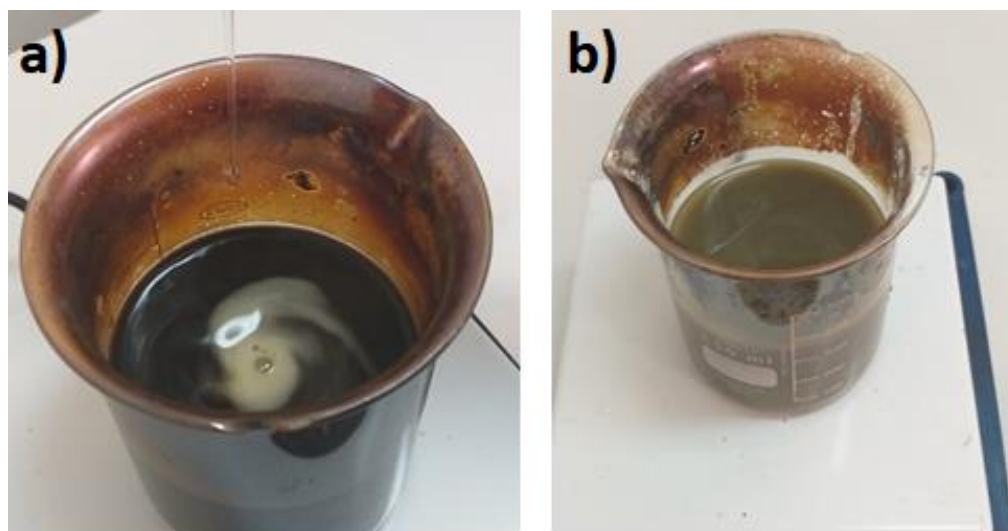


Figure 57 a) With the addition of H_2O_2 bubbling is observed due to O_2 gas being generated. b) After the H_2O_2 has been added, the mixture turns a green-brown colour.

The entire solution is then centrifugated at 4200 rpm for 20 min to isolate the solid graphite oxide in the form of a sediment (Figure 58). The sediment is washed with 200 ml of warm DI H_2O which has been previously heated to about 65°C. The sediment is then washed with DI H_2O at room temperature until the supernatant reaches neutral pH. Lastly, the sediment, which is now clean graphite oxide, is left to dry in an oven at 60°C for several days (Figure 59). Once the graphite oxide is dried, it is pulverised using a pestle and mortar until it is in the form of a fine powder (Figure 60).

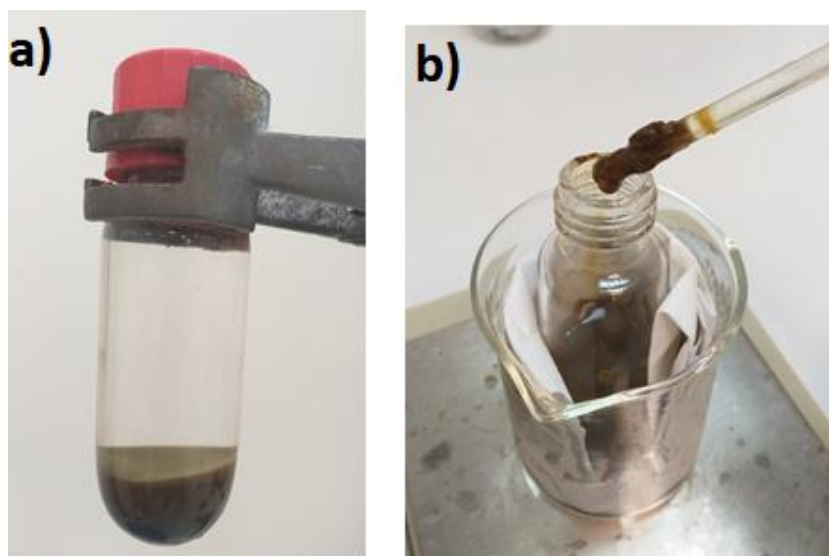


Figure 58 a) When the solution is centrifuged, graphite oxide and biproducts of the reaction are isolated in the form of a sediment. The graphite oxide must be thoroughly washed of the biproducts. b) During the washing process, the mixture has a gel-like form.



Figure 59 The washed graphite oxide is left to dry in an oven at 55°C for several days until it is completely dry.



Figure 60 When graphite oxide has fully dried, it is transferred to a mortar to be pulverised with a pestle into a fine powder.

The prepared GO was characterised via FT-IR and Raman spectroscopy which yielded the spectra shown in Figure 63.

7.2. Preparation of Reduced Graphite Oxide:

Reduced graphite oxide was prepared from graphite oxide synthesised previously via modified Hummer's method, using chemical reducing agents, namely hydroiodic acid (HI), a strong reductant and acetic acid (CH_3COOH or AcOH), a mild reductant. The reducing process can be described briefly by the following steps:

1. Addition of glacial AcOH (37 ml) to graphite oxide (1g). Ultrasonication bath.
2. Addition of HI 55% (2 ml). Ultrasonication bath.
3. Heat in oil bath at 60°C for 48 h.
4. Centrifugation at 4200 rpm for 20 min.
5. Washing of sediment with NaHCO_3 .
6. Washing of sediment with acetone.
7. Drying of sediment.

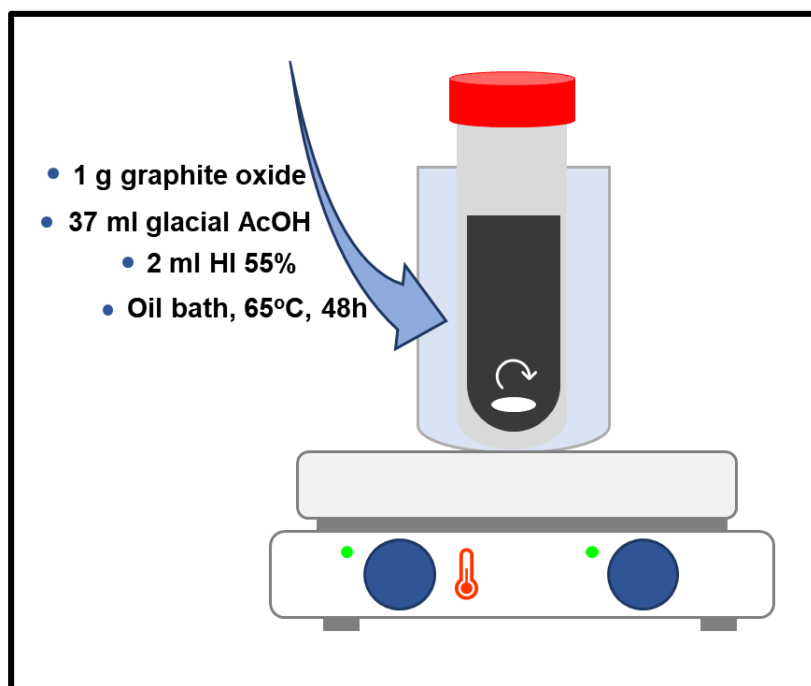


Figure 61 Reagents required for the reduction of graphite oxide.

Firstly, of graphite oxide (1g) are added to a centrifugation tube followed by glacial AcOH (37 ml). The solution placed in an ultrasonication bath at room temperature for 10 min to achieve uniformity. HI 55% (2 ml) is then added followed by another 5 min of ultrasonication. The centrifugation vial is then placed in a silicone bath at 60°C and the solution is left stirring for 48 h (Figure 62). When 48 h have passed, the solution is centrifugated at 4200 rpm for 20 min. The supernatant, which contains the majority of excess HI, is disposed of. The sediment is then washed 5 times with a saturated sodium hydrogen carbonate (NaHCO_3) solution to neutralise the excess HI. The reactions that take place are:



The sediment is then washed with acetone until the yellow colour of the supernatant has completely disappeared, showing that there are no traces of excess HI. The sediment is then placed in an oven at 60°C to dry overnight.

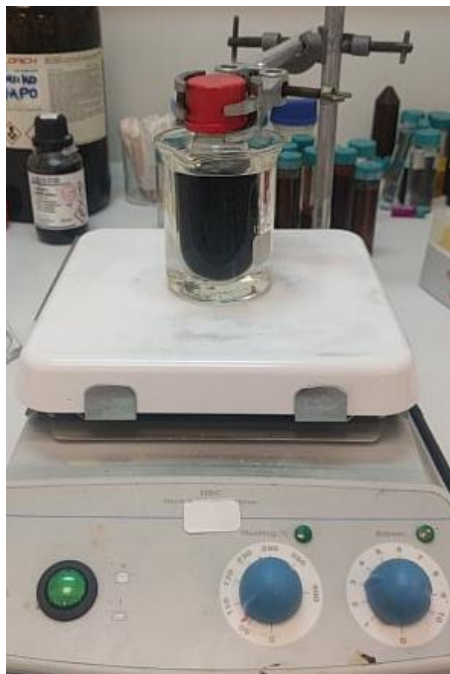


Figure 62 Graphite oxide reduction reaction left in a silicone bath at 60°C for 48h.

The chemically prepared graphite oxide and reduced graphite oxide were characterised via FT-IR and Raman spectroscopy to ensure the successful oxidation of graphite and the subsequent reduction of graphite oxide. The results are shown in Figure 63.

7.3. Characterisation of prepared materials:

7.3.1. FT-IR Spectroscopy:

FT-IR spectroscopy is one of the methods used for graphene oxide characterization. The oxygen functional groups which are present in graphite oxide, namely, hydroxyl, carbonyl, carboxyl groups and epoxide rings are active in the IR region and can thus be detected using FT-IR spectroscopy. By extension, FT-IR Spectroscopy can be an indicator for the level of oxidation of graphite and the level of reduction of graphite oxide.

For the present work, Attenuated total reflectance (ATR) infrared absorbance spectra were carried out with a Bruker Vertex 70v FT-IR vacuum spectrometer equipped with a A225/Q Platinum ATR unit with single reflection diamond crystal which allows the infrared analysis of unevenly shaped solid samples and liquids through total reflection measurements, in a spectral range of 7500 - 350 cm^{-1} .

When interpreting the FT-IR spectrum of graphite oxide obtained in this experiment, the peak at 1033cm^{-1} is attributed to the C-O bond of the epoxy group and the peak at 1163cm^{-1} is assigned to the stretching vibrations of the C-OH bonds of the hydroxyl groups. The peak at 1616cm^{-1} is attributed to the skeletal vibrations of the remaining graphitic domains after oxidation, whereas the stretching vibrations modes of the C=O bonds in carbonyl and carboxyl groups is responsible for the peak at 1716cm^{-1} . Finally, the large shoulder which appears at 3000cm^{-1} to 3500cm^{-1} is due to C-OH groups stretching vibrations and/or water molecules [83, 243]. Peaks that appear at $3280\text{-}3340\text{cm}^{-1}$ and $3000\text{-}3100\text{cm}^{-1}$ are generally attributed to -C-H and =C-H bonds respectively. Therefore, it is evident that the vibration of these bonds of graphite oxide contribute to the shoulder observed at $3000\text{-}3500\text{cm}^{-1}$ in the obtained spectrum. It is obvious that in the spectrum of reduced graphite oxide does not display these characteristic peaks, indicating that the respective oxygen functional groups have been reduced during HI/AcOH treatment. The C-C vibrational peak has also decreased. It is estimated that this is due to the breaking of C-C bond and creation of holes in the graphitic lattice.

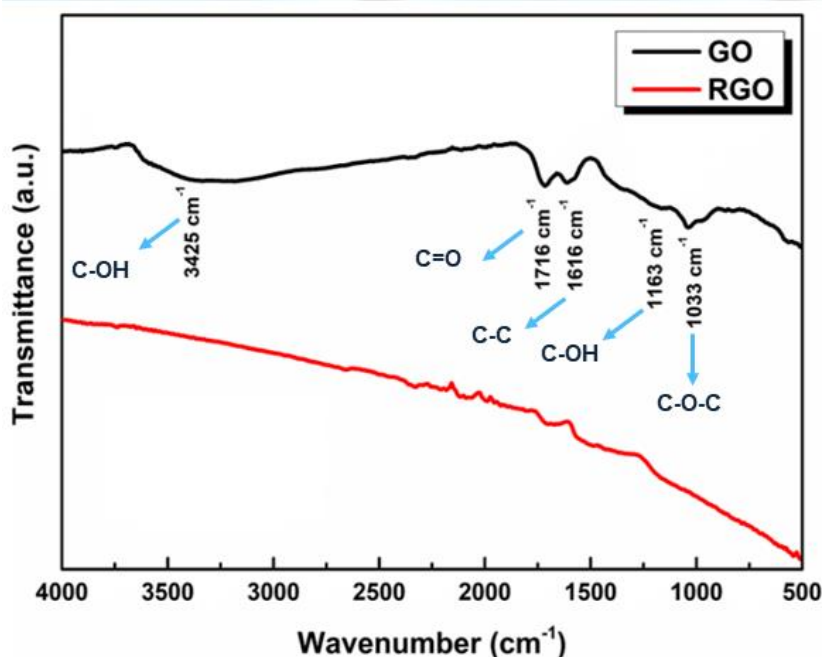


Figure 63 FT-IR spectrum of chemically prepared graphite oxide and reduced graphite oxide.

7.3.2. Raman Spectroscopy:

Raman spectroscopy is a powerful, non-invasive tool for the characterisation of graphene and its derivatives. The Raman spectrum of a graphene related material offers information on disorder, edge and grain boundaries, thickness, doping, strain and thermal conductivity [244]. Raman spectroscopy uses a monochromatic laser of suitable energy to interact with molecular vibrational modes and phonons in a sample, shifting the laser energy down (Stokes) or up (anti-Stokes) through inelastic scattering [245].

○ Graphene:

In graphene, the Stokes phonon energy shift caused by laser excitation creates two main peaks in the Raman spectrum: The G peak (at 1580 cm⁻¹ for a 532 nm laser), which is the primary in-plane vibrational mode of the sp² carbon atoms, and 2D peak at 2690 cm⁻¹, a second-order overtone of a different in-plane vibration which represents the stacking order. There exists a secondary peak at 1350 cm⁻¹ for a 532 nm laser known as the D peak [8]. Theoretically, pristine graphene does

not display a D peak, since the lattice contains no defects or structural imperfections. This band is correlated with defects in the graphitic lattice and it is known as the “disorder” or “defect” band [246, 247]. It represents a ring breathing mode of vibration of the sp^2 carbon rings that are adjacent to the graphene lattice edge or a defect. The G peak corresponds to the E_{2g} phonon at the Brillouin zone centre. The D peak is due to the breathing modes of six-atom rings and requires a defect for its activation. It comes from transverse optical phonons around the K or K' points in the first Brillouin zone [251]. The D peak is generally representative of the defects in the graphitic lattice. These defects are considered to be anything that disrupts the planar sp^2 conjugated system of graphene and may be the presence of hetero atoms such as oxygen groups in the case GO or RGO, or holes in the lattice created by the removal of carbon atoms.

Because of the additional forces from the Van der Waals interactions between the layers of stacked graphene, as the number of graphene layers increases, the spectrum will change. For few-layer graphene the intensity of the 2D peak decreases as the number of layers increases (Figure 64) [248]. As the number of layers increases further moving toward multi-layer graphene and graphite, the 2D peak splits into an increasing number of modes that can combine to give a wider, shorter, higher frequency peak [249]. The G peak also experiences a small red shift as the number of layers increases. This is demonstrated in Figure 65, in which Ferrari et al. used a 514 nm and a 633 nm laser to study the shift of the G peak with the increase of the number of layers, starting from mono-layer graphene and ending in graphite. Taking this information into account, it may be concluded that for stacked graphene, the number of layers can be derived from the ratio of peak intensities, I_{2D}/I_G , as well as the position and shape of these peaks [249].

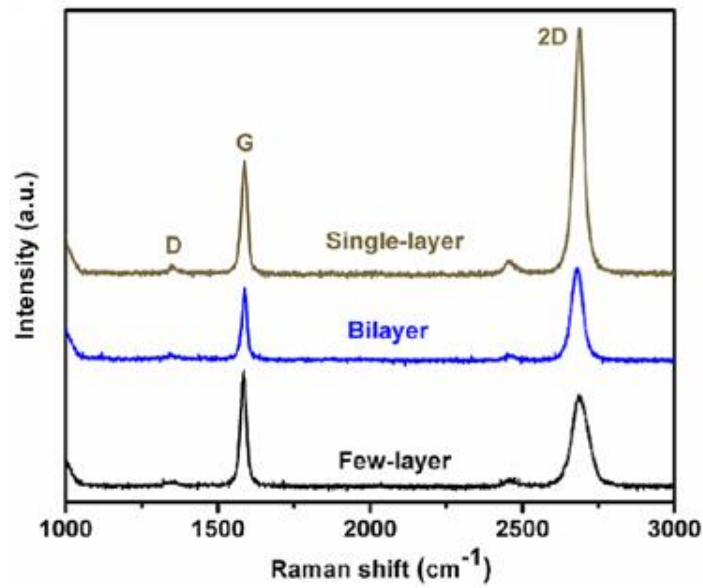


Figure 64 Raman spectra of single layer graphene (grey), bi-layer graphene (blue) and few-layer graphene (black). As the number of layers increases the intensity of the 2D peak decreases. Image source: quantumfrontiers.com

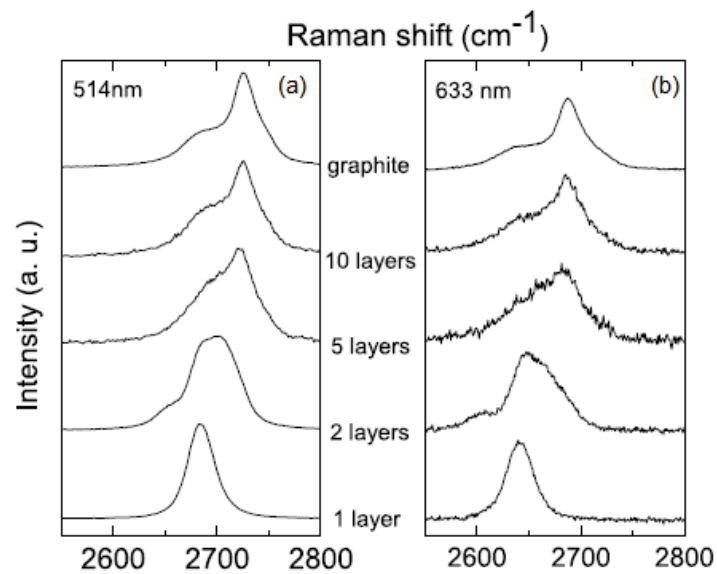


Figure 65 Red shift of G peak in graphene Raman spectrum as the number of layers increases from mono-layer to multi-layer (graphite), first using (a) a 514 nm laser and then (b) a 633 nm laser. Image taken from reference [249].

○ Graphite/graphene oxide:

When discussing graphene and its derivatives, the ratios of D/G relative intensity (I_D/I_G) and 2D/G relative intensity (I_{2D}/I_G) are used to quantify defects in the graphitic lattice and to qualify the number of stacked graphene layers, respectively [250].

One can use the ratio of peak intensities I_D/I_G to characterise the level of disorder. As disorder in graphene increases, the I_D/I_G ratio exhibits two different behaviours. There is a system of low defect density where I_D/I_G will increase as a higher defect density creates more elastic scattering. However, for a system of high defect density the reverse effect takes place; the I_D/I_G will begin to decrease as an increasing defect density results in a more amorphous carbon structure, attenuating all Raman peaks [251]. The low defect density system is referred to as “nanocrystalline graphite” and the high defect density structure is referred to as “mainly sp^2 amorphous carbon” [244].

With the oxidation of graphite and the subsequent reduction of graphite oxide, the G and D peaks are affected allowing for the distinction between these three materials through the studying of their Raman spectra. As mentioned earlier, the presence of oxygen groups in graphitic derivatives, which are considered defects, can be represented by the D peak. When graphite is oxidised, the D peak is notably increased due to the disruption of the sp^2 conjugated system of the graphene layers. When graphite oxide is then reduced, a decrease in the D peak is observed as a number of oxygen groups are removed and the sp^2 system is partially restored.

However, it should be noted that although oxygen atoms are removed there may be other defects in the graphitic plane that can attenuate the D peak such as holes in the lattice due to removal of carbon in atoms in the form of CO_2 gases. Therefore, although the I_D/I_G ratio is a good indicator for the extent of defects in the lattice, it is not a reliable indicator for the extent of oxidation or reduction of the graphene species at hand.

○ Reduced graphite/graphene oxide:

When graphite oxide or graphene oxide is reduced, the Raman spectrum of the resulting material reveals the appearance of the 2D peak, which corresponds to

the graphene region formation. This 2D peak becomes more prominent as the reduction of GO progresses.

Another important change is the intensity ratio of the D and G peaks (I_D/I_G). Through reduction, the sp^2 conjugated system is restored and the G peak becomes more prominent. Conversely, as oxygen atoms are removed, the defects generally decrease resulting in the decrease in the D peak intensity. The result of this is that the I_D/I_G decreases. This is a general indication that the structure and atomic consistency of GO is altered and can be taken as a sign of successful reduction.

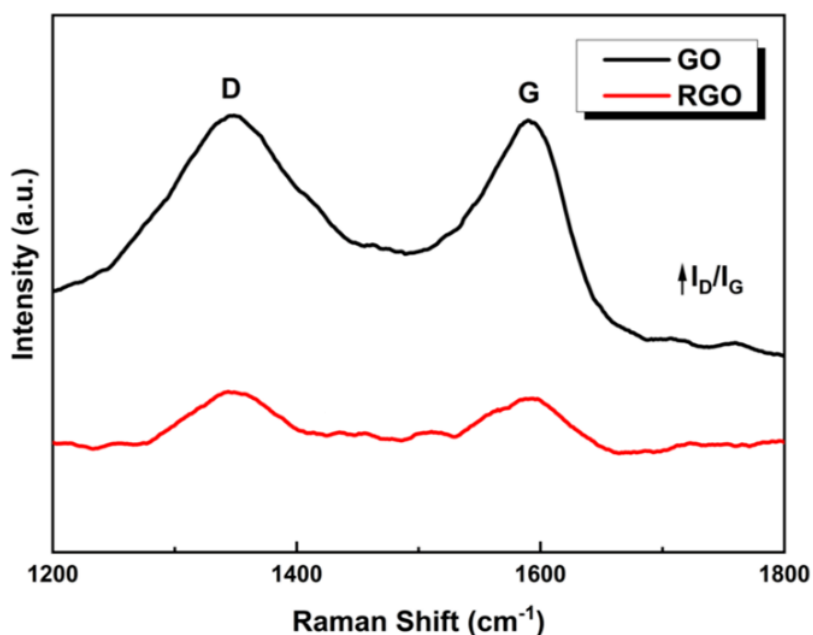


Figure 66 Raman spectrum of graphite oxide prepared via modified Hummers' method.

The Raman spectra for graphite oxide and reduced graphite oxide synthesised for this experiment are presented in Figure 66. Raman measurements were taken at room temperature through a Horiba LabRAM HR Evolution confocal microspectrometer, in backscattering geometry (180°), equipped with an air-cooled solid-state laser operating at 532 nm with 100 mW output power. The laser beam was focused on the samples using a 10 x Olympus microscope objective (numerical aperture of 0.25), providing a ~55mW power on each sample.

It should be mentioned that in the obtained Raman spectra, the 2D peak at ~ 2690 cm^{-1} is not featured. This is because the spectrometer used only measures from 0 to 2500cm^{-1} . Nevertheless, sufficient information can be derived from the obtained spectra by studying the D and G bands and their intensity ratios.

The G and D peaks for graphite oxide appear at 1597 cm^{-1} and 1361 cm^{-1} respectively. After reduction, these peaks shift to lower wavenumbers and appear at 1594 cm^{-1} and 1307 cm^{-1} respectively.

The I_D/I_G can be used as a typical measure for the number of defects and disorder introduced with the reduction of graphite oxide using HI and AcOH. The I_D/I_G ratio for graphite oxide was measured at 0.83 whereas for reduced graphite oxide I_D/I_G the ratio was 0.15, which means that the intensity ratio of the D and G bands was decreased by about 5.5 times with chemical reduction.

7.4. Preparation of GO and RGO dispersions with liquid phase ultrasonic exfoliation:

Liquid phase exfoliation is widely used for the production of 2D GO and RGO from bulk graphite oxide and reduced graphite oxide respectively. Ultrasonic exfoliation in the liquid phase is a very efficient, rapid and cost-effective method of dispersing graphene derivatives. The mechanics behind this method are as follows. The individual layers of GO and RGO are held together by weak Van der Waals forces. These forces are easy to overcome by contributing sufficient energy, such as ultrasounds, which are sound frequencies higher than 20KHz. These frequencies provide strong shear force which disrupts the van der Waals forces and exfoliates bulk graphite and its derivatives. The high frequencies of ultrasound cause particles to separate, increasing the surface area and achieving a uniform distribution. Ultrasounds radiate through the graphite oxide- solvent and reduced graphite-solvent mixtures with dense and sparse waves which produce a large number of tiny bubbles. These bubbles form and expand in the negative pressure region where the ultrasonic waves propagate longitudinally and are rapidly closed in the positive pressure region.

In the case of graphene-based materials, during ultrasonication, the van der Waals forces between the individual layers are overcome and the layers are separated (Figure 67). In addition, the presence of oxygen groups in both materials, mostly in GO, is responsible for intercalation, which makes ultrasonic exfoliation for GO and RGO easier than that of graphite.

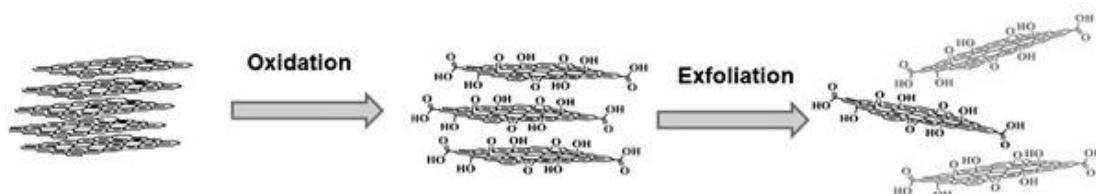


Figure 67 Preparation of graphene oxide sheets from graphite oxide via oxidation and exfoliation. (Images taken from ref [Error! Bookmark not defined.]).

Ultrasonic exfoliation offers the option of controllable parameters such as ultrasonication time, frequency and amplitude; the vibrational expansion and contraction at the ultrasonic probe, allowing for controllable GO and RGO flake size. Ultrasonic baths are widely used to prepare dispersions as they are low-cost and a common part of equipment in most labs. Most ultrasonic baths, however, do not have the option of controllable frequency, despite having controllable sonication time and temperature. Even though this method generally generates adequate dispersions, there exists equipment with improved performance, namely an ultrasonic probe.

An ultrasonic probe has enhanced performance in contrast to an ultrasonic bath because the source of the high frequency ultrasounds is in direct contact with the dispersion being prepared. In a bath, however, the glass walls of the receptacle (e.g. vial) intercepts the sample and the ultrasounds. The water which fills the bath allows the ultrasounds to travel unaffected, while glass partially reflects these frequencies, preventing them from fully reaching the sample. The probe, on the other hand, is immersed in the dispersion and has immediate contact. The frequency, attenuation and power of the probe are controllable as is the depth in which it is immersed (Figure 68). Furthermore, an ultrasonic probe provides higher power resulting in stronger shear force with which the bulk graphene derivatives are exfoliated.

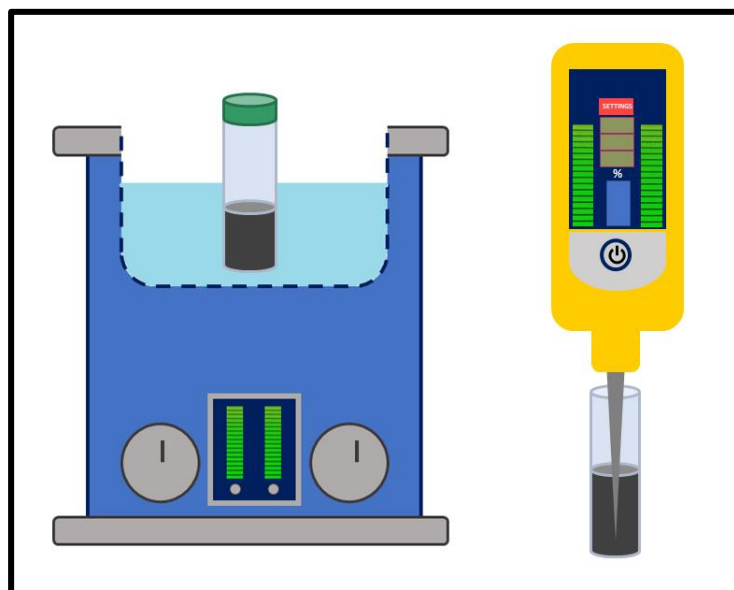


Figure 68 Exfoliation using ultrasonic bath (left) and ultrasonic probe (right).

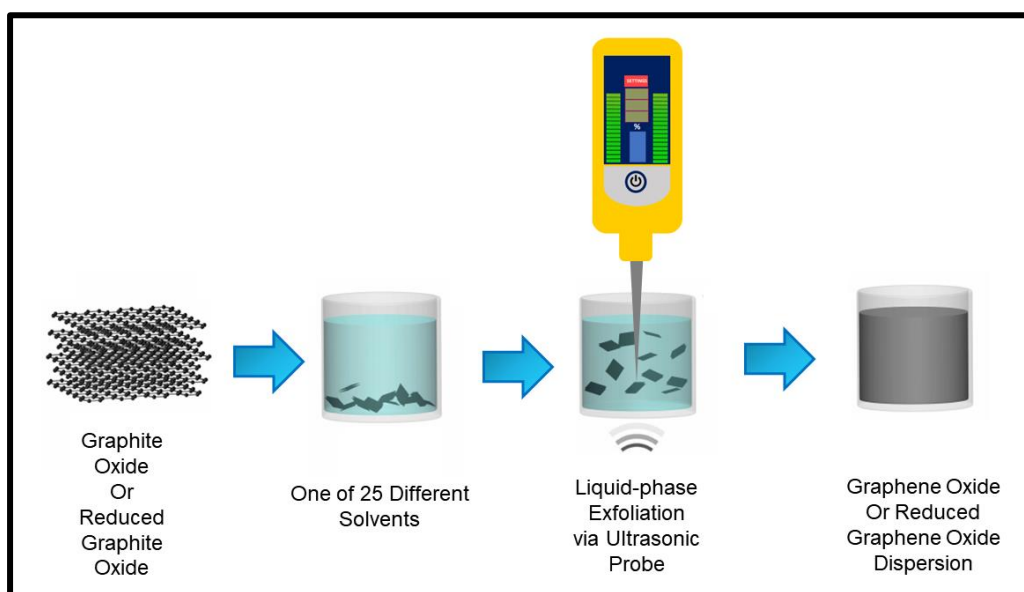


Figure 69 Liquid phase exfoliation process of graphite oxide and reduced graphite oxide via ultrasonic probe.

Graphene oxide (GO) and reduced graphene oxide (RGO) dispersions were prepared from graphite oxide and reduced graphite oxide respectively in 25 different solvents with an initial concentration of 0.5 g/ml. This was achieved with ultrasonic exfoliation using a Hielscher UP200Ht ultrasonic probe (Figure 70) [252]. Each sample was prepared by firstly weighing 0.5 g of graphite oxide and placing it in a 22 ml glass vial. 10 ml of each solvent is then added, and the sample is

ultrasonicated for 1.5 h at 26 KHz. The vial is placed in an ice bath during this process to avoid over heating due to ultrasonic (Figure 71). The ultrasonication set-up has an adjustable shelf which allows for control over how deeply into the mixture the probe is immersed (Figure 71Figure 72). Finally, each sample is centrifugated at 4200 rpm for 30 min and the supernatant is collected. The same process is repeated for each solvent with reduced graphite oxide. The result is 25 dispersions of graphene oxide (GO) and 23 dispersions of reduced graphene oxide (RGO) in various solvents which were mentioned in **Error! Reference source not found.**



Figure 70 Left: Ultrasonic probe used for the preparation of GO and RGO dispersions (Image taken from reference 252) Right: Settings screen of ultrasonic probe. Power is set at 100W and frequency is set at 26 KHz.

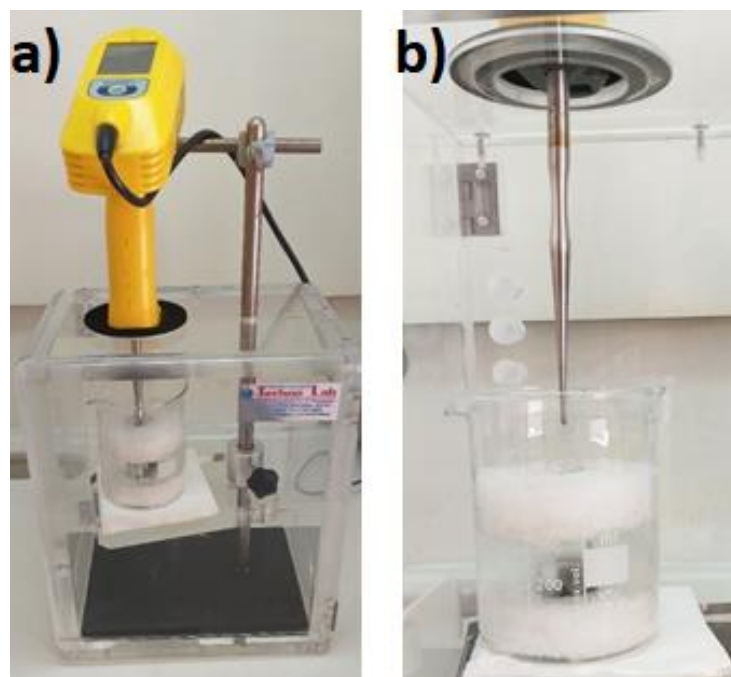


Figure 71 a) Mechanical exfoliation of graphite oxide in de-ionised water via ultrasonication to create GO dispersion. b) Ultrasonic probe before it is inserted into the aqueous mixture of graphite oxide.



Figure 72 The ice bath sits on a shelf whose height can be adjusted to control how deep the ultrasonic probe is immersed.

When each sample was ultrasonicated and centrifuged, the resulting dispersion was photographed for future comparison. The final GO and RGO dispersions are presented in the photographs below. In each photograph section the GO dispersion is on the left and the RGO dispersion is on the right.

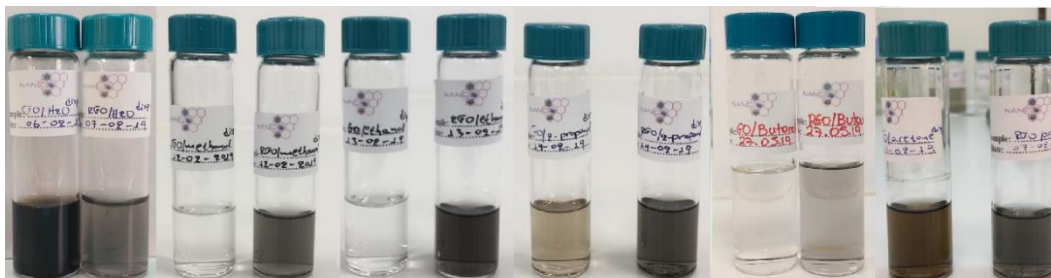


Figure 73 (From left to right) GO and RGO in DH₂O, MeOH, EtOH, IPA, BuOH, Acetone.

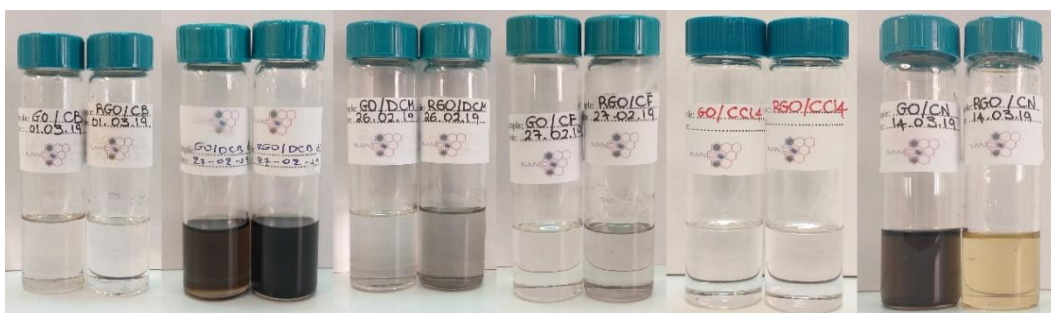


Figure 74 (From left to right) GO and RGO in CB, DCB, DCM, CF, CCl₄, CN.

5



Figure 75 (From left to right) GO and RGO in AcAc, EG, EA, DETr, GBL, Hex, Tol.



Figure 76 (From left to right) GO and RGO in DMF, DMSO, NMP, THF, DES.

All dispersions were left for at least 2 weeks in order to perform a stability study and the resulting dispersion are shown in Figure 77. All UV-Vis absorption measurements were performed on the samples that were left for at least 2 weeks.

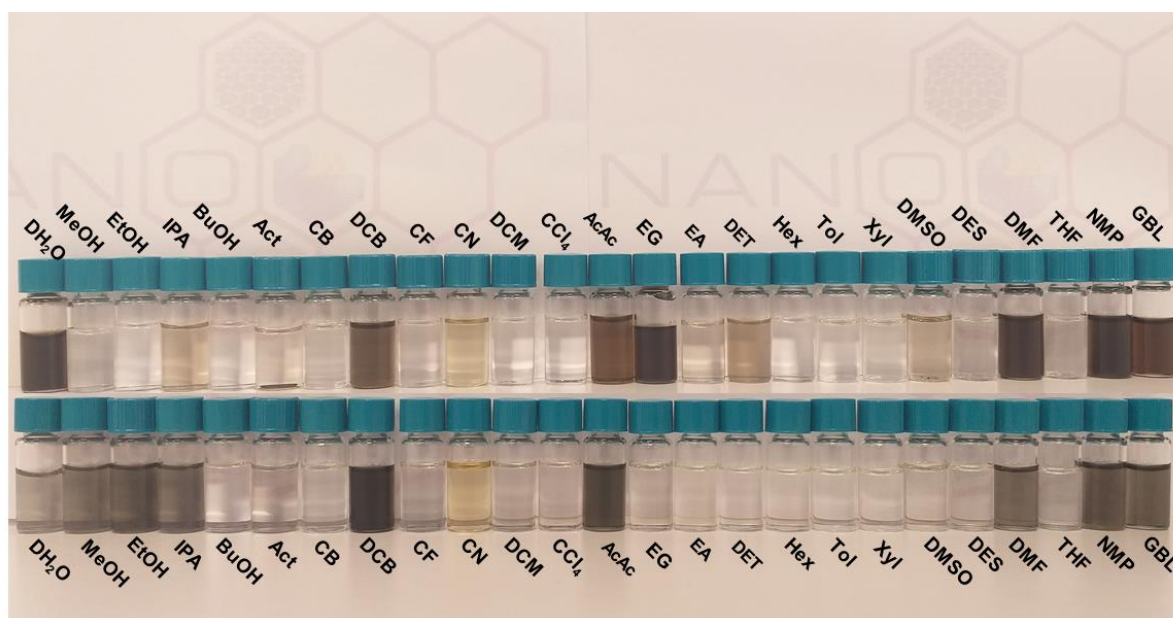


Figure 77 Samples of GO and RGO dispersions in all solvents after being left for 2 weeks. All vials contain only the supernatant. In case of precipitation during these 2 weeks, the supernatant was removed from the solid.

Chapter 8: Characterisation-Results-Discussion

8.1. Optical observation:

When studying the photographs of the dispersions immediately after centrifugation (Figure 73 to Figure 76), it is evident that neither GO or RGO disperse in BuOH, CCl₄, Hex, Tol, Xyl, EA, THF and DES, as the results in all these cases was a virtually clear liquid. In CN and DMSO, GO appears to give a dispersion whereas RGO seems to be indispersible. Conversely, EtOH, MeOH, BuOH ol and CF yield adequate RGO dispersion, whereas GO fails to disperse in these solvents. In all the other solvents, the result lie between these two cases. Both GO and RGO appear to have been successfully suspended to at least some degree.

GO at first yields extremely light brown dispersions in CB and EA, brown dispersions in IPA and acetylacetone and extremely dark brown dispersions in DH₂O, Act, CN, DCB, EG, DET DMF, NMP and GBL. Similarly, RGO gives light grey dispersions in DH₂O, MeOH, DCM, CF, dark grey dispersions in IPA, Act, DMF and NMP and very dark black-grey dispersions in EtOH, DCB, AcAc, EG, DET and GBL. In many solvents, however, this ceases to be the case after a time period of 2 weeks, when GO and/or RGO fails to remain suspended and precipitates. It should be noted that the vials featured in Figure 77 contain only the supernatant of every dispersion. In the case that GO or RGO precipitated during the 2 weeks, the supernatant was removed from the solid before the photograph was taken. This helps to better compare the initial colour of each dispersion and the final colour after being left for 2 weeks.

When comparing the photographs of the GO and RGO dispersions immediately after preparation with the respective dispersion after they have been left for at least 2 weeks (Figure 77), the stability can in some cases be evident even with simple observation.

On one hand, GO remains successfully suspended in DH₂O, DCB, acetylacetone, EG, DMF, NMP and GBL, although slight precipitation is observed over time. Nevertheless, the results were rather concentrated dispersions with adequate stability overtime. In the case of Act, CN and DET, however, GO had completely precipitated after 2 weeks, leaving behind a clear liquid, showing very poor stability in these solvents.

RGO, on the other hand, showed very poor stability in acetone, EG and Diethylether, as it appears to have completely precipitated after being left for 2 weeks. Conversely,

RGO showed acceptable stability in DH₂O, MeOH, EtOH, IPA, DCB, AcAc, DMF, NMP and GBL. Although precipitation is observed in these solvents, DH₂O being most prominent, RGO still remains adequately suspended.

8.2. Absorption measurement via UV-Vis Spectroscopy:

To accurately determine the dispersibility of GO and RGO on all 25 solvents, the maximum absorbance in the UV-Vis spectrum was measured, and the concentration of every dispersion was calculated through Beer-Lamberts law.

According to the Beer-Lambert law, $A = \alpha cl$, the absorption coefficient of GO and RGO can be determined by preparing a series of dispersions at different given concentrations. To determine the concentration of each dispersion, absorption measurements were carried out in the UV and visible light regions using a Shimadzu UV-2401PC spectrophotometer. The maximum absorbance values were obtained for GO and RGO in each solvent. The obtained spectra are featured presented below. It should be noted that the absorbance is displayed in arbitrary units.

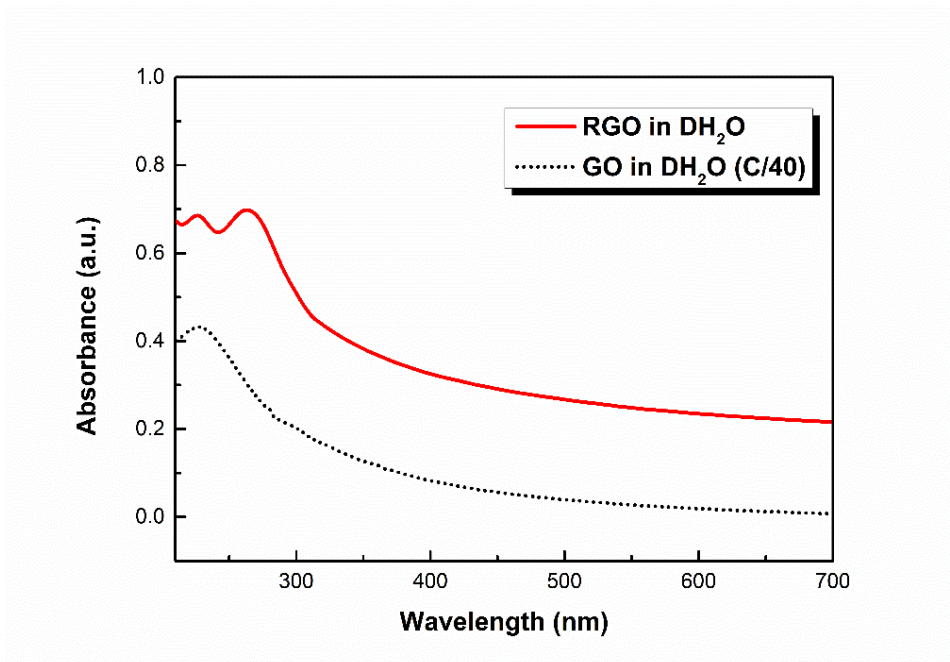


Figure 78 UV-Vis absorption spectra of GO and RGO in deionised water (DH₂O).

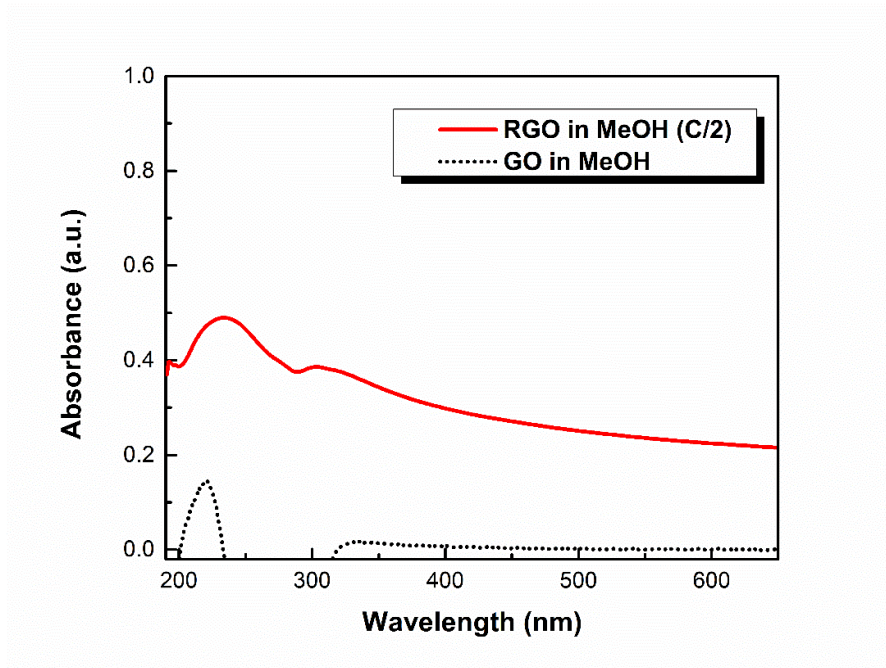


Figure 79 UV-Vis absorption spectra of GO and RGO in methanol (MeOH).

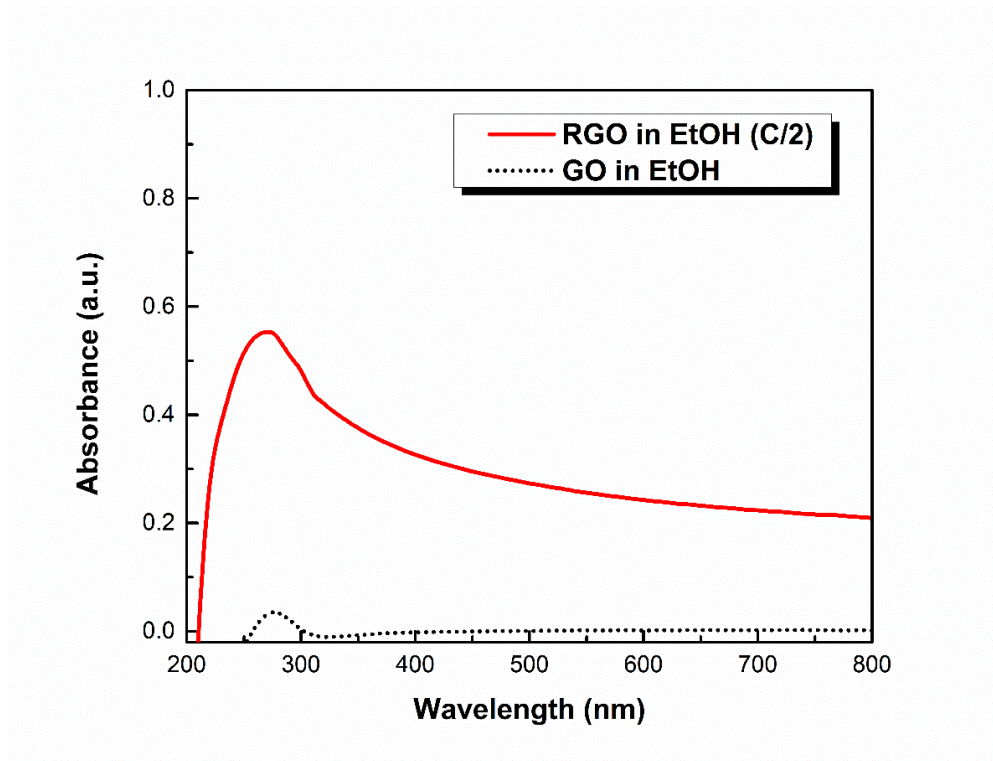


Figure 80 UV-Vis absorption spectra of GO and RGO in ethanol (EtOH).

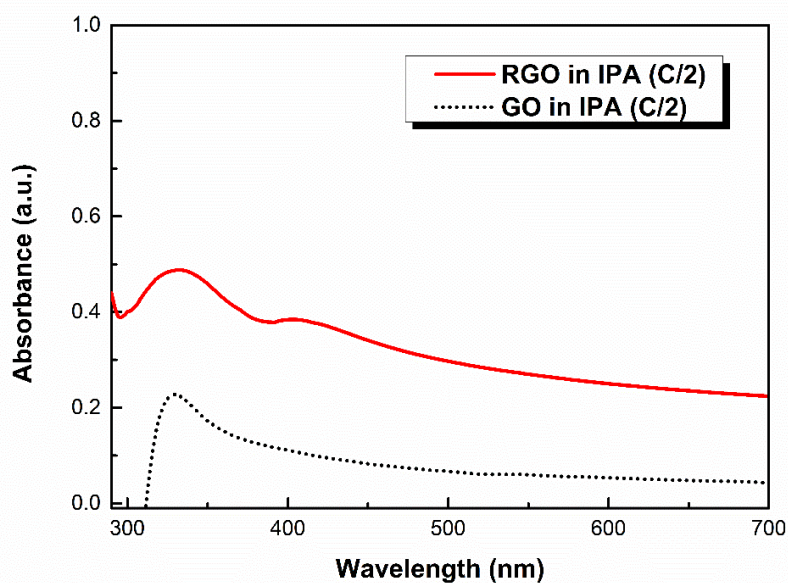


Figure 81 UV-Vis absorption spectra of GO and RGO in isopropyl alcohol (IPA).

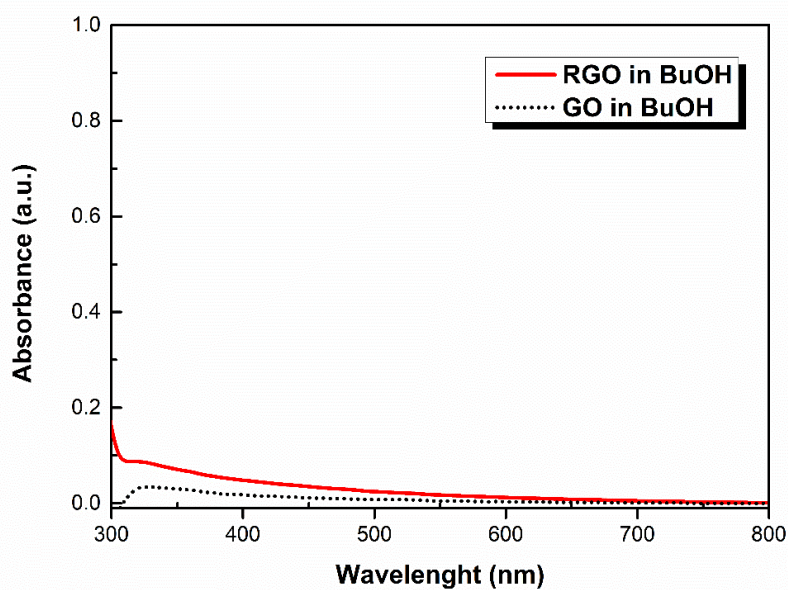


Figure 82 UV-Vis absorption spectra of GO and RGO in 1-Butanol (BuOH).

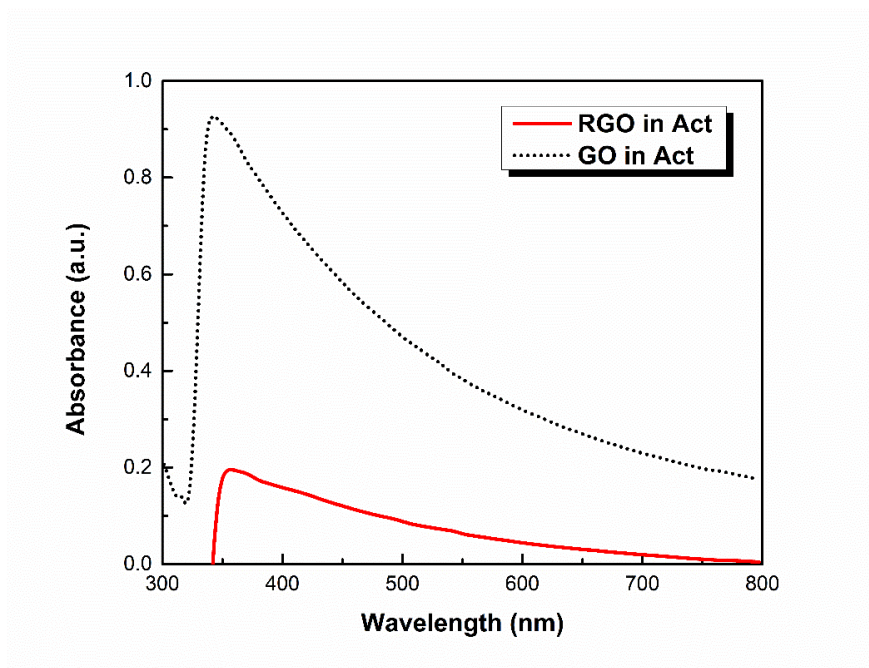


Figure 83 UV-Vis absorption spectra of GO and RGO in acetone (Act).

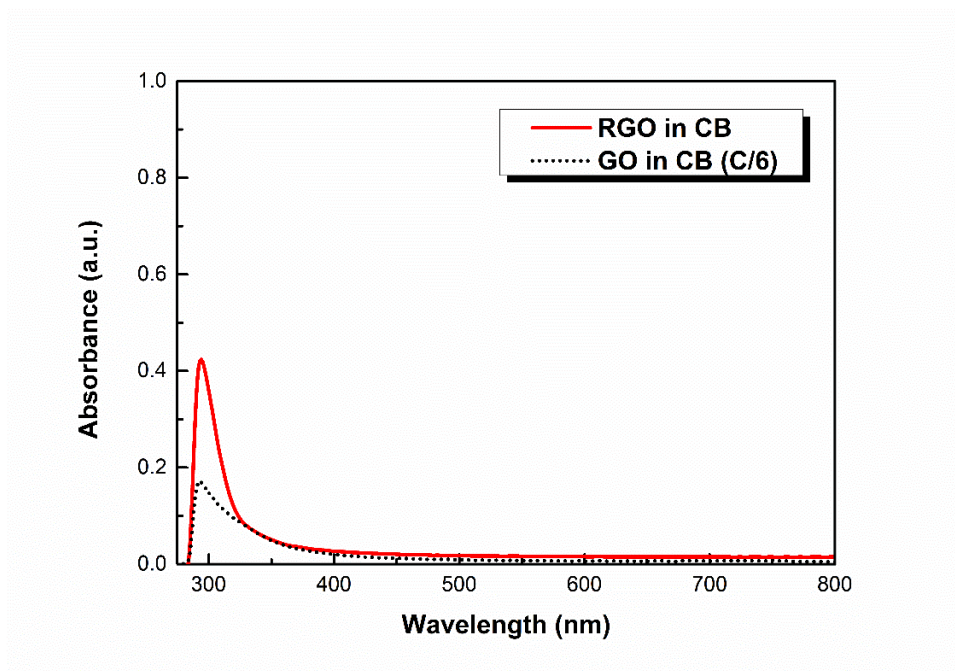


Figure 84 UV-Vis absorption spectra of GO and RGO in chlorobenzene (CB).

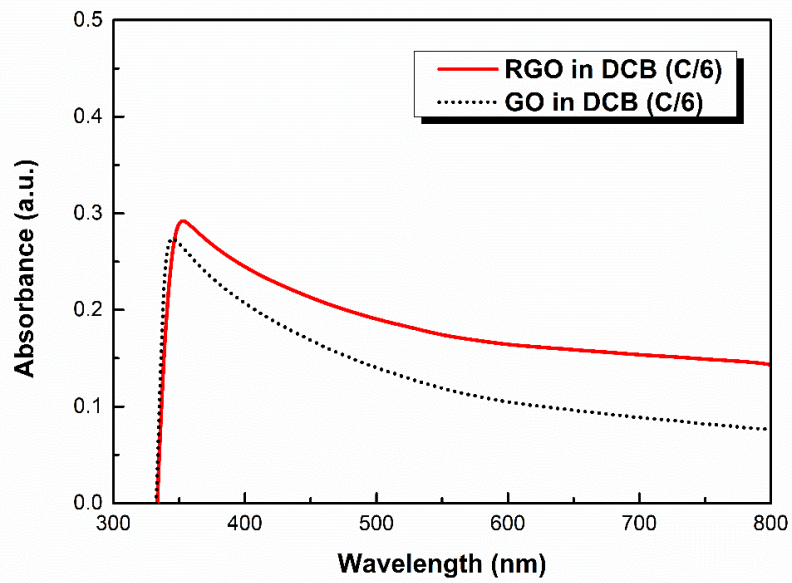


Figure 85 UV-Vis absorption spectra of GO and RGO in *o*-Dichlorobenzene (DCB).

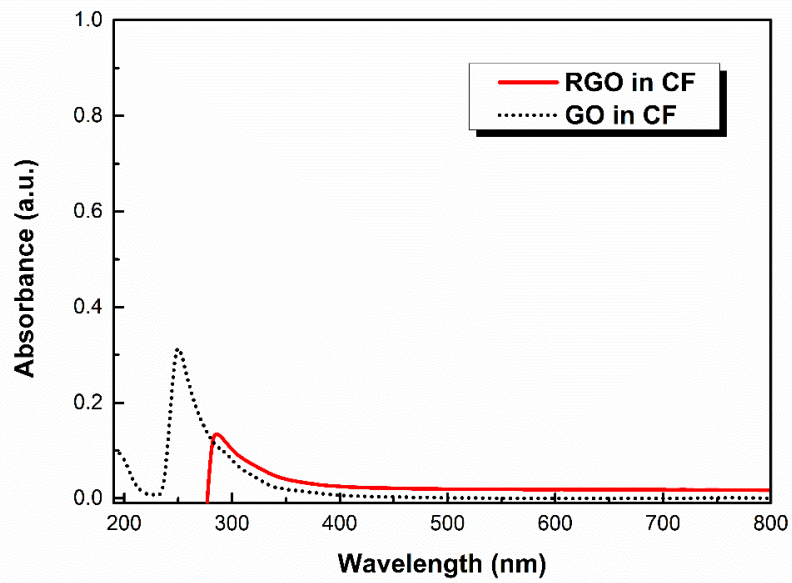


Figure 86 UV-Vis absorption spectra of GO and RGO in chloroform (CF).

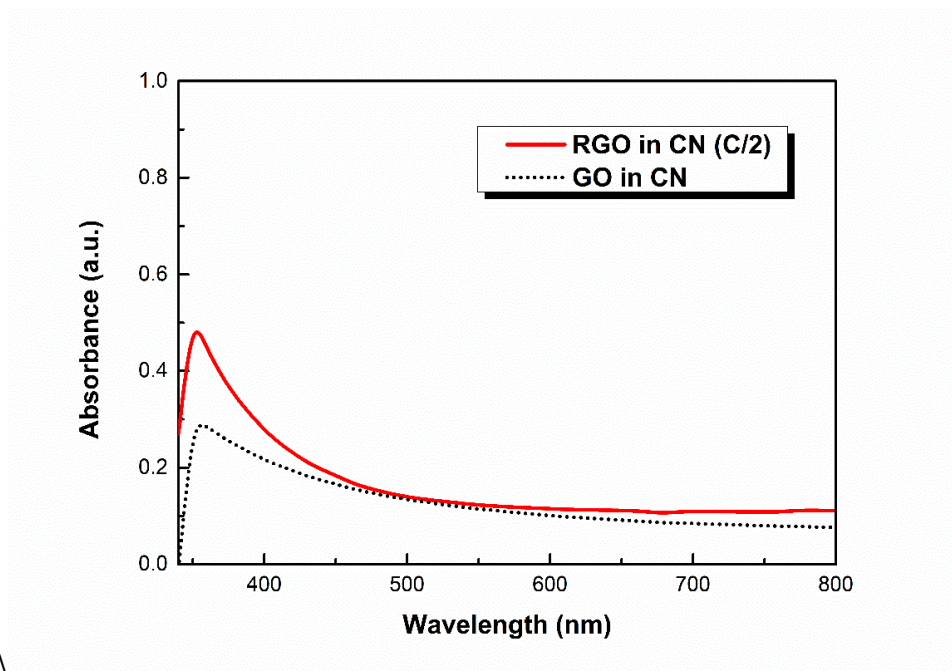


Figure 87 UV-Vis absorption spectra of GO and RGO in 1-Chloronaphthalene (CN).

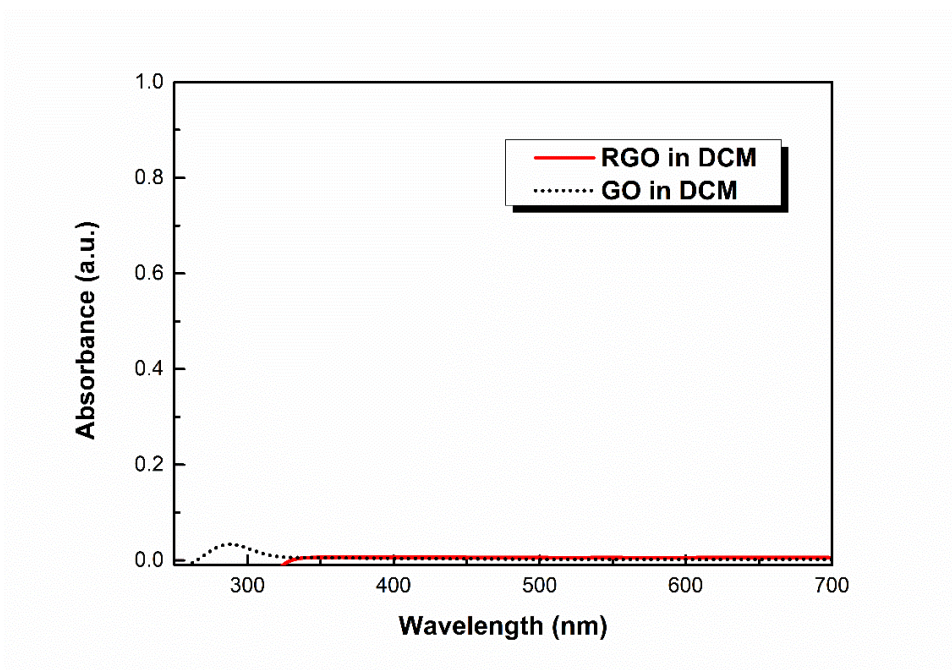


Figure 88 UV-Vis absorption spectra of GO and RGO in dichloromethane (DCM).

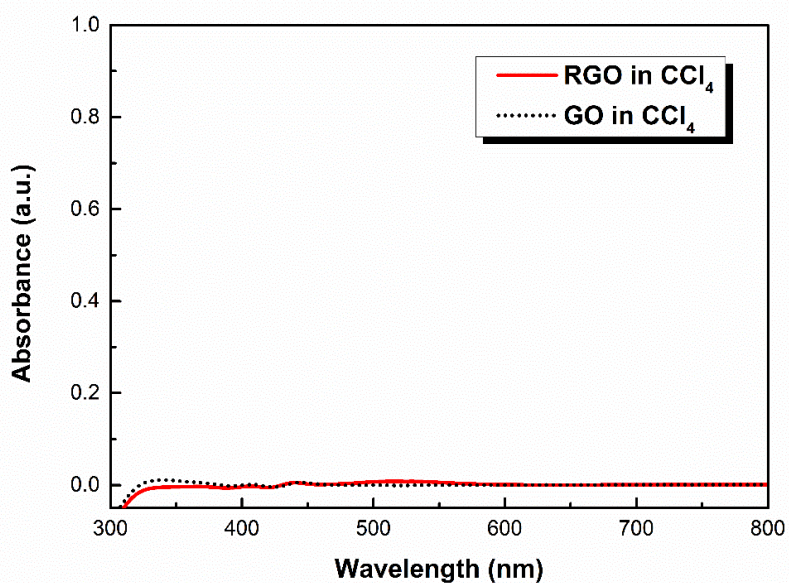


Figure 89 UV-Vis absorption spectra of GO and RGO in carbon tetrachloride (CCl₄).

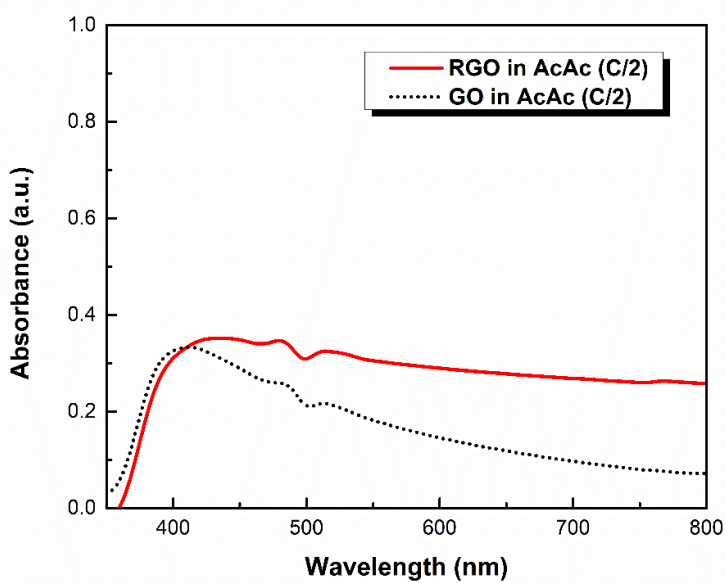


Figure 90 UV-Vis absorption spectra of GO and RGO in acetylacetone (AcAc).

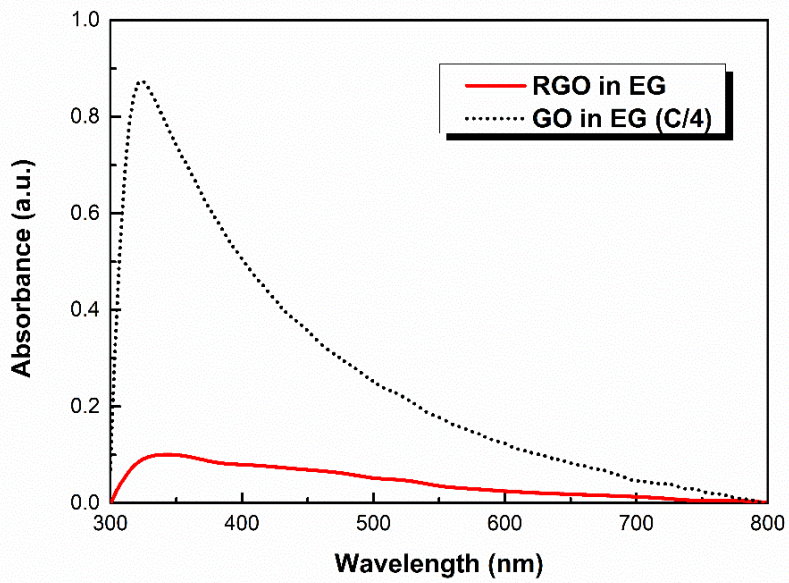


Figure 91 UV-Vis absorption spectra of GO and RGO in ethylene glycol (EG).

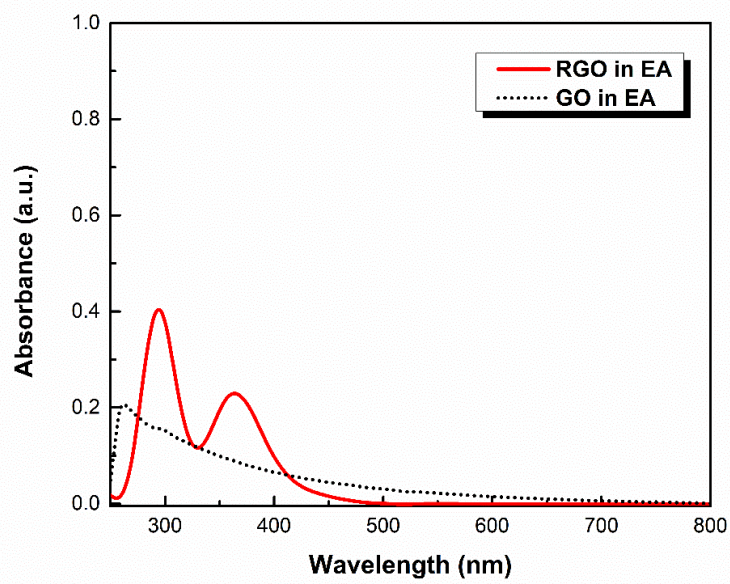


Figure 92 UV-Vis absorption spectra of GO and RGO in ethyl acetate (EA).

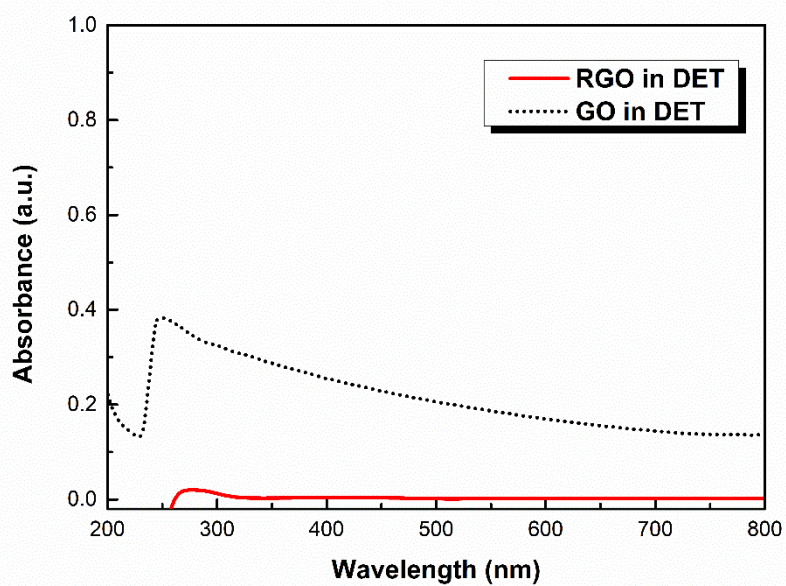


Figure 93 UV-Vis absorption spectra of GO and RGO in diethyl ether (DET).

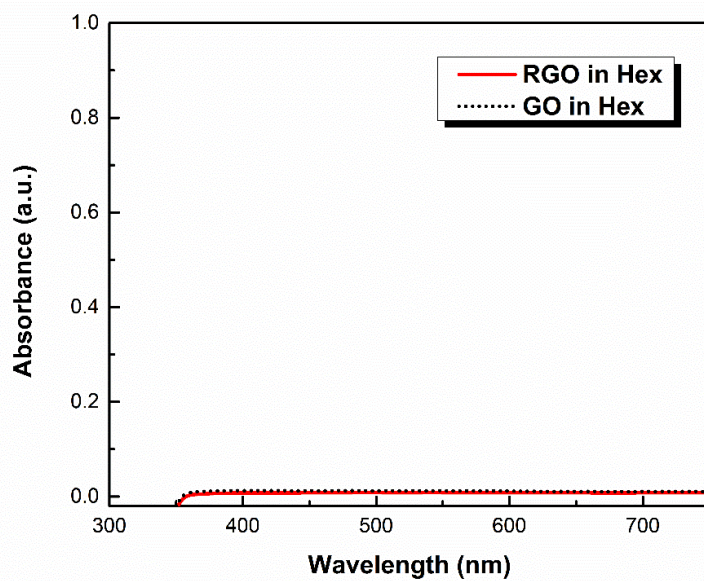


Figure 94 UV-Vis absorption spectra of GO and RGO in hexane (Hex).

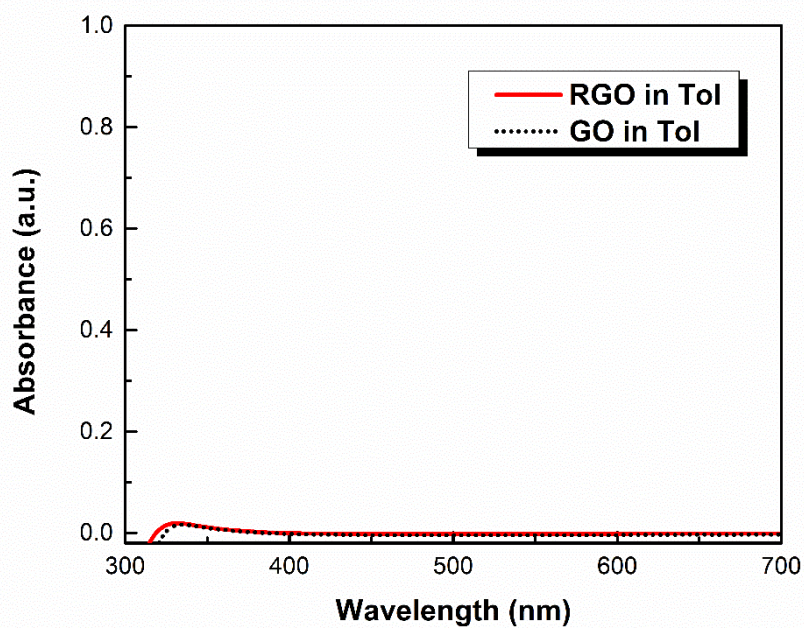


Figure 95 UV-Vis absorption spectra of GO and RGO in toluene (Tol).

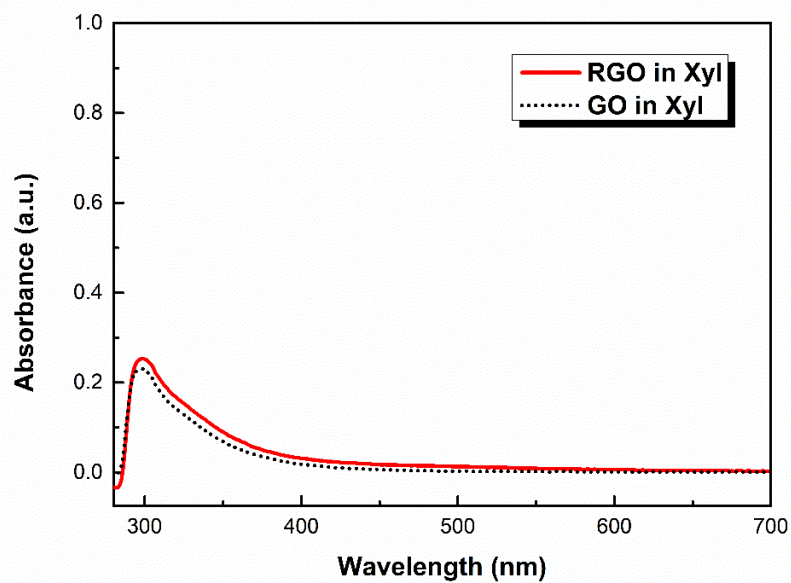


Figure 96 UV-Vis absorption spectra of GO and RGO in o-Xylene (Xyl).

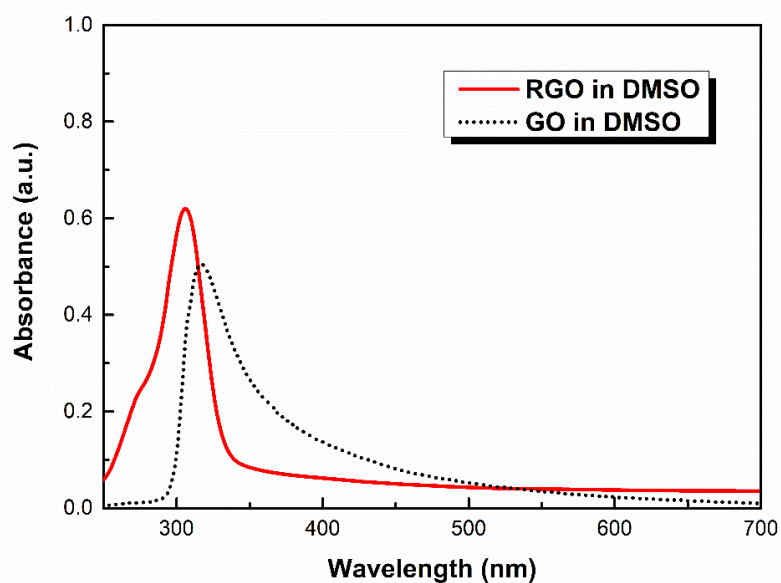


Figure 97 UV-Vis absorption spectra of GO and RGO in dimethyl sulfoxide (DMSO).

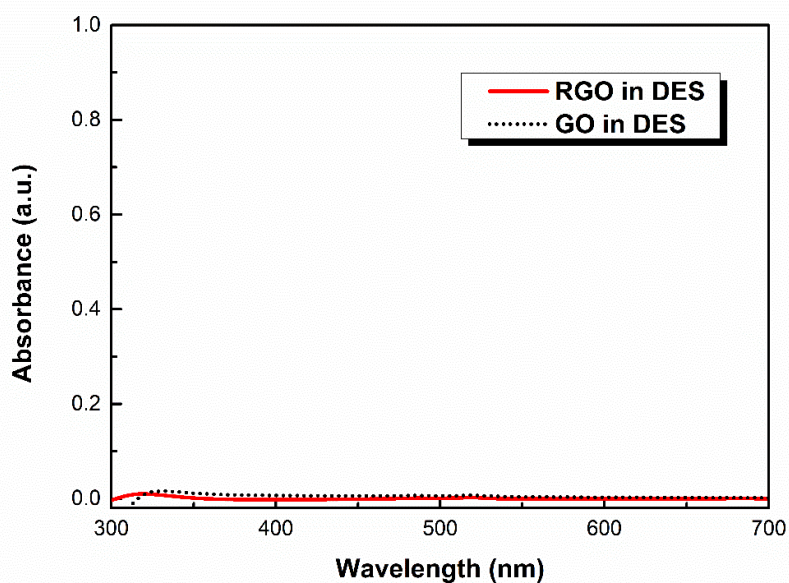


Figure 98 UV-Vis absorption spectra of GO and RGO in diethyl sulfate (DES).

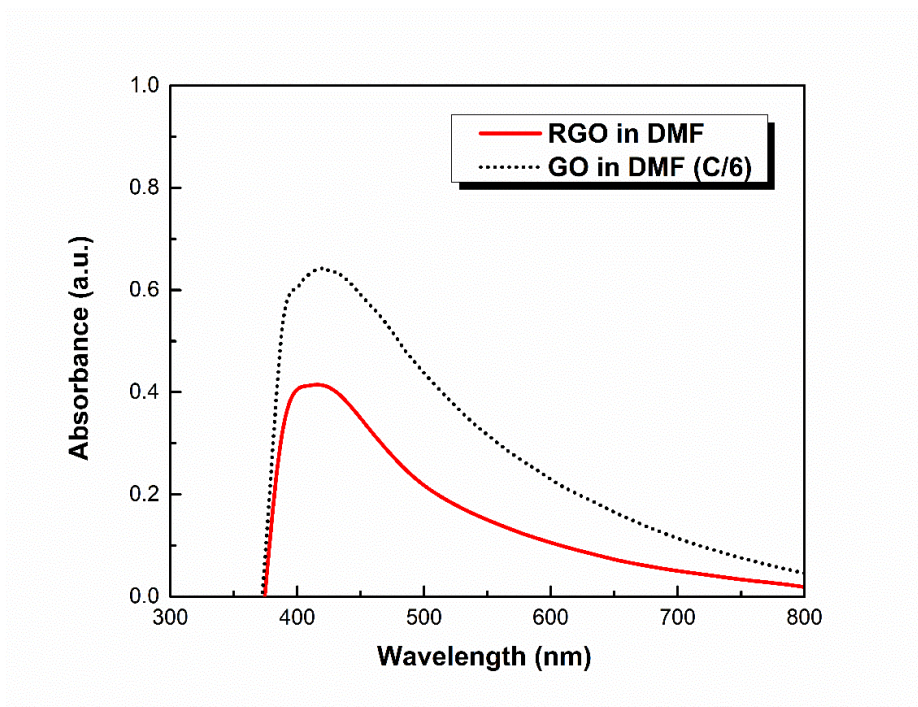


Figure 99 UV-Vis absorption spectra of GO and RGO in N,N-Dimethyl formamide (DMF).

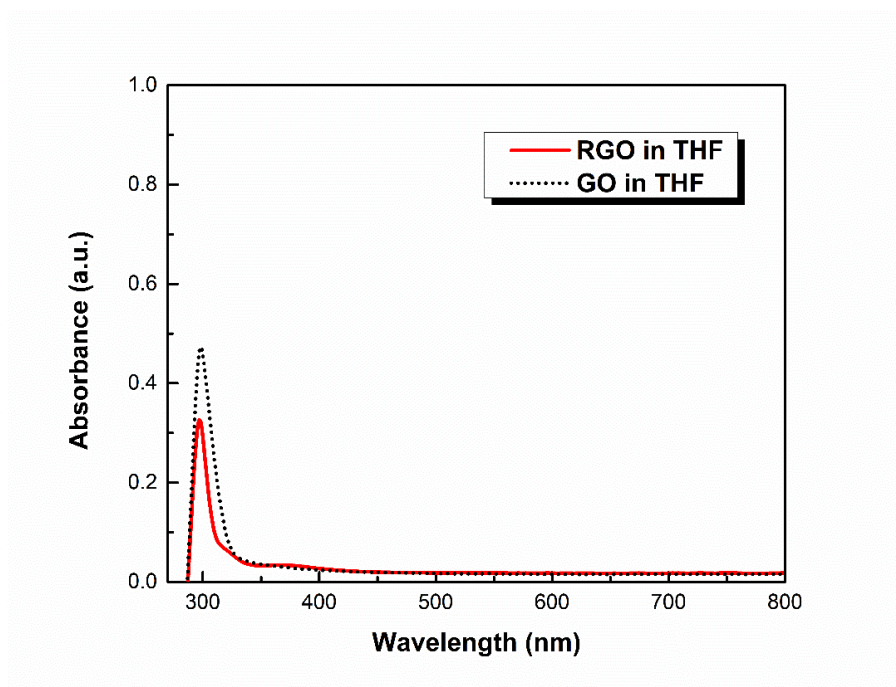


Figure 100 UV-Vis absorption spectra of GO and RGO in tetrahydrofuran (THF).

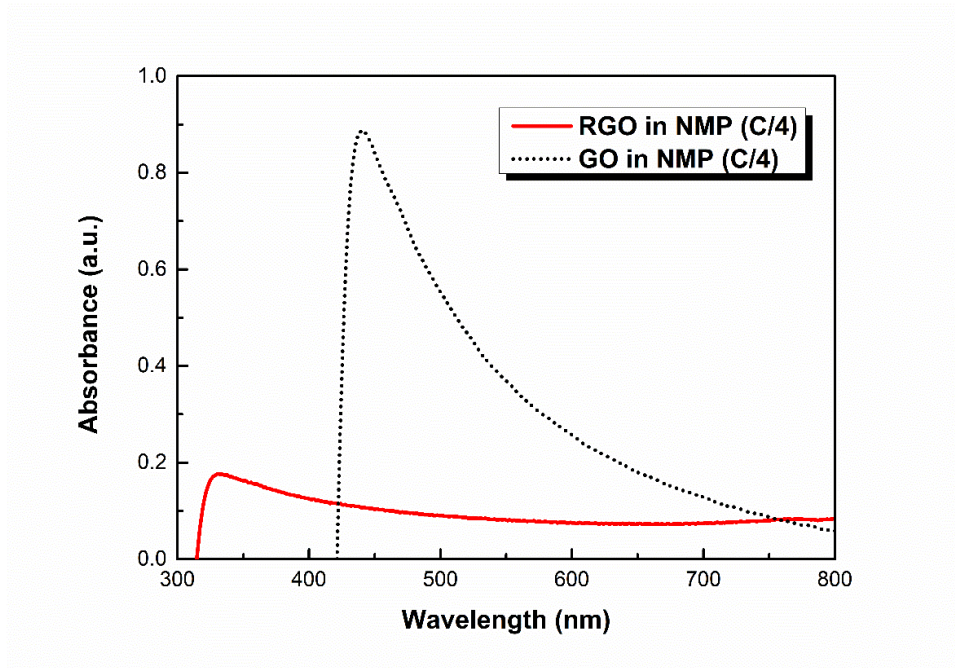


Figure 101 UV-Vis absorption spectra of GO and RGO in N-methyl-2-pyrrolidone (NMP).

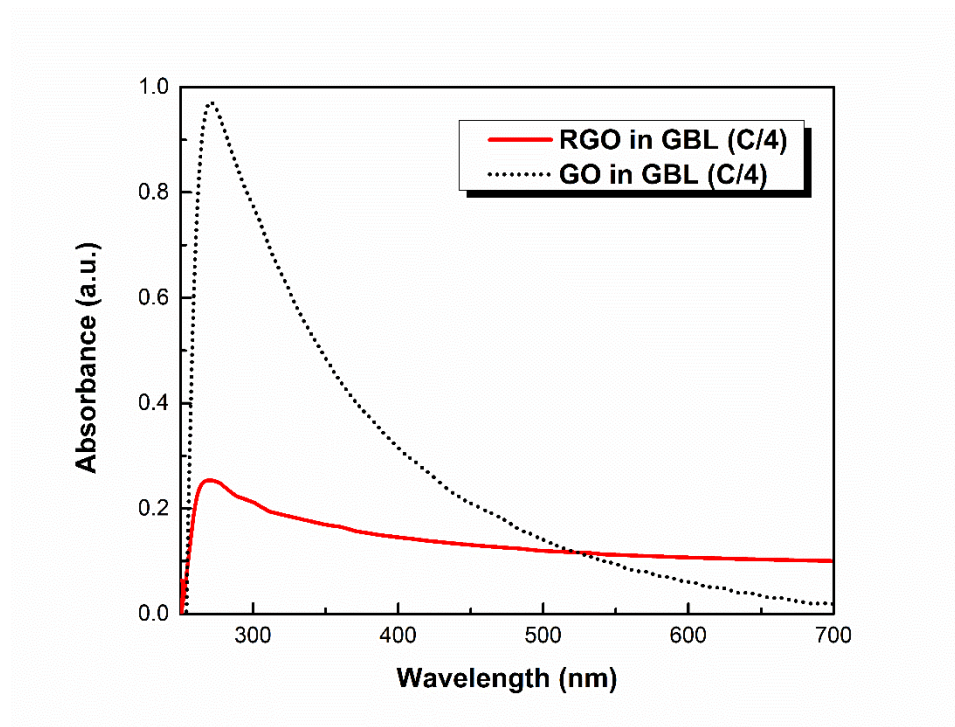


Figure 102 UV-Vis absorption spectra of GO and RGO in γ -butyrolactone (GBL).

To calculate the concentration of GO and RGO in each solvent using Beer-Lamberts law, the absorption coefficient (a) is needed. The value of a for the GO and RGO used

is calculated by constructing a calibration line by measuring the absorbance at $\lambda=660\text{nm}$ of four low concentration GO and RGO dispersions in each solvent. The absorbance values were divided by the cuvette length ($l=0.01\text{m}$) and then plotted against the concentration values of each dispersion. The value of a for GO and RGO is then determined by calculating the slope of each calibration line. Finally, the estimated a value can be used to determine the concentration of GO and RGO in each solvent through Beer-Lamberts law. An example of this procedure is shown in Figure 103 **Error! Reference source not found. Error! Reference source not found.**, where the a value of GO and RGO in de-ionised water was calculated by determining the slope in the respective graphs.

The absorption coefficient value for GO in de-ionised water was found to be $91.36 \text{ Lg}^{-1}\text{m}^{-1}$. This value deviates significantly from that calculated by Konios and his colleagues, which was $3592 \text{ Lg}^{-1}\text{m}^{-1}$ [238]. The most likely reason for this large difference is that the GO samples prepared in this thesis differ from those prepared by Konios et al. in a substantial way.

Firstly, although the graphite oxide used in this thesis was prepared in our laboratory using the same modified Hummers' as Konios et al., different amounts of the reagents was utilised. More specifically, Konios oxidised 1g graphite using 23ml H_2SO_4 , 98%, 0.5g NaNO_3 , 3g KMnO_4 and 3% H_2O_2 . The graphite oxide in this thesis, as described in Chapter 7.1., was prepared by oxidising 1g of graphite using 46ml H_2SO_4 , 1g NaNO_3 , 6g KMnO_4 and 20ml H_2O_2 30% and allowing for longer oxidation time. The different oxidation pathways result in different graphite oxide samples, namely different oxidation levels and, therefore, oxygen content. Secondly, Konios and his team performed mechanical liquid exfoliation of graphite oxide using an ultrasonic bath. The GO dispersion prepared for this thesis were the result of mechanical liquid exfoliation via ultrasonic probe. This results in a difference in the extent of exfoliation, the concentration of the resulting dispersion and the flake size of the suspended solid. Both factors mentioned above have an impact on the overall optical properties if the dispersed GO and, by extension, the absorption coefficient.

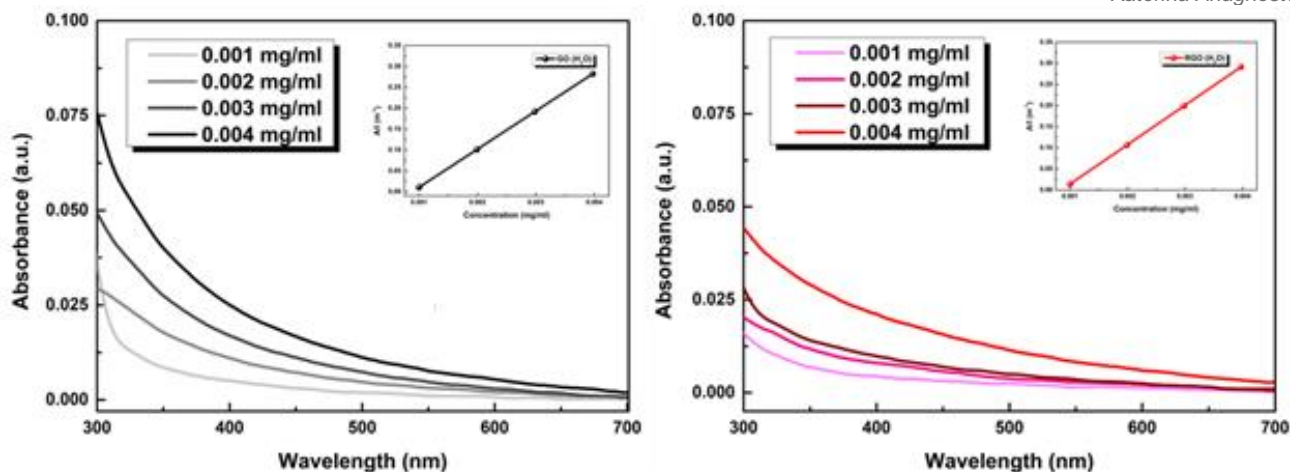


Figure 103 Calculation of absorption coefficient value for (a) GO and (b) RGO in de-ionised water. The absorbance value at 660nm is plotted against the known concentration of four samples of GO and RGO in de-ionised water respectively and the slope of each line (see insets) is equal to the absorption coefficient (ϵ).

In order to plot these calibration lines, the four diluted GO and RGO dispersions measured must be of known concentration. Therefore, the final concentration of every dispersion prepared must be determined. For this purpose, 1ml of each dispersion is evaporated on a clean, pre-weighed watch glass. The watch glass containing the residual solid after evaporation is weighed again and the concentration (mg/ml) is determined.

An issue was encountered during the process of calculating all absorption coefficient values; even though four samples of GO and RGO in acetylacetone with known concentration were prepared for the creation of a calibration line, the actual concentration of each sample may deviate from the expected concentration. The reason for this is that evaporation of 1ml proved to be difficult, as traces of this solute remained on the watch glass. For this reason, 0.5ml, 0.2ml, 0.1ml were evaporated to determine the mass of GO or RGO contained in this volume. The result was the same; traces of acetylacetone remained making it impossible to weigh the mass of each solid. Finally, longer evaporation time was allowed, but even after a week of heating the watch glass, the results did not change. In an attempt to overcome this obstacle, 0.2ml of GO and 0.2ml of RGO in acetylacetone were evaporated alongside 0.2ml of pristine acetylacetone as a reference. The remaining mass of the pristine acetylacetone film remaining after evaporation was subtracted from the mass of GO and RGO. This allowed for successful concentration determination for the creation of a calibration line as with the rest of the solvents.

Another phenomenon that may occur in the case of acetylacetone is that molecules of this solvent adsorb onto the graphitic lattice of GO and RGO flakes and are not removed during evaporation. This is supported by M. Xu et al. who used acetylacetone, in an alkaline environment, as a reducing agent for GO with the ultimate goal of creating a platform for heavy metal adsorption [253]. They suggest that acetylacetone acts as a reducing agent by changing GO’s epoxy groups into double bonds. However, the interesting result this group yielded was that acetylacetone also acts as a stabiliser by functionalising onto the surface and edges of GO (Figure 104).

For the reasons explained above, it must be noted that the concentration of the four samples used for plotting a calibration line may be lower than reported, resulting in a calculated absorption coefficient that deviates from the true value. In turn, this causes the final concentrations of GO and RGO in acetylacetone calculated via Beer-Lambert’s law to differ from the actual concentrations.

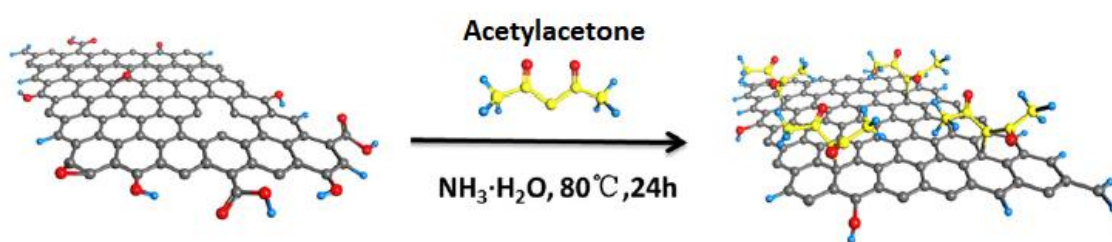


Figure 104 Reduction of GO using acetylacetone. The acetylacetone molecules interact with GO not only by removing epoxy oxygen groups but also by functionalising onto the edges and plane of the lattice and acting as a stabiliser.

The GO and RGO dispersibilities calculated from the Beer-Lambert law (shown in

Solvent	GO concentration (µg/ml)	RGO Concentration (µg/ml)
DH₂O	189.0	5.88
MeOH	1.6	15.98
EtOH	2.5	17.20
IPA	5.25	9.53
BuOH	0	0
Act	4.57	5.41
CB	1.66	3.4

DCB	9.93	87.46
CF	1.3	1.35
CN	5.55	4.91
DCM	0.21	0.02
CCl₄	0	0
AcAc	17	33.0
EG	44.87	4.9
EA	5.09	2.01
DET	6.67	0.4
Hex	0.1	0.6
Tol	1.57	4.14
Xyl	0	0
DMSO	5.93	0
DES	0	0
DMF	21.46	12.18
THF	1.44	2.15
NMP	37.86	15.79
GBL	26.98	15.12

) were plotted in a column graph for easier comparison (Figure 105). For solvents such as hexane and toluene, GO and RGO were virtually not dispersible. As seen in Figure 77, the results were practically transparent samples. In these cases, it was impossible to create a calibration line for the calculation of the absorption coefficients. All concentrations marked “zero” were not detectable and were considered to be <0.0001 mg/ml.

Table 7 Concentrations of GO and RGO in each solvent as calculated through Beer-Lamberts' law.

Solvent	GO concentration (µg/ml)	RGO Concentration (µg/ml)
DH₂O	189.0	5.88
MeOH	1.6	15.98
EtOH	2.5	17.20
IPA	5.25	9.53

BuOH	0	0
Act	4.57	5.41
CB	1.66	3.4
DCB	9.93	87.46
CF	1.3	1.35
CN	5.55	4.91
DCM	0.21	0.02
CCl₄	0	0
AcAc	17	33.0
EG	44.87	4.9
EA	5.09	2.01
DET	6.67	0.4
Hex	0.1	0.6
Tol	1.57	4.14
Xyl	0	0
DMSO	5.93	0
DES	0	0
DMF	21.46	12.18
THF	1.44	2.15
NMP	37.86	15.79
GBL	26.98	15.12

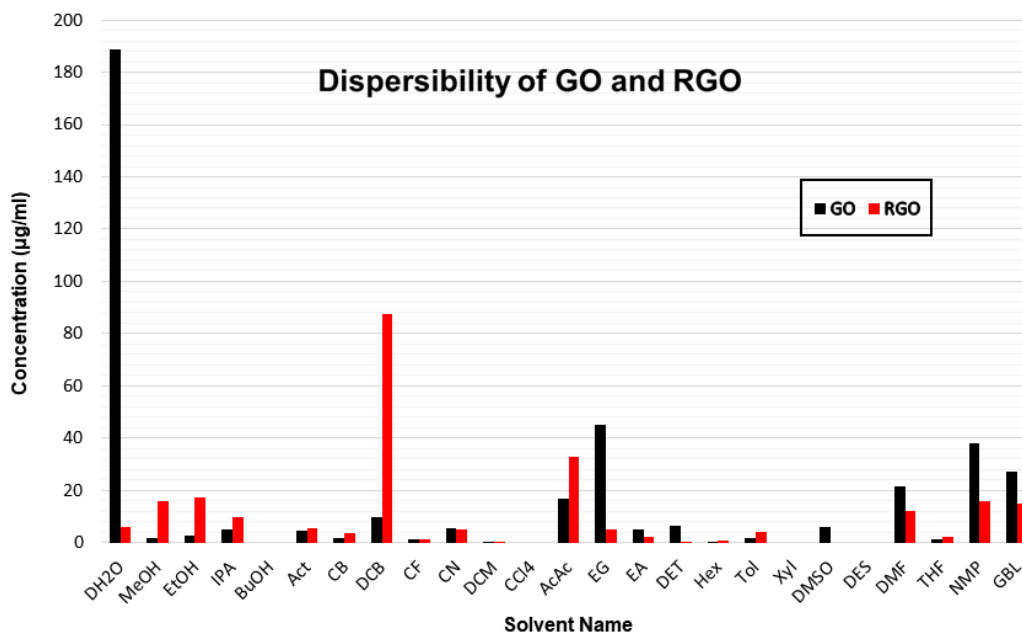


Figure 105 Dispersibility of GO and RGO in all solvents given in µg/ml.

In 1-Butanol, CCl₄, o-Xylene and DES neither GO or RGO were dispersed, as the samples appear to be virtually transparent and the concentrations were undetectable in the laboratory. This was also confirmed by the UV-Vis absorption spectra for these samples which shown extremely low absorbance, indicating that the concentrations of GO and RGO in these solvents are negligible, if not zero.

GO was successfully and stably dispersed in DH₂O, EG, NMP, GBL, DMF, AcAc and DCB with rather high concentrations, the highest being in DH₂O (189.0µg/ml). Lower concentration GO dispersions were achieved in IPA, Act, CB, CN, EA, diethylether and DMSO. High concentration dispersions of RGO were prepared in DCB and AcAc, the highest being in DCB (87.46 µg/ml). RGO dispersions of lower concentrations were achieved in EtOH, MeOH, NMP, GBL, DMF, IPA and DH₂O. Low concentrations for RGO were also calculated in Act, CF, CN, DCM and EA.

Only one solvent was able to disperse GO but not RGO, and that was DMSO. However, the concentration of RGO in DMSO was considered to be zero because when attempting to evaporate 1ml of this dispersion to determine the amount RGO contained within that 1ml, the mass of RGO was undetectable. Therefore, it was considered to be indispersible in water. Nevertheless, this should be taken with a grain of salt, as the UV-Vis absorption spectrum of RGO in DMSO showed a low absorption maximum peak, indicating that there exist indeed trace amounts of RGO in DMSO, but

they were undetectable during the evaporation process for the calculation of the absorption coefficient.

8.3. Calculation of Hansen solubility Parameters of GO and RGO:

The HSP for all solvents used in this thesis are presented in Table 8. The values were lifted from The Three-Dimensional Solubility Parameter and Solvent Diffusion Coefficient by Charles Hansen [226]. Also included are the dipole moment values and the surface tension values, as these play an important role in a solvent’s ability to efficiently dilute or disperse a material. The HSP of all the solvents as well as the dispersibilities of GO and RGO (Table 8Table 7) are needed to calculate the HSP of GO and RGO using Equation (14).

$$\langle \delta_i \rangle = \frac{\sum_{solv} C \delta_{i,solv}}{\sum_{solv} C} \quad (13)$$

The three HSP for GO were found to be $\delta_D=16.5 \text{ MPa}^{1/2}$, $\delta_P=13.5 \text{ MPa}^{1/2}$, $\delta_H=26.6 \text{ MPa}^{1/2}$ respectively giving a total of $\delta T=34.1 \text{ MPa}^{1/2}$ as given by Equation (10). Likewise, the values calculated for RGO were $\delta_D=17.6 \text{ MPa}^{1/2}$, $\delta_P=9.18 \text{ MPa}^{1/2}$, $\delta_H=9.05 \text{ MPa}^{1/2}$ giving a total of $\delta T=21.9 \text{ MPa}^{1/2}$ (Table 9).

As mentioned earlier, R_a represents the distance of the coordinates given by a particle’s HSP from those of a solute in Hansen space. The R_a value must be smaller or equal to the Hansen sphere radius (R_0) for the solvent to successfully disperse or dilute the material in question. There is no way to know the R_0 values for the GO and RGO prepared in this work in order to calculate the RED and clearly separate the “good” solvents from the “bad”. Nevertheless, the R_a values for GO and RGO were calculated using equation (11) in an attempt to establish a correlation with the concentration values. The results are presented in **Error! Reference source not found.** The R_a values for GO and RGO were compared to the calculated concentrations in each solvent to investigate if a pattern is formed i.e. whether dispersion concentration increases with the increase or decrease of R_a . Generally, there was no solid trend was observed for the relationship between R_a and dispersibility.

Table 8 Dispersibility values of GO and RGO used to calculate their HSP. Also presented, the HSP for all solvents used including the calculated R_a values. The HSP included in this table were lifted from Hansen’s research and calculations [226, 230, 254] and the δ_T was calculated using equation (10). R_a values calculated using Equation 11.

	Solvent name	GO Concentration (µg/ml)	RGO Concentration (µg/ml)	δ_D (MPa^{1/2})	δ_P (MPa^{1/2})	δ_H (MPa^{1/2})	δ_T (MPa^{1/2})	R_a(GO)	R_a (RGO)
1	DH ₂ O	189.0	5.88	15.5	16.0	42.3	47.89	16.06	34.21
2	MeOH	1.6	15.98	15.1	12.3	22.3	29.61	5.26	14.53
3	EtOH	2.5	17.20	15.8	8.8	19.4	26.52	8.70	10.99
4	IPA	5.25	9.53	15.8	6.1	16.4	23.57	12.67	8.78
5	BuOH	0	0	16.0	5.7	15.8	23.18	13.35	8.28
6	Act	4.57	5.41	15.5	10.4	7.0	19.93	19.91	4.91
7	CB	1.66	3.4	19.0	4.3	2.0	19.58	26.70	8.99
8	DCB	9.93	87.46	19.2	6.3	3.3	20.47	24.94	7.14
9	CF	1.3	1.35	17.8	3.1	5.7	18.95	23.46	6.95
10	CN	5.55	4.91	19.9	4.9	2.5	20.65	26.44	9.03
11	DCM	0.21	0.02	18.2	6.3	6.1	20.20	21.96	4.27
12	CCl ₄	0	0	17.8	0.0	0.6	17.81	29.38	12.48
13	AcAc	17	33.0	16.1	11.2	6.2	20.57	20.51	4.66
14	EG	44.87	4.9	17.0	11.0	26.0	32.95	2.76	17.09
15	EA	5.09	2.01	15.8	5.3	7.2	18.15	21.08	5.66
16	DET	6.67	0.4	14.5	2.9	5.1	15.64	24.28	9.73
17	Hex	0.1	0.6	14.9	0	0	14.90	29.98	14.01
18	Tol	1.57	4.14	18.0	1.4	2.0	18.16	27.55	10.52
19	Xyl	0	0	17.6	1.0	3.1	17.90	26.68	10.11
20	DMSO	5.93	0	18.4	16.4	10.2	26.67	17.03	7.46
21	DES	0	0	15.8	14.7	7.2	22.75	19.45	6.89
22	DMF	21.46	12.18	17.4	13.7	11.3	24.86	15.36	5.07
23	THF	2.15	1.44	16.8	5.7	8.0	19.46	20.15	4.01
24	NMP	37.86	15.79	18.0	12.3	7.2	22.96	19.62	3.69
25	GBL	26.98	15.12	19	16.5	7.3	47.89	20.12	7.99

Table 9 Calculated HSP for GO and RGO including the total Hansen parameter.

	δD (MPa ^{1/2})	δP (MPa ^{1/2})	δH (MPa ^{1/2})	δT (MPa ^{1/2})
GO	16.52	13.53	26.56	34.08
RGO	17.64	9.18	9.05	21.85

Table 10 Polarity indices, relative polarity values and dipole moments of all 25 solvents.

	Solvent name	Polarity Index	Relative Polarity	Dipole moment
1	DH ₂ O	10.2	1.0	1.85
2	MeOH	5.1	0.762	1.70
3	EtOH	4.3	0.654	1.69
4	IPA	3.9	0.546	1.66
5	BuOH	7	0.586	2.84
6	Act	5.1	0.355	2.88
7	CB	2.7	0.188	1.72
8	DCB	2.7	0.225	2.53
9	CF	4.1	0.259	1.02
10	CN	N/A	N/A	1.55
11	DCM	3.1	0.309	1.60
12	CCl ₄	2	0.052	0
13	AcAc	N/A	0.571	3.03
14	EG	6.9	0.79	2.31
15	EA	4.4	0.228	1.78
16	DET	2.8	0.117	1.15
17	Hex	0.1	0.009	0.085
18	Tol	2.5	0.099	0.38
19	Xyl	2	0.074	0.45
20	DMSO	7	0.444	3.96
21	DES	N/A	N/A	4.46
22	DMF	6.4	0.386	3.82
23	THF	4.0	0.207	1.75
24	NMP	6.7	0.4	3.75
25	GBL	6.3	N/A	4.27

Table 11 The 25 solvents used sorted from highest to lowest GO concentration and highest to lowest RGO concentration.

Solvent	GO Concentration (µg/ml)	Solvent	RGO Concentration (µg/ml)
DH ₂ O	189	DCB	87.46

EG	44.87	AcAc	33
NMP	37.86	EtOH	17.2
GBL	26.98	MeOH	15.98
DMF	21.46	NMP	15.79
AcAc	17	GBL	15.12
DCB	9.93	DMF	12.18
DET	6.67	IPA	9.53
DMSO	5.93	DH₂O	5.88
CN	5.55	Act	5.41
IPA	5.25	CN	4.91
EA	5.09	EG	4.9
Act	4.57	Tol	4.14
EtOH	2.5	CB	3.4
CB	1.66	THF	2.15
MeOH	1.6	EA	2.01
Tol	1.57	CF	1.35
THF	1.44	Hex	0.6
CF	1.3	DET	0.4
DCM	0.21	DCM	0.02
Hex	0.1	Xyl	0
BuOH	0	BuOH	0
CCl₄	0	CCl₄	0
Xyl	0	DMSO	0
DES	0	DES	0

8.3.1. Investigating the final concentrations of GO and RGO dispersions:

For easier comparison and interpretation of the resulting concentrations of GO and RGO, the solvents have been sorted in **Error! Reference source not found.** by descending concentration value for GO and RGO separately. The concentration values, which essentially reflect the dispersibility, were then compared to the following solvent characteristics to establish any possible correlation: dipole moment, relative polarity, polarity index (Table 10), surface tension (Table 3), δT , δP , δD , δH and R_a . When studying the dispersibility of GO and RGO in relation to the polarity of all the solvents, a concrete conclusion could not be established because no polarity indices were found in literature for CN, AcAc and DES nor relative polarity values for CN, GBL and DES. Therefore, the attempt to correlate these solvent characteristics with the dispersibility values was lacking. However, the dipole moments of all used solvents were available. No particular trends were observed to establish a clear correlation between these solvent properties and the resulting dispersibility of GO and/or RGO. However, a few interesting observations were made that may be of note.

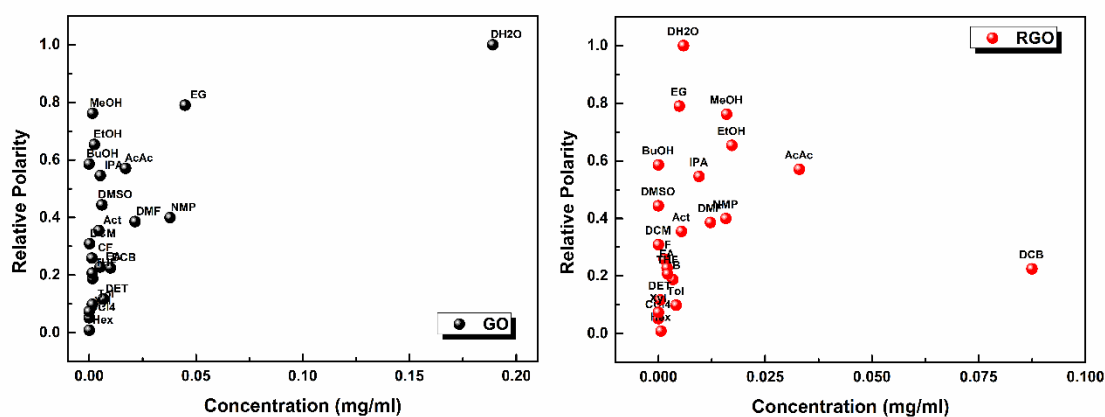


Figure 106 Relative polarity of solvents plotted against GO dispersion concentrations (left) and RGO dispersion concentrations (right). Not included: CN, DES and GBL, as their relative polarity values are not available.

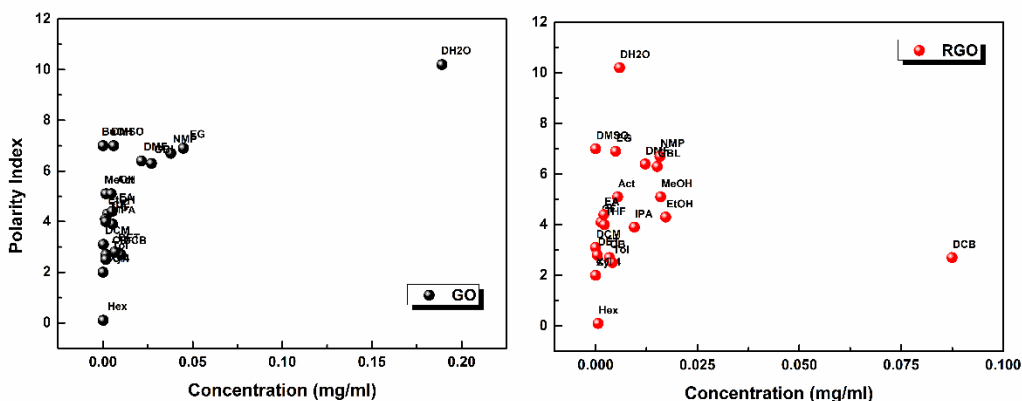


Figure 107 Polarity indices of solvents plotted against GO dispersion concentrations (left) and RGO dispersion concentrations (right). Not included: CN, AcAc and DES, as their polarity indices values are not available.

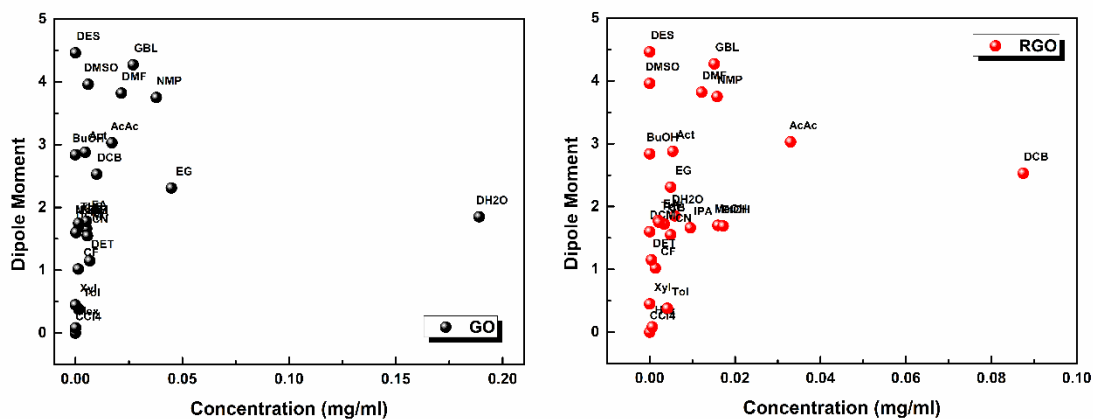


Figure 108 Dipole moments of solvents plotted against GO dispersion concentrations (left) and RGO dispersion concentrations (right).

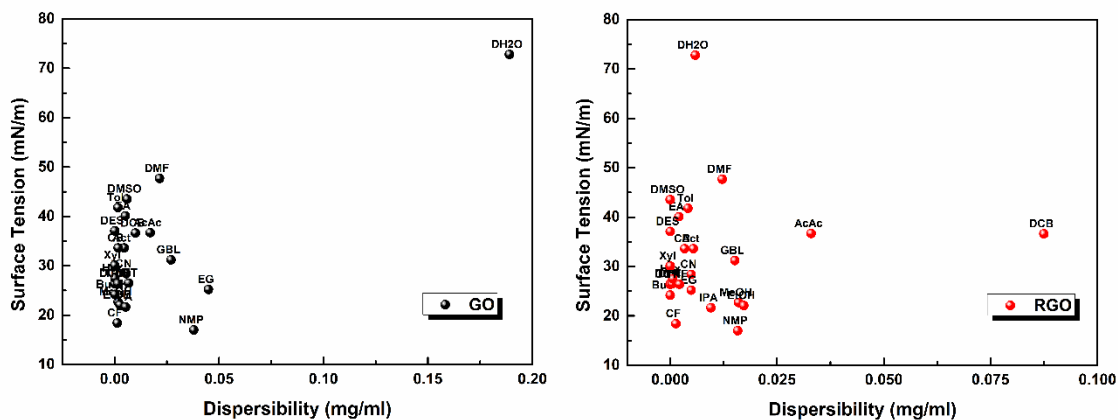


Figure 109 Dipole moments of solvents plotted against GO dispersion concentrations (left) and RGO dispersion concentrations (right).

When studying the data in Figures 106 to 109, the following observations were made:

1. **Relative Polarity:** The two highest concentration for GO were measured for DH₂O and EG. These solvents have the highest relative polarity values. The next solvents in line are MeOH, EtOH and BuOH with relative polarity values of 0.762, 0.654 and 0.586 respectively. Although GO “prefers” polar/hydrophilic solvents, it’s concentration in these alcohols is either extremely low or zero (see Table 11). Speculations on the reason GO is not readily dispersed in alcohols is presented in subchapter 8.3.2.
2. **Polarity Index:** For GO, the solvent that yielded the highest concentration (DH₂O) also has the highest polarity index (10.2). The solvents next in line are DMSO and BuOH, which both have a polarity index of 7. However, these two solvents yielded concentrations of 5.93 µg/ml and 0 µg/ml respectively. Therefore, polarity index alone is not a trustworthy criterion for choosing a good solvent. Furthermore, no relationship between RGO dispersibility and solvent polarity index is established.
3. **Dipole Moment:** CCl₄ has a dipole moment of zero and both GO and RGO are indispersible in this solvent. Conversely, DES has the highest dipole moment of all 25 solvents yet GO and RGO are indispersible in this solvent as well. Perhaps this serves as evidence that the dispersibility of graphene derivatives is irrelevant to the dipole moment of a solvent.
4. **Surface Tension:** For GO, DH₂O yielded the highest concentrated dispersion and is also the solvent with the highest surface tension value (72.8 mN/m). No relationship between RGO dispersibility and solvent surface tension is observed.

8.3.2. Investigating the calculated HSP for GO and RGO:

It is evident that the dispersibility behaviour of GO is altered through the process of reduction. After being reduced to yield RGO, the material now “prefers” different solvents. This is attributed to the alteration in structure and general chemical make-up. Firstly, oxygen groups are removed making RGO less affinitive toward highly polar

solvents, such as DH₂O. Secondly, defects, namely holes, may be created in the graphitic lattice, perhaps allowing for solvent molecule to be adsorbed into these defects. In this chapter, the calculation, study and comparison of the GO and RGO HSP based on the prepared dispersions is performed in hopes of drawing conclusions on the “relationship” of GO and RGO with the 25 investigated solvents. The HSP coordinates of GO, RGO and the 25 selected solvents is presented in Figure 110. Generally, the closer the coordinates of a solvent are to those of a solute in Hansen 3D space, the more likely it is that they will interact (i.e. form a solution or a dispersion).

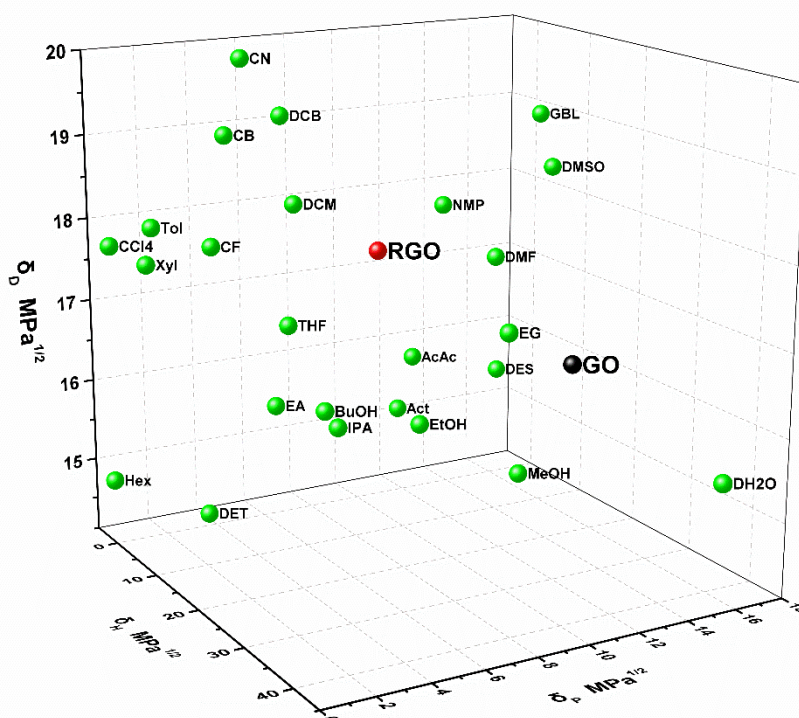


Figure 110 Coordinates (HSP) of GO, RGO and the 25 selected solvents in Hansen 3D space.

As discussed in the previous subchapter, the calculated HSP for the Hummers’ prepared GO were $\delta_D = 16.50$, $\delta_P = 13.50$, $\delta_H = 26.60$, $\delta_T = 34.10$, whereas for the HI/AcOH prepared RGO the HSP were $\delta_D = 17.60$, $\delta_P = 9.17$, $\delta_H = 9.05$, $\delta_T = 21.90$, given in $\text{MPa}^{1/2}$. The calculated HSP for RGO are close to previous reported HSP for graphene ($\delta_D \sim 18 \text{ MPa}^{1/2}$, $\delta_P \sim 9.3 \text{ MPa}^{1/2}$, $\delta_H \sim 7.7 \text{ MPa}^{1/2}$ and $\delta_T \sim 23 \text{ MPa}^{1/2}$), showing a high degree of graphitisation and dispersion behaviour similar to that of graphene [33]. This statement is supported by previous reports of higher levels of graphitisation through chemical reduction with HI, [110]. This fact explains that after

the reduction process, when RGO is dispersed in DH_2O , it yields a concentration ~ 32 times lower than GO in DH_2O . Generally, the hydrophobicity of GO increases as the oxygen content decreases with reduction, thus negatively effecting its dispersibility in aqueous media [255]. It is evident that the HI/AcOH prepared RGO is structurally closer to graphene, therefore showing low affinity for hydrophilic solvents.

However, RGO is dispersed in low concentrations in MeOH, EtOH and IPA, which are hydrophilic solvents since they contain a hydroxyl group. One would expect that GO would “prefer” these alcohols owing to its oxygen functional groups. This phenomenon is explained in V. V. Neklyudov’s publication in which they show that GO is not dispersible in alcohols due to the orientation of the established hydrogen bonds [211]. They support that when a hydrogen bonds between GO and the alcohol are formed, the alcohol’s alkyl groups are directed toward the exterior, making GO hydrophobic. The GO particles are now incapable of forming further hydrogen bonds with the rest of the alcohol molecules thus being rendered indispersible in the alcohol environment. Furthermore, it is speculated that solvent molecules were adsorbed into defects in the RGO lattice, thus aiding the suspension of the RGO flakes.

The concentrations of the GO and RGO dispersions were plotted against each HSP in an attempt to draw conclusions on which solvents these materials “prefer” to create a dense and stable dispersion.

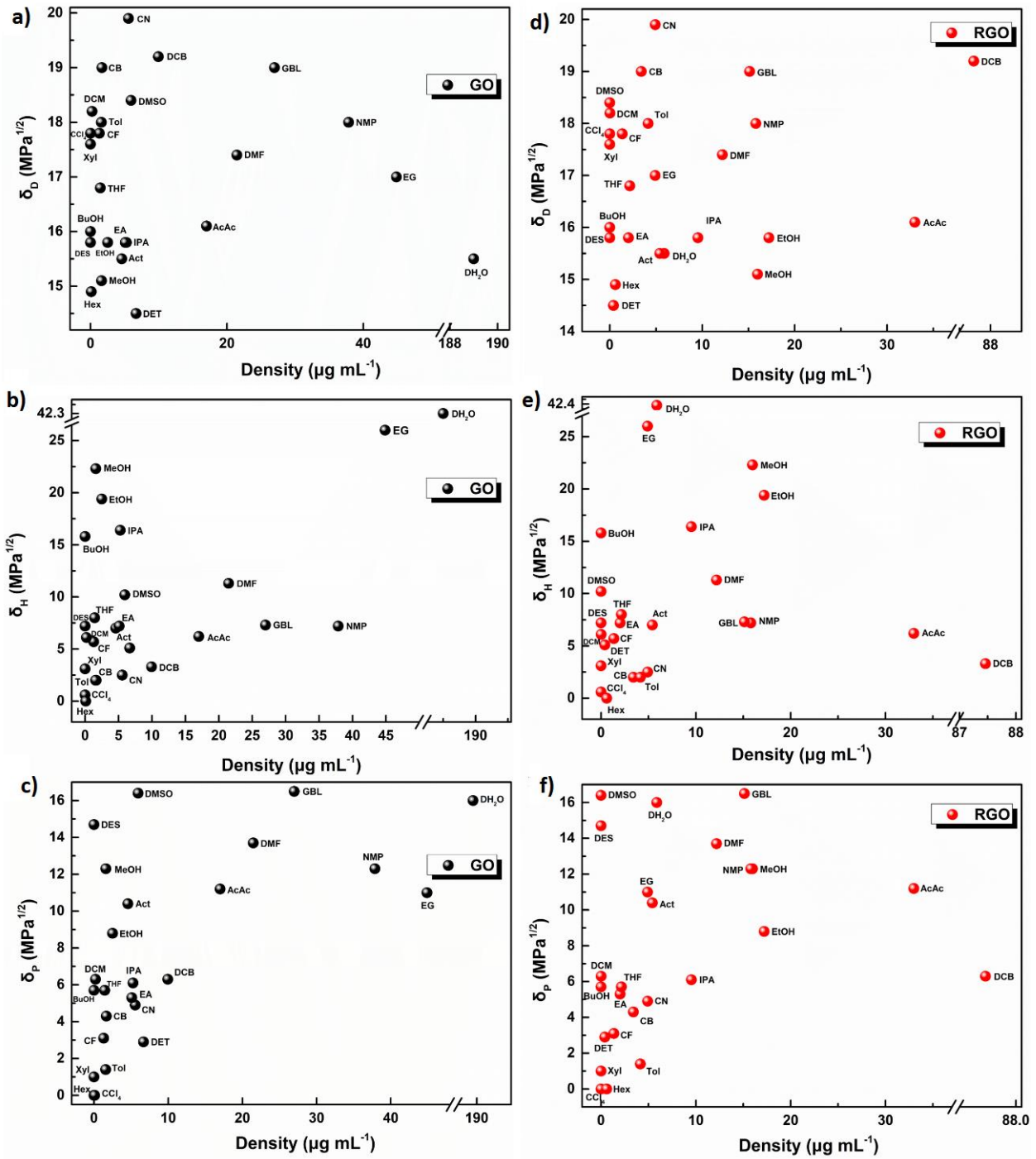


Figure 111 HSP of solvents plotted against the concentration of GO (a, b, c) dispersions and RGO dispersions (d, e, f).

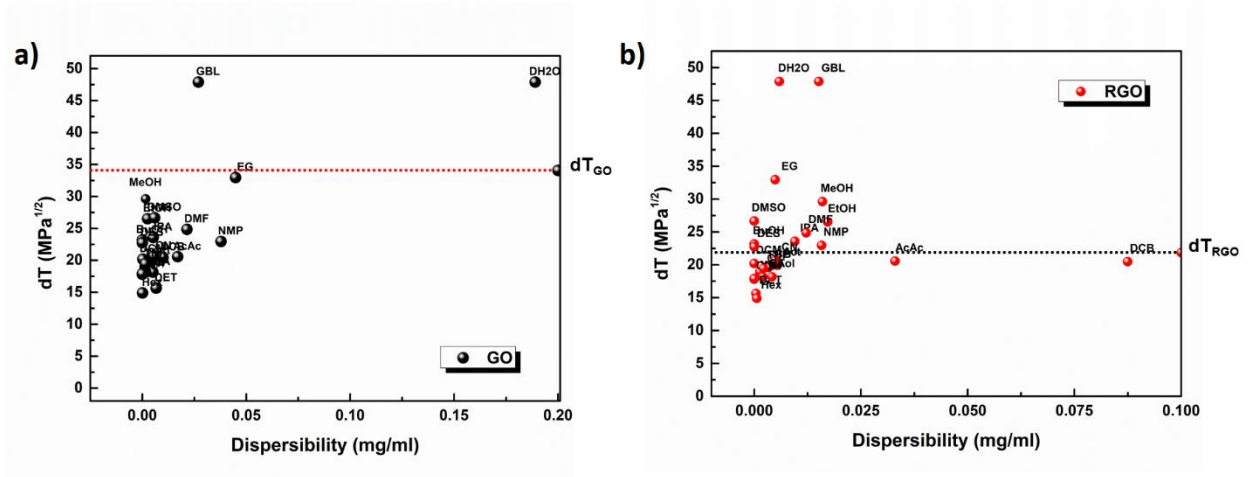


Figure 112 δT of solvents plotted against the concentration of a) GO dispersions b) RGO dispersions. The dotted lines indicate the δT of GO and RGO respectively in order to more plainly see which solvents have a δT value close to that.

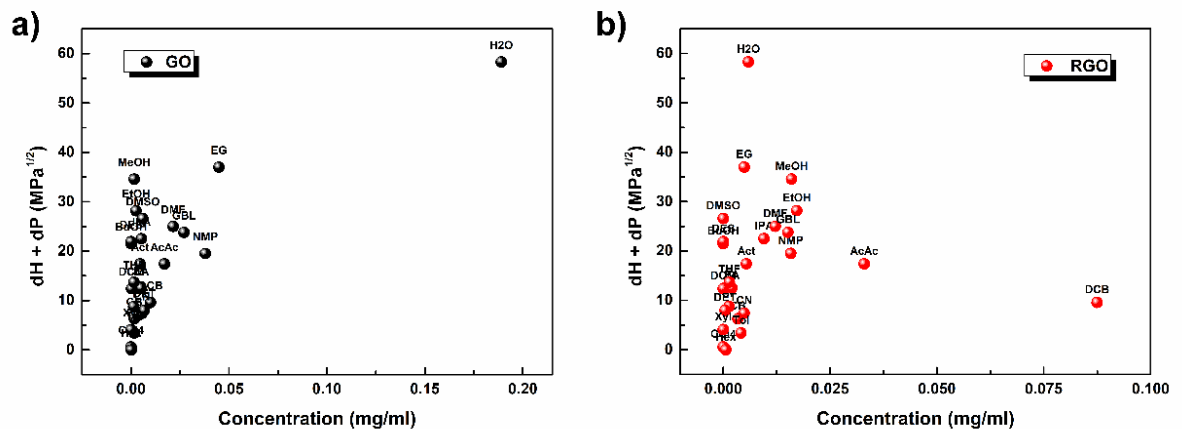


Figure 113 $\delta H + \delta P$ of solvents plotted against the concentration of a) GO dispersions b) RGO dispersions.

When studying the data presented in Figures 111 to 113, the following observations were made:

1. **δD :** Y. Hernandez et al. report that “good” solvents for graphene dispersion have a δ_D value between 15 MPa^{1/2} and 21 MPa^{1/2} [236]. For the HI/AcOH RGO in this work, the suited δ_D values appear to be from 15.1 to 19.2 MPa^{1/2}, values similar to those reported by Y. Hernandez. The reverse statement does not apply. “Good” solvents for RGO showed 15.1 MPa^{1/2} \leq $\delta_D \leq$ 19.2 MPa^{1/2}, this does not mean, however, that solvents with a δ_D within this range will

necessarily disperse RGO effectively. E.g. DCM has $\delta_D=18$ but RGO's concentration in this solvent was one of the lowest (0.018 $\mu\text{g/ml}$). For GO the respective range appeared to be $14.2 \text{ MPa}^{1/2} \leq \delta_D \leq 19.2 \text{ MPa}^{1/2}$, again, without meaning that a solvent showing a δ_D within this range will successfully disperse GO.

2. **δP** : Following the same route, GO “prefers” solvents with $2.9 \leq \delta P \leq 16.5$, $3.3 \leq \delta H \leq 42.3$ and $15.64 \leq \delta T \leq 47.89$ (all values given in $\text{MPa}^{1/2}$). RGO is better dispersed in solvents with $6.1 \leq \delta P \leq 16.5$, $3.3 \leq \delta H \leq 42.3$ and $19.93 \leq \delta T \leq 42.3$ (all values given in $\text{MPa}^{1/2}$).
3. **δH** : The two highest concentrations for GO were measured for DH_2O and EG. These solvents have the highest δH values.
4. **δT** : For RGO, the solvents which yielded the highest concentrated dispersions (DCB and AcAc) also had the δT very close to that of RGO, with $\delta T_{\text{DCB}}= 20.47 \text{ MPa}^{1/2}$, $\delta T_{\text{AcAc}}=20.57 \text{ MPa}^{1/2}$ and $\delta T_{\text{RGO}}=21.85 \text{ MPa}^{1/2}$. However, the “good” solvent for RGO with the closest δT value was NMP with $\delta T_{\text{NMP}}=22.96 \text{ MPa}^{1/2}$. For GO, although DH_2O yielded the densest GO dispersion, it is EG, the second-best solvent, that has a δT value closest to that of GO, with $\delta T_{\text{EG}}= 32.95 \text{ MPa}^{1/2}$ and $\delta T_{\text{GO}}= 34.08 \text{ MPa}^{1/2}$.
5. **$\delta P + \delta H$** : It has been reported that GO forms stable dispersion in solvents that have a $\delta P + \delta H$ value $>32 \text{ MPa}^{1/2}$ [256]. RGO, on the other hand, “prefers” solvents with a range of $10 \text{ MPa}^{1/2} < \delta P + \delta H < 30 \text{ MPa}^{1/2}$ [257]. They found that highly reduced GO they prepared using hydrazine does not yield good suspensions in solvents that have $\delta P + \delta H$ smaller than 10 or much higher than $30 \text{ MPa}^{1/2}$. According to our results (Figure 113), for GO, “good” solvents had $8 \text{ MPa}^{1/2} \leq \delta P + \delta H \leq 58.3 \text{ MPa}^{1/2}$, whereas for RGO it was $9.6 \text{ MPa}^{1/2} \leq \delta P + \delta H \leq 58.3 \text{ MPa}^{1/2}$. If for RGO DH_2O were to be classed as a “bad” solvent, then the range would be $9.6 \text{ MPa}^{1/2} \leq \delta P + \delta H \leq 34.6 \text{ MPa}^{1/2}$, which is similar to that reported by S. Park et al. [257]. However, the exist solvents that adhere to this range, yet do not form good GO and/or RGO dispersion, therefore, as previously explained, the reverse does not apply.

8.3.3. Investigating the calculated R_a values:

In Hansen's theory R_a is the distance between two materials (two solvents or a solvent and a solute) in Hansen space. Its value is derived from the HSP of the materials in question through Equation 11. Therefore, the R_a values also provide insight into the dispersion behaviour of GO and RGO. To this end, the R_a values were plotted against the GO and RGO dispersion concentrations and the individual HSP of all 25 solvents, as seen in Figures 114 to 118.

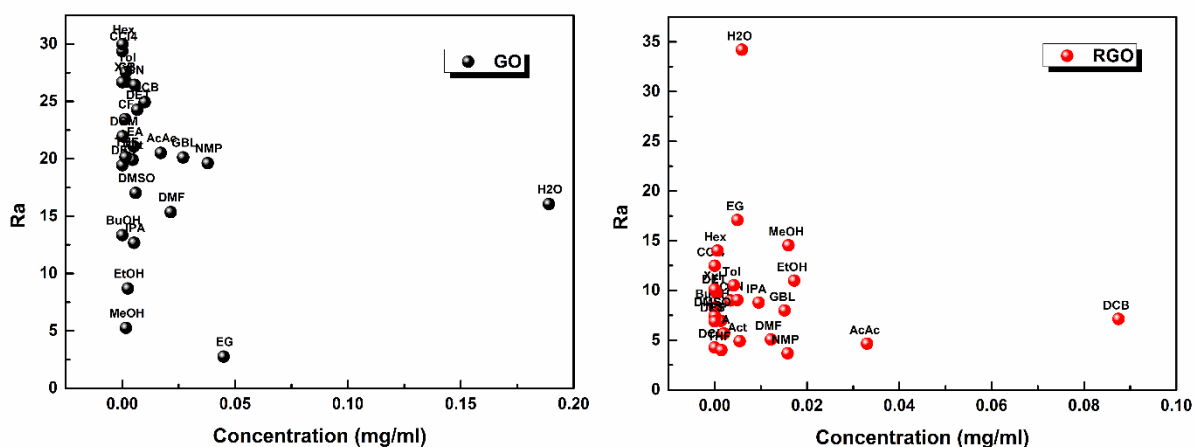


Figure 114 R_a values of GO (left) and RGO (right) in each solvent plotted against the respective dispersion concentrations.

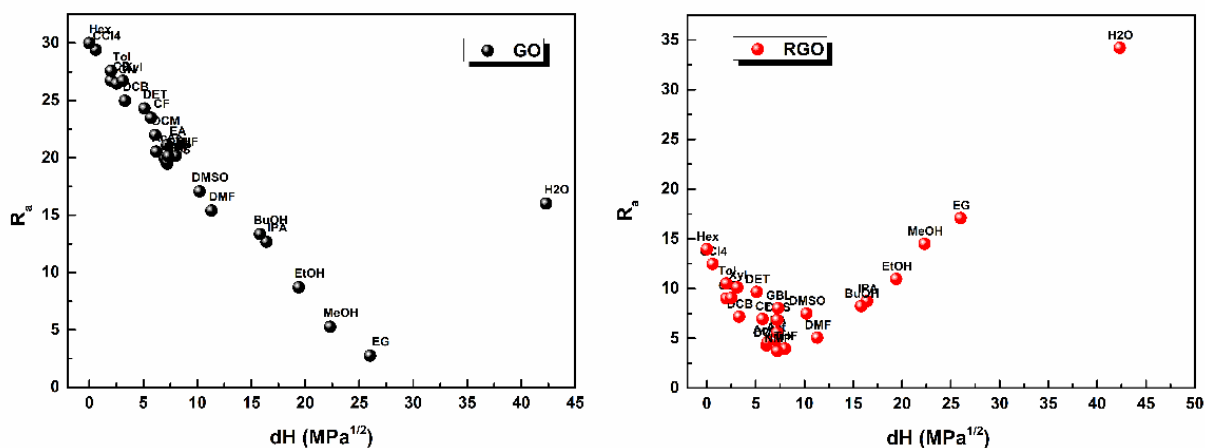


Figure 115 Distance (R_a) between GO (left) and RGO (right) and the 25 solvents in Hansen 3D space plotted against the δH value of every solvent. For GO, the R_a value decreases as the δH increases, with the exception of H_2O . For RGO R_a decreases as δH increases until we reach DMF, after which the opposite trend is observed. The largest R_a was calculated for H_2O the solvent with the largest δH .

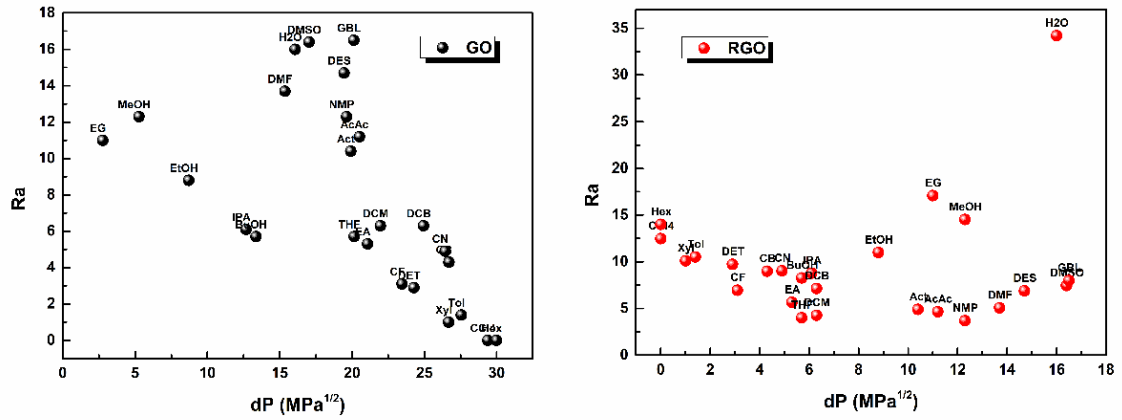


Figure 116 Distance (R_a) between GO (left) and RGO (right) and the 25 solvents in Hansen 3D space plotted against the δP value of every solvent.

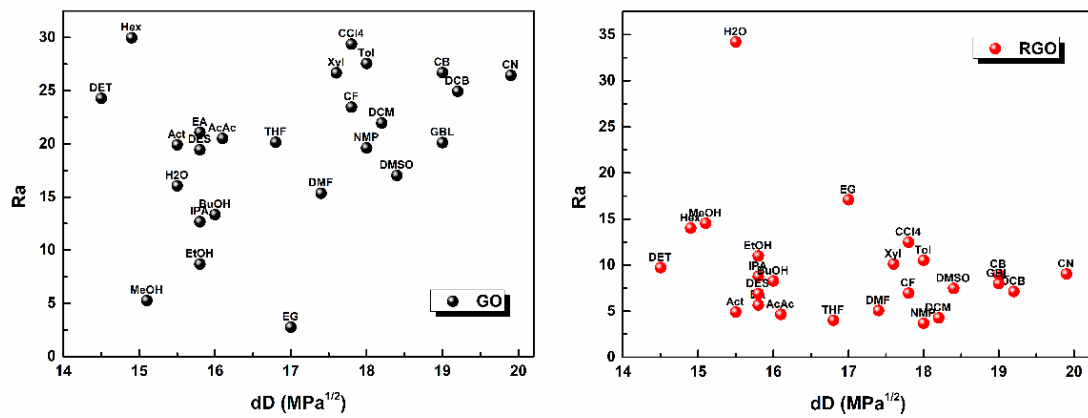


Figure 117 Distance (R_a) between GO (left) and RGO (right) and the 25 solvents in Hansen 3D space plotted against the δD value of every solvent.

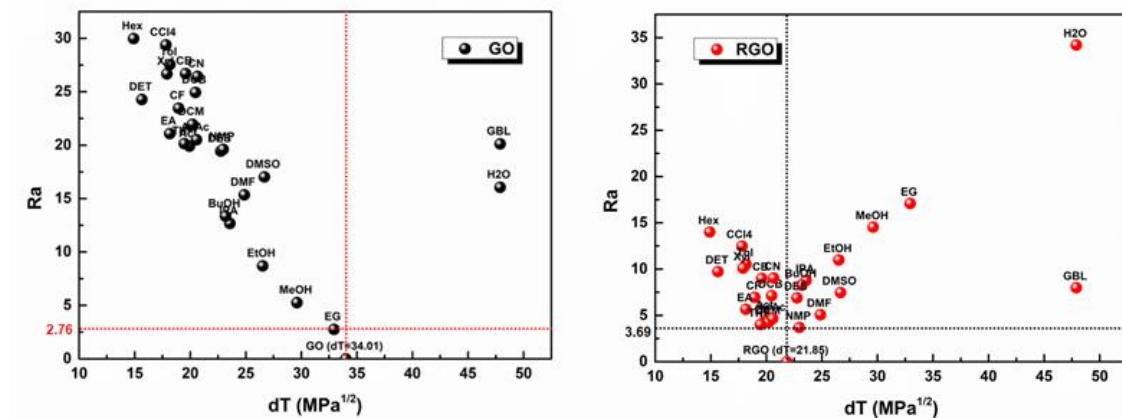


Figure 118 Distance (R_a) between GO (left) and RGO (right) and the 25 solvents in Hansen 3D space plotted against the δP value of every solvent. A similar trend to the relationship between R_a and δH is observed, with the exception of GBL.

According to Hansen's theory, the closer the δT of the solid to the δT of the solvent, the more likely it is that the solvent will dissolve or disperse the solid due to high affinity. This can be translated into terms of distance between solid and solvent. The smaller the R_a , meaning the closer the coordinates of the solid to those of the solvent, the more likely it is that two will mix. It can be derived from this notion that the closer the δT of a solvent to the δT of GO (or RGO) the smaller the respective R_a for that solvent will.

After studying the data in Figures 116 to 120, the following observations were noted:

1. The smallest R_a value for GO was calculated for EG, which yielded the 2nd most concentrated dispersion (44.87 $\mu\text{g/ml}$) after DH_2O .
2. For RGO, the smallest R_a was calculated for NMP ($R_a=3.69$), which is the solvent with a δT value closest to that of RGO ($\delta T_{\text{NMP}}=22.96 \text{ MPa}^{1/2}$). However, NMP was not the solvent that produced the most concentrated RGO dispersion. Instead, NMP yielded the 5th densest dispersion (15.79 $\mu\text{g/ml}$).
3. When plotting the δ_H of the solvents against the respective R_a values for GO, a trend is noticed. A trend is evident: as the δ_H of the solvent increases, the distance, R_a , between the solvent and GO in Hansen space decreases, with the exception of DH_2O , which has the largest δ_H but an intermediate R_a value. No similar trend is observed in the case of RGO, where the R_a value decreases with the δ_H of the solvents until $\delta_H \approx 11$ for DMF. Then the R_a value increases with the δ_H value, until the maximum R_a for the maximum δ_H for DH_2O .
4. The ten solvents with the smallest δ_H (Hex, CCl_4 , Toluene, CB, CN, Xyl, DCB, DET, CF and DCM) also had the smallest R_a values for GO. Conversely, the eight solvents with the highest δ_H values (DH_2O , EG, MeOH, EtOH, IPA, BuOH, DMF and DMSO) have the smallest R_a values for GO, with the exception of DH_2O , for which an intermediate R_a value was calculated. In the case of RGO, the three largest R_a values were calculated for DH_2O , EG and MeOH which are the solvents with the highest δ_H .

5. After noticing this somewhat trend in the relationship between R_a and δH , the R_a values were also plotted against δD , δP and δT of all the solvents. No similar trend was observed for the R_a and δP or R_a and δD , however, the relationship between R_a and δT is similar to that between R_a and δH for both GO and RGO. In the case of GO, the higher the δT value, the smaller the distance R_a , with the exception of DH_2O and GBL which both display the same highest δT value ($\delta T=47.89 \text{ MPa}^{1/2}$) yet have a large distance R_a from GO in Hansen 3D space. For RGO, on the other hand, the R_a value decreases as the δT value increases, until we reach NMP. After this point, the R_a value increases with the increase of δT until we reach the maximum R_a (34.21) for the maximum δT value ($\delta T=47.89 \text{ MPa}^{1/2}$ for DH_2O). GBL deviates from this trend, displaying a small R_a for the same δT value as DH_2O ($\delta T=47.89 \text{ MPa}^{1/2}$).

6. The two largest R_a values for GO were calculated for Hexane and CCl_4 . These solvents did not disperse GO ($C \leq 0.0001 \text{ mg/ml}$). RGO is also indispersible in CCl_4 , however the R_a value for RGO in CCl_4 is much smaller than that for GO in CCl_4 . Interestingly, Hexane and CCl_4 also have a δP of zero.

7. In the case of GO, one would expect that DH_2O , as the solvent that yielded the most concentrated concentration, would also yield the smallest R_a . Yet, it is EG, the solvent that produced the 2nd most concentrated GO concentration (44.87 $\mu\text{g/ml}$) that adheres to this theory is EG, which had the smallest R_a (2.76) and the closest δT to that of GO ($\delta T_{EG}=32.95 \text{ MPa}^{1/2}$) (Figure 111).

8.4. Zeta potential measurements

Zeta potential (ζ -potential), also termed electrokinetic potential, is a method used in colloidal chemistry to evaluate the stability of suspensions, dispersions and colloids. The ζ -potential is the electric potential in the interfacial double layer at the location of the slipping plane relative to a point in the bulk fluid away from the interface [258]. The double layer is a structure that forms when a solid particle is exposed to a fluid (Figure 119). An interfacial double layer occurs in colloids, where the surface area is large in relation to the volume.

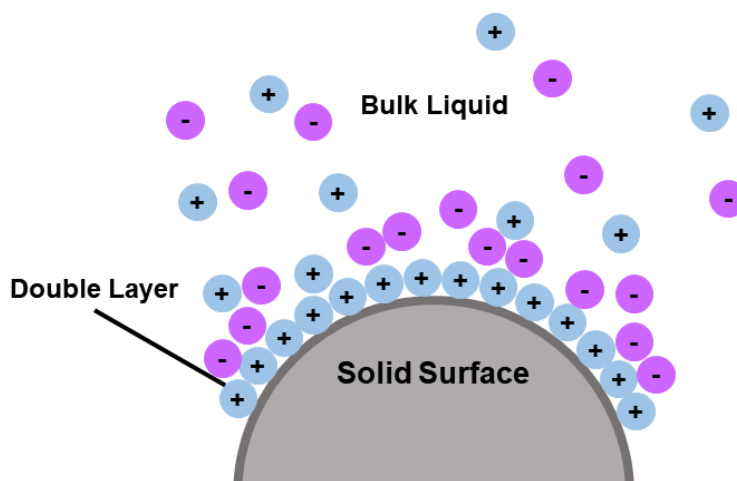
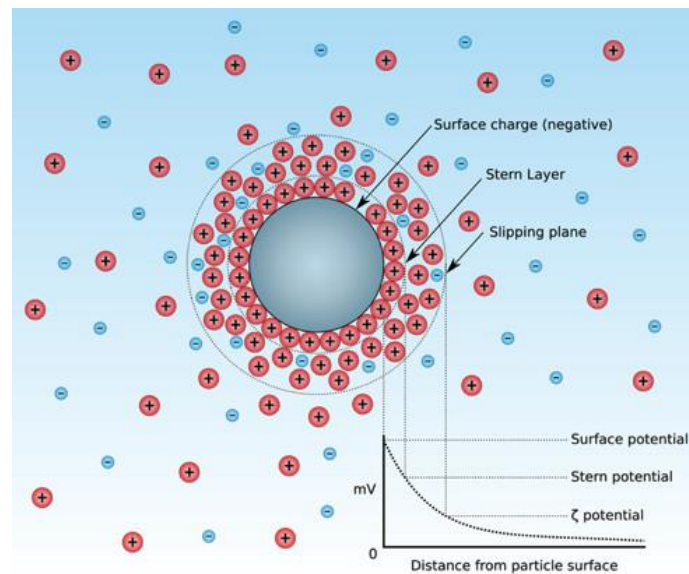


Figure 119 Schematic showing double layer formed around solid particle dispersed in a liquid medium.

The first layer of the double layer consists of ions which are adsorbed onto the solid's surface and this constitutes the surface charge. The second layer is comprised of ions which are attracted to first layer, the surface charge via electrostatic Coulomb forces, electrically screening the first layer. The second layer is loosely attached to the solid, because it is composed of free ions that move due to electric attraction and thermal motion. Therefore, the second layer is also referred to as the diffuse layer. Part of the diffuse layer can move under tangential stress. There exists a slipping plane that separates the mobile fluid from the static fluid around the solid surface. Electrical potential at this slipping plane is the ζ -potential and is typically measured in mV [259].

Table 12 Schematic representation of dispersed particle showing the slipping plane and the potential difference as a function of distance from the charged surface of the dispersed particle. Image lifted from reference [Error! Bookmark not defined.].



Essentially, the ζ -potential is the electric potential difference between the solute that a particle is dispersed in and the stationary layer of fluid around the dispersed particle. The potential difference is caused by the net electrical charge contained within the region of the bounded plane. This is the reason that the ζ -potential is used to measure the magnitude of charge and to characterise the properties of double layers.

The ζ -potential is an indicator for the stability of colloidal dispersions through the degree of electrostatic repulsion between similarly charged particles within the dispersion. The larger the magnitude of the zeta potential, either negative or positive, then the greater these repulsive forces are and the smaller the probability of flocculation, agglomeration or precipitation occurring [260]. In other words, a suspension or dispersion of particles showing a high absolute value of ζ -potential is more stable when compared to those exhibiting lower ζ -potential absolute values [259]. When the ζ -potential values are too low, then the attractive forces between particles exceed the repulsive forces resulting in agglomeration or flocculation. Some guidelines for stability of colloidal dispersions with respect to the ζ -potential are shown in (Table 13).

Table 13 Stability behaviour of the dispersed particles with respect to ζ -potential [261, 262].

Zeta Potential (mV)	Stability behaviour of the particles
0 to ± 5	Rapid Coagulation or Flocculation
± 10 to ± 30	Incipient Instability
± 30 to ± 40	Moderate Stability
± 40 to ± 60	Good Stability
More than ± 61	Excellent Stability

Zeta potential measurements have been widely used to evaluate the stability of various aqueous colloids [263, 264] and to investigate the effects of surfactants on dispersion stability [265, 266]. In regard to graphene-based materials, stability evaluation has been performed through ζ -potential measurements on aqueous colloidal dispersions of single- and multi-wall carbon nanotubes [267, 268, 269], and GO nanosheets [270,271]. The dispersion behaviour and stability of GO and RGO dispersions in aqueous media has also been investigated in the past with the aid of ζ -potential measurements [218, 272, 273]. However, ζ -potential has not yet been employed to evaluate the stability of GO and RGO dispersions in media beyond water. It has been made a point in the present thesis to address this gap in the literature

Efforts to measure the ζ -potential for all the prepared dispersions were made, as to further assess their stability. These measurements, however, were not feasible due to intense agglomeration which inhibited the characterisation process. A z-average size above 5000 nm and/or a PDI above 0.7 indicate the presence of large aggregates, which cannot be measured via this technique. More specifically, GO dispersions in MeOH, EtOH, Act and CF, as well as the RGO one in EA presented very intense aggregation during the measurement. On other hand, the formation of large agglomerates was detected for both GO and RGO dispersions in BuOH, CN, DCM, CCl₄, EG, DET, Hex, Tol, Xyl, DES and THF

8.5. Dynamic Light Scattering measurements

8.5.1. Particle Size Distribution

Dynamic light scattering (DLS), also known as Photon Correlation Spectroscopy, is a method for determining the size of extremely small particles in suspensions, colloids

and dispersions and has been used extensively for determination of graphene, GO and RGO flake size [274, 275, 276].

As a size determination method, DLS is non-destructive and offers advantages such as obtaining reproducible data quickly and easily. This technique involves shining a monochromatic light beam, e.g. a laser onto a liquid sample containing particles in Brownian motion, which is the random motion of particles modelled by the Stokes-Einstein equation [277]. When the light hits the moving particle, it causes a Doppler shift which changes the wavelength of the incoming light in a manner that is related to the size of the particle. This change in wavelength provides information about the size, distribution, shape, and structure of the particles. DLS offers the ability to calculate the particle size distribution by measuring diffusion coefficient (ΔT) of the particle using autocorrelation function [278]. The velocity of a particle under Brownian motion is defined by its translational diffusion coefficient which in turn can be used to measure the hydrodynamic diameter (D_h) of the particles as derived from the Stokes-Einstein equation. The hydrodynamic diameter, also known as the Stokes-Einstein diameter is determined as the diameter of a hypothetical hard sphere which has the same ΔT or viscosity (η) as the particle being examined. The D_h is the hydrodynamic size which may vary from the actual physical size of the particle.

It is important to note that ΔT also changes with the physical size of the examined particle, it's surface structure (i.e. roughness, charges etc.) and with the concentration of ions present in the liquid medium [278]. Any agglomeration phenomena also influence the measurement of particle size. This is most prominent in electrolytic media [279, 280].

Equation 15, which is a form of the Stokes-Einstein equation, is most often used for particle size analysis.

$$D_h = \frac{k_B T}{3\pi\eta D_t} \quad (15)$$

Where k_B is Boltzmann's constant, T is thermodynamic temperature and η is dynamic viscosity.

The measured data in a DLS experiment is the correlation curve. For a dispersion containing of the same, singular size, this curve is a smooth, single exponential decay function. The correlation curve embodies all the information regarding the diffusion of the suspended particles. By fitting the correlation curve to an exponential function, the D can be calculated as it is proportional to the lifetime of the exponential decay. If the

D is determined, so can the D_h be through calculation using a variation of the Stokes-Einstein equation (Equation 15). For a polydisperse sample this curve is a sum of exponential decays [285].

Because this method is based on light scattering, the diffraction indices of every solvent used is needed (Table 14 Table 14).

Table 14 Refractive indices of all solvents used to prepare GO and RGO dispersion. These values are needed to calculate particle size distribution in every dispersion

Solvent	Refractive Index
DH₂O	1.33
MeOH	1.32
EtOH	1.36
IPA	1.37
BuOH	1.39
Act	1.36
CB	1.52
DCB	1.55
CF	1.44
CN	1.6
DCM	1.42
CCl₄	1.46
AcAc	1.44
EG	1.44
EA	1.37
DET	1.35
Hex	1.37
Tol	1.49
Xyl	1.50
DMSO	1.47
DES	1.40
DMF	1.42
THF	1.40
NMP	1.47
GBL	1.44

The DLS size distribution curves that were obtained for GO and RGO are presented below (Figure 120 to Figure 137). The intensity autocorrelation function of the scattered light is fitted to obtain a size. Intensity is fitted using an algorithm that results in the cumulant size or the z-average size. The z-average is a size that is determined according to an ISO method ISO13321:1996/ISO22412:2008. The same ISO method is later used to determine the polydispersity index (PDI). The initial part of the correlation function is force-fitted to a single exponential decay. The decay is directly correlated to the overall z-average size. The particle size distribution offers information on the uniformity of a dispersion. The narrower the peak on the size distribution curve, the more uniform the particle size meaning the dispersion is closer to a monodisperse behaviour.

In the present work, not all samples yielded successful size distribution measurement through DLS. This is because DLS is not an ideal technique for dispersion containing large particles. Dispersions with a large flake size tend to be less stable and aggregate faster, in accordance with Stoke's Law, as a result of the gravitational force. For example, if the z-average of a dispersion was 20 μm and the distribution analysis yielded single broad peak in the 15-25 μm range then this peak would not be shown. Instead only a flat line would appear on the distribution plot. Z-average size above 5000 nm and/or a PDI above 0.7 indicate presence of large aggregates, which cannot be measured accurately by this technique. Conversely, dispersions with flake sizes below 0.5 μm present higher stability, as the Brownian motion has a more pronounced effect on these size ranges [281]. Successful size distribution measurements were obtained for both GO and RGO in 11 of the 25 solvents, for GO only in 2 solvents and for RGO only in 5 solvents. The missing data belongs to samples that contained particles too large to undergo successful DLS measurement (>5 μm).

GO dispersions in MeOH, EtOH, Act and CF, as well as RGO in EA presented very intense aggregation during the measurement. Furthermore, the formation of large agglomerates was detected for both GO and RGO dispersions in BuOH, CN, DCM, CCl₄, EG, DET, Hex, Tol, Xyl, DES and THF. In this context, GO presented good dispersion characteristics in DMF (Z-Ave size 50.92 nm, PDI 0.213), NMP (Z-Ave size 385.4 nm, PDI 0.281) and in DH₂O (Z-Ave size 309.1 nm, PDI 0.395), which were also the solvents with the highest density. In the solvents with the lowest density (tending to zero), low quality dispersions were observed (CCl₄, Hexane). Conversely, RGO exhibited better dispersion characteristics in polar solvents (EtOH, MeOH, DMF),

where it had moderate density, while in the solvents with the highest density (DCB, AcAc) larger sizes but with low PDI were observed.

The particle size in liquid suspension was measured at 25 °C using Zeta sizer Nano ZS (Malvern Instruments) model. A 633 nm, He–Ne laser was used as the light source while an avalanche photodiode (APD) served as the detector. Particle size was measured using dynamic light scattering method where the scattered light was collected at 173° DLS measuring the hydrodynamic diameter (dH) of a particle, which is the diameter of a hypothetical perfect sphere diffusing at the same speed as the particle under observation.

Table 15 Size distribution and polydispersibility indices of GO and RGO flakes in each solvent given in nm.

Solvent	Size distribution of GO (nm)	Size distribution of RGO (nm)
DH₂O	309.1	333.6
MeOH	6720.1	377.6
EtOH	2513.2	245.1
IPA	3521	195.2
BuOH	5763.4	3964
Act	17,601	136.0
CB	248.9	4809
DCB	3923	2358
CF	4192	1428
CN	20964	13784
DCM	28584	8806
CCl₄	1132	2752
AcAc	1200	637.5
EG	20134	8184
EA	986.3	1372
DET	1986	5275
Hex	1291	0.028
Tol	1183	2000
Xyl	4865	2856
DMSO	3362	263.7
DES	-	-
DMF	50.92	48.51
THF	6781	10891
NMP	385.4	451.7
GBL	184.4	2201

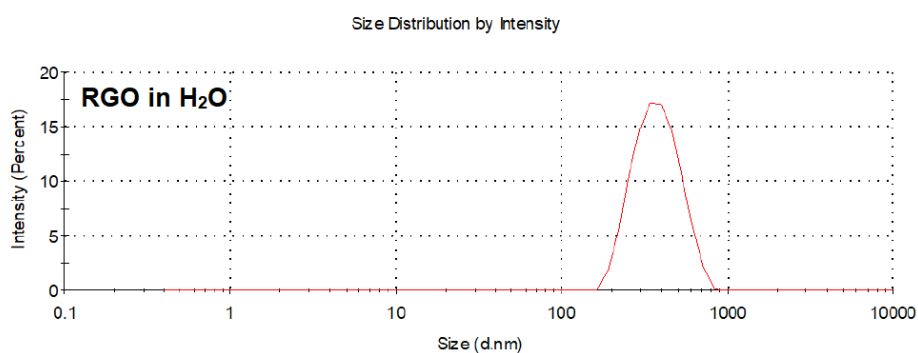
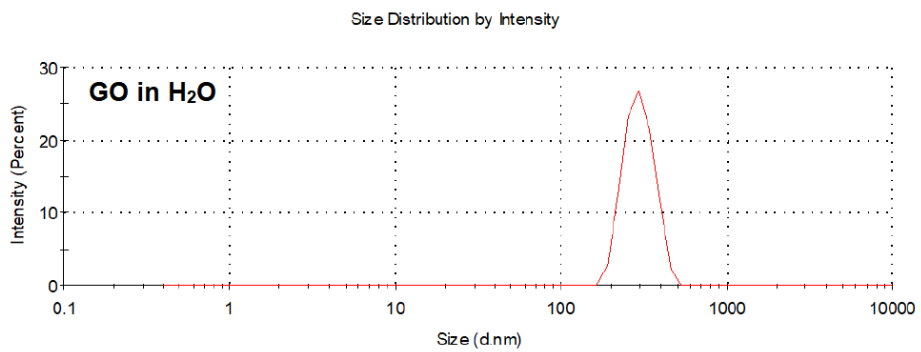


Figure 120 Dynamic light scattering (DLS) size distribution curve of GO and RGO in deionised water.

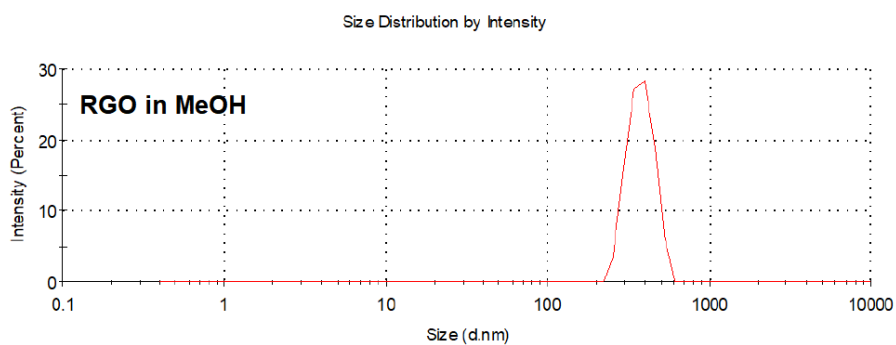


Figure 121 Dynamic light scattering (DLS) size distribution curve of RGO in methanol.

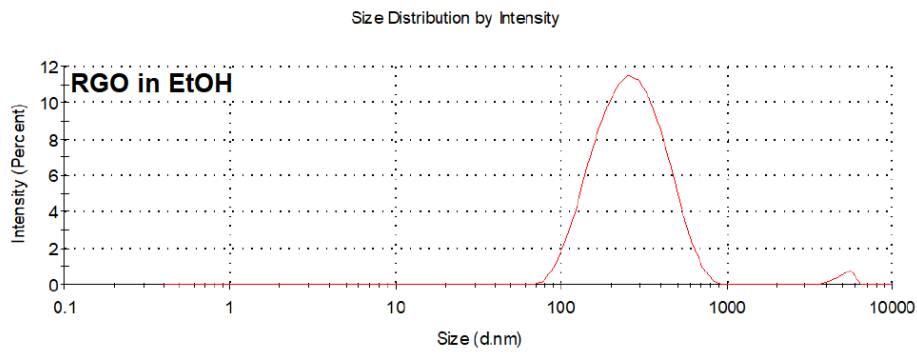


Figure 122 Dynamic light scattering (DLS) size distribution curve of RGO in ethanol.

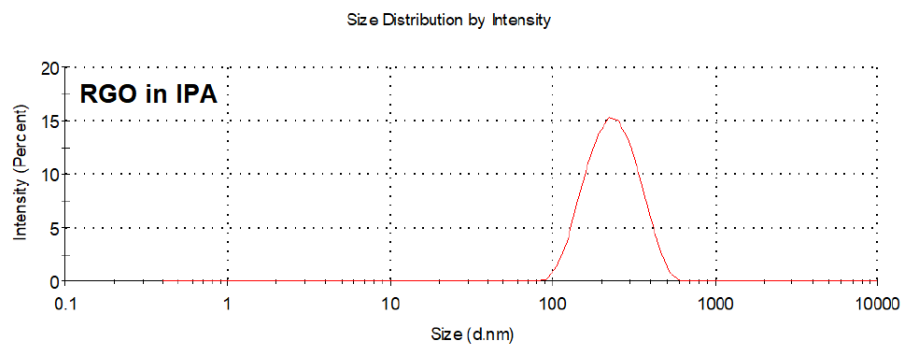
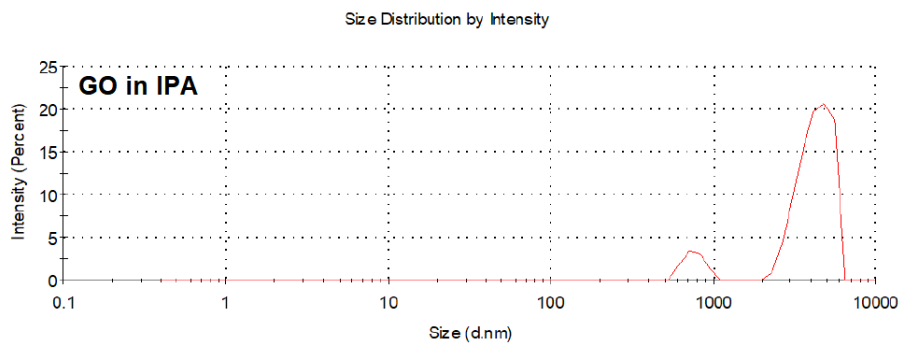


Figure 123 Dynamic light scattering (DLS) size distribution curve of GO and RGO in isopropyl alcohol.

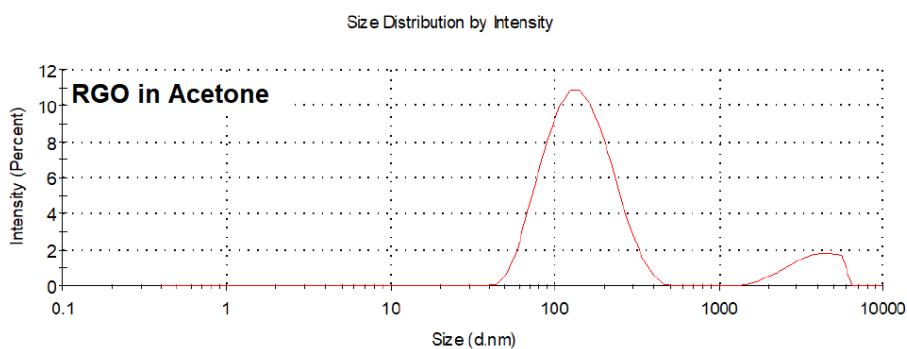


Figure 124 Dynamic light scattering (DLS) size distribution curve of RGO in acetone.

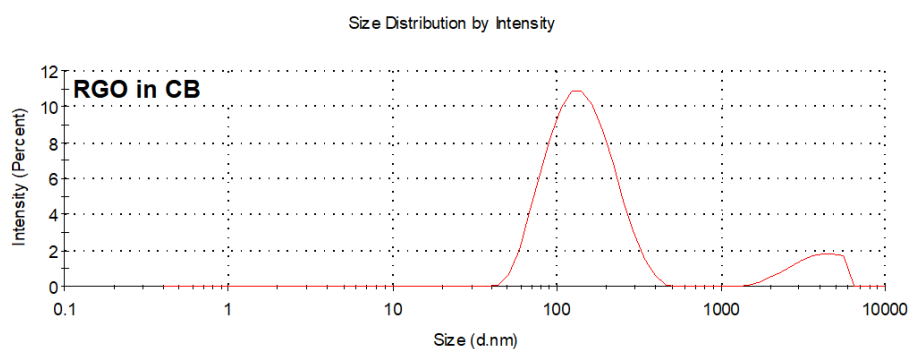


Figure 125 Dynamic light scattering (DLS) size distribution curve of RGO in chlorobenzene.

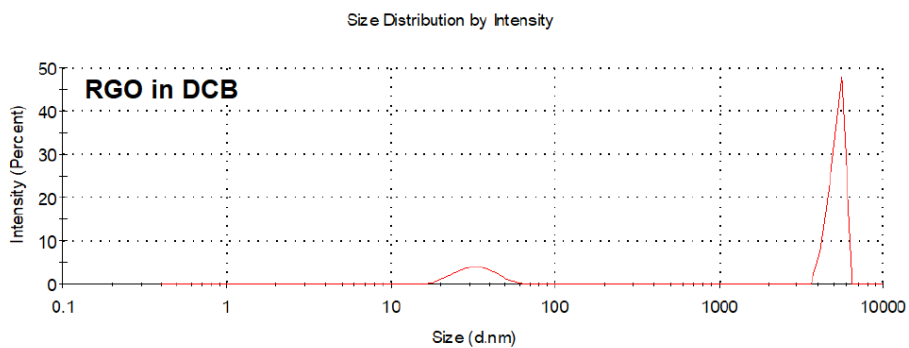


Figure 126 Dynamic light scattering (DLS) size distribution curve of RGO in o-dichlorobenzene.

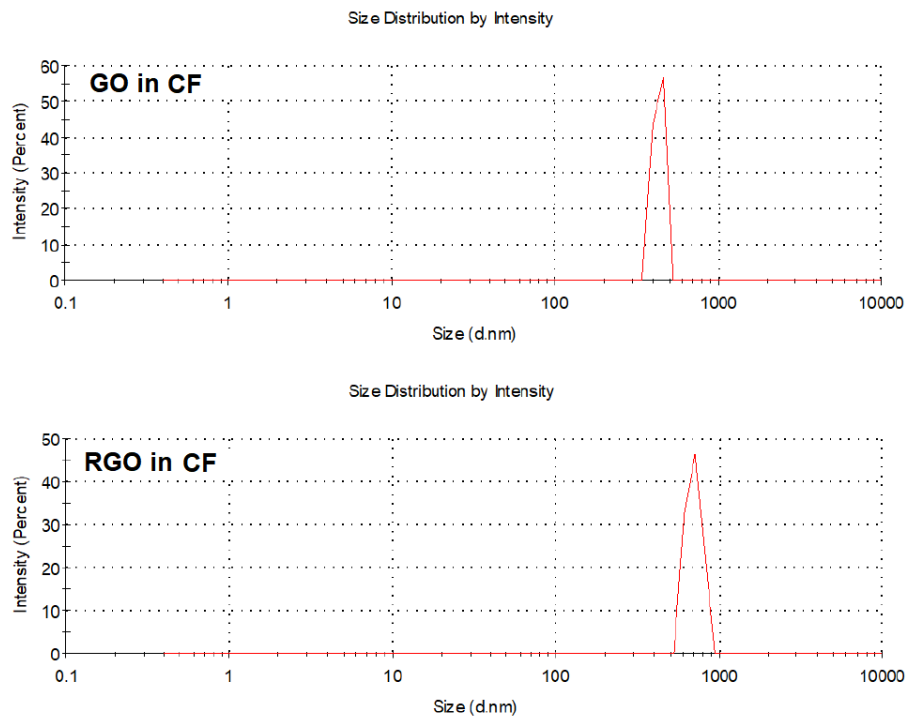


Figure 127 Dynamic light scattering (DLS) size distribution curve of GO and RGO in chloroform.

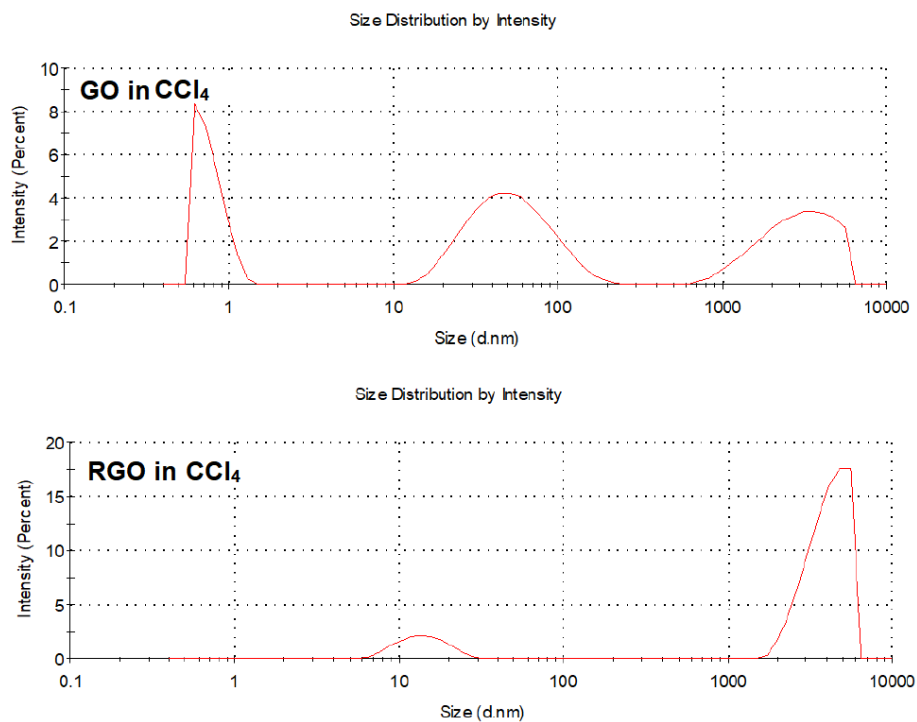


Figure 128 Dynamic light scattering (DLS) size distribution curve of GO and RGO in carbon tetrachloride.

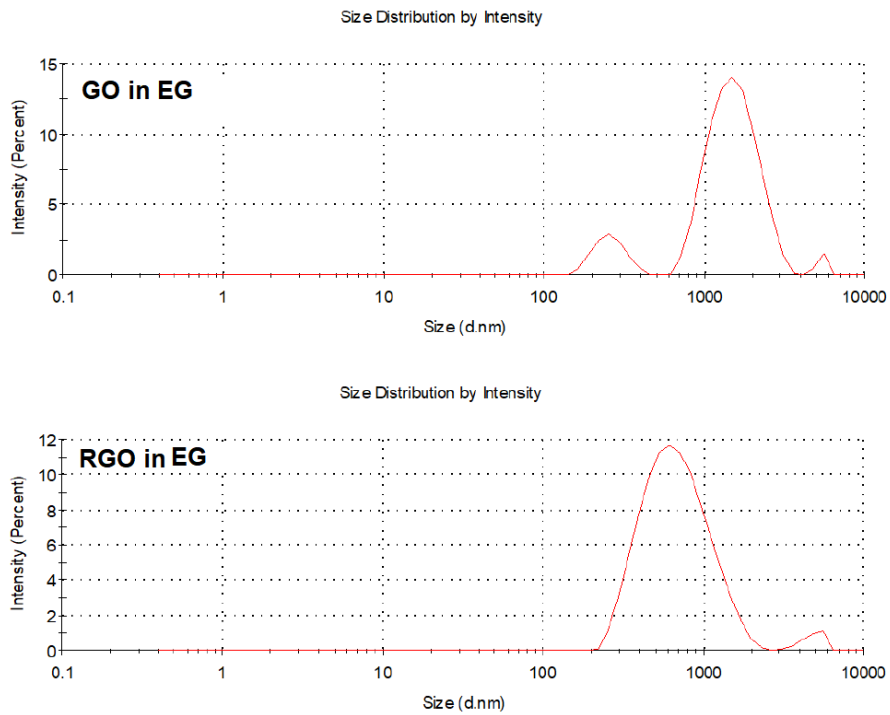


Figure 129 Dynamic light scattering (DLS) size distribution curve of GO and RGO in ethylene glycol.

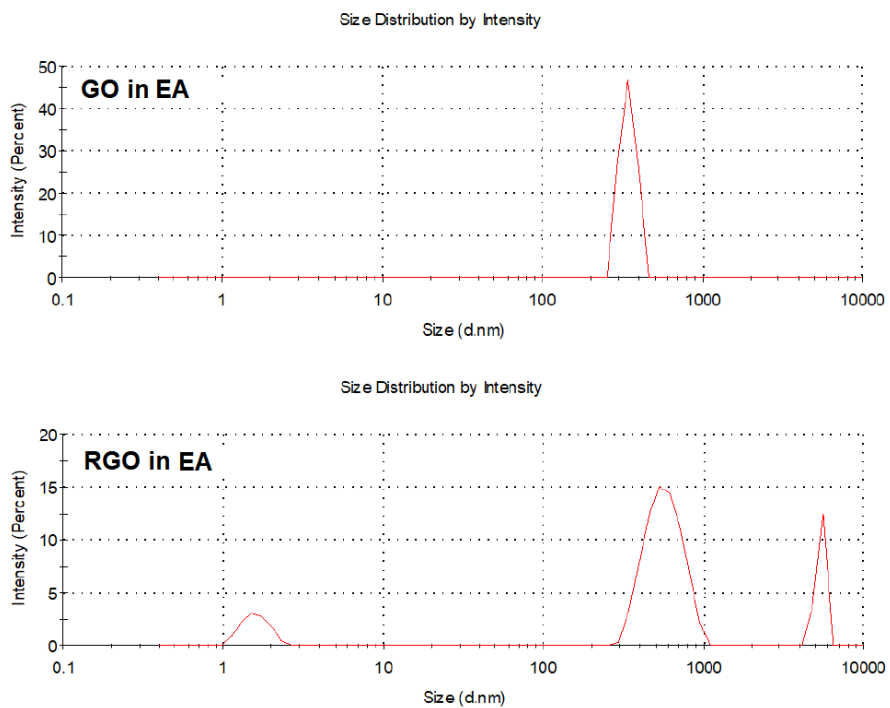


Figure 130 Dynamic light scattering (DLS) size distribution curve of GO and RGO in ethylacetate.

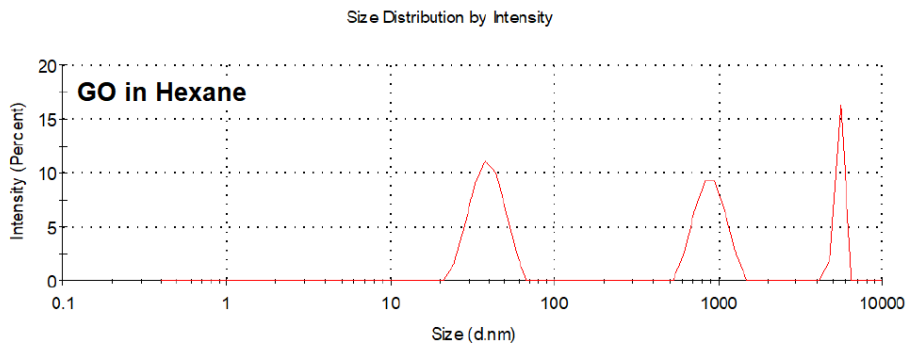


Figure 131 Dynamic light scattering (DLS) size distribution curve of GO in hexane.

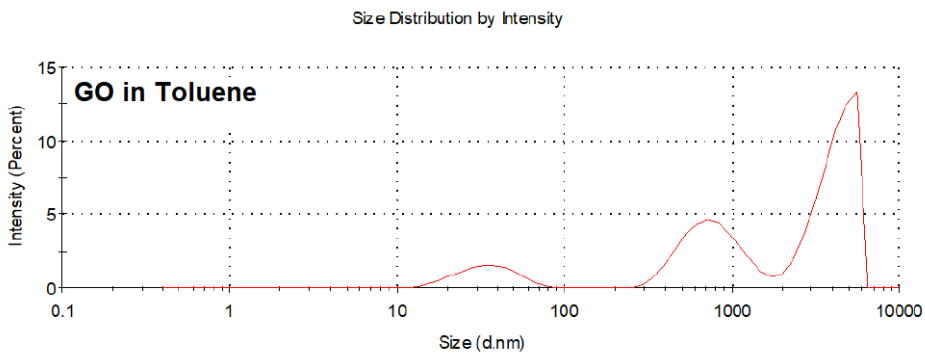


Figure 132 Dynamic light scattering (DLS) size distribution curve of GO in toluene.

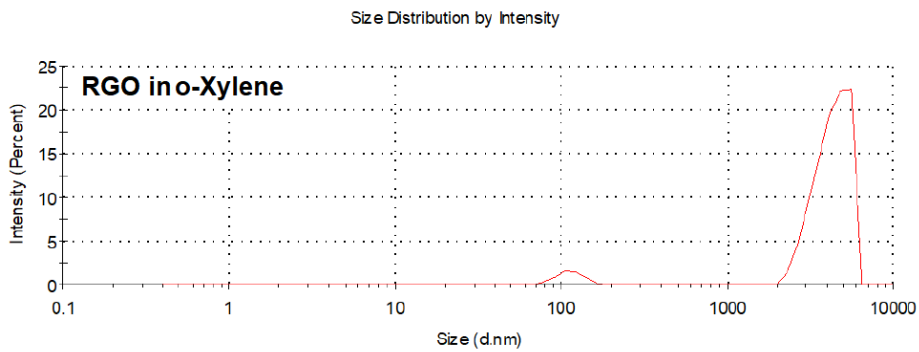


Figure 133 Dynamic light scattering (DLS) size distribution curve of RGO in o-Xylene.

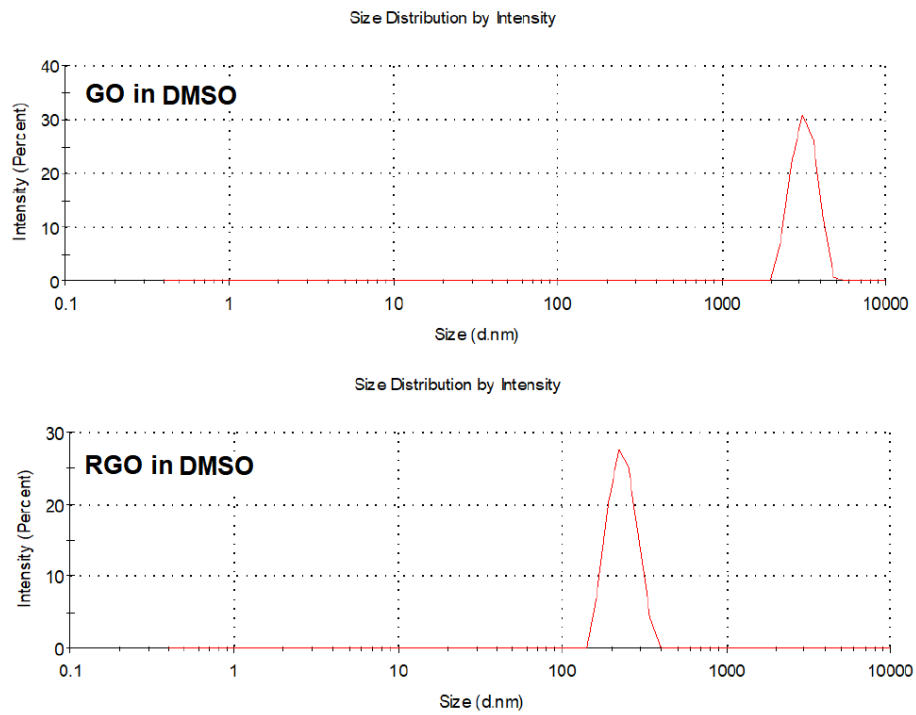


Figure 134 Dynamic light scattering (DLS) size distribution curve of GO and RGO in dimethyl sulfoxide.

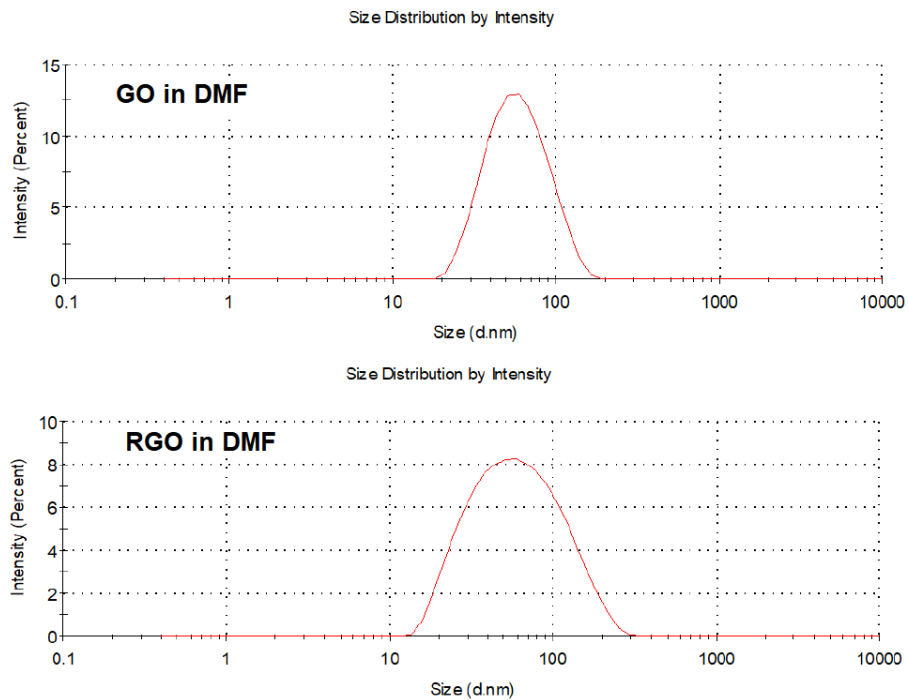


Figure 135 Dynamic light scattering (DLS) size distribution curve of GO and RGO in dimethylformamide.

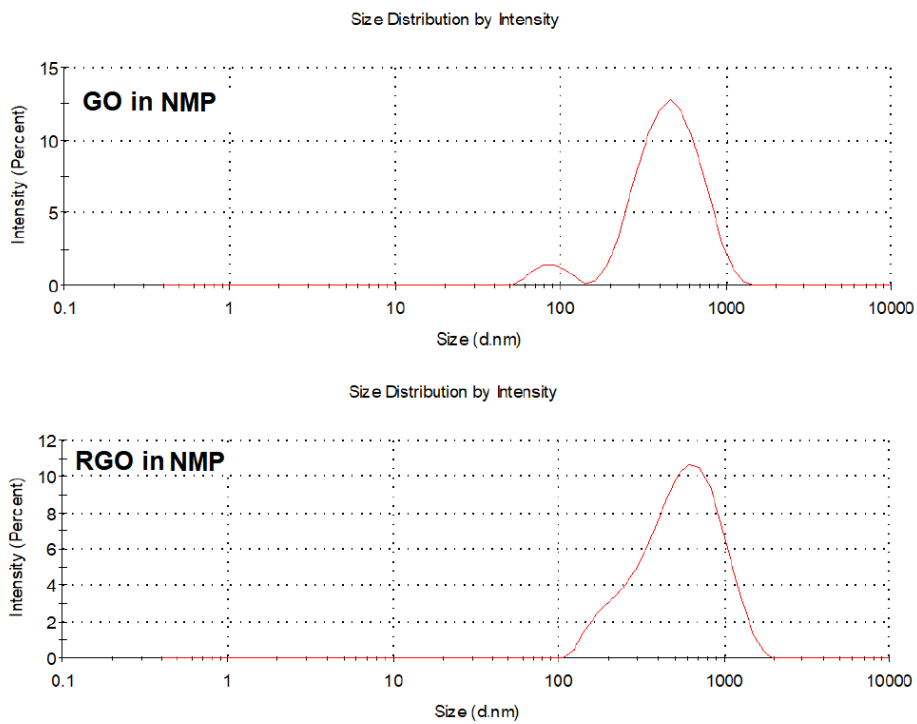


Figure 136 Dynamic light scattering (DLS) size distribution curve of GO and RGO in N-methyl-2-pyrrolidone.

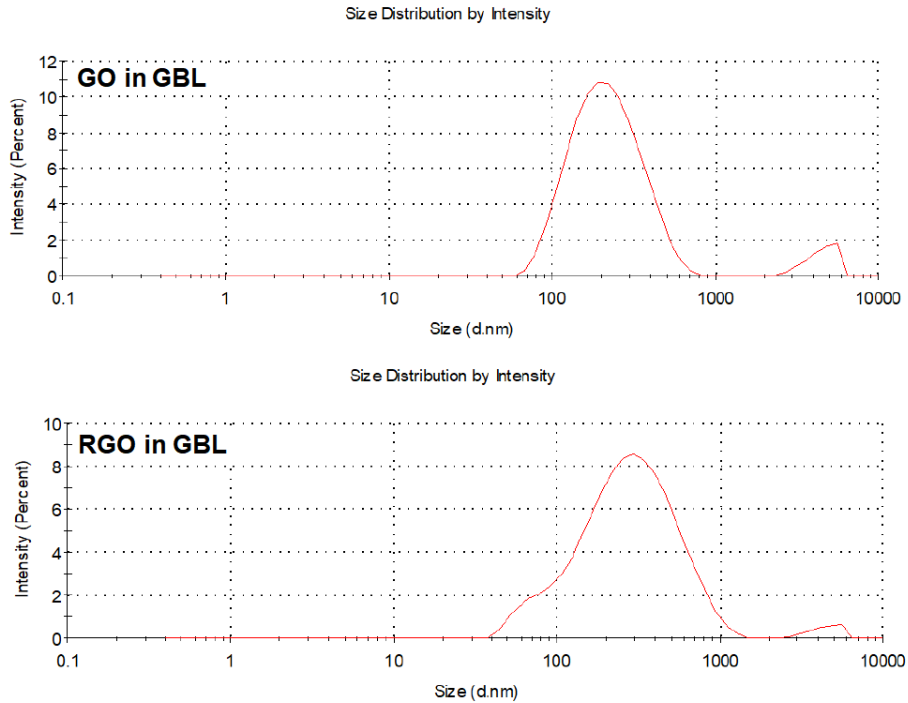


Figure 137 Dynamic light scattering (DLS) size distribution curve of GO and RGO in γ -Butyrolactone.

8.5.2. Polydispersity Index

DLS also provides the polydispersity index (PDI) of a suspended particle, which is also an indicator of a dispersion's stability. Samples with a high PDI are more likely to increase in size and agglomerate due to the Ostwald ripening process, a thermodynamically spontaneous phenomenon in which smaller particles dissolve and adsorb to larger particles causing agglomeration [282].

The PDI indicates the width of the particle size distribution which is calculated as $(\text{peak width/peak height})^2$. The PDI is a number calculated from a simple 2 parameter fit to the correlation data (the cumulants analysis) The calculations for these parameters are defined in the ISO standard document 13321:1996E and ISO 22412:2008 [283, 284]. PDI is dimensionless and its values range from 0 to 1, where zero is monodisperse and 1 is highly polydisperse. The closer the PDI is to 1, the broader the size distribution curve of the dispersed particles. A value of $\text{PDI} < 0.1$ indicates that the sample is monodisperse. Values smaller than 0.05 are rarely seen other than with highly monodisperse standards. A PDI value of $0.1 < \text{PDI} < 0.2$ indicates that the sample has a narrow size distribution peak, whereas $0.2 < \text{PDI} < 0.5$ suggests a wide particle size distribution. Values > 0.5 indicate that the sample has a very broad size distribution (highly polydisperse) and values > 0.7 correspond to a highly polydisperse system [274, 285, 286]. According to a report published by S. Bengtson et al., even PDI values between ~ 0.30 and ~ 0.35 for a GO or RGO dispersions is considered to be a sign of a fairly monodisperse system [287].

The measured size distributions and PDI values of GO and RGO particles in each solvent are presented in Table 16 given in nm and by descending value and colour coded to better decipher which dispersions are closer to a monodisperse or a polydisperse behaviour. DLS measurement were not possible for GO and RGO in DES due to agglomeration. Therefore, there are no size distribution results or PDI values for these samples.

- Monodisperse: Only RGO showed a highly monodisperse behaviour in hexane, even though the RGO dispersion prepared in this solvent has an extremely low concentration. Interestingly, hexane has the smallest relative polarity value, polarity index and dipole moment making it the least polar solvent used in this work. No dispersions of GO demonstrate highly monodisperse behaviour, however it yielded fairly monodisperse behaviour in many of the solvents, namely in DMF, EG, NMP, IPA, AcAc, DCB, GBL,

DH₂O, CB, EA, MeOH, Act, Xyl and BuOH with PDI values ranging from 0.213 to 0.490 in that order. Similarly, RGO exhibited fairly monodisperse behaviour in MeOH, DH₂O, IPA, AcAc, NMP, EtOH, DMSO, DMF, DCB, GBL and Acetone with PDIs from 0.127 to 0.356 in that order.

- *Polydisperse*: Fairly polydisperse behaviour with PDI values ranging from 0.526 to 0.669 were observed in DCM, Diethylether and CN for GO and CF, EG and EA for RGO. GO in EtOH, DMSO, Toluene and CF exhibited highly polydisperse behaviour with PDI values from 0.746 to 0.926 and polydisperse behaviour in CCl₄, Hexane and THF with PDI=1. Similarly, RGO yielded highly polydisperse dispersions in Xyl, CCl₄, DET and THF showing PDIs ranging from 0.719 to 0.964 and polydisperse behaviour in BuOH, CB, CN and DCM.

When attempting to compare the PDI values with the calculated dispersibilities, it can generally be said that the highest concentration dispersions also show fairly monodisperse behaviour. Conversely, the solvents which fail to adequately disperse GO and/or RGO also tend to show high PDI values, in many cases PDI=1, meaning GO and/or RGO exhibit highly polydisperse behaviours in these solvents.

After comparing the PDI values with the polar character of each solvent, namely relative polarity, polarity index and dipole moment a few key observations were made. Firstly, the lowest PDI for RGO (0.037 mg/ml) was measured in the most apolar solvent, hexane, with a relative polarity of 0.009, a polarity index of 0.1 and a dipole moment of 0.085. The three smallest PDI values for GO were observed in DMF, EG and NMP. These solvents have a polar index of 6.9, 6.7 and 6.4 respectively. Conversely, solvents with small polarity indices tend to have high PDI values, with the exception of DCB which has a polarity index of 2.7 yet has low PDI values for both GO and RGO. GO showed a PDI of 1 in hexane and CCl₄ which have the smallest relative polarity values at 0.009 and 0.0052 respectively. DES has the largest dipole moment, and both GO and RGO formed agglomerations in this solvent which inhibited DLS measurements.

Table 16 PDI values of GO and RGO in all solvents given in descending order. The different colours indicate the level of polydispersity.

Solvent	PDI (GO)		Solvent	PDI (RGO)	
DMF	0.213	Monodisperse	Hex	0.037	Highly Monodisperse
EG	0.234	Monodisperse	MeOH	0.127	Monodisperse
NMP	0.281	Monodisperse	H ₂ O	0.135	Monodisperse
IPA	0.295	Monodisperse	IPA	0.197	Monodisperse
AcAc	0.360	Monodisperse	AcAc	0.209	Monodisperse
DCB	0.387	Monodisperse	NMP	0.211	Monodisperse
GBL	0.391	Monodisperse	EtOH	0.215	Monodisperse
H ₂ O	0.395	Monodisperse	DMSO	0.249	Monodisperse
CB	0.428	Monodisperse	DMF	0.285	Monodisperse
EA	0.428	Monodisperse	DCB	0.306	Monodisperse
MeOH	0.433	Monodisperse	GBL	0.349	Monodisperse
Act	0.447	Monodisperse	Act	0.356	Monodisperse
Xyl	0.456	Monodisperse	CF	0.576	Polydisperse
BuOH	0.490	Monodisperse	EG	0.576	Polydisperse
DCM	0.526	Polydisperse	EA	0.669	Polydisperse
DET	0.537	Polydisperse	Xyl	0.719	Highly Polydisperse
CN	0.603	Polydisperse	CCl ₄	0.765	Highly Polydisperse
EtOH	0.746	Highly Polydisperse	DET	0.899	Highly Polydisperse
DMSO	0.757	Highly Polydisperse	THF	0.964	Highly Polydisperse
Tol	0.858	Highly Polydisperse	BuOH	1	Highly Polydisperse
CF	0.926	Highly Polydisperse	CB	1	Highly Polydisperse
CCl ₄	1	Highly Polydisperse	CN	1	Highly Polydisperse
Hex	1	Highly Polydisperse	DCM	1	Highly Polydisperse
THF	1	Highly Polydisperse	Tol	1	Highly Polydisperse
DES	N/A	N/A	DES	N/A	N/A

8.6. Scanning electron microscopy (SEM):

The morphology and structure of GO and RGO flakes was investigated via SEM imaging. The samples chosen for this purpose were GO and RGO in their most and least favourable solvents.

The scanning electron microscope (SEM) is one of the most widely utilised instruments for imaging of the micromorphology and examination of the chemical composition characterizations. The unaided eye can discriminate objects with a resolution of ~ 0.1 mm (at the optimum viewing distance of 25 cm) and optical microscopy has the limit of resolution of $\sim 2,000$ Å by enlarging the visual angle through optical lens. Electron microscopy has been developed by replacing the light source with a high-energy electron beam [288].

The scanning electron microscope (SEM) uses a focused beam of high-energy electrons to generate a variety of signals at the surface of solid samples. Image formation in the SEM is dependent on the acquisition of signals produced from the elastic and anelastic interactions between the electron beam and the examined specimen. The signals that derive from electron-sample interactions reveal information about the sample including external topography and morphology, chemical structure, crystallography and orientation of materials making up the sample. The most widely used signal is the secondary electron emission signal. When the primary electron beam strikes the sample surface causing the ionisation of the atoms, loosely bound electrons may be emitted. These electrons, referred to as secondary electrons, have low energy ($\sim 3\text{--}5$ eV) can only escape within a few nanometres of the material's surface. Therefore, secondary electrons accurately mark the position of the beam and give high resolution images. Secondary electrons are used primarily for topographic contrast, namely for the visualization of surface texture and roughness.

Some SEM images of graphite, graphite oxide, reduced graphite oxide, graphene GO and RGO are featured in Figure 138, Figure 139 and Figure 140.

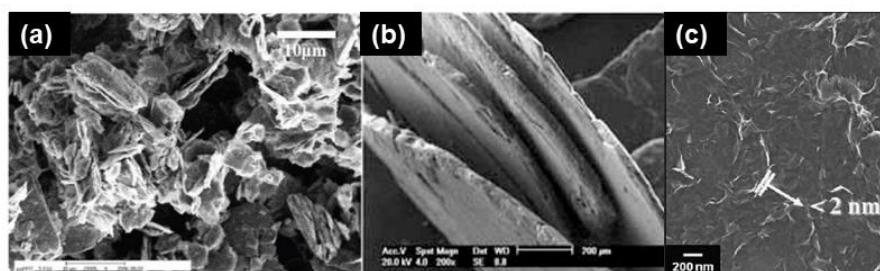


Figure 138 SEM images of (a) graphite powder with a diameter of $\sim 10 \mu\text{m}$ [289], (b) natural graphite flake [290] and (c) folded graphene sheets with a thickness of 2 nm [291].

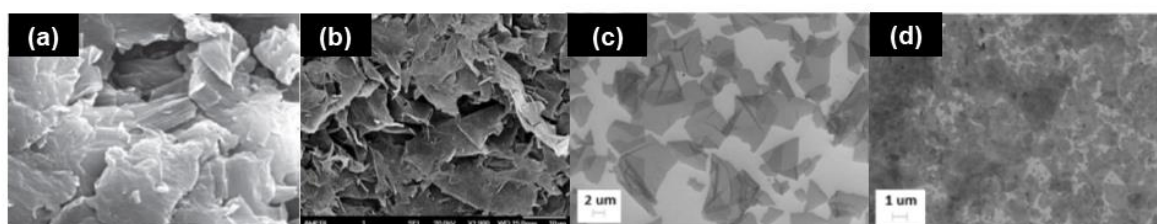


Figure 139 SEM images of (a) graphite oxide prepared with $\text{KClO}_3/\text{NaNO}_3/\text{H}_2\text{SO}_4$ [292], (b) single layer GO flakes [293], (c) large flake GO [294] and (d) small flake GO prepared using $\text{H}_2\text{SO}_4/\text{H}_3\text{PO}_4/\text{KMnO}_4$ [7].

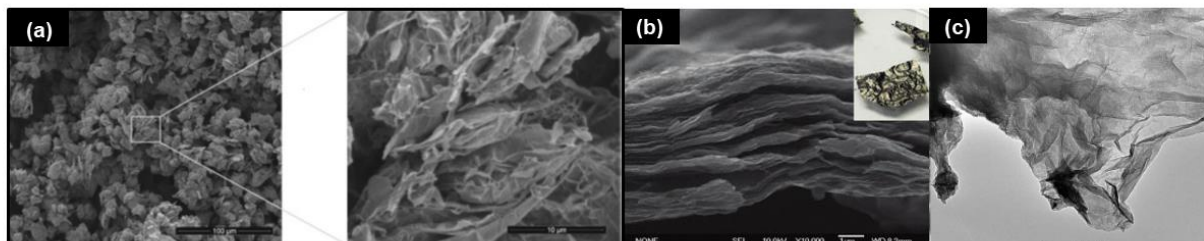


Figure 140 SEM image of (a) reduced graphite oxide prepared by annealing graphite oxide at 900°C for 5 minutes [295], (b) a cross-section of air-dried RGO film prepared solvo-thermally [296] and (c) a single layer sheet of RGO prepared by thermally reducing GO at 50°C 5 hours [297].

8.6.1. Sample Preparation:

The highest and lowest concentration dispersion of GO and RGO were selected for SEM characterisation. The goal is to view the GO and RGO flakes from each dispersion. Specifically GO in DH_2O (highest), GO in (BuOH) (lowest), RGO in DCB (highest) and RGO in (DCM) (lowest). For this, the GO and RGO samples must be in the solid phase. The samples were prepared via drop casting

on silicon (Si) substrates which were first thoroughly cleaned using the three-step cleaning method to remove any impurities. The three-step cleaning method is as follows:

First step: The substrates are first submerged in soapy deionised water inside a small beaker. The beaker is then placed in an ultrasonic bath at room temperature for 10 minutes. The substrates are then thoroughly rinsed with deionised water as to remove all traces of soap.

Second step: The substrates are then submerged in acetone in a different beaker. The beaker is again placed in an ultrasonic bath at room temperature for 10 minutes.

Third step: The substrates are removed from the acetone and the same process is repeated with isopropanol. Finally, the substrates are transferred to a clean Petri dish, covered with the lid to avoid dust particles and placed in an oven to dry.

Once the Si substrates are clean, each dispersion is deposited via drop casting in order to create a solid state GO or RGO sample once the solvent has evaporated. For this, the Si substrates are placed on a hotplate at about 65°C. Once they have reached this temperature, 10 µl of each dispersion were drop casted onto their assigned Si substrate. The samples were left on the hotplate for a few minutes to allow the solvents to dry. The result should be a solid film consisting of GO or RGO flakes. Once deposited, the highest concentration (GO in DH₂O) being visible to the naked eye.

8.6.2. SEM Images:

The following images are SEM results for GO and RGO in the highest concentration dispersions (DH₂O and DCB respectively) and the lowest concentration dispersion (RGO in DCM, as GO in CCl₄ yielded too low a concentration for successful SEM imaging).

The SEM images in Figure 141 show a large, uniform layer of GO from GO in H₂O, which forms wrinkles. These wrinkles are more evident when doubling the

magnitude from x5000 (Figure 141 a) to x10000 (Figure 141 Figure 141b). Figure 142 shows SEM images displaying RGO flakes from RGO in DCB with flake sizes ranging from about 100nm to just below 1 μ m, judging from the scale bars provided. Lastly, RGO in DCM yielded in tact flakes with a size of up to about 1.4 μ m (Figure 143 Figure 143). In this case, the RGO flakes appear to form clusters (Figure 143 a). When amplifying the magnitude from x20000 to x30000 (Figure 143 b) and then x50000 Figure 143 c), we can see that the RGO flakes form wrinkles in some areas.

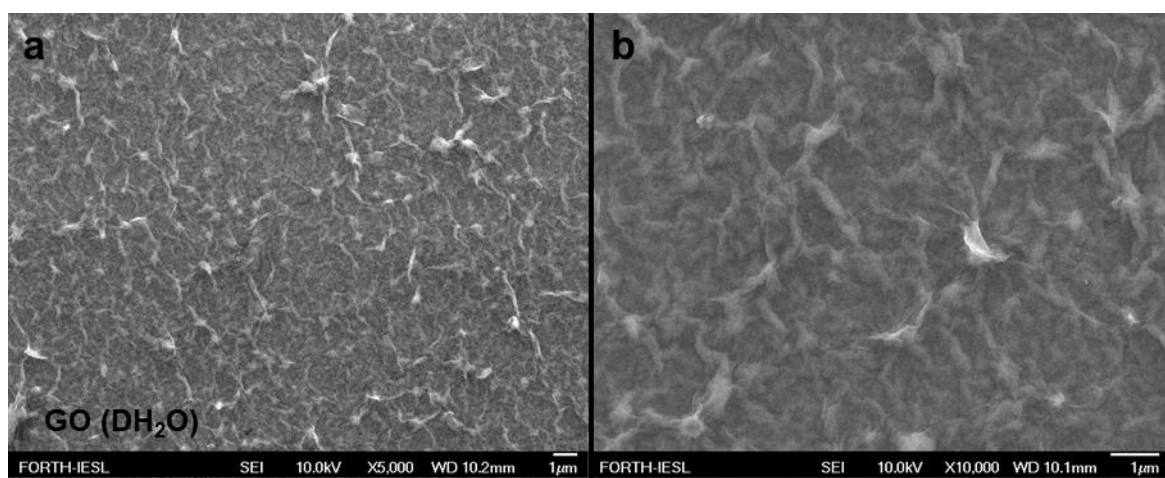


Figure 141 SEM images of GO flakes in DH₂O, the GO dispersion with the highest measured concentration.

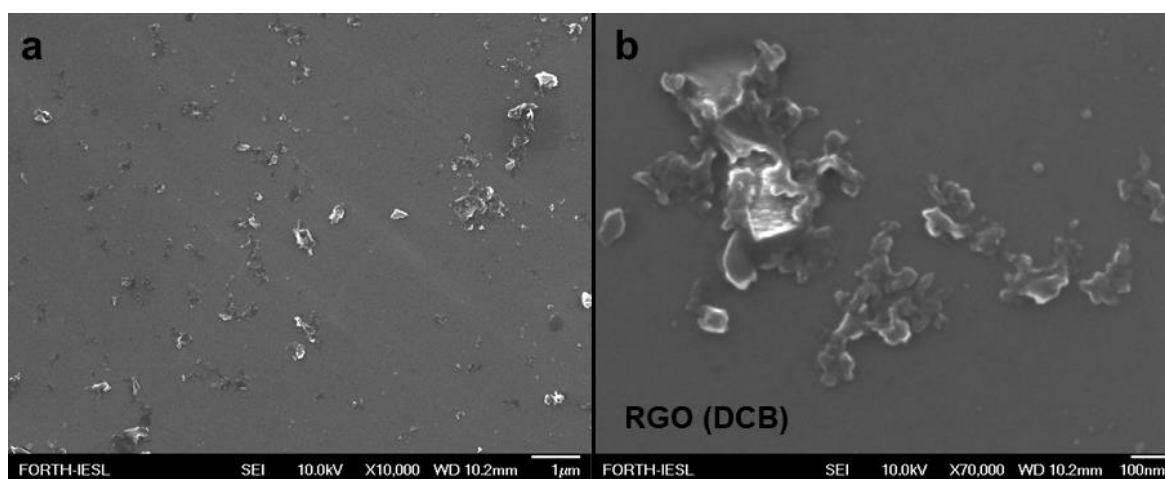


Figure 142 SEM images of RGO flakes in DCB the RGO dispersion with the highest measured concentration.

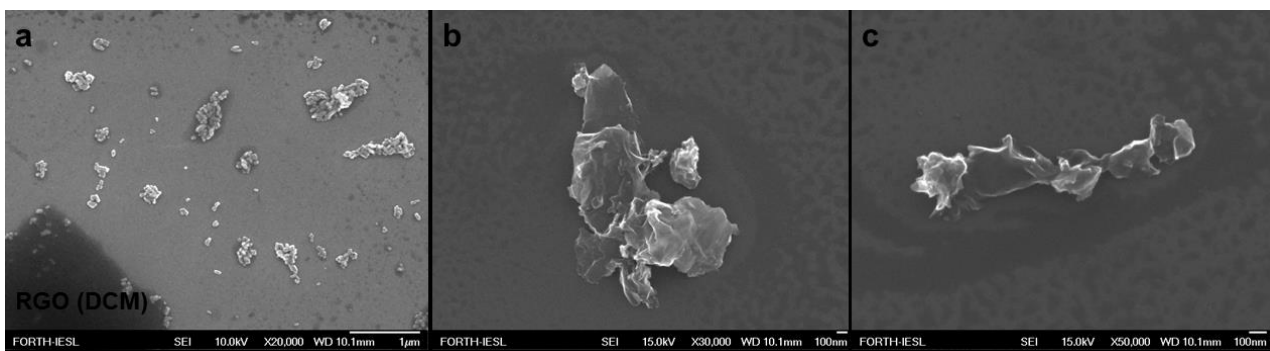


Figure 143 SEM images of RGO flakes in DCM, the RGO dispersion with the lowest measured concentration.

Chapter 9: Conclusions

Taking inspiration from previous literature which investigates the dispersion behaviour of GO and RGO, this thesis serves to further examine the interaction of these two graphene-based materials in various solvents.

By implementing a modified Hummer's method for GO preparation, HI/AcOH assisted chemical reduction for RGO preparation and the increased shear force of an ultrasonic probe for their liquid exfoliation, high concentrations of GO and RGO dispersions were achieved. More specifically, GO prepared by modified Hummers' method yielded stable dispersions in DH₂O, EG, NMP, GBL and DMF with the highest concentration being 0.189 mg/ml in DH₂O. RGO prepared from GO via reduction with HI and AcOH resulted in stable dispersions in DCB and AcAc with concentrations of 87.46 µg/ml and 33 µg/ml respectively. The dispersion behaviour of GO changes significantly after the reduction process in terms of which solvent the material "prefers" and the final concentration. This is evident when observing that dispersibility in DH₂O is decreases from 189 µg/ml to 5.8 µg/ml when GO is reduced. Conversely, dispersibility in DCB increases from 9.9 µg/ml to 87 µg/ml with HI/AcOH reduction. Another example of altered dispersibility is that although GO yields a low concentration yet stable dispersion in DMSO (5.9 µg/ml), RGO is completely indispersible in this solvent.

Despite their different "preferences" for solvents, GO and RGO found common ground as they were both virtually indispersible in BuOH, o-Xylene, CCl₄ and DES. The calculation of the HSP further verifies that the dispersion behaviour of GO is altered through the reduction process. The HSP calculated for GO and RGO in this work coincide with previous reports. No concrete correlation between the polar nature of a solvent and the ability to successfully disperse GO and/or RGO was established.

The measured particle size distribution and the calculated polydispersibility indices expanded the study of GO and RGO's dispersion behaviours. A small size distribution and PDI are indicators of a homogenous dispersion. The smallest PDI was calculated in DMF (0.213) for GO, which is fairly close to a monodisperse

behaviour. The smallest PDI for RGO was calculated in hexane (0.037), indicating that, although RGO has very low dispersibility in hexane, the result is a highly monodisperse dispersion. In terms of polydispersity GO yields fairly monodisperse samples in most of the solvents (PDI<0.5). Generally, RGO exhibited polydisperse behaviours in more solvents than GO, since most PDIs for RGO were >0.5.

Hansen's theory was implemented in hopes of interpreting the affinity of GO and RGO to certain solvents, or lack thereof. The calculated HSP were $\delta D = 16.50$, $\delta P = 13.50$, $\delta H = 26.60$, $\delta T = 34.10$) for GO and ($\delta D = 17.60$, $\delta P = 9.17$, $\delta H = 9.05$, $\delta T = 21.90$) for RGO in $\text{MPa}^{1/2}$. The calculated HSP for RGO are close to previous reported HSP for graphene ($\delta D \sim 18 \text{ MPa}^{1/2}$, $\delta P \sim 9.3 \text{ MPa}^{1/2}$, $\delta H \sim 7.7 \text{ MPa}^{1/2}$ and $\delta T \sim 23 \text{ MPa}^{1/2}$), showing a high degree of graphitisation and dispersion behaviour similar to that of graphene [33]. It appears that the HI/AcOH prepared RGO is structurally closer to graphene, explaining why it has a low affinity to aqueous media, which is evident when considering it yields a concentration in DH_2O about 32 times lower than GO.

Although Hansen's theory has been proven time and time again to be a valuable tool in dispersion investigation and interpretation, it is pivotal to note that the determination of HSP through experiments of this nature are of a semi-empirical approach. The categorization of solvents as "good" or "bad" depends considerably on the subjectivity of the observer. This means that the calculated HSP for GO and RGO may deviate from the actual values. Furthermore, dispersions, as colloidal systems, are by nature thermodynamically unstable due to surface effects [298]. The suspended solids aggregate because of the inherent tendency to decrease the large specific surface area and the excess surface energy causing agglomeration [299]. HSP theory is by default based on thermodynamic equilibrium since they are derived from the cohesive energy density of the system. It is, therefore, to be considered that Hansen's theory may exhibit deviations when being applied to colloidal systems such as dispersions. For molecules that dissolve in solvents, Hansen's theory proposes and has proven experimentally that the rule "like dissolves like" applies. The closer the HSP of the molecule are to the HSP of the solvent, the more likely that the molecule will be dissolved in that solvent. However, this rule of "like dissolves like" may not apply fully to other materials such as nanoparticles or graphene derivatives. This especially applies

to RGO due to its structure. The reduction process of GO results in defects in the graphitic lattice, namely holes, which result in a structure that lacks uniformity. We speculate that in some cases, such as RGO in GBL, solvent molecules may adsorb to these defects thus aiding in suspending the RGO flakes and resulting in a successful dispersion (15.12 mg/mL), even though the calculated δT for RGO (21.9 MPa^{1/2}) differs from the δT of the solvent (47.89 MPa^{1/2}). We speculate that these reasons, along with the different preferred synthesis methods for GO and RGO, are responsible for deviations when comparing our calculated HSP to those of our previous work.

It is clear that the study of surfactant-free GO and RGO dispersibility behaviours in different solvents may aid in expanding the range of applications of these materials in various fields. Although studies of the dispersibility of GO have been accomplished in aqueous and organic media, including solvent mixtures, similar investigation for RGO is limited in comparison and should be expanded upon in the future for further insight. Considering the unique properties and the wide range of application that these materials have, it is apparent that more extensive investigation is needed on their dispersibility in order to fully unleash their potential as advanced nanomaterials.

Chapter 10: Future work

As demonstrated throughout this thesis, there exist some reports on the dispersion behaviour of graphene and its derivatives, such as carbon nanotubes, GO and RGO. These studies aim to identify the most suitable solvents and methods with which to successfully to prepare ample dispersions of the aforementioned graphene-based materials. However, these investigations must be extended and improved upon before these materials are optimally dispersed in the most suitable solvents, rendering them sufficiently processable in the liquid phase and, by extent, broadening their area of application. During the realization of this thesis, a number of suggestions for future improvement of this work were recognised.

Firstly, when studying the dispersions of GO and RGO in any solvent, it is important to acknowledge that GO and RGO samples differ in terms of structure and oxygen content depending on the preferred preparation method, resulting in different dispersion behaviours. Different oxidation and reduction methods yield different GO and RGO samples, respectively. The resulting products vary in structure, oxygen content and sp^2 hybridised carbon regions. These characteristics immediately affect the properties of the synthesised products. As a result, different preparation methods yield different GO and RGO samples in terms of properties, such as conductivity, and immediately affect their dispersibility. For this reason, the present work does not cover all types of GO and RGO samples. Similar studies should be conducted on GO and RGO samples prepared with different methods with varying structural characteristics, so as to obtain insight on the impact this factor has on their dispersion behaviour. Discovering and developing preparation methods that result in GO and RGO that are both optimally dispersed in a variety of solvents but also carry enhanced desired properties is important for the advancement of these materials.

Another crucial factor on the dispersion concentration and dispersed particle size is the chosen method of liquid exfoliation. Ultrasonic frequencies in the form of a bath or, in the case of this thesis, an ultrasonic probe, have been utilised for

exfoliation of graphite oxide and reduced graphite oxide in the liquid phase. These methods may be expanded upon and optimised to achieve higher dispersion concentrations and more uniform or, ideally, monodisperse GO and RGO suspensions. The ultrasonication method can be expanded upon in terms of changing the ultrasonic frequency and the exfoliation time. Attempting different solvent volumes and temperatures during GO and RGO dispersion preparation may provide more insight into how these factors affect their dispersibility. In terms of investigating the optimum solvent, further research should be realised on using solvent mixtures of different ratios to disperse GO and RGO. By combining the physical nature of two or more solvents, a new “solvent” is developed that may provide enhanced dispersibility.

Lastly, it would be of great interest to establish how much HSP values can deviate depending on the preparation method of these materials. Different GO and RGO samples will possess different HSP values and, by extent, they will “prefer” different solvents or solvent mixtures in which to be dispersed. A catalogue generated through extensive investigations, of the variety of GO and RGO preparation methods, the HSP of each respective material they generate and the liquid media they are optimally dispersed in, will serve as a powerful tool for future processing and utilization of these advanced nanomaterials.

References:

1. Godwin, H. "Half-life of radiocarbon". *Nature*, 195, (1962).
2. N.N. Greenwood and A. Earnshaw, Chemistry of the Elements, *Cryst. Res. Technol*, (1985).
3. Properties and Characteristics of Graphite, Poco Graphite, Specialty Materials. Available online: <http://poco.com/Portals/0/Literature/Semiconductor/IND-109441-0115.pdf>
4. Deprez, N.; McLachlan, D. S., "The analysis of the electrical conductivity of graphite conductivity of graphite powders during compaction". *Jour. of Physics: Applied Physics.*, 21, 1, (1988).
5. Collins, A. T., "The Optical and Electronic Properties of Semiconducting Diamond", *Philosophical Transactions of the Royal Society A.*, 342, 166 ,(1993).
6. L. Yang, H. Y. He, and B. C. Pan, Theoretical prediction of new carbon allotropes, *J. Chem. Phys.* 138, 2, (2013).
7. L.A. Burchfield, M.A. Fahim, R.S. Wittman, F. Delodovici, N. Manini, Novamene: A new class of carbon allotrope, *Heliyon*. 3 (2) (2017).
8. Tagami, Makoto; Liang, Yunye; Naito, Hisashi; Kawazoe, Yoshiyuki; Kotani, Motoko, "Negatively curved cubic carbon crystals with octahedral symmetry", *Carbon*, 76, (2014).
9. M. Scarselli, P Castrucci and M De Crescenzi, Electronic and optoelectronic nano-devices based on carbon nanotubes, *J. Phys.: Condens. Matter*, 24, (2012).
10. F. P. Bundy; J. S. Kasper, Hexagonal Diamond—A New Form of Carbon, *J. Chem. Phys.* 46, (1967).
11. C. Piskoti; J. Yarger; A. Zettl, C36, a new carbon solid, *Nature*, 393, (1998).
12. W. Saidia, T. Abrama, L. Bejjita, Mohammed Bouachrineb, New Organic Compounds Based on Biphenyl for Photovoltaic Devices: DFT Theoretical Investigation, *Chemical Methodologies*, 2, (2018)
13. S. Iijima, Helical Microtubules of Graphitic Carbon. *Nature*, 354, (1991).

-
14. Ahmad Aqel; Kholoud M.M.; Abou El-Nour; Reda A.A. Ammar; Abdulrahman Al-Warthan, Carbon nanotubes, science and technology part (I) structure, synthesis and characterisation, *Arabian Journal of Chemistry*, 5, (2012).
 15. www.superiorgraphite.com
 16. Delhaes, P., Graphite and Precursors. CRC Press. ISBN 978-90-5699-228-6) (2001).
 17. Chung, D. D. L. , "Review Graphite". *Journal of Materials Science*. 37 (8): 1475–1489 (2002).
 18. A. Yaya, B. Agyei-Tuffour, D. Doodoo-Arhin, E. Nyankson, et al., Layered Nanomaterials-A Review, *G.J. E.D.T.*, 1, 2, (2012).
 19. H. Lipson, A. R. Stokes, A New Structure of Carbon, *Nature.*, 149, (1942).
 20. Wyckoff, W.G. *Crystal Structures*. New York, London: John Wiley & Sons, (1963).
 21. IUPAC, Compendium of Chemical Terminology, 2nd ed. (the "Gold Book") (1997). Online corrected version: (2006–) "Rhombohedral graphite".
 22. Z. Zhen, H. Zhu, Structure and Properties of Graphene, Graphene Fabrication, Characterizations, Properties and Applications, *Elsevier*, (2018).
 23. S. Zhao, S. P. Surwade, Z. Li, H. Liu, Photochemical oxidation of CVD-grown single layer graphene, *Nanotechnology*, 23, (2012).
 24. C. Y. Su, A. Y. Lu, Y. Xu, F. R. Chen, A. N. Khlobystov, L. J. Li, High-Quality Thin Graphene Films from Fast Electrochemical Exfoliation, *ACS Nano*, 5, 3, (2011).
 25. N. Krane, Preparation of Graphene, *Selected Topics in Physics: Physics of Nanoscale Carbon*.
 26. W. Zhao, F. Wu, H. Wu, G. Chen, Preparation of Colloidal Dispersions of Graphene Sheets in Organic Solvents by Using Ball-Milling, *Journal of Nanomaterials*, 6, (2010).
 27. M. Lotya, P. J. King, U. Khan, S. De, J. N. Coleman, High-Concentration, Surfactant-Stabilized Graphene Dispersions, *ACS Nano*, 4, 6, (2010).
 28. S.Park, R.S. Ruoff, Chemical methods for the production of graphene, *Nature Nanotechnology*, 4, (2009).

-
29. S. Stankovich, D.A. Dikin, R. D. Piner, K.A. Kohlhaas, A. Kleinhammes, Y. Jia, Y. Wu, S. T. Nguyen, R. S. Ruoff, Synthesis of graphene-based nanosheets via chemical reduction of exfoliated graphite oxide, *Carbon*, 45, (2007).
 30. T. Ghosh, C. Biswas, J. Oh, G. Arabale, T. Hwang, N. D. Luong, M. Jin, Y. H. Lee, J. D. Nam, Solution-Processed Graphite Membrane from Reassembled Graphene Oxide, *Chem. Mater.*, 24, (2012).
 31. S. Homaeigohar, M. Elbahri, Graphene membranes for water desalination, *NPG Asia Materials*, 9, (2017).
 32. E.P. Randviir, D. A. C. Brownson, J. P. Metters, R. O. Kadara, C. E. Banks, The fabrication, characterisation and electrochemical investigation of screen-printed graphene electrode, *Phys. Chem. Chem. Phys.*, 16, (2014).
 33. E. Kymakis, E. Stratakis, M.M. Stylianakis, E. Koudoumas, C. Fotakis, Spin coated graphene films as the transparent electrode in organic photovoltaic devices, *Thin Solid Films*, 520, (2011).
 34. V. H. Pham, T. V. Cuong, S. H. Hur, Eun Woo Shin, J. S. Kim, J. S. Chung, E. J. Kim, Fast and simple fabrication of a large transparent chemically-converted graphene film by spray-coating, *Carbon*, 48, (2010).
 35. W. J. Hyun, O. O. Park, B. D. Chin, Foldable Graphene Electronic Circuits Based on Paper Substrates, *Adv. Mater.*, 25, (2013).
 36. M. Eizenberg, J.M. Blakely, Carbon monolayer phase condensation on Ni (111), *Surface Science* 82, (1979).
 37. Grabke, H. J., et al., *Surf Sci*, 63, 377, (1977).
 38. Hamilton, J. C., and Blakely, J. M., *Surf Sci*, 91, 119, (1980).
 39. Z.-Y. Juang, C.-Y. Wu, A.-Y. Lu, C.-Y. Su, K.-C. Leou, F.-R. Chen, C.-H. Tsai, Graphene synthesis by chemical vapor deposition and transfer by a roll-to-roll Process, *Carbon*, 48, 11, (2010).
 40. P. V. Pham, Atmospheric Pressure Chemical Vapor Deposition of Graphene, *Chemical Vapor Deposition for Nanotechnology*, (2018).

-
41. B. Partoens, F. M. Peeters, From graphene to graphite: Electronic structure around the K point, *Phys. Rev. B*, 74, (2006).
 42. Novoselov, K. S. et al., Electric field effect in atomically thin carbon films, *Science*, 306, (2004).
 43. K. S. Kim, Y. Zhao, H. Jang, S. Y. Lee, J. M. Kim, K. S. Kim, J. H. Ahn, P. Kim, J. Y. Choi, B. H. Hong, Large-scale pattern growth of graphene films for stretchable transparent electrodes, *Nature*, 457, (2009).
 44. K.I. Bolotina, K.J. Sikesb, Z. Jianga, M. Klimac, G. Fudenberg, J. Honec, P. Kima, H.L. Stormera, Ultrahigh electron mobility in suspended graphene, *Solid State Communications*, 146, (2008).
 45. Y. Zhang, Y. W. Tan, H.L. Stormer, P. Kim, Experimental observation of the quantum Hall effect and Berry's phase in graphene, *Nat. Letters*, 438, (2005).
 46. Abid, Poonam Sehwat, S. S. Islam, P. Mishra, S, Ahmad, Reduced graphene oxide (rGO) based wideband optical sensor and the role of Temperature, Defect States and Quantum Efficiency, *Scientific Reports*, 8, 3537, (2018).
 47. G. Wu, X. Tang, M. Meyyappan, K. W., C. Lai, Doping Effects of Surface Functionalization on Graphene with Aromatic Molecule and Organic Solvents, *Applied Surface Science, Elsevier*, 425, (2017).
 48. K. S. Novoselov, A. K. Geim, S. V. Morozov, D. Jiang, M. I. Katsnelson, I. V. Grigorieva, S. V. Dubonos, A. A. Firsov, Two-dimensional gas of massless Dirac fermions in graphene, *Nat. Letters*, 438, (2005).
 49. A. A. Balandin, S. Ghosh, W. Bao, I. Calizo, D. Teweldebrhan, F.Miao, C. N. Lau, Superior Thermal Conductivity of Single-Layer Graphene, *Nano Letters*, 8, 3, (2008).
 50. Meryl D. Stoller, Sungjin Park, Yanwu Zhu, Jinho An, and Rodney S. Ruoff, Graphene-Based Ultracapacitors, *Nano Letters*, 8, 10, (2008).
 51. H. Li, K. Leifer, Determining the Elasticity of Graphene, *Imaging & Microscopy*, (2019).
 52. R.R. Nair, P. Blake, A.N. Grigorenko, et al., Fine structure constant defines visual transparency of graphene, *Science*, 320, (2008).
 53. C. Casiraghi A. Hartschuh, E. Lidorikis, H. Qian, H. Harutyunyan, T. Gokus, K. S. Novoselov, A. C. Ferrari Rayleigh Imaging of Graphene and Graphene Layers, *Nano Lett.*, 7, 9, (2007).

54. F. Bonaccorso, Z. Sun, T. Hasan and A. C. Ferrari, Graphene photonics and optoelectronics, *Nat. Photonics* 4, 9, (2010).
55. K. F. Mak, J. Shan, T.F. Heinz, Electronic structure of few-layer graphene: experimental demonstration of strong dependence on stacking sequence, *Phys. Rev. Lett.*, 104, (2009).
56. F. Wang, Y. Zhang, C. Tian, C. Girit, A. Zettl, M. Crommie, Y. R. Shen, Gate-Variable Optical Transitions in Graphene, *Science*, 320, (2008).
57. J. I. Paredes, S. Villar-Rodil, P. Solis-Fernandez, A. Martinez-Alonso, J. M. D. Tascon, Atomic Force and Scanning Tunneling Microscopy Imaging of Graphene Nanosheets Derived from Graphite Oxide, *Langmuir*, 25, 10, (2009).
58. D. Li, M. B. Muller, S. Gilje, R.B. Kaner, G.G. Wallace, Processable aqueous dispersions of graphene nanosheets, *Nat. Nanotechnology*, 3, (2008).
59. R. Su, S. F. Lin, D. Q. Chen, G. H. Chen, Study on the Absorption Coefficient of Reduced Graphene Oxide Dispersion, *J. Phys. Chem.*, 118, (2014).
60. Y. Hernandez, V. Nicolosi, M. Lotya et al., High-yield production of graphene by liquid-phase exfoliation of graphite, *Nature Nanotechnology*, 3, 9, (2008).
61. U. Khan, A.O'Neill, M. Lotya, S. De, J. N. Coleman, High-Concentration Solvent Exfoliation of Graphene, *small*, 6, 7, (2010).
62. M. Lotya, Y. Hernandez, P. J. King, Liquid Phase Production of Graphene by Exfoliation of Graphite in Surfactant/Water Solutions, *J. Am. Chem. Soc.*, 131, (2009).
63. M. Lotya, P. J King, U. Khan, S.De, J. N Coleman, High-Concentration, Surfactant-Stabilized Graphene Dispersions, *ACS Nano*, 4, 6, (2010).
64. U. Khan, H. Porwal, A. O'Neill, K. Nawaz, P. May, J. N. Coleman, Solvent-Exfoliated Graphene at Extremely High Concentration, *Langmuir*, 27, (2011).
65. M. Hashemi, B. Muralidharan, M. Omid, J. Mohammadi, Y. Sefidbakht, E. S. Kima, C.H. D.C. Smyth, M. Shalhaf, T. E. Milnera, Effect of size and chemical composition of graphene oxide nanoparticles on optical absorption cross-section, *J. of Biomedical Optics*, 23, 8, (2018).
66. L.Sun, Structure and Synthesis of graphene oxide, (2019).

67. A. Lerf, H. He, M. Forster, J. Klinowski, Structure of Graphite Oxide Revisited, *J. Phys. Chem. B*, 102, (1998).
68. H. He, J. Klinowski, M. Forster, A. Lerf, A new structural model for graphite oxide, *Chemical Physics Letters*, 287, (1998).
69. K. Erickson, R. Erni, Z. Lee, N. Alem, W. Gannett, A. Zettl, Determination of the Local Chemical Structure of Graphene Oxide and Reduced Graphene Oxide, *Adv. Mater.*, 22, (2010).
70. J. T. Paci, T. Belytschko, G. C. Schatz, Computational Studies of the Structure, Behavior upon Heating, and Mechanical Properties of Graphite Oxide, *J. Phys. Chem. C*, 111, 49, (2007).
71. S. H. Dave, C. Gong, A. W. Robertson, J. H. Warner, J. C. Grossman, Chemistry and Structure of Graphene Oxide via Direct Imaging, *ACS Nano*, 10, (2016).
72. B.C., Brodie, On the Atomic Weight of Graphite. *Philosophical Transactions of the Royal Society of London*, 149, (1859).
73. R. K. Singh, R. Kumar, D. P. Singh, Graphene oxide: strategies for synthesis, reduction and frontier applications, *RSC Adv.*, 6, (2016).
74. M. Aliofkhaezai, N. Ali, W. I. Milne, C. S. Ozkan, S. Mitura, J. L. Gervasoni, *Graphene Science Handbook*, (2016).
75. L. Staudenmaier, Verfahren zur Darstellung der Graphitsäure, *Ber. Dtsch. Chem. Ges.*, 31, (1898).
76. T. Nakajima, Y. Matsuo, Formation Process and Structure of Graphite Oxide, *Carbon*, 32, 3, (1994).
77. H. L. Poh, F. Sanek, A. Ambrosi, G. Zhao, Z. Sofer, M. Pumera, Graphenes prepared by Staudenmaier, Hofmann and Hummers methods with consequent thermal exfoliation exhibit very different electrochemical properties, *Nanoscale*, 4, (2012).
78. U. Hofmann, Untersuchungen über Graphitoxyd, E. König, *Z. Anorg., Allg. Chem.*, 234, (1937).
79. C. K. Chua, Z. Sofer, M. Pumera, Graphite Oxides: Effects of Permanganate and Chlorate Oxidants on the Oxygen Composition, *Chem. Eur. J.*, (2012).

-
80. O. Jankovsky, P. Marvan, M. Nováček, J. Luxa, V. Mazánek, K. Klímová, D. Sedmidubský, Z. Sofer, Synthesis procedure and type of graphite oxide strongly influence resulting graphene properties, *Applied Materials Today*, 4, (2016).
81. W. Hummers Jr., R. Offeman, Preparation of Graphitic Oxide, *J. Am. Chem. Soc.*, 80, 6, (1958).
82. R. Muzyka, M. Kwoka, Ł. Smędowski, N. Diez, G. Gryglewicz, Oxidation of graphite by different modified Hummers Methods, *New Carbon Materials*, 32, 1, (2017).
83. D.C. Marcano, D. V. Kosynkin, J. M. Berlin, A. Sinitskii, Z. Sun, A. Slesarev, L. B. Alemany, W. Lu, J. M. Tour, Improved Synthesis of Graphene Oxide, *ACS Nano*, 4, 8, (2010).
84. N.I. Zaabaa, K.L. Foa,*, U. Hashima,d, S.J.Tanb,c, Wei-Wen Liua, C.H. Voona, Synthesis of Graphene Oxide using Modified Hummers Method: Solvent Influence, *Procedia Engineering* 184, (2017).
85. M. Sohail, M. Saleem, S. Ullah, N. Saeed, A. Afridi, M. Khan, Modified and improved Hummer's synthesis of graphene oxide for capacitors applications, *Modern Electronic Materials*, 3, 3, (2017).
86. A. Saini, A. Kumar, V. K. Anand, S. C. Sood, Synthesis of Graphene Oxide using Modified Hummer's Method and its Reduction using Hydrazine Hydrate, *International Journal of Engineering Trends and Technology (IJETT)*, 40, 2, (2016).
87. J. H. Kang, T. Kim, J. Choi, J. Park, Y. S. Kim, M. S. Chang, H. Jung, K. T. Park, S. J. Yang, C. R. Park, Hidden Second Oxidation Step of Hummers Method, *Chem. Mater.*, 28, (2016).
88. J. Chen, Y. Li, L. Huang, C. Li, G. Shi, High-yield preparation of graphene oxide from small graphite flakes via an improved Hummers method with a simple purification process, *Carbon*, 81, (2015).
89. A. Ibarra-Hernández, A. Vega-Rios, V. Osuna, Synthesis of Graphite Oxide with Different Surface Oxygen Contents Assisted Microwave Radiation, *Nanomaterials*, 8, 106, (2018).
90. H. L. Poh, F. Sanek, A. Ambrosi, G. Zhao, Z. Soferb, M. Pumera, Graphenes prepared by Staudenmaier, Hofmann and Hummers methods with consequent thermal exfoliation exhibit very different electrochemical properties, *Nanoscale*, 4, (2012).
91. Chun Kiang Chua, Zdenek Sofer, Martin Pumera, Graphite Oxides: Effects of Permanganate and Chlorate Oxidants on the Oxygen Composition, *Chem. Eur. J.* (2012).

-
92. M. Ciszewski, A. Mianowski, Survey of graphite oxidation methods using oxidizing mixtures in inorganic acids, *Chemik*, 67, 4, (2013).
93. L. Tang,ab X. Li, R. Ji, K. S. Teng,d G. Tai, J. Ye, C. Weia, S. P. Lau, Bottom-up synthesis of large-scale graphene oxide nanosheets, *J. Mater. Chem.*, 22, (2012).
94. Y. Dong, J. Shao, C. Chen, H. Li, R. Wang, Y. Chi, X. Lin, G. Chen, Blue luminescent graphene quantum dots and graphene oxide prepared by tuning the carbonization degree of citric acid, *Carbon*, 50, (2012).
95. R. J. Price, P. I. Ladislaus, G. C. Smith, T. J. Davies, A novel ‘bottom-up’ synthesis of few- and multi-layer graphene platelets with partial oxidation via cavitation, *Ultrasonics - Sonochemistry* 56, (2019).
96. Fauzi F B, Ismail E, Ani M H, et al. A critical review of the effects of fluid dynamics on graphene growth in atmospheric pressure chemical vapor deposition. *J. Mater. Res.*, 33, 9, (2018).
97. M. J. McAllister, J.-L. Li, D. H. Adamson, H. C. Schniepp, A. A. Abdala, J. Liu, M. Herrera-Alonso, D. L. Milius, R. Car, R. K. Prud’homme, I. A. Aksay, Single Sheet Functionalized Graphene by Oxidation and Thermal Expansion of Graphite, *Chem. Mater.*, 19, 18, (2007).
98. H. C. Schniepp, J.-L. Li, M. J. McAllister, H. Sai, M. Herrera-Alonso, D. H. Adamson, R. K. Prud’homme, R. Car, D. A. Saville, I. A. Aksay, Functionalized Single Graphene Sheets Derived from Splitting Graphite Oxide, *J. Phys. Chem. B*, 110, 17, (2006).
99. S. N. Alam, N. Sharma, L. Kumar, Synthesis of Graphene Oxide (GO) by Modified Hummers Method and Its Thermal Reduction to Obtain Reduced Graphene Oxide (rGO), *Graphene*, 6, (2017).
100. H. A. Becerril, J. Mao, Z. Liu, R. M. Stoltenberg, Z. Bao, Y. Chen, Evaluation of Solution-Processed Reduced Graphene Oxide Films as Transparent Conductors, *ACS Nano*, 2, 3, (2008).
101. X. Wang, L. Zhi, K. Mulle, Transparent, Conductive Graphene Electrodes for Dye-Sensitized Solar Cells, *Nano Lett.* 8, 1, (2008).
102. D. Yang, A. Velamakanni, G. Bozoklu, S. Park, M. Stoller, R. D. Piner, S. Stankovich, I. Jung, D.A. Field, C. A. Ventrice Jr., R. S. Ruoff, Chemical analysis of graphene oxide films after heat and chemical treatments by X-ray photoelectron and Micro-Raman spectroscopy, *Carbon*, 47, (2009).

-
103. H. M. A. Hassan, Victor Abdelsayed, A. E. R. S. Khder, K. M. AbouZeid, J. Ternier, M. S. El-Shall, S. I. Al-Resayes, A. A. El-Azharyb, Microwave synthesis of graphene sheets supporting metal nanocrystals in aqueous and organic media, *J. Mater. Chem.*, **19**, 3832-3837, (2009).
104. Y. Zhu, S. Murali, M. D. Stoller, A. Velamakanni, R. D. Piner, R. S. Ruoff, Microwave assisted exfoliation and reduction of graphite oxide for ultracapacitors, *Carbon*, **48**, 2106 – 2122, (2010).
105. Y. Zhang, L. Guo, S. Wei, Y. He, H. Xia, Q. Chen, H.-B. Sun, F.-S. Xiao, Direct imprinting of microcircuits on graphene oxides film by femtosecond laser reduction, *Nano Today*, **5**, (2010).
106. L. J. Cote, R. Cruz-Silva, J. Huang, Flash Reduction and Patterning of Graphite Oxide and Its Polymer Composite, *J. Am. Chem. Soc.*, **131**, 31, (2009).
107. L. Pei, Y.-F. Li, Rapid and efficient intense pulsed light reduction of graphene oxide inks for flexible printed electronics, *RSC Adv.*, **7**, (2017).
108. S. Pei, J. Zhao, J. Du, W. Ren, H.-M. Cheng, Direct reduction of graphene oxide films into highly conductive and flexible graphene films by hydrohalic acids, *Carbon*, **48**, (2010).
109. Q. Meng-Meng, J. Wei, F. Yi-Yu, F. Wei, Transparent conductive graphene films prepared by hydroiodic acid and thermal reduction, *Chin. Phys. B*, **23**, 2, (2014).
110. I. K. Moon, J. Lee, R. S. Ruoff, H. Lee, Reduced graphene oxide by chemical graphitization, *Nat. Commun.*, **1**, 73, (2010).
111. H.-J., Shin, K. K. Kim, A. Benayad, S.-M. Yoon, H. K. Park, et al. Efficient Reduction of Graphite Oxide by Sodium Borohydride and Its Effect on Electrical Conductance, *Advanced Functional Materials*, **19**, 12, (2009).
112. Z. Yang, Q. Zheng, H. Qiu, J. Li, J. Yang, A simple method for the reduction of graphene oxide by sodium borohydride with CaCl₂ as a catalyst, *New Carbon Materials*, **30**, 1, (2015).
113. A. Ambrosi, C. K. Chua, A. Bonanni, M. Pumera, Lithium Aluminum Hydride as Reducing Agent for Chemically Reduced Graphene Oxides, *Chem. Mater.*, **24**, 12, 2 (2012).
114. H.-J. Shin, K. K. Kim, A. Benayad, S.-M. Yoon, H. K. Park, I.-S. Jung, M. H. Jin, H.-K. Jeong, J. M. Kim, J.-Y. Choi, Y. H. Lee, Efficient Reduction of Graphite Oxide by Sodium Borohydride and Its Effect on Electrical Conductance, *Adv. Funct. Mater.*, **19**, (2009).

-
115. R. Ortega-Amaya, Y. Matsumoto, E. Díaz-Torres, C. D. Gutierrez-Lazos, M. A. Pérez-Guzmán, M. Ortega-López, Green Routes for Graphene Oxide Reduction and Self-Assembled Graphene Oxide Micro- and Nanostructures Production, *InTech*, Chapter 6, (2017).
116. Reduction of graphene oxide via L-ascorbic acid, J. Zhang, H. Yang, G. Shen, P. Cheng, J. Zhang, S. Guo, *Chem. Commun.*, *46*, (2010).
117. X. Zhu, Q. Liu, X. Zhu, C. Li, M. Xu, Y. Liang, Reduction of Graphene Oxide Via Ascorbic Acid and Its Application for Simultaneous Detection of Dopamine and Ascorbic Acid, *Int. J. Electrochem. Sci.*, *7*, (2012).
118. K. Kanishka H. De Silva, H.-H. Huang, M. Yoshimura, Progress of reduction of graphene oxide by ascorbic acid, *Applied Surface Science*, *447*, (2018).
119. S. Bose, T. Kuila, A. K. Mishra, N. H. Kim, J. H. Lee, Dual role of glycine as a chemical functionalizer and a reducing agent in the preparation of graphene: an environmentally friendly method, *J. Mater. Chem.*, *22*, (2012).
120. J. Wang, E. C. Salihi, L. Šiller, Green reduction of graphene oxide using alanine, *Materials Science and Engineering C*, *72*, (2017).
121. D. Chen, L. Li, L. Guo, Environment-friendly preparation of reduced graphene oxide nanosheets via amino acid, *Nanotechnology*, *22*, (2011).
122. C. Zhu, S. Guo, Y. Fang, S. Dong, Reducing Sugar: New Functional Molecules for the Green Synthesis of Graphene Nanosheets, *ACS Nano*, *4*, *4*, (2010).
123. H. Liu, T. Li, Y. Liu, G. Qin, X. Wang, T. Chen, Glucose-Reduced Graphene Oxide with Excellent Biocompatibility and Photothermal Efficiency as well as Drug Loading, *Nanoscale Research*, *11*, *211*, Letters (2016).
124. F. A. Shammala, B. Chiswell, Glucose-Reduced Nano-Graphene Oxide with Excellent Accumulation Removal of Pharmaceuticals and Personal Care Products from Water, *J. Environ. Anal. Chem.*, *5*, *3*, (2018).
125. A. Moosa, J. N. Jaafar, Green Reduction of Graphene Oxide Using Tea Leaves Extract with Applications to Lead Ions Removal from Water, *Nanoscience and Nanotechnology*, *7*, (2017).
126. M. J.-Y. Tai, W.-W. Liu, C.-S. Khe, N. M. S. Hidayah, Y.-P. Teoh, C. H. Voon, H. Cheun Lee, and P. Y. P., Adelyn, Green synthesis of reduced graphene oxide using green tea extract, *AIP Conference Proceedings*, *2045*, (2018).

127. M. Z. Ansari, W. A. Siddiqui, Deoxygenation of graphene oxide using biocompatible reducing agent *Ficus carica* (dried ripe fig), *Journal of Nanostructure in Chemistry*, 8, 4, (2018).
128. D. Suresh, P.C. Nethravathi, U. C. Gowda, N. Bhushana, S.C. Sharma, Spinach assisted green reduction of graphene oxide and its antioxidant and dye absorption properties. *Ceramics Internationa*, 41, (2015).
129. S. Pei, H.-M. Cheng, The reduction of graphene oxide, *Carbon*, 50, (2012).
130. S. Stankovich, Dmitriy A. Dikin, Richard D. Piner, Kevin A. Kohlhaas, Alfred Kleinhammes, Y. Jia, Y. Wu, S. T. Nguyen, R.S. Ruoff, Synthesis of graphene-based nanosheets via chemical reduction of exfoliated graphite oxide, *Carbon*, 45, (2007).
131. S. C. Youn, J. Geng, B.S. Son, S.B. Yang, D.W. Kim, H. Cho, H.T. Jung, Effect of the exposure time of hydrazine vapor on the reduction of graphene oxide films, *J. Nanosci. Nanotechnol.*, 11, 7, (2011).
132. K.-H. Shin, Y.Jang, B.-S. Kim, J. Jang, S. H. Kim, Highly conductive reduced graphene oxide via pressure-assisted reduction at mild temperature for flexible and transparent electrodes, *Chem. Commun.*, 49, (2013).
133. M.J. Fernández-Merino, L. Guardia, J.I. Paredes, S. Villar-Rodil, P. Solís-Fernández, A. Martínez-Alonso, J.M.D. Tascón, Vitamin C is an ideal substitute for hydrazine in the reduction of graphene oxide suspensions, *J. Phys. Chem. C*, 114, 14, (2010).
134. Peng Su, Hui-Lin Guo, Lei Tian, Sheng-Ke Ning, An efficient method of producing stable graphene suspensions with less toxicity using dimethyl ketoxime, *Carbon*, 50, (2012).
135. S. Mao, K. Yu, S. Cui, Z. Bo, G. Lu, J. Chen, A new reducing agent to prepare single-layer, high-quality reduced graphene oxide for device applications *Nanoscale*, 3, (2011).
136. C. A. Amarnath, C. E. Hong, N. H. Kim, B.-C. Ku, T. Kuila, J. H. Lee, *Carbon*, 49, (2011).
137. X. Mei, X. Meng, F. Wu, Hydrothermal method for the production of reduced graphene oxide, *Physica E Low-dimensional Systems and Nanostructures*, 68, (2015).
138. J.-L. Shi, W.-C. Du, Y.-X. Yin, Y.-G. Guo, L.-J. Wan, Hydrothermal reduction of three-dimensional graphene oxide for binder-free flexible supercapacitors, *J. Mater. Chem. A*, 2, (2014).

-
139. X. Zheng, Y. Peng, Y. Yang, J. Chen, H. Tian, X. Cui, W. Zheng, Hydrothermal reduction of graphene oxide: effect on surface-enhanced Raman scattering, *J. Raman Spectrosc.*, **48**, 97–103, (2017).
140. X. Wang, L. Zhi, K. Mullen, Transparent, Conductive Graphene Electrodes for Dye-Sensitized Solar Cells, *Nano Lett.*, **8**, 1, (2008).
141. Y. S. Woo, Transparent Conductive Electrodes Based on Graphene-Related Materials, *Micromachines*, **10**, 13, (2019).
142. M. Savchak, N. Borodinov, *ACS Appl. Mater. Interfaces*, **10**, 4, (2018).
143. D. H. Wang, J. K. Kim, J. H. Seo, I. Park, et al., *Angew. Chem. Int. Ed.*, **52**, (2013).
144. D. Li, J. Cui, H. Li, D. Huang, M. Wang, Y. Shen, Graphene oxide modified hole transport layer for CH₃NH₃PbI₃ planar heterojunction solar cells, *Solar Energy*, **131**, (2016).
145. T. Durkop, S. A. Getty, E. Cobas, M. S. Fuhrer, *Nano Lett.*, **4**, (2004).
146. S. N. Habisreutinger, T. Leijtens, G. E. Eperon, S. D. Stranks, R. J. Nicholas and H. J. Snaith, *Nano Lett.*, **14**, (2014).
147. F. Schedin, A. K. Geim, S. V. Morozov, E. W. Hill, P. Blake, M. I. Katsnelson, K. S. Novoselov, Detection of individual gas molecules adsorbed on graphene, *Nature Materials*, **6**, (2007).
148. Wenchao Tian, Xiaohan Liu * and Wenbo Yu, Research Progress of Gas Sensor Based on Graphene and Its Derivatives: A Review, *Appl. Sci.*, **8**, (2018).
149. Yue Peng, Junhua Li, Ammonia adsorption on graphene and graphene oxide: a first-principles study, *Frontiers of Environmental Science & Engineering*, **7**, 3, (2013).
150. L. Guo, H.-B. Jiang, R.-Q. Shao et al., Two-beam-laser interference mediated reduction, patterning and nanostructuring of graphene oxide for the production of a flexible humidity sensing device, *Carbon*, **50**, 4, (2012).
151. E. Singh, M. Meyyappan, Hari S. Nalwa, Flexible Graphene-Based Wearable Gas and Chemical Sensors, *ACS Appl. Mater. Interfaces*, **9**, 40, (2017).
152. H. Choi, H.Y. Jeong, D.S. Lee, C.G. Choi, S.Y. Choi, Flexible NO₂ gas sensor using multilayer graphene films by chemical vapor deposition, *Carbon Lett.*, **14**, 3, (2013).

-
153. H. J. Yoon, D. H. Junb, J. H. Yanga, Z. Zhouc, S. Sik Yang, M. M.-C. Cheng, Carbon dioxide gas sensor using a graphene sheet, *Sensors and Actuators B Chemical*, 157, 1,(2011).
154. F. Shen, D. Wang, R. Liu, X. Pei, T. Zhang, J. Jin, Edge-tailored graphene oxide nanosheet-based field effect transistors for fast and reversible electronic detection of sulphur dioxide, *Nanoscale* 5, 2, (2013).
155. H. Zhang, A. Kulkarni, H. Kim, D. Woo, Y.-J. Kim, B.H. Hong, J.-B. Choi, T. Kim, Detection of acetone vapor using graphene on polymer optical fiber. *J. Nanosci. Nanotechno.*, 11, 7, (2011).
156. V.V. Singh, A.K. Nigam, S.S. Yadav, B.K. Tripathi, A. Srivastava, M. Boopathi, B. Singh, Graphene oxide as carbo electrocatalyst for in situ electrochemical oxidation and sensing of chemical warfare agent simulant. *Sens. Actuators B*, 188, (2013).
157. Q. H. Wang, K. Kalantar-Zadeh, A. Kis, J. N. Coleman, M.S. Strano, Electronics and optoelectronics of two-dimensional transition metal dichalcogenides. *Nat. Nanotechnol.*, 7, (2012).
158. X. Li, W. K. Cho, B. Hussain, H.S. Kwok, C. P. Yue, Micro-led display with simultaneous visible light communication function, *SID Symp. Dig. Tech. Pap.*, 66 (3) (2018).
159. M. Sang, J. Shin, K. Kim, K. Jun Yu, Electronic and Thermal Properties of Graphene and Recent Advances in Graphene Based Electronics Applications, *Nanomaterials*, 9, 374, (2019).
160. S.H. Park, A. Roy, S. Beaupré, S. Cho, et al. Bulk heterojunction solar cells with internal quantum efficiency approaching 100%, *Nat. Photonics*, 3, 297, (2019).
161. A.K. Kulkarni, K.H. Schulz, T.S. Lim, M. Khan, Dependence of the sheet resistance of indium-tin-oxide thin films on grain size and grain orientation determined from x-ray diffraction techniques. *Thin Solid Film*, 345, (1999).
162. N. Li, S. Oida, G.S. Tulevski, S.-J. Han, et al. Efficient and bright organic light-emitting diodes on single-layer graphene electrodes. *Nat. Commun.*, 4, (2013).
163. Z. Wu, Z. Chen, X. Du, J.M. Logan, J. Sippel, M. Nikolou, et al. Transparent, conductive carbon nanotube films. *Science*, 305, (2004).
164. Y. Huang, Z. Huang, Z. Zhong, X. Yang, Q. Hong, Q. Wang et al., Highly transparent light emitting diodes on graphene encapsulated Cu nanowires network. *Sci. Rep.*, 8, (2018).

-
- 165 J. Hassoun, F. Bonaccorso, M. Agostini, M. Angelucci et al., An Advanced Lithium-Ion Battery Based on a Graphene Anode and a Lithium Iron Phosphate Cathode, *Nano Lett.*, 14, (2014).
166. H. Ki, K.-Y. Park, J. Hong, K. Kang, All-graphene-battery: bridging the gap between supercapacitors and lithium ion batteries, *Scientific Reports*, 4, (2014).
167. N. Ghavihaa, J. Campilloa, M. Bohlinb , E. Dahlquist, Review of Application of Energy Storage Devices in Railway Transportation, *Energy Procedia*, 105, (2017).
168. M. D. Stoller, S. Park, Y. Zhu, J. An, R. S. Ruoff, Graphene-Based Ultracapacitors, *Nano Lett.*, 8, 10, (2008).
169. L. L. Zhang , S. Zhao , X. N. Tian , X. S. Zhao , Layered Graphene Oxide Nanostructures with Sandwiched Conducting Polymers as Supercapacitor Electrodes, *Langmuir*, 26, (2010).
170. X. Zhanga , J. Zhanga , Y. Chena , K. Chenga, et al., Freestanding 3D Polypyrrole@Reduced Graphene Oxide Hydrogels as Binder-Free Electrode Materials for Flexible Asymmetric Supercapacitors, *Journal of Colloid and Interface Science*, 536, (2019).
171. J. Peña-Bahamonde, H. N. Nguyen, S. K. Fanourakis, D. F. Rodrigues, Recent advances in graphene-based biosensor technology with applications in life sciences, *J Nanobiotechnol*, 16, 75, (2018).
172. Y. Wang, Z. Li, Jun Wang, J. Li, Y. Lin, Graphene and graphene oxide: biofunctionalization and applications in biotechnology, *Trends in Biotechnology*, 29, 5, (2011).
173. P.R. Selvin, The renaissance of fluorescence resonance energy transfer, *Nature Structural Biology*, 7, 9, (2000).
174. T. Cohen-Karni, Q. Qing, Q. Li, Y. Fang, C. M. Lieber, Graphene and Nanowire Transistors for Cellular Interfaces and Electrical Recording, *Nano Lett.*, 10, (2010).
175. Z. Liu, J. T. Robinson, X. Sun, Ho. Dai, PEGylated Nanographene Oxide for Delivery of Water-Insoluble Cancer Drugs, *J. Am. Chem. Soc.*, 130, (2008).
176. L. Feng, Z. Liu, Graphene in biomedicine: opportunities and challenges, *Nanomedicine*, 6, 2, (2011).
177. Z. Singh, R. Singh, Recent Approaches in Use of Graphene Derivatives in Anticancer Drug Delivery Systems, *J Drug Des Res* 4, 3, (2017).

-
178. D. Jasinski, F. Haque, D. W. Binzel, P. Guo, Advancement of the Emerging Field of RNA Nanotechnology, *ACS Nano.*, 1, 2, (2017).
179. R. G. Bai, K. Muthoosamy, S. Manickam, A. Hilal-Alnaqbi, Graphene-based 3D scaffolds in tissue engineering: fabrication, applications, and future scope in liver tissue engineering, *International Journal of Nanomedicine*, 14, (2019).
180. P. A. L. Lima, C. X. Resende, G. D. de Almeida Soares, K. Anselme, L.E. Almeida, Preparation, characterization and biological test of 3D-scaffolds based on chitosan, fibroin and hydroxyapatite for bone tissue engineering. *Mater Sci Eng C.*, 33 (6), (2013).
181. A. Mihic, J. Li, Y. Miyagi, et al. The effect of cyclic stretch on maturation and 3D tissue formation of human embryonic stem cell-derived cardiomyocytes, *Biomaterials*, 35 (9), (2014).
182. K. Anagnostou, M. Stylianakis, S. Michaleas, A. Skouras, Biodegradable nanomaterials, *Nanomaterials for Clinical Applications*, (2020).
183. N. Shadjou, M. Hasanzadeh, B. Khalilzadeh, Graphene based scaffolds on bone tissue engineering, *Bioengineered*, 9 (1), (2018).
184. Q. Wang, Y. Chu, J. He, W. Shao, Y. Zhou, K. Qi, et al., A graded graphene oxide-hydroxyapatite/silk fibroin biomimetic scaffold for bone tissue engineering, *Mater. Sci. Eng. C Mater. Biol. Appl.* 80 (2017).
185. H. Jo, M. Sim, S. Kim, S. Yang, Y. Yoo, J.-H. Park, et al., Electrically conductive graphene/polyacrylamide hydrogels produced by mild chemical reduction for enhanced myoblast growth and differentiation, *Acta Biomater.*, 48, (2017).
186. A.S.T. Smith, H. Yoo, H. Yi, E.H. Ahn, J.H. Lee, G. Shao, et al., Micro- and nano-patterned conductive graphene-PEG hybrid scaffolds for cardiac tissue engineering, *Chem. Commun.*, 53, (2017).
187. B. Nyambat, C.-H. Chen, P.-C. Wong, C.-W. Chiang, M. K. Satapathy, E.-Y. Chuang, Genipin-crosslinked adipose stem cell derived extracellular matrix-nano graphene oxide composite sponge for skin tissue engineering, *J. Mater. Chem. B*, 6, (2018).
188. R. Guazzo, C. Gardin, G. Bellin, L. Sbricoli et al. Graphene-Based Nanomaterials for Tissue Engineering in the Dental Field, *Nanomaterials*, 8, 349, (2018).
189. S. Gronthos, M. Mankani, J. Brahim, P. G. Robey, S. Shi, Postnatal human dental pulp stem cells (DPSCs) in vitro and in vivo, *Proc. Natl. Acad. Sci.*, 97, (2000).

190. S. Shi, P. G. Robey, S. Gronthos, Comparison of human dental pulp and bone marrow stromal stem cells by cDNA microarray analysis, *Bone*, 29, (2001).
191. V. Rosa, H. Xie, N. Dubey, T. T. Madanagopal, S. S. Rajan, et al., Graphene oxide-based substrate: Physical and surface characterization, cytocompatibility and differentiation potential of dental pulp stem cells, *Dent. Mater.*, 32, (2016).
192. Y. Jiang, P. Biswas, J. D. Fortner, A review of recent developments in graphene enabled membranes for water treatment, *Environ. Sci.: Water Res. Technol.*, 2, 915, (2016).
193. H. Wang, X. Mi, Y. Li, S. Zhan, 3D Graphene-Based Macrostructures for Water Treatment, *Adv. Mater.*, 32, 3, (2019).
194. A. Boretti, S. Al-Zubaidy, M. Vaclavikova, M. Al-Abri, S. Castelletto, S. Mikhalovsky, Outlook for graphene-based desalination membranes, *npj Clean Water*, 1, (2018).
195. Y. Yang, X. Yang, L. Liang, Y. Gao, H. Cheng, Large-area graphene-nanomesh/carbon-nanotube hybrid membranes for ionic and molecular nanofiltration, *Science*, 364, (2019).
196. M. Abolhassani, C. S. Griggs, L. A. Gurtowski, J. A. Mattei-Sosa et al., Scalable Chitosan-Graphene Oxide Membranes: The Effect of GO Size on Properties and Cross-Flow Filtration Performance, *ACS Omega*, 2, (2017).
197. F. Perreault, M. E. Tousley, Menachem Elimelech, Thin-Film Composite Polyamide Membranes Functionalized with Biocidal Graphene Oxide Nanosheets, *Environ. Sci. Technol. Lett.*, 1, 1, (2014).
198. US EPA, Drinking Water and Groundwater Quality Standards, (2014).
199. C.N. Nupearachchi, Kushani Mahatantila, M. Vithanage, Application of Graphene for Decontamination of Water; Implications for Sorptive Removal, *Groundwater for Sustainable Development*, (2017).
200. Z.-H. Huang, X. Zheng, W. Lv, M. Wang, Q.-H. Yang, F. Kang, Adsorption of Lead(II) Ions from Aqueous Solution on Low-Temperature Exfoliated Graphene Nanosheets, *Langmuir*, 27, (2011).
201. R. Sitko, E. Turek, B. Zawisza, E. Malicka et al. Adsorption of divalent metal ions from aqueous solutions using graphene oxide, *Dalton Trans.*, 42, (2013).

-
202. S.-T. Yang, Y. Chang, H. Wang, G. Liu, S. Chen, et al., Folding/aggregation of graphene oxide and its application in Cu²⁺ removal, *Journal of Colloid and Interface Science*, 351, 1, (2010).
203. L. Chaabanea, E. Beyoua, A. El Ghalic, M. H. V. Baouab, Comparative studies on the adsorption of metal ions from aqueous solutions using various functionalized graphene oxide sheets as supported adsorbents, *Journal of Hazardous Materials*, (2019).
204. C. Zhao, L. Xing, J. Xiang, L. Cui, J. Jiao, H. Sai, Z. Li, F. Li, Formation of uniform reduced graphene oxide films on modified PET substrates using drop-casting method, *Particuology*, 17, (2014).
205. E. Kymakis, E. Stratakis, M. M. Stylianakis, E. Koudoumas C. Fotakis, Spin coated graphene films as the transparent electrode in organic photovoltaic devices, *Thin Solid Films*, 520, 4, (2011).
206. S. Elmas, T. Nann, M. R. Andersson, Deposition Methods of Graphene as Electrode Material for Organic Solar Cells Rajni Garg, *Adv. Energy Mater.*, (2016).
207. P. S. Das, S. H. Park, K. Y. Baik, J. W. Lee, J. Y. Park, Thermally reduced graphene oxide-nylon membrane based epidermal sensor using vacuum filtration for wearable electrophysiological signals and human motion monitoring, *Carbon*, 158, (2020).
208. C. Travan, M. Mischitz, A. Zöpfl, U. Krumbein, P. Makaram, Development of Graphene Based Inks for Deposition via Inkjet Printing for Sensing Application, *Proceedings*, 2, (2018).
209. E. K. Goharshadi, G. Akhlamadi, S. Jalil Mahdizadeh, Investigation of Graphene Oxide Nanosheets Dispersion in Water Based on Solubility Parameter: A Molecular Dynamics Simulation Study, *RSC Advances*, 5, 129, (2015).
210. M. Wang, Y. Niu, J. Zhou, H. Wen et al. Dispersion and Aggregation of Graphene Oxide in Aqueous Media, *Nanoscale*, 8, (2016).
211. V. V. Neklyudov, N. R. Khafizov, I. A. Sedov, A. M. Dimiev, New Insights to Solubility of Graphene Oxide in Water and Alcohols, *Phys. Chem. Chem. Phys.*, 19, (2017).
212. J. I. Paredes, S. Villar-Rodil, A. Martinez-Alonso, aJ. M. D. Tascon, Graphene Oxide Dispersions in Organic Solvents, *Langmuir*, 24, (2008).
213. S. Park, J. An, I. Jung, R. D. Piner, S. J. An, X. Li, A. Velamakanni, R. S. Ruoff, Suspensions of Highly Reduced Graphene Oxide in a Wide Variety of Organic Solvents, *Nano Lett.*, 9, 4, (2009).

214. Y. Hernandez, M. Lotya, D. Rickard, S. D. Bergin, J. N. Coleman, Measurement of Multicomponent Solubility Parameters for Graphene Facilitates Solvent Discovery, *Langmuir*, 26, 5, (2010).
215. J. Jang, V. H. Pham, S. H. Hur, J. S. Chung, Dispersibility of reduced alkylamine-functionalized graphene oxides in organic solvents, *Journal of Colloid and Interface Science*, 424, (2014).
216. M. S. Khan, A. Shakoor, G. T. Khan, S. Sultana, A. Zia, A Study of Stable Graphene Oxide Dispersions in Various Solvents, *J. Chem. Soc. Pak.*, 37, 1, (2015).
217. V. V. Neklyudov, V. N. Agieienko, M. A. Ziganshin, A. M. Dimiev, On the solvation behavior of graphene oxide in ethylene glycol/water mixtures, *ChemPhysChem*, 19, 11, (2018).
218. B. Konkana, S. Vasudevan, Understanding Aqueous Dispersibility of Graphene Oxide and Reduced Graphene Oxide through pKa Measurements, *J. Phys. Chem. Lett.*, 3, (2012).
219. M. Ayan-Varela, J.I. Paredes, S. Villar-Rodil, R. Rozada, A. Martinez-Alonso, J.M.D. Tascon, A quantitative analysis of the dispersion behaviour of reduced graphene oxide in solvents, *Carbon*, 75, (2014).
220. M. Y. Song, Y. S. Yun, N. R. Kim, H.-J. Jin, Dispersion stability of chemically reduced graphene oxide nanoribbons in organic solvents, *RSC Adv.*, 6, (2016).
221. J. H. Hildebrand, The Solubility of Non-Electrolytes; *New York: Reinhold*, (1936).
222. M. Belmares, M. Blanco, W. A. Goddard, III, R. B. Ross et al., Hildebrand and Hansen Solubility Parameters from Molecular Dynamics with Applications to Electronic Nose Polymer Sensors, *J. Comput. Chem.*, 25, 15, (2004).
223. D. Patterson, G. Delmas, New Aspects of Polymer Solution Thermodynamics, *Off. Dig. Fed. Soc. Paint Technol.*, 34, 450, (1962).
224. J. H. Hildebrand, R. L. Scott, Regular Solutions, (1962).
225. D. Delmas, D. Patterson, T. Somcynsky, Thermodynamics of Polyisobutylene-n-Alkane Systems, *J. Polym. Sci.*, 57, (1962).
226. Hansen, C.M., The Three-Dimensional Solubility Parameter - Key to Paint Component Affinities I. - Solvents, Plasticizers, Polymers, and Resins, *J. Paint Techn.*, 39, 505, (1967).

227. J. Burke, Solubility Parameters: Theory and Application, (1984).
228. R. L. Feller, N. Stolow, E.H. Jones, On picture varnishes and their solvents, (1971).
229. S. Süß, T. Sobisch, W. Peukert, D. Lerche, D. Segets, Determination of Hansen parameters for particles: A standardized routine based on analytical centrifugation, *Advanced Powder Technology*, 29, (2018).
230. C. M. Hansen, Hansen Solubility Parameters, A User's Handbook, (2000).
231. F. M. Raoult, General law of vapor pressures of solvents, *Comptes rendus*, 104, (1886).
232. C. M., Hansen, Solvents for Coatings, *Chemical Technology*, 2, 9, (1972).
233. www.hansen-solubility.com
234. K.-Y. Liang, W.-D. Yang, Prediction the concentration of graphite direct exfoliation by liquid solution with solubility parameters map, *AIP Advances*, 8, (2018).
235. H.J. Salavagione, J. Sherwood, M. De bruyn, V.L. Budarin, G.J. Ellis, a J.H. Clark, P.S. Shuttleworth, Identification of High-Performance Solvents for the Sustainable Processing of Graphene, *Green Chem.*, 19, (2017).
236. Y. Hernandez, M. Lotya, D. Rickard, S. D. Bergin, J. N. Coleman, Measurement of Multicomponent Solubility Parameters for Graphene Facilitates Solvent Discovery, *Langmuir*, 26, 5, (2009).
237. C. M. Hansen, A.L. Smith, Using Hansen solubility parameters to correlate solubility of C₆₀ fullerene in organic solvents and in polymers, *Carbon*, 42, (2004).
- 238 D. Konios, M. M. Stylianakis, E. Stratakis, E. Kymakis, Dispersion behaviour of graphene oxide and reduced graphene oxide, *Journal of Colloid and Interface Scienc*, 430, (2014).
239. J. Brandrup, E. H. Immergut, E. A. Grulke, Polymer Handbook, (1999).
240. D. R. Chowdhury, C. Singh, A. Paul, Role of graphite precursor and sodium nitrate in graphite oxide synthesis, *RSC Adv.*, 4, (2014).
241. M. Aliofkhazraei, N. Ali, W. I. Milne, C. S. Ozkan, S. Mitura, J. L. Gervasoni, Graphene Science Handbook, (2016).

242. A. M. Dimiev, J. M. Tour, Mechanism of Graphene Oxide Formation, *ACS Nano*, 8, 3, (2014).
243. S. Verma, H.P. Mungse, N. Kumar, et al. Graphene oxide: An efficient and reusable carbocatalyst for aza-Michael addition of amines to activated alkenes. *Chem. Commun.*, 47, (2011)
244. I. Childres, L. A. Jauregui, W. Park, H. Cao, Y. P. Chen, Raman Spectroscopy of Graphene and Related Materials, *New Developments in Photon and Materials Research*, 2013).
245. D. J. Gardiner, Practical Raman Spectroscopy, *Springer-Verlag: Berlin*, (1989).
246. A. Kaniyoor, S. Ramaprabhu, A Raman spectroscopic investigation of graphite oxide derived graphene, *AIP Advances*, 2, (2012).
247. L. Xu, L. Cheng ,Graphite Oxide under High Pressure: A Raman Spectroscopic Study, *Journal of Nanomaterials*, (2013).
248. R. Saito , M. Hofmann , G. Dresselhaus , A. Jorio & M. S. Dresselhaus, Raman spectroscopy of graphene and carbon nanotubes, *Advances in Physics*, 60, 3, (2011).
249. A. C. Ferrari, J. C. Meyer, V. Scardaci, C. Casiraghi et al., Raman Spectrum of Graphene and Graphene Layers, *Phys. Rev. Lett.*, 97, (2006).
250. C. R. Yang, S. F. Tseng, Y. T. Chen, Characteristics of Graphene Oxide Films Reduced by Using an Atmospheric Plasma System, *Nanomaterials*, 8, 802, (2018).
251. L. G. Cancado, A. Jorio, E. H. Martins Ferreira, F. Stavale et al. Quantifying Defects in Graphene via Raman Spectroscopy at Different Excitation Energies, *Nano Lett.*, 11, (2011).
252. www.hielscher.com
253. M. Xu, J. Chai, N. Hu, D. Huang, Y. Wang, X. Huang, H. Wei, Z. Yang, Y. Zhang, Facile synthesis of soluble functional graphene by reduction of graphene oxide via acetylacetone and its adsorption of heavy metal ions, *Nanotechnology*, 25, (2014).
254. S. Abbott, C. M. Hansen, H. Yamamoto, Hansen Solubility Parameters in Practice, (2008).
255. S. Azizighannad, S. Mitra, Stepwise Reduction of Graphene Oxide (GO) and Its Effects on Chemical and Colloidal Properties, *Scientific Reports*, 8, (2018).

-
256. B. Tang, X. Yun, Z. Xiong, X. Wang, Formation of Graphene Oxide Nanoscrolls in Organic Solvents: Toward Scalable Device Fabrication, *ACS Appl. Nano Mater.*, *1*, (2018).
257. S. Park, J. An, I. Jung, R. D. Piner, S. J. An, X. Li, A. Velamakanni, R. S. Ruoff, Colloidal Suspensions of Highly Reduced Graphene Oxide in a Wide Variety of Organic Solvents, *Nano Lett.*, *9*, *4*, (2009).
258. R. J. Hunter, Zeta Potential in Colloid Science; Principles and Applications, *Elsevier*, (1981).
259. D. Hanaor, M. Michelazzi, C. Leonelli, C. C. Sorrell, The effects of carboxylic acids on the aqueous dispersion and electrophoretic deposition of ZrO₂, *Journal of the European Ceramic Society*, *32* (2012).
260. R. Greenwood, K. Kendall, Selection of Suitable Dispersants for Aqueous Suspensions of Zirconia and Titania Powders using Acoustophoresis, *Journal of the European Ceramic Society*, *19* (1999).
261. Zeta Potential of colloids in water and waste water, *American Society for Testing and Materials*, (1985).
262. P. M. V. Raja, A. R. Barron, Physical Methods in Chemistry and Nano Science, *Connexions*, Rice University, (2012).
263. X. Xu, Z. Yu, Y. Zhu, B. Wang, Effect of sodium oleate adsorption on the colloidal stability and zeta potential of detonation synthesized diamond particles in aqueous solutions, *Diamond & Related Materials*, *14*, (2005).
264. M. Cerbelaud, A. Videcoq, F. Rossignol, M.A. Piechowiak, D. Bochicchio, R. Ferrando, Heteroaggregation of ceramic colloids in suspensions, *Advances in Physics: X.*, *2*, (2017).
265. H. Cao, B. An, Y. Wang, K. Zhou, Naiyan Lu, Investigation of Surfactant AOT Mediated Charging of PS Particles Dispersed in Aqueous Solutions, *Coatings*, *9*, *471*, (2019).
266. K. Cacia, F. Ordoñez, C. Zapata, B. Herrera, E. Pabón, R. Buitrago-Sierra, Surfactant concentration and pH effects on the zeta potential values of alumina nanofluids to inspect stability, *Colloids and Surfaces A: Physicochemical and Engineering Aspects*, *583*, (2019).
267. L. Jiang, L. Gao, J. Sun, Production of aqueous colloidal dispersions of carbon nanotubes, *Journal of Colloid and Interface Science*, *260*, (2003).

-
268. E. F. de la Cruz, Y. Zheng, E. Torres, W. Li, W. Song, K. Burugapalli, Zeta Potential of Modified Multi-walled Carbon Nanotubes in Presence of poly (vinyl alcohol) Hydrogel, *Int. J. Electrochem. Sci.*, 7, (2012).
269. L. Helian, Q. Yanhua, Dispersion, sedimentation and aggregation of multi-walled carbon nanotubes as affected by single and binary mixed surfactants, *R. Soc. open sci.*, 6, (2019).
270. B. Şimşek, G. Ultav, H. Korucu, A. Yartaşı, Improvement of the Graphene Oxide Dispersion Properties with the Use of TOPSIS Based Taguchi Application, *Periodica Polytechnica Chemical Engineering*, 62, 3, (2018).
271. D. Li, M. B. Muller, S. Gilje, Richard B. Kaner, G. G. Wallace, Processable aqueous dispersions of graphene nanosheets, *Nature Nanotechnology*, 3, (2008).
272. U. K. Sur, A. Saha, A. Datta et al., Synthesis and characterization of stable aqueous dispersions of graphene, *Bull. Mater. Sci.*, 39, 1, (2016).
273. S. Kashyap, S. Mishra, S. K. Behera, Aqueous Colloidal Stability of Graphene Oxide and Chemically Converted Graphene, *Journal of Nanoparticles*, (2014).
274. J. A. Gahete, A. Benítez, R. Otero et al. A Comparative Study of Particle Size Distribution of Graphene Nanosheets Synthesized by an Ultrasound-Assisted Method, *Nanomaterials (Basel)*, 9, 2, (2019).
275. P.F.M. Nogueira, D. Nakabayashi, V. Zucolott, The effects of graphene oxide on green algae *Raphidocelis subcapitata*, *Aquat. Toxicol.*, 166, (2015).
276. N.S. Andryushina, O. L. Stroyuk, I. B. Yanchuk, A. V. Yefanov, A dynamic light scattering study of photochemically reduced colloidal graphene oxide, *Colloid Polym Sci*, 292, (2014).
277. B. J. Berne, R. Pecora, *Dynamic Light scattering*, (1975).
278. E. H. M. Sakho, E. Allahyari, O. S. Oluwafemi, S. Thomas, Nandakumar Kalarikkal, *Dynamic Light Scattering (DLS)*, (2017).
279. J. Nickel, R. Angelstorf, C. Bienert, S. Burkart, S. Gabsch, et al., Dynamic light-scattering measurement comparability of nanomaterial suspensions, *J. Nanopart. Res.*, 16, (2014).
280. C. Bantz, O. Koshkina, T. Lang, H.J. Galla, C.J. Kirkpatrick, R.H. Stauber, M. Maskos, The surface properties of nanoparticles determine the agglomeration state and the size of the particles under physiological conditions, *J. Nanotechnol.*, 5, (2014).

281. T. Szaboa, P. Maronib, I. Szilagyia, Size-Dependent Aggregation of Graphene Oxide, *Carbon*, 130, (2020).
282. T. Tadros, *Encyclopaedia of Colloid and Interface Science*, (2013).
283. International Standard ISO13321 Methods for Determination of Particle Size Distribution Part 8: Photon Correlation Spectroscopy, International Organisation for Standardisation (ISO) (1996).
284. International Standard ISO22412 Particle Size Analysis – Dynamic Light Scattering, International Organisation for Standardisation (ISO) (2008).
285. *Dynamic Light Scattering Common Terms Defined*, Malvern Instruments Worldwide, (2011).
286. R. H. Müller, R. Schuhmann, K. Thode, *Teilchengrößenmessung der Laborpraxis, Wissenschaftliche Verlagsgesellschaft*, (1996).
287. S. Bengtson, K. Kling, A. Mette Madsen, A. W. Noergaard, et al., No Cytotoxicity or Genotoxicity of Graphene and Graphene Oxide in Murine Lung Epithelial FE1 Cells in Vitro, *Environmental and Molecular Mutagenesis*, 57, (2016).
288. Weilie Zhou, Robert P. Apkarian, Zhong Lin Wang, David Joy, *Fundamentals of Scanning Electron Microscopy*, Springer New York, (2007).
289. W.-P. Shih, L.-C. Tsao, C.-W. Lee, M.-Y. Cheng, C. Chang, Y.-J. Yang, K.-C. Fan, Flexible Temperature Sensor Array Based on a Graphite-Polydimethylsiloxane Composite, *Sensors*, 10, (2010).
290. L. S. Montagna, F. de Carvalho Fim, G. Barrera Galland, N. R. de Souza Basso, Synthesis of Poly(propylene)/Graphite Nanocomposites by in Situ Polymerization, *Macromol. Symp.*, (2011).
291. V. Mani, S.-M. Chen, B.-S. Lou, Three-Dimensional Graphene Oxide-Carbon Nanotubes and Graphene-Carbon Nanotubes Hybrids, *Int. J. Electrochem. Sci.*, 8, (2013).
292. B. Kartick and S. K. Srivastava, Simple Facile Route for the Preparation of Graphite Oxide and Graphene, *J. Nanosci. Nanotechnol.*, 11, (2011).
293. R. Agrawal, C. Chen, and C. Wang, Lithium-Ion Capacitor Based on Electrodes Constructed Via Electrostatic Spray Deposition, *ECS Transactions*, 72, 8, (2016).

294. J. Jagiełło, Ma. Sekuła-Stryjewska, S.Noga, E. Adamczyk et al. Impact of Graphene-Based Surfaces on the Basic Biological Properties of Human Umbilical Cord Mesenchymal Stem Cells: Implications for Ex Vivo Cell Expansion Aimed at Tissue Repair, *Int. J. Mol. Sci.*, 20, (2019).
295. S. E. Drewniak, T. P. Pustelny, R Muzyka², A. Plis, Studies of physicochemical properties of graphite oxide and thermally exfoliated/reduced graphene oxide, *Pol. J. Chem. Tech.*, 17, 4, (2015).
296. S. Dubin, S.Gilje, K. Wang, V. C. Tung, K. Cha et al. A One-Step, Solvothermal Reduction Method for Producing Reduced Graphene Oxide Dispersions in Organic Solvents, *ACS Nano*, 4, 7, (2010).
297. A. Al-Saygh, D. Ponnamma, M. A. AlMaadeed, P. Vijayan P, A.Karim, M. K. Hassan, Flexible Pressure Sensor Based on PVDF Nanocomposites Containing Reduced Graphene Oxide-Titania Hybrid Nanolayers, *Polymer*, 9, 33, (2017).
298. K. Gonzatti, P. A. Netz, L. A. Fielc, A. R. Pohlmann, Colloidal Dispersion Stability: Kinetic Modeling of Agglomeration and Aggregation Guilherme, *J. Braz. Chem. Soc.*, 26, 2, (2015).
299. Physical Stability of Disperse Systems, Lubrizol Life Science, (2019).